



HAL
open science

P-T-deformation-time evolution of the Akeyasi HP/UHP complex (SW-Tianshan, China) and implications for subduction dynamics

Zhou Tan

► **To cite this version:**

Zhou Tan. P-T-deformation-time evolution of the Akeyasi HP/UHP complex (SW-Tianshan, China) and implications for subduction dynamics. Earth Sciences. Sorbonne Université; Institute of geology and geophysics, Chinese academy of sciences, 2018. English. NNT : 2018SORUS185 . tel-02451564

HAL Id: tel-02451564

<https://theses.hal.science/tel-02451564>

Submitted on 23 Jan 2020

HAL is a multi-disciplinary open access archive for the deposit and dissemination of scientific research documents, whether they are published or not. The documents may come from teaching and research institutions in France or abroad, or from public or private research centers.

L'archive ouverte pluridisciplinaire **HAL**, est destinée au dépôt et à la diffusion de documents scientifiques de niveau recherche, publiés ou non, émanant des établissements d'enseignement et de recherche français ou étrangers, des laboratoires publics ou privés.

Sorbonne Université

ED 398 - Géosciences, Ressources Naturelles et Environnement

Institut des Sciences de la Terre de Paris

Équipe Dynamique et Évolution des Marges et Orogènes

Pour l'obtention du grade de :

DOCTEUR

**P-T-deformation-time evolution of the Akeyasi HP/UHP complex
(SW-Tianshan, China) and implications for subduction dynamics**

Présentée et soutenue par

Zhou TAN

Thèse de doctorat en Science de la Terre

Présentée et soutenue publiquement le 12 Décembre 2018

Devant un jury composé de :

Philippe AGARD (Professeur-Sorbonne Université)	Directeur de thèse
Jun GAO (Professeur-Chinese Academy of Sciences)	Co-directeur de thèse
Karel SCHULMANN (Professeur-Université de Strasbourg)	Rapporteur
Yann ROLLAND (Maître de Conférences-Université Nice-Sophia Antipolis)	Rapporteur
Christian CHOPIN (Directeur de Recherches-Ecole Normale Supérieure)	Examineur
Pierre TRAP (Maître de Conférences-Université de Franche-Comté)	Examineur
Loïc LABROUSSE (Professeur-Sorbonne Université)	Examineur
Bo WAN (Professeur-Chinese Academy of Sciences)	Invité

Résumé

Les zones de subduction sont des frontières de plaques convergentes le long desquelles une plaque plonge sous une autre. Les processus associés à la dynamique des zones de subduction (séismes, transfert de matière ou de fluide ou encore le couplage mécanique à l'interface des plaques) contrôlent au première ordre la tectonique des plaques et le recyclage de matière dans le manteau, et impactent fortement une large partie de la population mondiale vivant au niveau de ces frontières de plaques. Cependant, ces processus restent relativement peu contraints car inaccessibles à l'observation directe.

Ainsi, ce projet de thèse a pour objectif de contraindre les processus gouvernant les zones de subduction à environ 80 km, profondeur critique au-delà de laquelle des données géophysiques et des modèles montrent un changement du couplage mécanique et les roches océaniques ne sont la plupart du temps pas récupérées. Pour ce faire, notre travail s'est concentré sur la caractérisation de matériels fossiles équilibrés à de telles profondeurs le long d'une zone de subduction fossile, qui se trouve à présent exhumée au niveau de la Ceinture Métamorphique du Sud Tianshan (Chine).

Cette ceinture métamorphique est en partie structurée d'un empilement de roches métavolcanoclastiques de haute pression (HP) à ultra haute pression (UHP) sur une épaisseur (inhabituelle) de 5 km. Ces unités contiennent localement des fragments d'éclogites préservant des reliques de coésite. Cette séquence d'environ 30 km d'épaisseur forme le complexe métamorphique d'Akeyazi (AMC) dans la vallée de la Kebuerte. Des études structurales portant sur l'AMC ont précédemment révélé que sa géométrie actuelle est semblable à celle d'un dôme métamorphique formé d'un « mélange » de roches HP/UHP.

A partir d'une étude de terrain détaillée, couplée à une fine étude pétrologique, géochimique et isotopique, il nous a été cependant possible de subdiviser la structure de complexe métamorphique en six sous-unités d'échelles kilométriques possédant des histoires P-T-temps-déformations bien distinctes. Au moins quatre de ces six unités ont été enfouies en zones de subductions: l'unité UH (480-560°C et 2,75 GPa, soit ~ 85 km

de profondeur), l'unité EB (505°C et ~2,1GPa, soit ~65 km de profondeur), l'unité MU (485°C et ~1,45GPa, soit ~ 45 km de profondeur) et l'unité GT (470-520°C et > 0,7-1,0 GPa, soit > 30 km de profondeur). Ces unités sont également caractérisées par une déformation pénétrative développée dans le faciès des schistes bleus et associée à un cisaillement top vers le nord synchrone de leur exhumation.

La reconstitution de l'histoire détaillée P-T-temps d'un échantillon représentatif des éclogites océaniques à coésite suggère un pré-pic d'enfouissement dans des conditions de UHP il y a 318 Ma (à $\sim 2,95 \pm 0,2$ GPa et $510 \pm 20^\circ\text{C}$) suivi d'un pic d'enfouissement à environ 315 Ma ± 5 . D'autre part, des datations ^{40}Ar - ^{39}Ar in situ à la sonde laser sur des phengites et U-Pb sur zircon pour treize échantillons donnent des âges pour le pic d'enfouissement de 320 ± 1 , 332 ± 2 , 359 ± 2 et 280-310 Ma pour les sous-unités UH, EB, MU et GS (GS1, GS2 et GT) respectivement. Cela suggère l'existence de plusieurs épisodes transitoires de détachement de matériel de la plaque plongeante lors de la subduction du Sud Tianshan sous la marge continentale Paléo-Kazakhstan. Le gradient métamorphique diminue d'environ $12^\circ\text{C}/\text{km}$ à environ 5 - $7^\circ\text{C}/\text{km}$ au cours du temps, ce qui reflète possiblement le refroidissement progressif du système en subduction. La juxtaposition et l'exhumation des sous-unités UH, EB, MU et GT à des profondeurs crustales (environ 20 km) et à une vitesse de l'ordre de 1-3mm/an s'est terminée aux alentours de 290-300 Ma. L'existence d'unités métavolcanoclastiques à glaucophane âgées d'environ 300 Ma (GT et une partie de l'unité GS1) suggère que la subduction était encore active à la fin du Carbonifère.

L'étude des compositions en éléments majeurs et traces des grenats révèle une zonation annulaire (notamment en Mn, Y et terres rares lourdes) contemporaine d'une augmentation transitoire de la température d'environ 80°C (montrée par le Zr dans le rutile). Les modèles de croissance à diffusion limitante du grenat supportent l'idée d'une excursion thermique transitoire d'une durée d'environ 300 000 ans afin de reproduire la zonation observée dans les grenats (en prenant en compte une durée de croissance totale de 5 Ma pour le grenat). Nous proposons qu'une telle excursion thermique est liée au mouvement rapide des morceaux océaniques UHP vers le coin de manteau plus chaud.

Abstract

This study attempts to characterize, using a field, petrological, geochemical and isotopic approach, some key fossil fragments of material equilibrated along the subduction plate boundary, now exhumed and exposed in the Chinese South Tianshan Metamorphic Belt (STMB) as high-pressure low-temperature (HP-LT) metamorphic rocks. Subduction zone processes (e.g., earthquake generation, mass/fluid transfer or mechanical coupling), which control Earth dynamics or material recycling into the mantle and impact a large fraction of the human population, remain indeed poorly constrained and inaccessible to direct observation. We herein shed light on some of these processes, across a critical depth range of ~80 km, beyond which geophysical evidence and models infer a change in mechanical coupling and oceanic rocks are usually not recovered. This study focuses on an unusually thick (~5 km) pile of well-preserved HP/UHP metavolcanoclastics, wrapping eclogite boudins/slices and preserving pervasive coesite relics in both lithologies, along a ~30km-long transect across the Akeyazi metamorphic complex (AMC) in the Kebuerte valley.

Structural investigations reveal that the present-day geometry of the AMC is that of a metamorphic dome preserving evidence for internal nappe stacking. What was previously described as a HP/UHP “mélange” should be subdivided into several coherent, km-scale, essentially metavolcanoclastic tectonic units bearing contrasting P-T-time-deformation histories. At least four of the six sub-units identified here, namely the UH (480-560°C and 2.75 GPa), EB (~2.1 GPa and 505°C), MU (~1.45 GPa and 485°C) and GT units (>~0.7-1.0 GPa and 470-520°C) experienced subduction and were buried to depths of ~85, 65, 45 and 30 km respectively. Pervasive deformation following eclogite and/or blueschist-eclogite peak burial is marked by pervasive BS facies, exhumation-related shear senses with a top to the north component.

The reconstruction of the detailed P-T-time-isotopic history of a representative coesite-bearing oceanic eclogite suggests pre-peak burial to UHP conditions at 318 Ma (~2.95 GPa \pm 0.2 and 510 °C \pm 20) and peak ages around 315 \pm 5 Ma. In situ laser probe ⁴⁰Ar-³⁹Ar radiometric dating of phengite and zircon U-Pb dating on thirteen samples

yield peak burial ages of 320 ± 1 , 332 ± 2 , 359 ± 2 Ma and ~ 280 - 310 Ma, respectively, for the UH, EB, MU and GS facies units (GS1, GS2 and GT). This suggests the existence of several short-lived episodes of detachment of material from the downgoing plate during subduction of the South Tianshan ocean beneath the Paleo Kazakhstan Continent. The tectono-metamorphic evolution from $\sim 12^\circ\text{C}/\text{km}$ to ~ 5 - $7^\circ\text{C}/\text{km}$ with time may reflect progressive cooling of the subduction system. Juxtaposition and exhumation of the UH, EB, MU and GT units to mid-crustal depth (~ 20 km), at rates on the order of 1-3 mm/yr, was accomplished around 290-300 Ma. The existence of ~ 300 Ma glaucophane-bearing metavolcanoclastic units (i.e., GT and part of the GS1 unit) suggests that subduction was still active during the Late Carboniferous.

Petrological investigations on garnet major and trace element chemistry reveal a specific zoning (i.e., in Mn, Y and heavy rare earth elements) coeval with a transient $\sim 80^\circ\text{C}$ increase in temperature (revealed by Zr-in-rutile thermometry). Diffusion-controlled garnet growth modeling supports the necessity of a ~ 300 kyr transient thermal excursion to reproduce this garnet zonation (assuming a 5 Myr duration for the overall garnet growth). Such a transient thermal excursion is tentatively tied to the fast movement of detached UHP oceanic slices towards the hotter mantle wedge.



—— *An untouched photography took by sony a77 (17mm, F8, 1/100) during the 1st year (fall 2013) field excursion of the PhD candidate in the Akeyazi-Kongguerbulake area, Zhaosu county, Xinjiang province, China.*

This beautiful scenery indeed inspires my interest and love for natural earth sciences and unknown fields. Just as Liu CiXin wrote down in <the ball lightning>: the key to a wonderful and unrepentant life is to fascinate something, forever young.

Acknowledgements

About three years ago, I arrived the 'Capitale romantique'-Paris to seek further studying, with feeling like 'a homeless ranger'. Not exaggerated, the fact that I am a 26 years old father with a 2 years old daughter essentially gave me a very limited time for abroad studying, before she really grew up enough to remember the time she should have with her father. Family issues also make it impossible to move my wife and daughter to stay with me in Paris, that is why when everybody joked to me that you worked too hard, I always replied time is not enough for me to enjoy the life and work in Paris.

As a poor self-control guy with also poor foundation of geology, hard-working is probably the only way, for me, to manage to finish this PhD thesis, a prerequisite of a promising future. The beginning of my PhD thesis here is difficult and the rest time before I really finished the writing of this PhD thesis, for sure, is not easy at all, since as a young and 'remote' father I am always struggling between work and family stuff. The accompanying of several TACATACA & close friends (Guillaume, Michele and Mathieu) really dilutes those pressures and makes me survived. They tolerate and enjoy the difference of culture, behavior and habit between eastern and western, and help me a lot in both life living and working. Despite some complaints, from my wife and parents, to remind me of coming back as soon as possible that really make me depressed, I inwardly understand their 'misunderstanding'. Because the foundation of a promising future that I am seeking abroad, in fact, stands on the sacrificing of their life, especially for my daughter. Heartfelt gratefulness, therefore, must be typed down in this thesis for

whatever supports or pressures from my family. It is my responsibility and pleasure to live for them.

Last but the most important, the gratefulness for my two PhD superiors. As a Chinese, our 5000 years history civilized us to keep best respect to our teacher--‘One day as a teacher, a life as a father’. Great thanks should be given to my Chinese superior prof. Jun Gao who always tolerated my weakness and guided me with unwearied helps. Although there are some argument and misunderstanding between us, mainly because of my immature behavior and bad performance. Speechless acknowledgement must be typed down to my French ‘boss’ prof. Philippe Agard. His meticulous help, during my three years PhD life in Paris, really motivates me to move forward. The unrestrained thought of his guided me to think more logically and independently. He also led by example to teach me how to behave as a rigorous, neutral and selfless geologist. For sure, I am still way far away from the standard of a good student if considering how good and unsurpassable their previous PhD students are (e.g., S. Angiboust, P. Yamato for P.A.; Ji-Lei Li, Xin-Shui Wang for J.G.), I therefore never dare to dream that they will be proud of me. However, no matter what happens in the future, whatever be rich or poor, be in power or stay unknown in a quiet corner of the world, I sincerely and honestly maintain proud and grateful to the fact that I used to be they PhD student, and they indeed sharpened my thought, civilized my ages and visualized my time.

Contents

<i>Résumé</i>	- 2 -
<i>Abstract</i>	- 4 -
<i>Acknowledgements</i>	- 6 -
<i>Contents</i>	- 9 -
1. Introduction	- 17 -
1.1. Plate Tectonics and Subduction	- 17 -
1.2. Fossil Subduction Remnants: An Ideal Target?	- 19 -
1.3. Burial and Recovery of Formerly Subducted Lithologies	- 22 -
1.4. Using The STMB to probe the plate interface: a fossil, deeply buried and cold package (dominantly) made of metavolcanoclastics	- 25 -
1.5. Structure of the Thesis	- 29 -
2. Geological Setting of the STMB	- 30 -
2.1. Geological Background	- 30 -
2.2. The Akeyazi Metamorphic Complex	- 32 -
3. Methods	- 40 -
3.1. Field Work	- 40 -
3.2. Bulk-rock and Mineral Chemistry	- 41 -
3.2.1. Bulk-rock Major and Trace Elements	- 41 -
3.2.2. Mineral Major and Trace Elements.....	- 42 -
3.2.3. Zircon Oxygen Isotope.....	- 43 -
3.3. P-T Constraints	- 44 -
3.3.1. Perple_X Pseudosection Modeling	- 44 -
3.3.2. THERMOCALC Multi-equilibrium Average PT	- 45 -
3.3.3. Zr-in-Rutile Thermometry	- 46 -
3.3.4. Raman Spectrometry Carbonaceous Material Thermometry (RSCM)	- 47 -
3.3.5. Ti-in-Biotite Thermometry	- 48 -
3.4. Radiometric Constraints	- 48 -
3.4.1. Zircon U-Pb Geochronology.....	- 48 -
3.4.2. Sm-Nd Geochronology	- 50 -
3.4.3. ⁴⁰ Ar- ³⁹ Ar Step-heating Geochronology.....	- 51 -
	- 9 -

3.4.4. ^{40}Ar - ^{39}Ar In Situ Laser Ablation Probing Geochronology	- 52 -
4. <i>P-T-time-isotopic evolution of coesite-bearing eclogites: Implications for exhumation processes in SW Tianshan</i>	- 54 -
Abstract.....	- 55 -
4.1. Introduction.....	- 56 -
4.2. Geological setting	- 58 -
4.2.1. The Chinese Southwestern Tianshan HP-UHP/LT metamorphic complex	- 58 -
4.2.2. Previous age constraints on the P-T evolution of tectonic slices/blocks	- 60 -
4.2.3. Controversy on regional exhumation	- 62 -
4.3. Sample selection and whole-rock composition	- 64 -
4.4. Petrology.....	- 66 -
4.5. Mineral chemistry	- 69 -
4.5.1. Garnet.....	- 70 -
4.5.2. Omphacite	- 71 -
4.5.3. Amphibole.....	- 73 -
4.5.4. White mica	- 73 -
4.5.5. Epidote-group minerals.....	- 73 -
4.5.6. Chlorite	- 74 -
4.5.7. Rutile/Titanite	- 74 -
4.6. Trace-element pattern of zircon and garnet.....	- 74 -
4.6.1. Trace-element pattern and oxygen isotopes of zircon.....	- 75 -
4.6.2. Trace-element pattern of garnet	- 77 -
4.7. Geochronology and oxygen isotope	- 79 -
4.7.1. U-Pb dating and isotopes of zircon	- 79 -
4.7.2. Sm-Nd isotopic chronology	- 81 -
4.8. Pressure-Temperature estimates	- 82 -
4.8.1. Multi-equilibrium thermobarometry	- 82 -
4.8.2. Phase equilibrium modeling.....	- 84 -
4.9. Discussion.....	- 86 -
4.9.1. Nature of the protolith and P-T-(fluid) constraints	- 86 -
4.9.2. Linking garnet with zircon growth.....	- 89 -
4.9.3. Age constraints and regional-scale tectonic implication	- 92 -
4.10. Conclusions.....	- 95 -
ACKNOWLEDGMENTS	- 97 -
APPENDIX.....	- 97 -
Analytical methods	- 97 -

Supplementary Figures and Tables:.....	103 -
5. Concordant pulse in Mn, Y and HREEs concentrations during UHP eclogitic garnet growth: transient rock dynamics along a cold subduction plate interface	106 -
Abstract.....	106 -
5.1. Introduction.....	107 -
5.2. Geological setting	109 -
5.3. Sample description.....	112 -
5.4. Mineral geochemistry	113 -
5.4.1. Garnet compositional profile and mapping	113 -
5.4.2. Major/trace elements composition of associated minerals	116 -
5.4.3. Trace elements composition of rutile and Zr-in-rutile thermometry.....	117 -
5.5. Thermodynamic modeling.....	119 -
5.6. Diffusion modeling.....	120 -
5.6.1. Influence of key parameters (for a linear T-t path).....	121 -
5.6.2. Parameter space and boundary conditions.....	122 -
5.6.3. Modeling garnet zoning with a transient thermal pulse.....	126 -
5.7. Discussion.....	127 -
5.7.1. Interpretation of petrological patterns.....	127 -
5.7.2. Necessity of a transient thermal pulse and implications for thermodynamic modeling-	131 -
5.7.3. Geodynamic significance of a transient thermal pulse	133 -
5.8. Conclusion.....	136 -
Acknowledgements.....	136 -
Appendix A. Thermodynamic modeling for the estimate of mineral modes evolution and effective partition coefficient	137 -
Appendix B. Finite volume diffusion modeling	140 -
Appendix C. Analytical methods	143 -
Major elements electron microprobe analyses and mapping.....	143 -
Laser-ablation ICP-MS trace elements analyses	144 -
Zirconium contents of rutile electron microprobe analyses.....	144 -
Supplementary figures and tables	146 -
6. Contrasting P-T-deformation-time evolutions in the SW-Tianshan (Akeyasi HP/UHP complex, China): implications for Late Carboniferous subduction dynamics.....	153 -
Abstract.....	155 -

6.1. Introduction	- 156 -
6.2. Geological Setting of SW-Tianshan Accretionary Complex	- 157 -
6.3. Structural Data	- 160 -
6.3.1. Overall structural organization of the Akeyasi Metamorphic Complex.....	- 163 -
6.3.2. Deformation stages and deformation patterns.....	- 167 -
6.4. Sampling strategy and sample description	- 170 -
6.5. Analytical Methods	- 176 -
6.5.1. Whole-rock chemistry.....	- 176 -
6.5.2. Mineral Chemistry	- 177 -
6.5.3. Thermobarometry	- 177 -
6.5.4. Radiochronology.....	- 179 -
6.6. Results	- 183 -
6.6.1. Bulk chemistry of major lithologies.....	- 183 -
6.6.2. Mineral compositions.....	- 186 -
6.6.3. Thermobarometric results	- 193 -
6.6.4. Radiochronological results.....	- 196 -
6.7. Discussions	- 199 -
6.7.1. Distinct metamorphic sub-units?.....	- 199 -
6.7.2 P-T-t trajectories, exhumation rates and tectonic stacking.....	- 203 -
6.7.3 Implications for subduction dynamics and Late Carboniferous subduction history	- 207 -
6.8. Conclusions	- 208 -
Acknowledgements	- 210 -
Supplementary figures and tables	- 211 -
7. Discussion and Perspective	- 220 -
7.1. Insight from regional P-T-time-lithologies review	- 220 -
7.2. Structure and Deformation Pattern	- 225 -
7.3. P-T constraints	- 227 -
7.4. Radiometric age constraints Implication for Late Carboniferous cold subduction dynamics	- 229 -
7.5. A witness of transient rock dynamics	- 232 -
7.6. Perspective	- 233 -
8. Conclusions	- 233 -
Appendix	- 266 -
References	- 235 -

Table of figures

Figure 1: (a) Global seismicity distribution pattern ($M \geq 4$, depth < 70 Km, 1964-1998) with locations presented as black dots; (b) The surface subdivision with the major tectonic plates of earth.	- 17 -
Figure 2: Schematic illustration of the Plate tectonics theory.	- 18 -
Figure 3: (a) Structure of subducted slabs as inferred from mantle tomography (Engdahl et al., 1998).	- 19 -
Figure 4: The global distribution pattern of fossil subduction remnants along plates sutured boundaries.	- 21 -
Figure 5: Sketch of subduction accretion versus erosion, indicating variations in material incorporation in the subduction zone.	- 22 -
Figure 6: Schematic sketch of the plate interface in subduction setting, according to present understanding.	- 23 -
Figure 7: Compilation of the Pmax-T condition of global HP/UHP remnants . . .	- 26 -
Figure 8: Tectonic sketch showing the middle to western segments of the Central Asian metallogenic domain.	- 30 -
Figure 9: Simple sketch showing the relationship between main contacts and tectonic units in the South Tianshan Orogen and adjacent region.	- 31 -
Figure 10: Geological map of the Southwestern Tianshan HP/UHP metamorphic belt (STMB). . .	- 32 -
Figure 11: Brief geological map of the AMC, with emphasizing the finding of key lithologies and coesite.	- 33 -
Figure 12: The collection of the protolith feature of samples of previous works. .	- 34 -
Figure 13: The compilation of previous P-T estimates for diverse lithologies in the STMB.	- 35 -
Figure 14: The compilation of regional age reports.	- 37 -
Figure 15: Sampling location of this thesis in the AMC.	- 40 -
Figure 16: Simplified geological map of (a) the Chinese Western Tianshan and (b) close-up map for the area.	- 58 -
Figure 17: Compilation of age data (a) as a function of estimated Pmax and (b) shown as a histogram.	- 60 -
Figure 18: (a) Schematic outline of the studied outcrop; (b) field view of the sampling and (c) location of the samples in the layered eclogite.	- 63 -
Figure 19: Whole-rock discrimination diagrams for the samples.	- 67 -
Figure 20: Mineral assemblages and microstructures of the studied coesite-bearing eclogites.	- 68 -
Figure 21: Thin-section scale shear senses in eclogite and greenschist facies for the UHP eclogite and its meta-volcano-sedimentary host-rock, respectively.	- 69 -

Figure 22: selected garnet porphyroblast and relevant mineral inclusions information.	- 70 -
Figure 23: Cathodoluminescence imaging and sketches of analyzed zircon grains, showing multistage growth features.	- 75 -
Figure 24: Chondrite-normalized (Sun and McDonough, 1989) REE abundances of the various zircon (a) and garnet domains (b).	- 78 -
Figure 25: Results of SIMS U-Pb isotopic dating and $\delta^{18}\text{O}$ compositions for various zircon domains.	- 79 -
Figure 26: WR-garnet-omphacite Sm-Nd isochron age for the oriented sample.	- 82 -
Figure 27: P-T estimates for the studied UHP eclogites, inferred from Perple_X pseudosection modeling and Thermocalc averagePT calculation.	- 85 -
Figure 28: P-T trajectory estimates from this study (a) and previous works (b)..	- 87 -
Figure 29: (a-b) Patterns of trace element distribution coefficients between various possibly coexisting zircon and garnet domains. (c) sketch summarizing the various growth zones observed in zircon and garnet.	- 90 -
Figure 30: Sketch depicting the petrologic evolution of mineral growth within metabasalts and inferred mobility of elements (mainly REEs) within the garnet-zircon-matrix metamorphic system during subduction and exhumation.	- 91 -
Figure 31: Previous radiometric data (see Table 2) and results from this study place constraints on the main tectonic stages for the area.	- 92 -
Figure 32: Simplified geodynamic cartoon setting back the studied samples and the overall time constraints inferred from this study within the evolution of the Chinese Southwestern Tianshan HP-UHP/LT metamorphic belt.	- 93 -
Figure 33: BSE imaging of mineral inclusion distribution in the studied garnet porphyroblast.	- 103 -
Figure 34: Rutile armored by sphene in both omphacite matrix (a, b) and later stage retrograde-growth quartz (c, d).	- 103 -
Figure 35: Rb vs K, Nb/U vs U, K/Th vs Ba/Th and Ba/Nb vs U/Nb diagrams (Bebout, 2007, 2013) for discriminating between LILE enrichment by metamorphism and seafloor alteration.	- 104 -
Figure 36: Continued from Figure 23: (a-i): cathodoluminescence images of other studied zircon grains; (m-n): typical HP (or UHP) metamorphic minerals (omphacite and rutile) revealed from Raman analyses.	- 104 -
Figure 37: Geological background of the SW-Tianshan LT-HP/UHP metamorphic complex. (a) Location of the research area with respect to other key UHP reports in China; (b) Close-up view showing the regional geological setting and sampling location: previous UHP reports based on coesite inclusions in garnet are highlighted by red stars.	- 107 -
Figure 38: Key features of the specific garnet zoning investigated here, exemplified by garnet A1.	- 109 -

Figure 39: Variations in the concentrations of (a) major divalent cations, (b-d) HREEs and Yttrium, (e-f) MREEs and (g-h) other key trace elements for garnet A1, along the profile shown in Figure 38b.	111 -
Figure 40: (a-b) Mn concentration profiles for diverse sized garnets.	116 -
Figure 41: Influence of key parameters on diffusion-controlled garnet growth. · -	120 -
Figure 42: Modelling of the concordant MnYHREE garnet zoning for diverse size garnets and in garnet A1.	125 -
Figure 43: Simplified sketches depicting the impact of diffusion-controlled garnet growth (here during a transient thermal pulse).	130 -
Figure 44: Tentative interpretation of the thermal excursion in terms of rock dynamics along a cold subduction plate interface.	132 -
Figure 45: (a) Ti, (b) P, (c) Ca and (d) Mg mapping reveal the relationships between garnet A1 and associated Ti, P, Ca, Mg-bearing inclusion/matrix minerals.	146 -
Figure 46: EMPA-BSE, transmitted light and cross-polarized light images of investigated garnet grains (A1-3, B1-4, C1), sampled from different parts of the outcrop (Figure 37d).	147 -
Figure 47: The Ca, Mg and Mn mapping as well as corresponding compositional profiles of the rest of investigated garnet grains.	148 -
Figure 48: Systematic garnet size survey. The three main groups and estimated mineral modes (vol %) for investigated UHP eclogite samples are shown.	148 -
Figure 49: Polynomial fitting for estimating effective bulk rock compositions during garnet growth (and uptake of major elements, HREEs and Y).	149 -
Figure 50: (a) Tectonic sketch showing the middle to western segments of the Central Asian metallogenic domain.	154 -
Figure 51: (a) Close-up views of the Akesayi metamorphic complex (AMC) showing sampling localities and reappraised tectonic sub-units & contacts.	160 -
Figure 52: (a) Close-up view of the area along the Kebuerte valley showing sampling sites, measured shear senses and the location of field observations.	161 -
Figure 53: Panoramic views of the main sub-units and contacts in the AMC, with representative sample localities.	162 -
Figure 54: (a) The structural sketch showing the extension on E-W of the revised AMC, with (b, c) the detail data of field structural measurements for the schistosity and lineation.	166 -
Figure 55: Outcrop observation of representative samples in this study. The letter of sub-figures corresponds to the localities marked in Figure 52c.	168 -
Figure 56: Microphotographs of samples investigated in the present study.	169 -
Figure 57: Primitive mantle-normalized spider diagram and chondrite-normalized REE pattern for samples in this study.	183 -
Figure 58: Mineral plots of compositions determined with the electron probe microanalysis.	185 -

Figure 59: P-T plot showing the results of our P-T estimates using THERMOCALC (Holland & Powell, 1990) together with estimates of metamorphic temperature by the Raman spectroscopy of carbonaceous material (RSCM, Beyssac et al., 2002; Beyssac et al., 2004) and Ti-in-biotite geothermometry (Henry et al., 2005). ······ - 191 -

Figure 60: (a) Radiometric ages obtained for all samples, with respect to respective localities on Kebuerte section. ······ - 195 -

Figure 61: (a, b, c, d) The compilation of regional age reports with respect to sampling localities (ages versus latitude). Ages reported in key valleys are listed respectively from the top to bottom. ······ - 202 -

Figure 62: (a) Paleogeographic reconstruction during the Gondwana assembly at ~510-470 Ma and Pangea assembly at ~300-280 Ma. (b) Interpretative sketches relating the formation and exhumation of the SW-Tianshan HP/UHP-LT accretionary complex during the period 360-280 Ma. ······ - 206 -

Figure 63: Panoramic views of the main north and south contacts in between the AMC and the SCTSZ mylonitized shear zone (GS1, GS2). ······ - 211 -

Figure 64: Outcrop observation of representative samples in this study. ······ - 212 -

Figure 65: Microphotographs of samples investigated in the present study. ······ - 213 -

Figure 66: The rest of in situ ^{40}Ar - ^{39}Ar laser probe ablation results. ······ - 214 -

Figure 67: The phengite ^{40}Ar - ^{39}Ar step-heating results of regional GS to lower BS facies samples (J2, 22, 157 and 147), and the LA-ICP-MS zircon U-Pb radiometric results of meta-basite sample (158). ······ - 215 -

Figure 68: Examples of later stage phengite recrystallization in samples from distinct sub-units (UH versus GT units). ······ - 216 -

Figure 69: Geological map with the locality of previous age reports. ······ - 217 -

Figure 70: The comparison between ages from metamorphic indications (this study+ previous works) and those from magmatic indications (previous works) that related to the Paleo South Tianshan Ocean Basin subduction setting. ······ - 219 -

Figure 71: Major elements composition of selected samples in this PhD thesis and those from previous works. ······ - 221 -

Figure 72: P-T-density pseudosections conducted for representative compositions of metavolcanoclastics (regional and global) ······ - 224 -

Figure 73: P-T-density pseudosections conducted for representative compositions of regional eclogite, blueschist and serpentinite. ······ - 224 -

Figure 74: (a) Close-up view of the area along the Kebuerte valley showing sampling sites, measured shear senses and the location of field observations. ······ - 225 -

Figure 75: The compilation of regional Pmax-T estimates and P-T paths. ······ - 228 -

Figure 76: The summary of radiometric age constraints in this PhD thesis. ······ - 230 -

1. Introduction

1.1. Plate Tectonics and Subduction

Though seemingly beyond human reach, subduction zones play a fundamental role in our daily life, as well as in the formation and evolution of the Earth (since this is where the Earth's lithosphere gets recycled). High rates of volcanic eruptions, earthquakes and tsunamis (directly or indirectly caused by the energy release from the mechanical coupling between the plates) characterize those active subduction zones

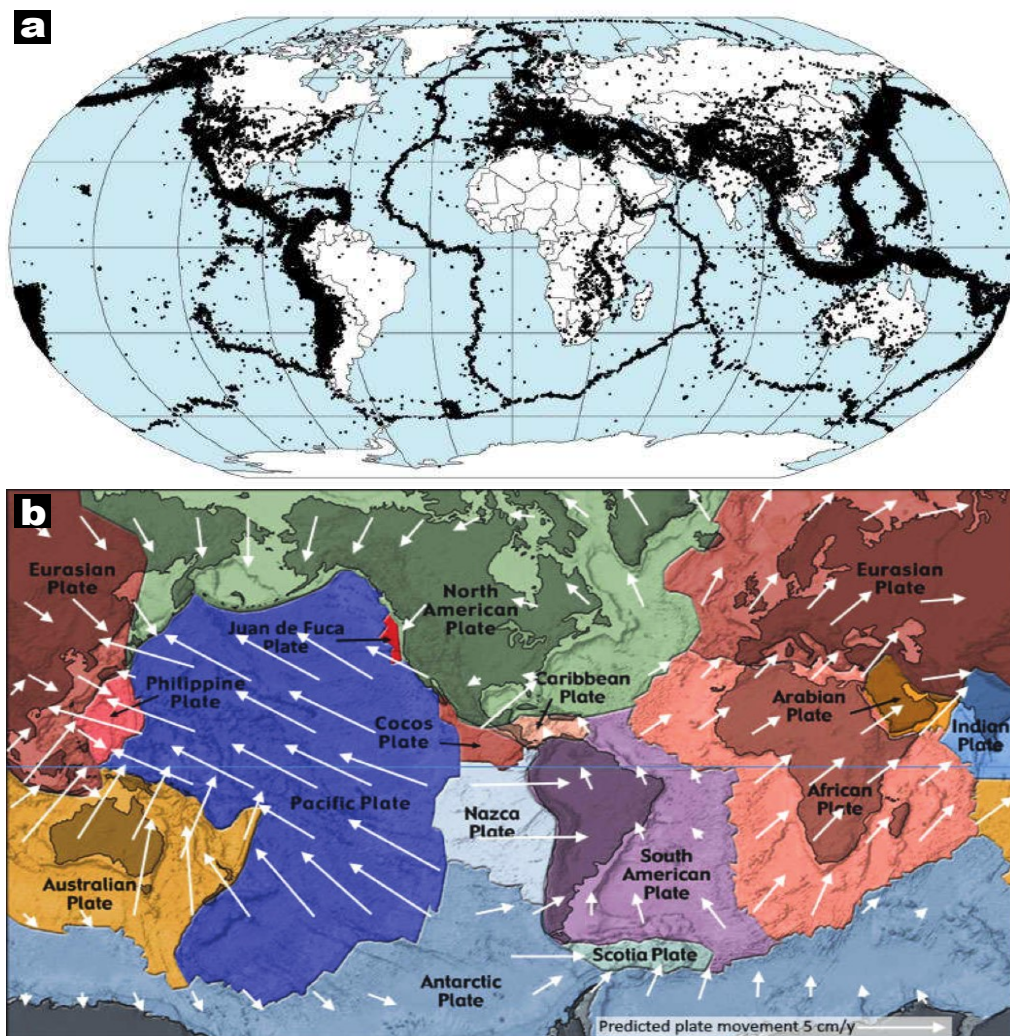


Figure 1:(a) Global seismicity distribution pattern ($M \geq 4$, depth < 70 Km, 1964-1998) with locations presented as black dots; (b) The surface subdivision with the major tectonic plates of earth. The independent movement of each plate with the sense of motion is shown by the white arrows (Su, 2010).

worldwide and repeatedly impact half of the world's population living on top or nearby one of them.

Subduction earthquakes were first tied to the plate tectonics theory by McKenzie and Parker (1967), following up on the imagination and observations from the paper “Die Entstehung der Kontinente” of Wegener (1912), which proposed that the surface of Earth is covered by large, rigid mosaic-like continents that move relative to each other causing tectonic activity at their boundaries. In the zone of convergence one plate is dragged down or overridden by another one along the subduction zone, namely at the junction of two plates (Figure 2). The first models of asymmetrical subduction zones were soon after proposed by Dewey and Bird (1970), who described them as the direct result of lateral buoyancy contrasts between convergent plates and Wilson (1973) introduced the direct correlation between subduction zones and seismicity, pointing out the earthquake generation in correspondence to the plates' interface. Famous examples

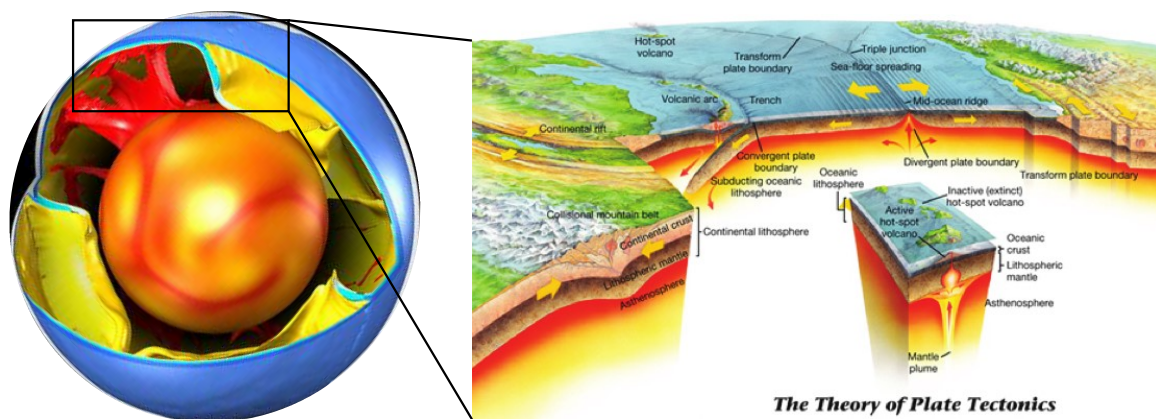


Figure 2: Schematic illustration of the Plate tectonics theory.

of devastating earthquakes in active subduction zones include are Tohoku in 2011 (M~9.0; Simons et al., 2011), Alaska in 1964 (M~9.4; Plafker, 1965) and the 1960

Valdivia earthquake (considered the most powerful earthquake ever recorded, with $M \sim 9.5$; Moreno et al., 2009).

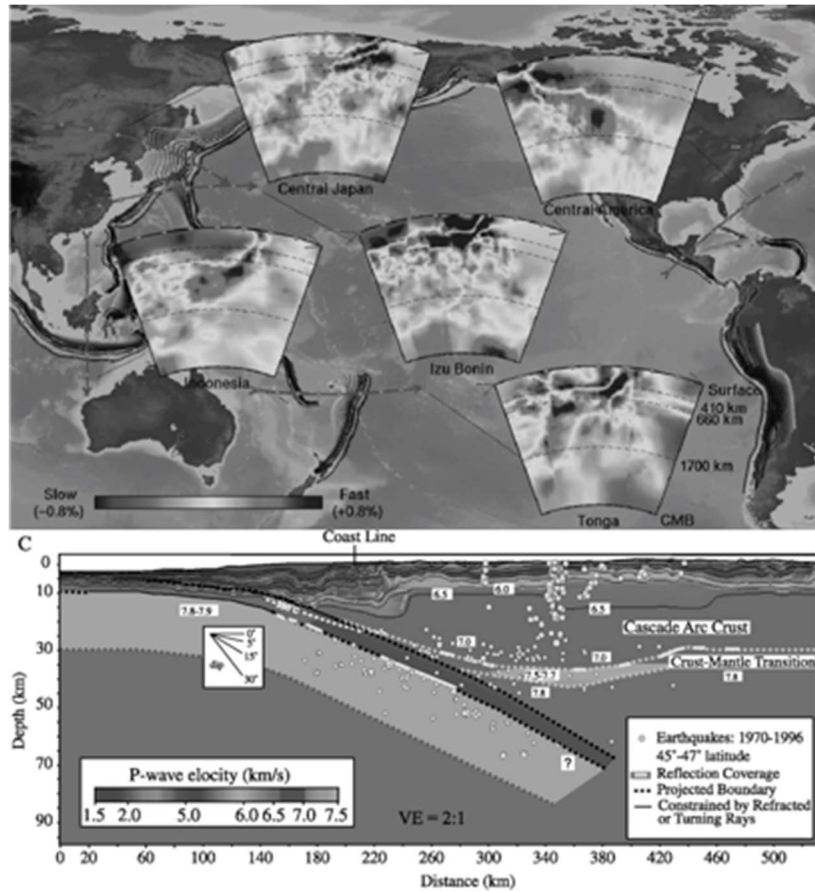


Figure 3: (a) Structure of subducted slabs as inferred from mantle tomography (Engdahl et al., 1998). Red lines show the surface projection of each section. The base of each section is the core-mantle boundary (CMB); dashed lines show the location of mantle discontinuities at 410, 660, and 1700 km. Red and blue colors in each section denote regions where the P wave velocities are relatively slow and fast, respectively, compared to average mantle at the same depth. (b) P wave velocity structure across the Cascadia Subduction zone depicting the structure and the expected depth for typical seismic events in subduction zones.

1.2. Fossil Subduction Remnants: An Ideal Target?

Subduction zones are almost inaccessible to direct observation (even the ongoing NantroSeize drilling project will reach no deeper than ~ 7 km) and, as a result, the nature, structure and properties of the plate interface are still largely unknown. Even if the developing geophysical data acquisition technology (e.g., tomography), to some

extent, shed a light on the deep structure of subduction zone down to mantle depth, instrumental uncertainties within the range of several hundred meters to a few kilometers indeed affect the relocation of earthquake hypocenter, with depth even more poorly constrained than the epicenter (Kuge et al., 2010; Waldhauser and Schaff, 2008).

Alternatively, one can use former subducted materials, ultimately exhumed to the surface along fossil subduction/suture zones (Agard et al., 2009, 2018), to track both chemical and mechanical processes operating along the subduction interface (Ague and Nicolescu, 2014; Angiboust et al., 2012; Gao et al., 2007; John et al., 2009; Li et al., 2013; Sverjensky et al., 2014), even deep to > 150 km depth (Ye et al., 2000).

However, the interplay between fluids, rheology and seismicity, and the way they impact mechanical coupling along the interface, earthquake triggering and/or overall subduction dynamics is still largely circumstantial. Besides, the mechanisms and processes accounting for (i) the exhumation of dense oceanic (ultra-) high pressure low temperature (UHP/HP-LT) rocks that are negatively buoyant with respect to the surrounding mantle (unlike the relatively lighter continental material, sedimentary rocks or serpentinites) and are commonly irreversibly buried, and (ii) the juxtaposition of HP and UHP tectonic slices on exhumation are still to some extent perplexing (Agard et al., 2018, 2009; Burov et al., 2014; Chen et al., 2013; Gerya et al., 2002; Guillot et al., 2009; Warren, 2013; Warren et al., 2008). It is thus important to retrieve information from exhumed, fossil fragments of subduction plate interface through field investigations. Well-exposed, typical fossil subduction remnants preserving a pristine

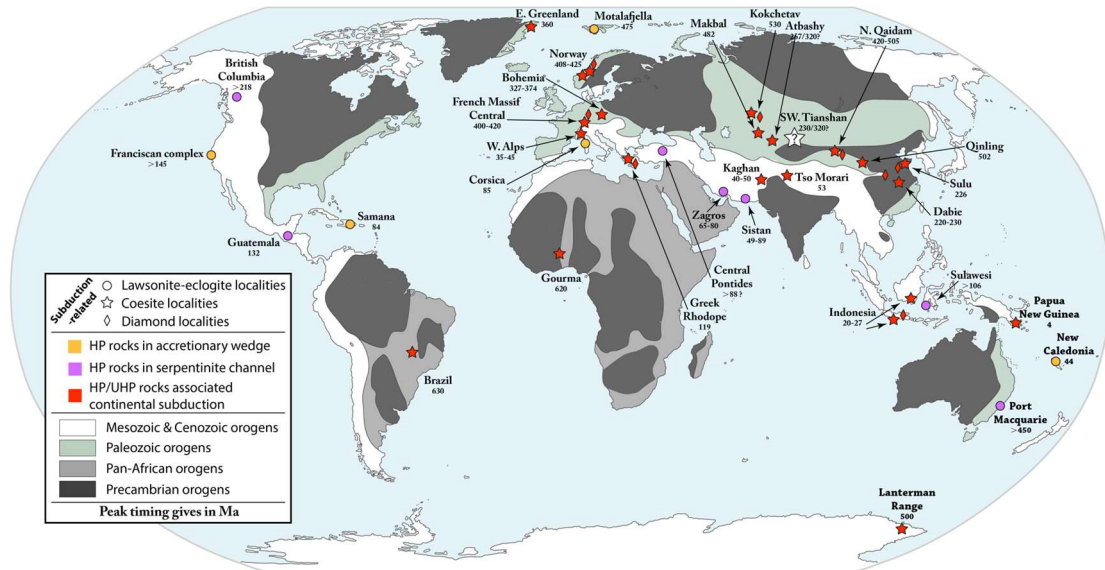


Figure 4: The global distribution pattern of fossil subduction remnants along plates sutured boundaries. Modified from Karason and Van Der Hilst (2000) and Stern (2002).

tectonic and/or mineralogical record are extremely rare within former suture zones, particularly those recording deep subduction of oceanic crust (down to 70~100km).

A compilation of worldwide key HP/UHP fossil subduction remnants is presented in Figure 4 with grouping strategies based on index minerals (i.e., lawsonite, coesite and diamonds) for high or ultra-high pressure metamorphism and peak metamorphic timing. The occurrence of lawsonite in metamorphic rocks outlines typical cold fossil subduction (e.g., Tsujimori et al., 2006; Tsujimori and Ernst, 2013; Vitale Brovarone et al., 2014), with metamorphic gradients as low as 5°C /km, while coesite and diamond (generally as inclusions) are proxies for UHP metamorphism (e.g., Chopin, 1984; Okay et al., 1989; Shutong et al., 1992; Smith, 1984). As shown in Figure 4, almost all UHP fossil subduction remnants relate to continental subduction, with exhumation assisted by buoyancy forces following the subduction of light continental crust and/or serpentinite (e.g., W. Alps and Dabieshan; Agard et al., 2009; Guillot et al., 2015). In contrast, only a few of HP fossil subduction remnants are associated within a

metavolcanoclastics-dominated accretionary wedge, with exhumation mechanism yet unknown but possibly related to tectonic thinning/underthrusting/underplating (e.g., analogous but deeper than the Schistes Lustrés, W. Alps. Agard et al., 2009).

1.3. Burial and Recovery of Formerly Subducted Lithologies

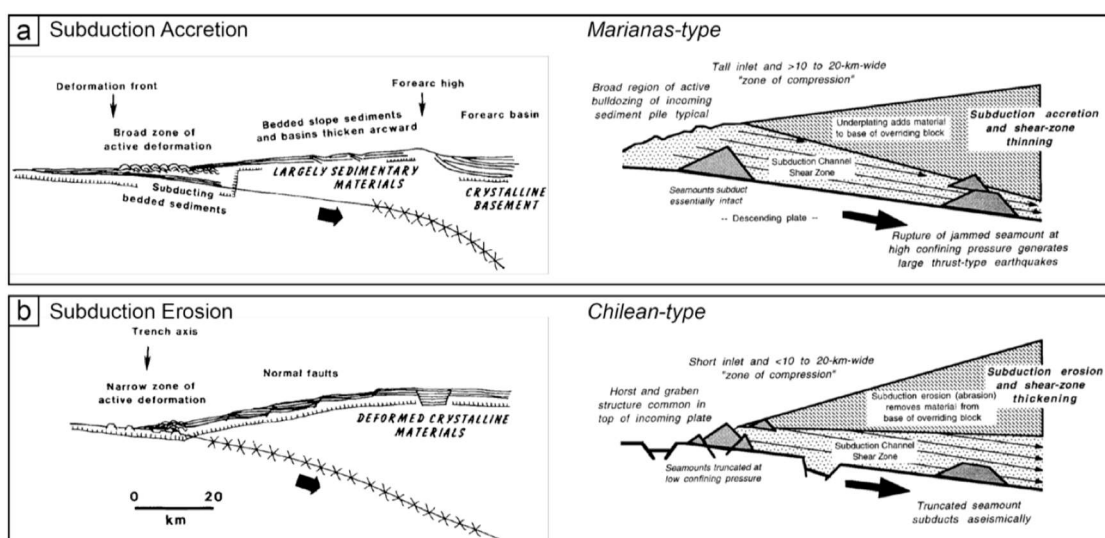


Figure 5: Sketch of subduction accretion versus erosion, indicating variations in material incorporation in the subduction zone (after Cloos and Shreve, 1996, 1988b). (a) Model of subduction accretion, with the Marianas subduction as an example. (b) Model of subduction erosion, with the Chilean subduction as an example.

Opposite routes characterize burial (i.e., subduction s.s.) and recovery (i.e., detachment and exhumation) of subducted lithologies. Slices of the upper part of the down-going lithosphere make their way back to the surface only at certain time periods and in minor amounts (Agard et al., 2009; Guillot et al., 2009; Warren, 2013). These fragments can be relatively complete sections of oceanic lithosphere (i.e., seafloor sediments, basalts, gabbros and serpentinized peridotite; e.g., Monviso/Zermatt-Saas, W.Alps), oceanic and/or terrigenous sediments offscraped from the accretionary wedge (e.g., Schistes Lustrés, W.Alps; Franciscan complex, California), detrital material basally eroded from the upper plate (e.g., Cloos and Shreve, 1996; Vannucchi et al.,

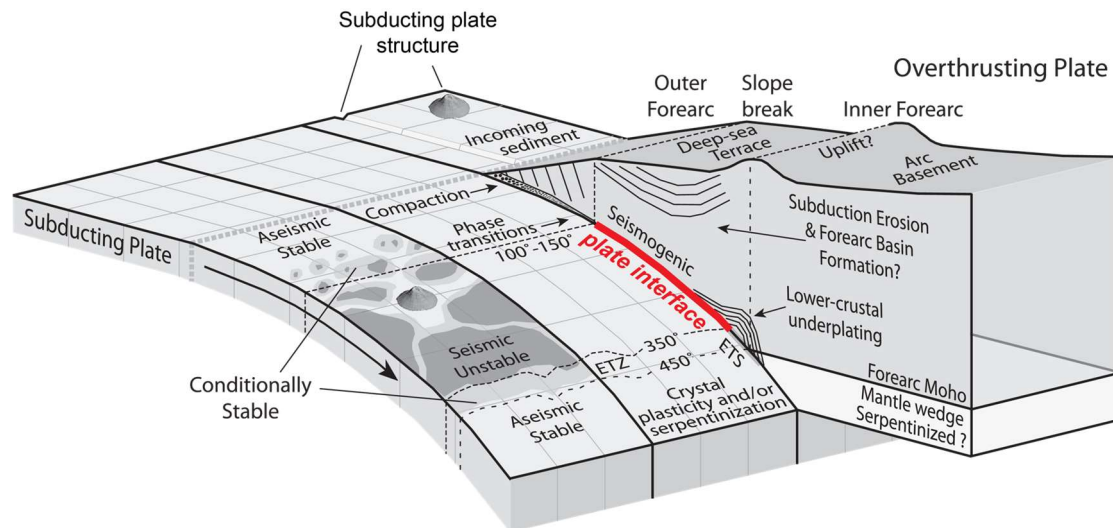


Figure 6: Schematic sketch of the plate interface in subduction setting, according to present understanding (modified after Bassett and Watts (2015)).

2012, 2008) and/or subducted seamounts (e.g., Bassett and Watts, 2015; John et al., 2010). In addition, ashes formed by arc volcanism could be transport over long distance and later incorporated into the trench (e.g., Kutterolf et al., 2008). The different subduction types (i.e., accretionary versus erosive, Figure 5) also result in contrasting material supply within wedge or even down to mantle depths, and play a significant role on material recycling (Clift and Vannucchi, 2004; Cloos and Shreve, 1996, 1988).

In contrast (to the burial), the recovery of subducted lithologies is of prerequisite on i) how rock/block/slice can detach from subducting slab and ii) subsequently exhume along the plate interface (Figure 6). On one hand, the detachment is essentially facilitated either by the existence of a décollement layer (i.e., decoupling zone) where the ductile-brittle transition, mechanical coupling (i.e., strain localization and stress accumulation) and/or serpentinization had taken place in oceanic subduction settings (e.g., Agard et al., 2009; Blake Jr et al., 1995; Guillot et al., 2009; Philippot and van Roermund, 1992; Tsujimori et al., 2006), or by the separation of the buoyant upper crust from the denser lithosphere when shearing exceeds the strength of the binding

force of rocks in continental subduction zones (e.g., Norway; Jolivet et al., 2005). On other hand, a 'weak' channel will be required for the exhumation of HP/UHP lithologies. Fluid released from subducting slab during progressive metamorphic dehydration could not only facilitate the lubrication of the subduction plane but also assist the formation of low strength minerals (e.g., lawsonite, phengite, antigorite and talc) (Guillot et al., 2009; Stöckhert and Renner, 1998). This concept was mainly used to discuss exhumation of rigid mafic blocks wrapped in a soft serpentinite matrix within a serpentinite subduction channel (Blake et al., 1995; Federico et al., 2007; Gerya et al., 2002), but not so much for continental exhumation since their buoyancy is considered sufficient for their return, even from UHP conditions (e.g., Chemenda et al., 1995; Ernst, 2006; Guillot et al., 2009).

The recovery (of subducted lithologies) frequently occurs during a ~15 Ma short-lived period in a given subduction zone, as concluded by recent compilations (Agard et al., 2018, 2009). This, in fact, suggests that a steady-state regime such as proposed by Platt (1987, 1986), i.e., underplating coupled with shallow extension that would allow HP rocks to be exhumed to upper crustal levels, is in general not effective since only punctuated exhumation is observed. Moreover, most sedimentary accretionary prisms (reaching about ~20 km depth on average, and exceptionnally ~40-60 km: Chile, Glodny et al., 2005; Cascadia, Hyndman (1995); Schistes Lustrés, Agard et al. (2002, 2001)) are not deep enough to form UHP or even HP rocks (Guillot et al., 2009). Importantly too, no exhumation of HP/UHP lithologies is happening at present in most subduction zones (e.g., Cascadia), further implying that the exhumation of HP/UHP

only take place during potential perturbations of a subduction setting (Agard et al., 2018, 2009, 2006), for example in response to a change in slab geometry (i.e., subduction angle and convergence velocity) and/or transient increase in mechanical coupling (e.g., docking of a subducted seamount).

1.4. Using The STMB to probe the plate interface: a fossil, deeply buried and cold package (dominantly) made of metavolcanoclastics

Regardless of various subduction types, subducted materials and contrasting exhumation mechanisms, mechanisms and processes responsible for the occasional recovery of ocean-derived HP-UHP/LT metavolcanics/metavolcanoclastics equilibrated along the subduction plate interface are essential to constrain subduction dynamics and gain insights on long-/short-term processes along the plate boundary (Bachmann et al., 2009; Stöckhert, 2012; Agard et al., 2018 and references therein). The diversity of subducted material (§1.3) is likely to influence viscosity, density and thus buoyancy, and to control chemical and mechanical behaviors within the plate interface (Bebout, 2007, 2013; Yamato et al., 2007; Krebs et al., 2011). In particular there is a strong need for ‘good’ exposures recording plate interface processes in a critical depth range around 80 km, beyond which no deeper oceanic rocks are recovered in general (Agard et al., 2018; the only exception so far is a 10-50 m thick UHP slice in Lago di Cignana from Zermatt-Saas, W.Alps; Frezzotti et al., 2011; Groppo et al., 2009) and where geophysicists and modellers infer a change in large-scale mechanical

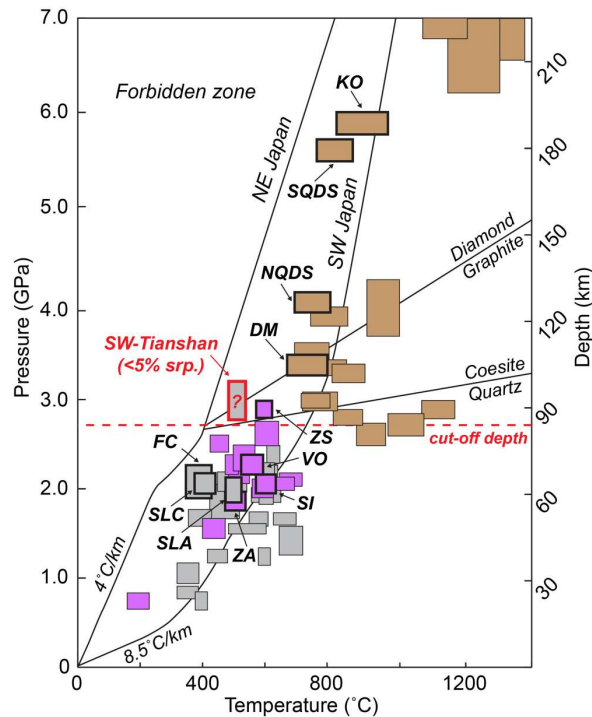


Figure 7: Compilation of the P_{max} - T condition of global HP/UHP remnants (according to the data collection from Guillot et al. (2009)). Grey box represents HP rocks recovered within accretionary wedge; Purple box marks exhumed HP/UHP oceanic rocks wrapped in serpentinite mélangé; Brown box indicates UHP crustal rocks associated with continental subduction. Abbreviation: KO, Kokchetav; N/SQDS: North/South Qinling-Dabie; DM: Dora Maira; ZS: Zermatt Saas; VO: Voltri Italy; SI: Sistan Iran; ZA: Zagros Iran; FC: Franciscan Complex; SLC/A: Schistes Lustrés Corsica/W.Alps.

type subduction (e.g., Schistes Lustrés Corsica/W.Alps and Franciscan complex), but still very distinct because of (i) its pervasive coesite findings not only in oceanic metabasites (Lü et al., 2009; Lü and Zhang, 2012) but also in the metavolcanoclastic matrix (Bayet et al., 2018; Yang et al., 2013) and (ii) relatively high peak metamorphic records at ~3.0 GPa (~550°C; e.g., Wei et al., 2009; Yang et al., 2013; Zhang et al., 2003).

coupling between the plates (e.g., Wada and Wang, 2009; Syracuse et al., 2010; van Keken et al., 2011).

To document key processes operating in that depth range, the Chinese South Tianshan Metamorphic Belt (STMB) is a potentially important/exceptional example.

The STMB is indeed characterized by an unusually thick (~5 km) pile of well-preserved HP/UHP metavolcanoclastics (Bayet et al., 2018) wrapping eclogite boudins/slices (e.g., Gao and Klemd, 2003), resembling classic accretionary

To explain its recovery, the SMTB both lacks significant serpentinite exposures ($\ll 5$ vol%; Li et al., 2007; see §2), making the existence of a serpentinite channel unlikely, and evidence for continental subduction (i.e., coesite/diamond gneisses \pm felsic amphibolites \pm garnet-bearing peridotites, such as in Dora Maira, Dabie-Sulu, or Kokchetav; Guillot et al., 2009), although it was recently tentatively proposed for the STMB (Loury et al., 2018). When set back against the global compilation (e.g., Agard et al., 2018, 2009; Guillot et al., 2009), the STMB sits somewhere in the middle in terms of P-T record and lithological composition, between accretionary-/serpentinite-types and continental-type subduction (Figure 7).

Overall, the pervasively coesite-bearing metavolcanoclastics-dominated STMB may serve as a nicely preserved remnant in the right depth range (~ 80 km depth) to address questions regarding material rheology/viscosity, fluid-rock interactions and deformation (i.e., stress accumulation & strain localization). This PhD thesis focuses on the following ones:

- 1) why is it so thick so deep, and what can we learn from this ‘exceptional’ example across a depth range critical for mechanical coupling (~ 80 km; Syracuse et al., 2010; Wada & Wang, 2009)?
- 2) How well constrained are processes occurring at such depth?
- 3) What is the role of coupling-decoupling mechanisms on the rock recovery at such depth?
- 4) Are we able to track short-lived processes within the plate interface?

So far, despite numerous studies providing detailed petrological, geochemical evolutions, fluid activity or geochronology data (e.g., Gao et al., 2007; John et al., 2008; Klemm et al., 2011; Meyer et al., 2016; van der Straaten et al., 2012) from the STMB, especially in the Akeyazi metamorphic complex (AMC, Figure 11), contrasting hypotheses still exist on i) the fundamental architecture of the SMTB, i.e. internal structures and tectonic evolution (HP/UHP *mélange* versus HP-UHP sub-belts; Klemm et al., 2011; Li et al., 2016; Lü et al., 2012) and ii) the timing of peak metamorphism and of ocean basin closure (i.e., Triassic versus Late Carboniferous; Su et al., 2010; Zhang et al., 2007). In order to refine our understanding of the overall architecture and evolution of the STMB (which, incidentally, is a prerequisite for any further study of deep subduction processes; e.g., fluid-rock interaction), more local and specific questions will be addressed in this PhD thesis:

- 1) Can we refine the architecture and deformation pattern of the STMB?
- 2) Can we assess the P-T conditions in a more evenly distributed way (i.e., P-T mapping)?
- 3) When do HP/UHP rocks detach from the slab, and is this happening continuously or at specific times?
- 4) Can we get an idea about how these tectonic slices were assembled (or 'mélanged')?
- 5) When did the Paleo South Tianshan ocean basin close?

1.5. Structure of the Thesis

A systematic review of previous works is presented in '*Chapter 2- Geological Setting of the STMB*'. This chapter provides the geological background for the STMB and our studied area, the Akeyazi metamorphic complex (AMC), and reviews previous P-T(-time-lithologies) investigations on individual samples. Relevant methods for geochemical & radiometric experimental measurements and P-T estimates are briefly introduced in '*Chapter 3-Methods*'. Three manuscripts written during this PhD thesis, either published or submitted, are presented respectively in '*Chapter 4. P-T-time-isotopic evolution of coesite-bearing eclogites: Implications for exhumation processes in SW Tianshan*' (*Lithos*, 2017), '*Chapter 5. Concordant pulse in Mn, Y and HREEs concentrations during UHP eclogitic garnet growth: transient rock dynamics along a cold subduction plate interface*' (*EPSL*, under review) and '*Chapter 6. Contrasting P-T-deformation-time evolutions in the SW-Tianshan (Akeyazi HP/UHP complex, China): implications for Late Carboniferous subduction dynamics*' (prepare to submit to *Lithos*). '*Chapter 7-Discussion and Perspective*' and '*Chapter 8-Conclusions*' provide a general integration of the results and discuss their implications for subduction dynamics and for regional scale tectonics.

2. Geological Setting of the STMB

2.1. Geological Background

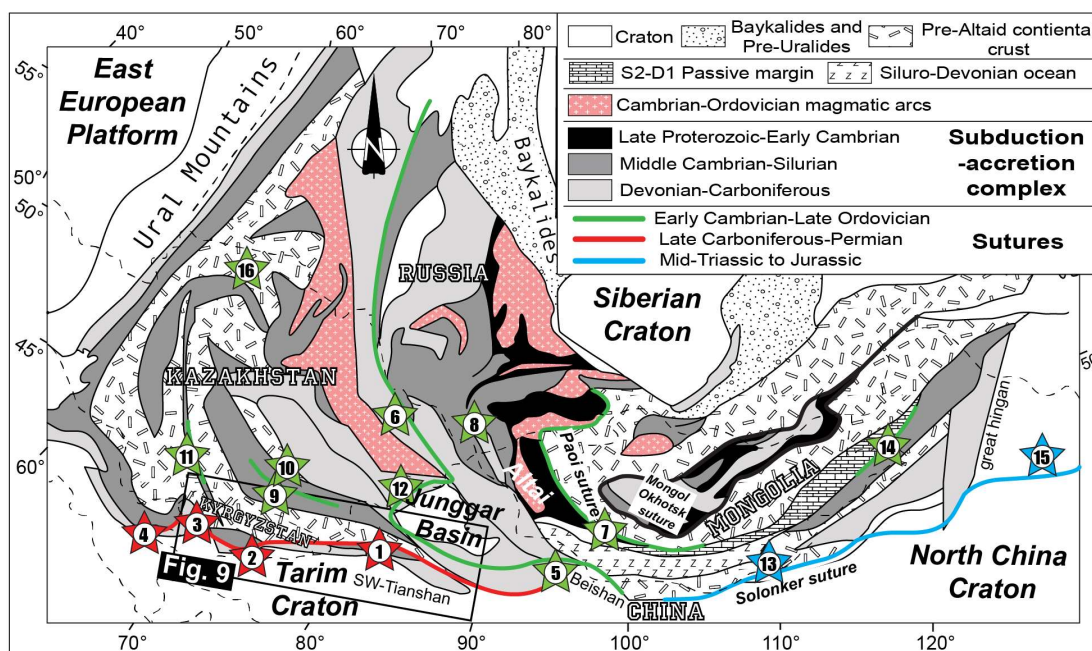


Figure 8: Tectonic sketch showing the middle to western segments of the Central Asian metallogenic domain, modified after Gao et al. (2017), Soldner et al. (2017) and Xiao et al. (2015). Colored stars with number marked the occurrence of high (lira-high) pressure/low temperature metamorphic rocks (see Gao et al. (2017) and references therein): 1. Akesayi, ~320 Ma; 2. Atbashi, ~320 Ma; 3. Chatkal, ~301 Ma; 4. FanKarategin, ?; 5. Beishan, ~465 Ma; 6. Chara Zone, ~445 Ma; 7. SW Mongolia, ~540 Ma; 8. Gony Altai, ~630 Ma; 9. Aktyuz, ~460-470 Ma; 10. Chu-Yili, ~490 Ma; 11. Makbal, ~475-500 Ma; 12. Barleik, ~492-504 Ma; 13. Central inner Mongolia, <235 Ma; 14. Toudaoqiao, ~490-510 Ma; 15. Yilan, ~180-210 Ma; 16. Kokchetav, ~524-537 Ma.

The Chinese Southwestern Tianshan high- to ultrahigh-pressure low-temperature (HP/UHP-LT) accretionary complex constitutes the eastern part of the Kazakhstan collage system (Gao et al., 2017; and references therein) within the Altaids (also called the Central Asian Orogenic Belt; Figure 8). It extends for about 200 km along the Southwestern Central Tianshan Suture Zone (SCTSZ, Figure 9), and correlates with the Atbashi (Hegner et al., 2010; Loury et al., 2018; Simonov et al., 2008), Chatkal (Loury et al., 2016; Mühlberg et al., 2016) and Fan-Karategin (U)HP metamorphic complexes (Volkova and Budanov, 1999) in the Kyrgyzstan part of the South Tianshan Orogenic Belt (STOB). The SCTSZ bounds to the north the Chinese section of the HP-UHP/LT

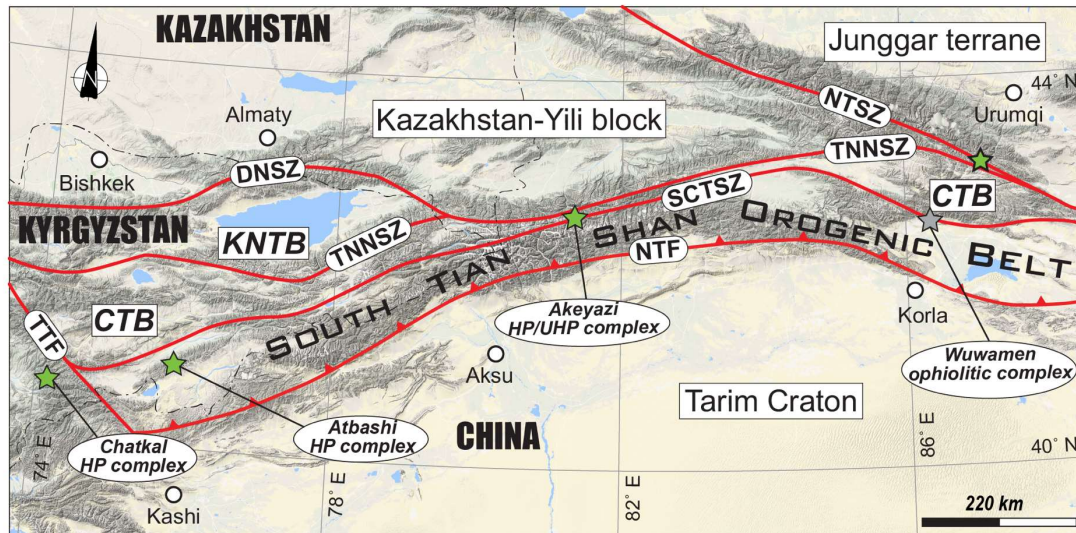


Figure 9: Simple sketch showing the relationship between main contacts and tectonic units in the South Tianshan Orogen and adjacent region. CTB = Central Tianshan Block, KNTB = Kyrgyzstan North Tianshan Block, NTSZ = North Tianshan Suture Zone, TNNSZ = Terskey-North Nalati Suture Zone, SCTSZ = South Central Tianshan Suture Zone, DNSZ = Djalair-Naiman Suture Zone, NTF = North Tarim Fault, TTF = Talas-Fergana Fault.

metamorphic complex, known as the Akeyazi metamorphic complex (AMC, Figure 10). This contact, now a ~0.5 km-wide dextral strike-slip shear zone, was active from the Early Permian to Early Triassic (Gao & Klemd, 2003; Laurent-Charvet et al., 2003). To the north lies a LP-HT Palaeozoic active continental margin (Allen et al., 1993; Gao et al., 1998; Klemd et al., 2015), mainly made of amphibole- and granulite-facies rocks, along with Late Silurian and Early Carboniferous continental arc-type volcanic, volcanoclastic rocks and granitoids (Gao et al., 2009a; Xia et al., 2014). To the south the AMC is overlain by unmetamorphosed and/or low grade Palaeozoic sedimentary strata, which also represent the northern, passive continental margin of the Tarim plate (Carroll et al., 1995).

2.2. The Akeyazi Metamorphic Complex

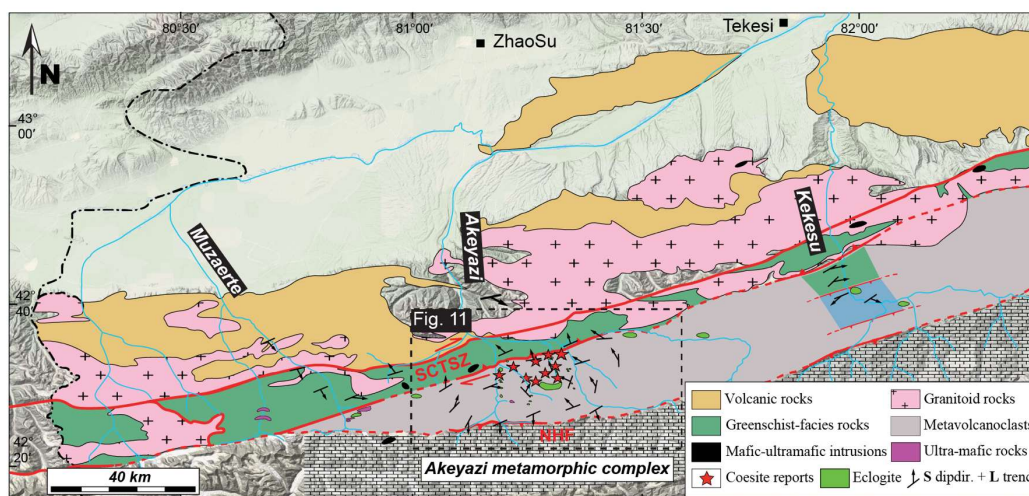


Figure 10: Geological map of the Southwestern Tianshan HP/UHP metamorphic belt (STMB). The structural data was plotted according to the measurement from this study, Bayet et al. (2018), Gao et al. (1998), Lin et al. (2008) and Soldner et al. (2017). The location of coesite reports follows the compilation of Tan et al. (2017) and Bayet et al. (2018).

The AMC is predominantly composed of strongly schistosed metavolcanoclastics hosting mafic metavolcanics as pods, lenses, boudins, thin layers (Figure 11a) or massive blocks (Figure 11b; Gao & Klemd, 2003) and marble horizons (Bayet et al., 2018), as well as very rare ultramafic rocks (Li et al., 2010; Shen et al., 2014). Some well-preserved pillow-shape eclogitic meta-basalts were also identified (Figure 11c). Whole-rock geochemical data for the mafic metavolcanics suggest oceanic basalt or arc-related affinities (Gao & Klemd, 2003; John et al., 2008; Liu et al., 2014; Meyer et al., 2016; Tan et al., 2017) while the metavolcanoclastics have characteristics similar to upper continental crust and trench sediments (Liu et al., 2014; Meyer et al., 2016; Tan et al., 2017) (Figure 12).

Previous work mostly focused on individual HP/UHP rocks/outcrops for the reconstruction of P-T-(time) histories (e.g., Li et al., 2016; Lü et al., 2012; Tan et al., 2017), fluid-rock interaction processes and/or geochemical budgets (e.g., Beinlich et

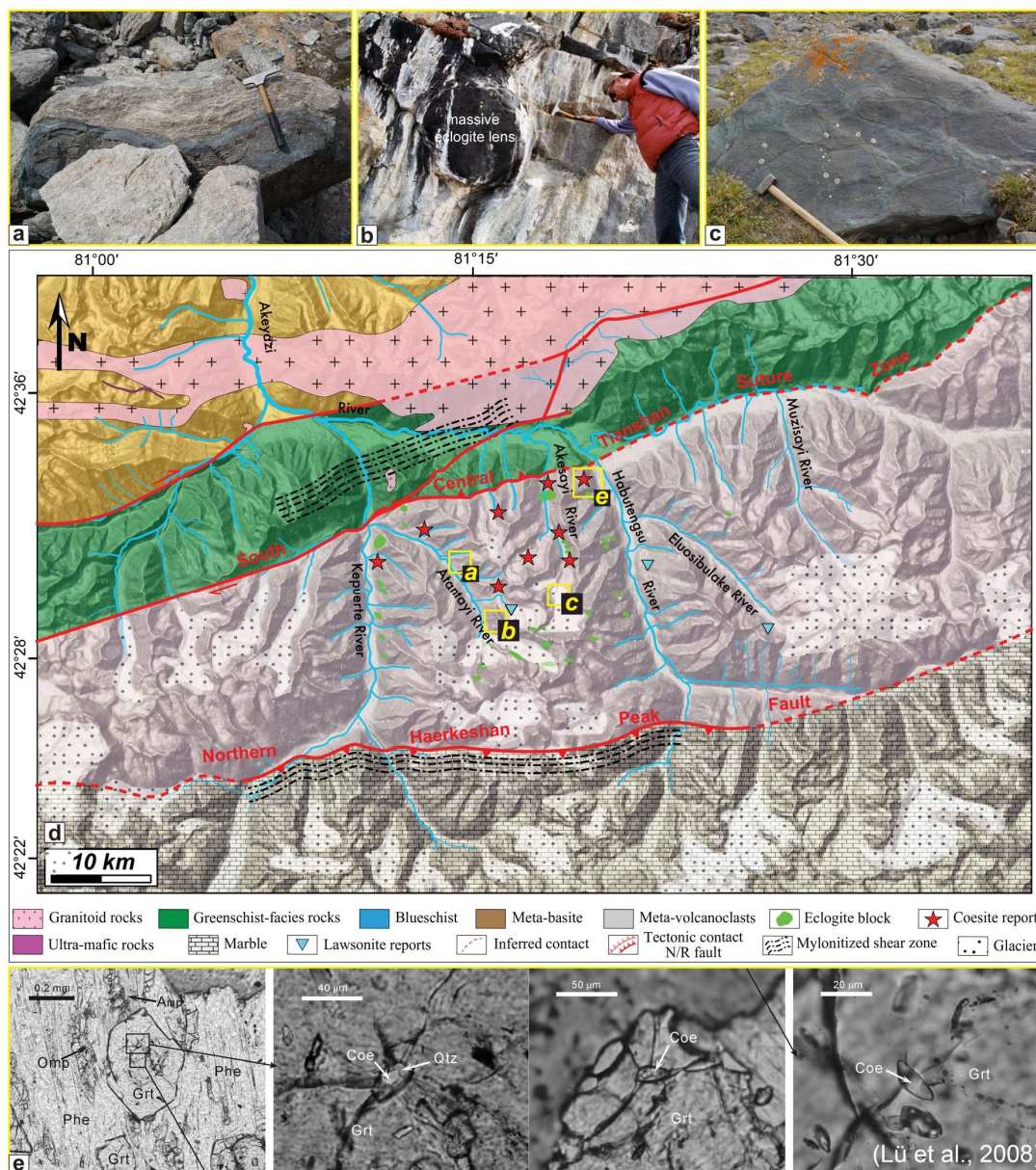


Figure 11: Brief geological map of the AMC, with emphasizing the finding of key lithologies and coesite. The location of coesite reports were marked as red stars after the compilation of Tan et al. (2017) and Bayet et al. (2018). The location of lawsonite reports were presented as light blue according to Du et al. (2011), Du et al. (2014) and Li et al. (2013). (a) mafic block wrapped by metavolcanoclastics matrix. (b) massive eclogite block in metavolcanoclastics matrix. (c) eclogitic facies pillow-shape metabasalt block (not in place). (e) The first coesite inclusion found in the metabasalt (Lü et al., 2008).

al., 2010; John et al., 2012; van der Straaten et al., 2008). The compilation of regional P-T (-time) constraints (Figure 13; also see Tan et al., 2017) indicates that most peak metamorphic estimates for eclogite and prograde blueschist yield eclogite facies (EC facies) HP-LT conditions within the range 480-580°C and 1.5-3.0 GPa. A range of P-

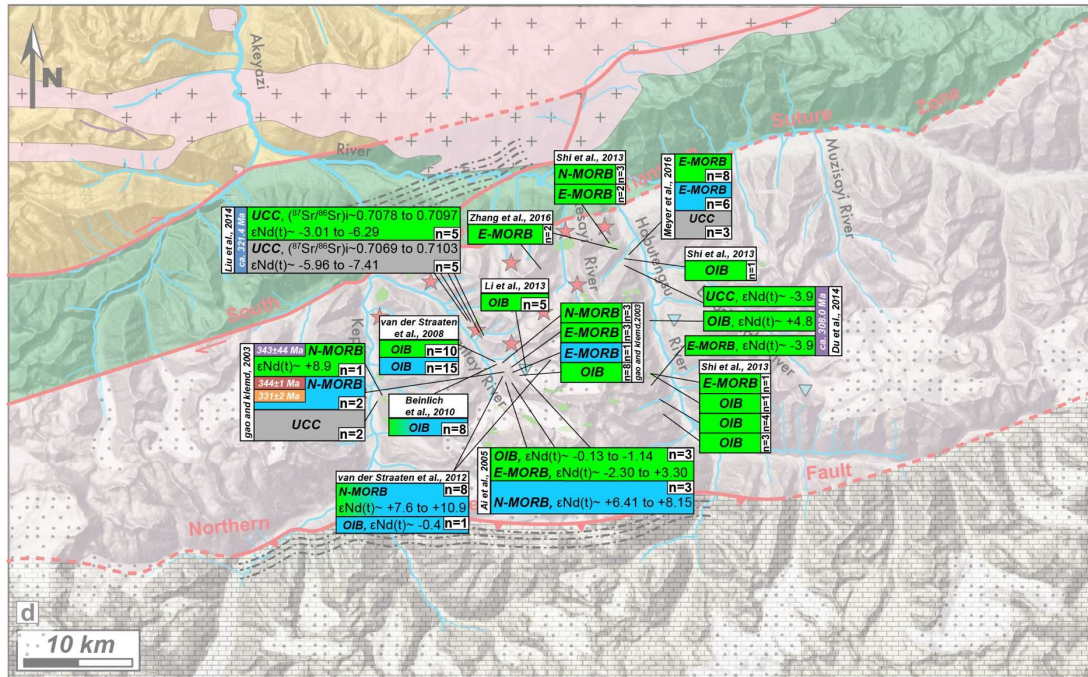


Figure 12: The collection of the protolith feature of samples from previous works. The legend follows those of Figure 11. Colors in the protolith boxes correspond to the lithology: Green, eclogite; Blue, blueschist; Grey, metavolcanoclastics. Abbreviation: N/E-MORB: Normal-/Enriched-middle ocean ridge basalt; OIB: Oceanic island basalt; UCC: Upper continental crust.

T conditions $\sim 450\text{-}570^\circ\text{C}$ at 2.7-3.3 GPa was obtained for some EC facies metavolcanoclastics (Figure 13). Evidence for UHP metamorphism comes from both coesite relics in garnet (from several localities: stars in Figure 11) and thermodynamic calculation. The spread of regional P-T estimates (Figure 13a, Table 1), whatever the lithologies, could a priori arise from contrasting assumptions for thermodynamic modeling (e.g., difficulties in determining effective bulk rock composition and Fe^{3+} content and/or assessing H_2O activity) or from the complexity of metamorphic evolutions in individual HP-UHP tectonic slices (Bayet et al., 2018).

The exhaustive compilation of age data (Figure 14a, Table 2), and the comparison of previous age data versus their assessed P_{max} estimates (Figure 14b, c), evidence a considerable spread in ages too, with an overlap between eclogite and blueschist ages,

al., 2010) and similar to a U-Pb age of 318 ± 7 Ma obtained for eclogite-facies rutile (Li et al., 2011). Du et al. (2014) also reported a suite of relative consistent Sm-Nd isochron ages of 309 ± 4.6 Ma, 306 ± 15 Ma and 305 ± 11 Ma for eclogites from the Habutengsu river (Fig. 1b). An age of 317 ± 5 Ma was obtained on high-pressure veins crosscutting a blueschist wall-rock, interpreted as the prograde dehydration-related transformation of blueschist to eclogite (Rb-Sr multi-point isochron; John et al., 2012). Recent Sm-Nd and Lu-Hf isochron ages of 318.4 ± 3.9 Ma and 326.9 ± 2.9 Ma on blueschists (Soldner et al., 2017) were interpreted as peak eclogite-facies and prograde metamorphism, respectively. Post-peak cooling was constrained by white mica K-Ar, Ar-Ar and Rb-Sr ages at around 310 Ma (Klemd et al., 2005). Ages < 280 Ma or $>$ than ~ 325 Ma were considered by most authors as resulting from limitations of isotopic dating (e.g. excess Ar in Ar-Ar system; Nd disequilibrium in Sm-Nd system; difficulties to relate zircon U-Pb ages to metamorphic stages) or taken as evidence for distinct HP-UHP episodes.

No.	Source	Area	Coordinate s	Lithology	Protolith	P _{max} -T				Age			
						Methods	P _{max}	1σ	-T	1σ	Methods	abs. age	2σ
1	Gao et al., 1995	Kekesu valley	n.m.	Blueschist	E-MORB	PG	9.5	0.5	450	10	Ph Ar-Ar	345.4	6.51
2	Gao et al., 1999	Akeyazi-Kebuerte	n.m.	Edogite	n.c.	PG+CTB	17.5	3.5	530	50	n.c.	-	-
3	Klemm et al., 2002	Akeyazi-Kebuerte	n.m.	Edogite	n.c.	PG+CTB	19.5	1.5	530	40	n.c.	-	-
4	Zhang et al., 2002a	Akeyazi valley-Atantayi	n.m.	Edogite	n.c.	avPT	>27.5	0.5	566	41	n.c.	-	-
5	Zhang et al., 2002b	Akeyazi valley-Atantayi	n.m.	Edogite	n.c.	CTB	26.2	0.5	547	51	n.c.	-	-
6	Gao et al., 2003	Akeyazi-Atantayi/Kebuerte	n.m.	Edogite	N- E-MORB, OIB	PG	20	1	530	40	Ph/Crs Al- Ar, Grt Omp-Gln- WR Sm- Nd	344	-
7	Wei et al., 2003	Akeyazi-Atantayi/Kebuerte	n.m.	Edogite	n.c.	TcPS+Mineral mol% isopleth	17	2	580	30	n.c.	-	-
8	Zhang et al., 2003	Muzaerte	n.m.	Metapelite	n.c.	CTB	50	6	580	20	n.c.	-	-
9	Lin et al., 2005	Akeyazi-Konguerbulake	n.m.	Edogite	n.c.	avPT+CTB	23	1	515	20	n.c.	-	-
10	Li et al., 2007	Muzaerte	n.m.	Rodingite	n.c.	CTB	11	1	480	30	n.c.	-	-
11	Van der Straaten et al., 2008	Akeyazi-Atantayi	n.m.	Blueschist	n.c.	PxPS+CTB	21	1	630	20	n.c.	-	-
12	Lv et al., 2009	Akeyazi-Habutengsu	n.m.	Edogite	n.c.	DtPS+Prp/Grs isopleths+CTB	25.5	1.5	490	20	n.c.	-	-
13	Wei et al., 2009	Akeyazi-Habutengsu/Muzisayi	n.m.	Pelitic/Felsic schists	n.c.	TcPS+Prp/Grs isopleths	22.5	-	550	-	n.c.	-	-
14	Beinlich et al., 2010	Akeyazi-Atantayi	n.m.	Blueschist	OIB	PxPS+CTB	21	1.5	510	30	n.c.	-	-
15	Du et al., 2011	Akeyazi-Habutengsu	n.m.	Law-bearing cld-gln schist	n.c.	TcPS+Gln/Car mol% isopleth	24.3	1.1	509	10	n.c.	-	-
			42° 30'59.4" 81° 18'49.6"				21	2	570	30			
16	Klemm et al., 2011	Akeyazi-Habutengsu/Muzisayi	32°14.1' 81° 27'8.4"	Edogite/Ab-gln-grt schist	n.c.	CTB	18	2	540	40	n.c.	-	-
			42° 30'59.4" 81° 18'49.6"				17	2	380	50			
			42° 32'54.2" 81° 19'40.6"				28.5	1.5	488	13			
			42° 32'28" 81° 19'49"				27	1	465	5			
17	Lv et al., 2012	Akesayi-Habutengsu/Eluosibulake	42°33'57" 81° 21'43.1"	Pelitic/Felsic schists	n.c.	DtPS+Prp/Grs isopleths	26.5	0.5	475	5	n.c.	-	-
			42°31'24" 81°20'52"				27.5	1.5	455	15			
			42°30'28" 81°25'31"				19.5	0.5	465	5			
			42°29'50" 81°21'12"				20	1	470	20			
18	Li et al., 2013	Akeyazi-Atantayi	n.m.	Edogite	n.c.	PxPS+Prp/Grs isopleths	23	-	590	-	n.c.	-	-
19	Lv et al., 2013	Akeyazi-Habutengsu	n.m.	Marble/Pelitic schist	n.c.	PxPS+Prp/Grs isopleths+Jd/Si-in-Ph isopleths	31	1	590	10	n.c.	-	-
							31	2	500	30			
20	Yang et al., 2013	Akeyazi-Kebuerte	n.m.	Pelitic schist	n.c.	TcPS+Prp/Grs isopleths	29	-	565	-	Zircon U-Pb	320.4	3.7
							29.5	0.5	533	7			
21	Tian and Wei., 2013	Akeyazi-Atantayi/Kebuerte	n.m.	Edogite	n.c.	TcPS+Prp/Grs isopleths	25.5	1.5	590	-	n.c.	-	-
							22	-	540	-			
22	Du et al., 2014a	Akeyazi-Habutengsu	n.m.	Edogite	E-MORB/OIB	TcPS+Prp/Grs isopleths	25	1	530	10	Grt-Omp- WR Sm- Nd	310	4.5
							23	1	495	15		305	15
							25.5	1.5	510	20		305	11
23	Du et al., 2014b	Akeyazi-Habutengsu	n.m.	Edogite	n.c.	TcPS+Prp/Grs isopleths	24.3	1.3	498	7	n.c.	-	-
							20	-	560	10			
24	Li et al., 2015	Akeyazi-Kebuerte	n.m.	Edogite/Pelitic schist	n.c.	PxPS+Prp/Grs isopleths	24	1	495	5	n.c.	-	-
							22.5	0.5	465	5			
25	Shen et al., 2015	Muzaerte-Changawuzi	n.m.	serpentinized wehrlite	n.c.	PxPS+Alg XAl/XMg isopleths	37	7	520	10	n.c.	-	-
26	Li et al., 2016	Akeyazi-Akesayi	n.m.	Edogite	n.c.	PxPS+Prp/Grs isopleths	23.5	1	505	5	n.c.	-	-
27	Lv and Zhang., 2016	Akeyazi-Habutengsu	n.m.	Pelitic schists	n.c.	TcPS+Prp/Grs isopleths	30	2	520	10	Ph Ar-Ar	315.3	1.6
			42°32.66' 81°20.01'	Pelitic schists			25	2	530	30		315.3	1.7
			42°32.64' 81°20.03'	Edogite			18.5	-	510	-			
			42°32.67' 81°20.04'	Edogite			24	-	530	-			
			42°32.70' 81°19.83'	Pelitic schists			20.5	-	550	-			
28	Meyer et al., 2016	Akeyazi-Habutengsu	42°32.68' 81°19.80'	Edogite	N- E-MORB, UCC	PxPS+Prp/Grs isopleths+avPT+RSCM+CTB	22	-	550	-	n.c.	-	-
			42°32.66' 81°19.74'	Pelitic schists			21	-	513	12			
			42°32.69' 81°19.74'	Edogite			21.5	1	525	15			
			42°32.68' 81°19.74'	Edogite			22.8	-	540	-			
			42°32.66' 81°19.74'	Edogite			24	-	540	-			
29	Soldner et al., 2016	Akeyazi-Atantayi/Kebuerte	n.m.	Edogite/Blueschist	n.c.	PxPS+Prp/Grs isopleths+CTB	25.5	0.5	463	38	Grt-Gln- WR Sm- Zircon U-Pb	318.4	3.9
							12.5	0.5	550	-		326	2.9
30	Tan et al., 2017	Akeyazi-Atantayi	42°31'57" 81°12'37"	Edogite	N-MORB	PxPS+Prp/Grs isopleths+avPT	29.5	2	510	20	n.c.	-	-
31	Zhang et al., 2017	Akeyazi-Atantayi	n.m.	Edogite	n.c.	TcPS+Prp/Grs isopleths	24	1	550	10	n.c.	-	-
32	Zhang et al., 2018	Akeyazi-Akesayi	n.m.	Edogite	n.c.	TcPS+Prp/Grs isopleths	30	-	560	10	Zircon U-Pb	320	-

Table 1: Notes: Exhaustive collection of regional P_{max}-T estimates and their relevant data was done above, mainly focusing on the collection of locality, lithology, protolith, P-T estimate method and result, whether did age dating or not, and relevant detail of thermodynamic modeling presetting if present. "n.m." in Coordinates column means not mention; "n.c." in Protolith and Age column means not conducted; "Px-, Tc-, DtPs" in P_{max}-T column represent pseudosection calculation, respectively, by Perple_x, Thermocalc and Domino. PG, CTB, avPT respectively represent petrological grid, conventional thermobarometer (e.g., grt-cpx thermometer) and Thermocalc average PT multi equilibrium calculation; "n.c. and not int." in solid solution mode column respectively means not considered and not international (i.e., can not be found in solid solution mode databases of both Perple_x and Thermocalc); * marked solid solution modes only existed in Thermocalc database, and

Method	Age (Ma)	2σ-error (Ma)	Lithology	Precise P-T constraints	Pmax (GPa)	P error (GPa)	T _{max} (°C)	T error (°C)	Interpretation of age	Origin
Zircon U-Pb	320.4	3.7	UHP mica schist	UHP-EC	2.7	0.2	560	15	UHP EC facies metamorphism	Yang et al., JAES, 2013
Zircon U-Pb	226.3	4.6	Eclogite	-	2.0-3.2 ^a	-	500-600 ^a	-	(HP/UHP?) EC facies metamorphism	Zhang et al., Lithos, 2007
Zircon U-Pb	234	6	Eclogite	-	2.0-3.2 ^a	-	500-600 ^a	-	(HP/UHP?) EC facies metamorphism	Zhang et al., Lithos, 2007
Zircon U-Pb	310	6	Eclogite	-	2.0-3.2 ^a	-	500-600 ^a	-	Formation of ocean crust	Zhang et al., Lithos, 2007
Zircon U-Pb	318	2	Eclogite	-	2.0-3.2 ^a	-	500-600 ^a	-	(HP/UHP?) EC facies metamorphism	Liu et al., Lithos, 2014
Zircon U-Pb	319.8	3.1	Eclogite	-	2.0-3.2 ^a	-	500-600 ^a	-	(HP/UHP?) EC facies metamorphism	Su et al., EJM, 2010
Zircon U-Pb	291	15	Rodingite	Near-surface	-	-	-	-	rodingitization after exhumated to near-surface	Li et al., Lithos, 2010
Zircon U-Pb	422	10	Rodingite	Before subduction	-	-	-	-	seafloor metamorphism before subducted	Li et al., Lithos, 2010
Rutile U-Pb	318	7	Eclogite	-	2.0-3.2 ^a	-	500-600 ^a	-	(HP/UHP?) EC facies metamorphism	Li et al., Lithos, 2011
Ar-Ar crs	344	1	Eclogite	-	2.0-3.2 ^a	-	500-600 ^a	-	cooling or recrystallization	Gao et al., Lithos, 2003
Ar-Ar gln	370	1	Blueschist	BS	1.0-2.2 ^b	-	400-500 ^b	-	BS facies overprint	Gao et al., 2000, chinese publication
Ar-Ar gln	401	1	Eclogite	-	2.0-3.2 ^a	-	500-600 ^a	-	(HP/UHP?) EC facies metamorphism	Gao et al., 2000, chinese publication
Ar-Ar gln	345.4	0.7	Blueschist	BS	1.0-2.2 ^b	-	400-500 ^b	-	(HP/UHP?) EC facies metamorphism	Gao et al., 2006, chinese publication
Ar-Ar white-mica	345.4	6.5	Blueschist	BS	1.0-2.2 ^b	-	400-500 ^b	-	Retrograde GS facies metamorphism	Gao et al., TP, 1995
Ar-Ar white-mica	315.3	1.6	Metapelite	UHP-EC	3.00	0.18	530	15	recrystallization age of UHP phengite	Lv and Zhang, 2016
Ar-Ar white-mica	315.3	1.7	Metapelite	HP-EC	2.45	0.20	535	35	recrystallization age of HP phengite	Lv and Zhang, 2016
Ar-Ar white-mica	331	2	Eclogite	-	2.0-3.2 ^a	-	500-600 ^a	-	GS facies overprint	Gao et al., Lithos, 2003
Ar-Ar white-mica	311.6	0.5	Blueschist	BS	1.0-2.2 ^b	-	400-500 ^b	-	cooling or recrystallization	Klemm et al., AMG, 2005
Ar-Ar white-mica	311.6	0.4	Blueschist	BS	1.0-2.2 ^b	-	400-500 ^b	-	cooling or recrystallization	Klemm et al., AMG, 2005
Ar-Ar white-mica	327.8	0.5	Blueschist	BS	1.0-2.2 ^b	-	400-500 ^b	-	cooling or recrystallization	Klemm et al., AMG, 2005
Ar-Ar white-mica	321	0.5	Blueschist	BS	1.0-2.2 ^b	-	400-500 ^b	-	cooling or recrystallization	Klemm et al., AMG, 2005
Ar-Ar white-mica	322.9	0.8	Blueschist	BS	1.0-2.2 ^b	-	400-500 ^b	-	cooling or recrystallization	Klemm et al., AMG, 2005
Ar-Ar white-mica	321.4	1.6	grt-gln mica schist	BS	1.0-2.2 ^b	-	400-500 ^b	-	BS facies overprint	Xia et al., IGR, 2015
Ar-Ar white-mica	318.6	1.6	grt-phn schist	BS	1.0-2.2 ^b	-	400-500 ^b	-	BS facies overprint	Xia et al., IGR, 2015
Ar-Ar white-mica	293.3	1.5	epidote mica schist	GS	0.5-0.8 ^c	-	300-400 ^c	-	GS facies overprint	Xia et al., IGR, 2015
Ar-Ar white-mica	364	1	Blueschist	GS	0.5-0.8 ^c	-	300-400 ^c	-	GS facies overprint	Gao et al., 2000, chinese publication
Ar-Ar white-mica	381	1	Eclogite	-	2.0-3.2 ^a	-	400-500 ^b	-	(HP/UHP?) EC facies metamorphism	Gao et al., 2000, chinese publication
Ar-Ar white-mica	316	2	Retrograde blueschist	BS	1.0-2.2 ^b	-	400-500 ^b	-	cooling or recrystallization	Wang et al., JG, 2010
Ar-Ar white-mica	331	1	Retrograde blueschist	BS	1.0-2.2 ^b	-	400-500 ^b	-	cooling or recrystallization	Wang et al., JG, 2010
Ar-Ar white-mica	323	1	Retrograde mica-quartz schist	BS	1.0-2.2 ^b	-	400-500 ^b	-	cooling or recrystallization	Wang et al., JG, 2010
Ar-Ar white-mica	334.7	0.9	grt-gln mica schist	BS	1.0-2.2 ^b	-	400-500 ^b	-	cooling or recrystallization	Gao et al., 2006, chinese publication
Ar-Ar white-mica	317.1	0.2	grt-gln mica schist	BS	1.0-2.2 ^b	-	400-500 ^b	-	cooling or recrystallization	Gao et al., 2006, chinese publication
Ar-Ar white-mica	310.3	0.3	Blueschist	BS	1.0-2.2 ^b	-	400-500 ^b	-	cooling or recrystallization	Gao et al., 2006, chinese publication
Ar-Ar white-mica	313	3.8	Blueschist	BS	1.0-2.2 ^b	-	400-500 ^b	-	cooling or recrystallization	Klemm et al., AMG, 2005
Rb-Sr white-mica	301.6	3.4	Blueschist	BS	1.0-2.2 ^b	-	400-500 ^b	-	cooling or recrystallization	Klemm et al., AMG, 2005
Rb-Sr white-mica	309.4	2.3	Blueschist	BS	1.0-2.2 ^b	-	400-500 ^b	-	cooling or recrystallization	Klemm et al., AMG, 2005
Rb-Sr white-mica	309	3	Blueschist	BS	1.0-2.2 ^b	-	400-500 ^b	-	cooling or recrystallization	Klemm et al., AMG, 2005
Rb-Sr white-mica	310.7	3.2	Blueschist	BS	1.0-2.2 ^b	-	400-500 ^b	-	cooling or recrystallization	Klemm et al., AMG, 2005
Rb-Sr white-mica	310.1	3.1	Blueschist	BS	1.0-2.2 ^b	-	400-500 ^b	-	cooling or recrystallization	Klemm et al., AMG, 2005
Sm-Nd grt-gln	346	3	Eclogite	-	2.0-3.2 ^a	-	500-600 ^a	-	(HP/UHP?) EC facies metamorphism	Gao et al., Lithos, 2003
Sm-Nd grt-omp-WR	309.8	4.6	Eclogite	HP-EC	2.5	0.2	550	20	HP EC facies metamorphism	Du et al., Lithos, 2014
Sm-Nd grt-omp-WR	306	15	Eclogite	HP-EC	2.3	0.2	560	15	HP EC facies metamorphism	Du et al., Lithos, 2014
Sm-Nd grt-omp-WR	305	11	Eclogite	HP-EC	2.4	0.2	550	20	HP EC facies metamorphism	Du et al., Lithos, 2014
Sm-Nd grt-gln-WR	318.4	3.9	Blueschist(used to be EC)	HP-EC	2.5-2.6	-	425-500	-	HP EC facies metamorphism	Soldner et al., GR, 2016
Lu-Hf multi-point in grt	313	12	mafic rock	-	2.0-3.2 ^a	-	500-600 ^a	-	(HP/UHP?) EC facies metamorphism	Klemm et al., EPSL, 2011
Lu-Hf multi-point in grt	315.8	2.9	mafic schist	-	2.0-3.2 ^a	-	500-600 ^a	-	(HP/UHP?) EC facies metamorphism	Klemm et al., EPSL, 2011
Lu-Hf multi-point in grt	315.2	1.6	mafic schist	-	2.0-3.2 ^a	-	500-600 ^a	-	(HP/UHP?) EC facies metamorphism	Klemm et al., EPSL, 2011
Lu-Hf multi-point in grt	313.9	4.8	mafic schist	-	2.0-3.2 ^a	-	500-600 ^a	-	(HP/UHP?) EC facies metamorphism	Klemm et al., EPSL, 2011
Lu-Hf grt-gln-WR	326.9	2.9	Blueschist(used to be EC)	Prograde before HP-EC	2.5-2.6	-	425-500	-	Prograde HP EC facies metamorphism	Soldner et al., GR, 2016

Table 2: The compilation of previous age reports with relevant P-T estimates.

detailed P-T-time-isotopic studies; ii) representative lithologies with interesting mineral zonation were also chosen for in-depth investigation; iii) ~20 samples with relative clear senses of shear, and representative in terms of lithologies and sampling locations along the ~ 30km transect, were selected for P-T-in situ Ar-Ar probing-deformation mapping.

3.2. Bulk-rock and Mineral Chemistry

3.2.1. Bulk-rock Major and Trace Elements

Bulk-rock chemical analyses (§4, 5, 6) were performed both at the Institute of Geology and Geophysics, Chinese Academy of Sciences (IGGCAS), China and Institut des Sciences de la Terre de Paris (ISTeP), Sorbonne Université, France. Major oxides were determined by a PHILLIPS PW1480 X-ray fluorescence spectrometer (XRF) on fused glass disks. Loss on ignition (LOI) was measured after heating to 1000 °C. Uncertainties for most major oxides are ca. 2%, for MnO and P₂O₅ ca. 5%, and totals are within 100 ± 1 wt.%. Whole rock Fe₂O₃ content is constrained by potassium permanganate titration. Trace element concentrations were analyzed by inductively coupled plasma mass spectrometry (ICP-MS) using a Finnigan MAT ELEMENT spectrometer at IGGCAS and an ICP-MS 8800 Triple Quadrupole at ISTeP. The detailed analytical procedure is identical to that used by Qian et al. (2006). Relative standard deviations (RSD) are within ±10% for most trace elements but reach ±20% for V, Cr, Co, Ni, Th and U according to analyses of rock standards.

3.2.2. Mineral Major and Trace Elements

Major element compositions of minerals and relevant mapping (§4, 5, 6) were obtained from polished thin sections by electron microprobe analyses at IGGCAS with JEOL JXA 8100 and ITeP with CAMECA SX Five. Quantitative analyses were performed using wavelength dispersive spectrometers with an acceleration voltage of 15 kV, a beam current of 15 nA, a 3 µm beam size and 30 s counting time. Natural minerals and synthetic oxides were used as standards, and a program based on the ZAF procedure was used for data correction.

Concentrations of Zirconium in rutile (§5) were determined by electro microprobe following the method outlined by Zack et al. (2004). All analyses were conducted with a CAMECA SX Five in ITeP, Sorbonne Université, France. EMPA conditions were optimised specifically for Zr so that detect limitation could be improved by four times (20 µg/g compared with 80 µg/g). Acceleration voltage was set at 20 kV with 120 nA beam current and 5 µm beam diameter. A H-type spectrometer was chosen for measuring Zr-L α because of its highest sensitivity for this element. Detailed settings for spectrometers followed the Table. 2 of Zack et al. (2004). Every 10 analyses of unknown rutile were bracketed by 2 analyses of synthetic rutile standard for true zero-concentration count rates on the peaks and to exclude any machine drift.

In situ trace element point and profile analyses of zoned garnet, zircon and associated matrix mineral were performed by LA-ICP-MS at IGGCAS with a single collector quadrupole Agilent 7500a ICM-MS, equipped with an UP193Fx argon fluoride New Wave Research Excimer laser ablation system. Glass reference material

NIST SRM 610 and NIST SRM 612 were used as standards for external calibration. LA-ICP-MS measurements were conducted using a spot size diameter of 60 μm with a laser frequency of 15 Hz and 0.63 GW/cm² and a fluence of 3.32 J/cm². Acquisition time was 20 s for the background and 120 s for the mineral analyses. The relevant element content of minerals determined by EMPA was used as internal standards. Reproducibility and accuracy, which were determined for NIST SRM 610 and NIST SRM 612, are usually < 8% and < 6%. Trace element concentrations were then calculated using GLITTER Version 3 (Van Achtenbergh et al., 1999).

3.2.3. Zircon Oxygen Isotope

Oxygen isotope analyses (§4) at the exact locations of U-Pb isotope zircon were also processed with the use of the Cameca IMS-1280 SIMS at IGGCAS. After U-Pb dating, the mount was carefully repolished for the O isotope analyses. The Gaussian focused Cs⁺ ions are used as a primary beam to sputter zircon for O-isotope analyses. The primary beam size is ~10 μm in diameter, and 2.5-3.0 nA in intensity. The ¹⁶O and ¹⁸O ions are detected simultaneously by two Faraday cups, and the currents are amplified by 1010 ohms and 1011 ohms resistors, respectively. Each spot analysis consists of pre-sputtering, beam centering in apertures, and a signal collecting process. A single spot analysis lasts 3 mins, including 2 mins for pre-sputtering and centering the secondary beam, and 1 min to collect 16 cycles of ¹⁶O and ¹⁸O signals. Oxygen isotopes were measured using the multi-collection mode. The instrumental mass fractionation (IMF) was corrected using an in-house zircon standard Penglai with $\delta^{18}\text{OVSMOW} = 5.31 \pm 0.10\text{‰}$ (Q.-L. Li et al., 2010). The measured ¹⁸O/¹⁶O ratios were

normalized to the VSMOW composition, then corrected for IMF as described in (Li et al., 2010b): $IMF = \delta^{18}O_M - \delta^{18}O_{Standard}$, and $\delta^{18}O_{Sample} = \delta^{18}O_M + IMF$, where $\delta^{18}O_M = [(^{18}O/^{16}O)_M / 0.0020052 - 1] \times 1000$ (‰) and $\delta^{18}O_{Standard}$ is the recommended $\delta^{18}O$ value for the zircon standard on the VSMOW scale. Corrected $\delta^{18}O$ values are reported in the standard per mil notation with 2σ errors. Analytical conditions, instrumentation and operation conditions are similar to Li et al. (2010) and Tang et al. (2015).

3.3. P-T Constraints

3.3.1. Perple_X Pseudosection Modeling

Pseudosection modeling (§4, 5) was performed in the system MnNCKFMASHTO for key metavolcanic eclogite samples (No. 11AT06, §4) with excess SiO_2 (i.e., quartz or coesite), for either P-T estimates or investigation of mineral mode evolution. TiO_2 must be considered due to the presence of rutile and/or titanite in the matrix or as inclusions in porphyroblasts. The fluid phase is assumed to be pure H_2O and was set in excess or specific a_{H_2O} value. CO_2 was neglected as only small amounts of carbonate occur as thin secondary veins. Fe_2O_3 was set at fixed ratio of total FeO according to XRF data.

In order to take into account the sequestration of elements induced by the growth zoning of garnet porphyroblast, effective bulk compositions were adjusted from XRF compositions by removing part of the garnet modal abundance, following the method of Carson et al. (1999). For the modelling of prograde and peak conditions, half of the

modal abundance of zoned garnet (e.g., Warren and Waters, 2006; Wei et al., 2009) was removed from the XRF composition. For the retrograde path, the entire fractionated composition by garnet porphyroblasts were subtracted from the bulk-rock composition.

The P-T pseudosections were calculated using the software *Perple_X* 6.68 (Connolly, 2005, 1990) and an internally consistent thermodynamic dataset (hp02ver.dat or hp04ver.dat; Connolly and Kerrick, 2002; Holland and Powell, 2003) based on the effective recalculated bulk rock composition. Mineral solid-solution models are Gt(HP) for garnet (Holland and Powell, 1998), Omph(GHP) for omphacite (Green et al., 2007), Amph (DP) for amphibole (Diener et al., 2007), Mica(CHA) for white mica (Coggon and Holland, 2002), Chl(HP) for chlorite (Holland and Powell, 1998), Ep(HP) for epidote/clinozoisite (Holland and Powell, 1998), and H₂O-CO₂ fluid solution model is from Connolly and Trommsdorff (1991). P-T conditions were further constrained by comparing predicted garnet end-member isopleths with measured garnet compositions and incorporate typical uncertainties on EMPA analyses (ca. 3% to 5%; Lifshin and Gauvin, 2001; Williams and Jercinovic, 2006).

3.3.2. THERMOCALC Multi-equilibrium Average PT

THERMOCALC multi-equilibrium average PT calculations (§6) were conducted for metavolcanoclastics/metavolcanics for the regional P-T-time mapping.

The internally consistent thermodynamic dataset (tc-ds55) of Holland & Powell (1998) and the program THERMOCALC v3.33 (Holland and Powell, 1998, 1990) were applied for multi-equilibrium P-T estimates. Recalculation of the analyses (e.g., the calculations of Fe³⁺ and mineral end-member activities) was performed with the

program AX of Holland and Powell (<ftp://www.esc.cam.ac.uk/pub/minp/AX/>). Only P-T estimates, which satisfies the equilibrium test criteria (e.g., sigfit, hat (Holland and Powell, 1998)), have been considered. The accuracy of P-T estimates, as predicted by the error ellipse parameters, is generally on the order of 0.05-0.2GPa for pressure and 10-30°C for temperature. Some end-members merely present in small amounts (e.g., Fe-celadonite/celadonite for some phengite), which yield a large uncertainty on the results, were removed during calculation.

3.3.3. Zr-in-Rutile Thermometry

Diffusion of Zr in rutile generally depends on both oxygen fugacity and temperature, via interstitial tetravalent ion migration (Sasaki et al., 1985). Zack et al. (2004, 2002) revealed the temperature dependence of Zr incorporation in rutile and proposed a thermometer. This empirical thermometer is based on Zr incorporation in rutile and is calibrated on natural rocks, with temperatures ranging from 430 to 1100 °C. Electron microprobe analysis (EMPA) is used to measure the Zr concentration in rutile grains (§5), which is log-linear correlated to temperature according to the equation:

$$T(\text{in } ^\circ\text{C}) = 127.8 \times \ln(\text{Zr in } \mu\text{g/g}) - 10$$

Watson et al. (2006) proposed a new calibration for the Zr in rutile thermometer from natural and synthetic rutiles in the presence of quartz in the range of 470 to 1450 °C. Ferry and Watson (2007) updated the equation to:

$$\log(\text{Zr in } \mu\text{g/g}) \times \log a_{\text{SiO}_2} = A + \frac{B}{T(\text{in } \text{K})}$$

with $A = 7.420 \pm 0.105$ and $B = -4530 \pm 111$. The activity of the quartz was assumed =1, as quartz was always present in most of our samples.

Tomkins et al. (2007) specified new thermometer equations with considering the secondary pressure effect accompanying the primary temperature dependence of the Zr content of rutile:

in the α -quartz field:

$$T(\text{in } ^\circ\text{C}) = \frac{83.9 + 0.410P}{0.1428 - R\ln(\text{Zr in } \mu\text{g/g})} - 273$$

in the β -quartz field:

$$T(\text{in } ^\circ\text{C}) = \frac{85.7 + 0.473P}{0.1453 - R\ln(\text{Zr in } \mu\text{g/g})} - 273$$

in the coesite field

$$T(\text{in } ^\circ\text{C}) = \frac{88.1 + 0.206P}{0.1412 - R\ln(\text{Zr in } \mu\text{g/g})} - 273$$

in which P is in kbar and R is the gas constant, 0.0083144 kJ/K.

3.3.4. Raman Spectrometry Carbonaceous Material Thermometry (RSCM)

The Raman spectroscopy of carbonaceous material (RSCM, Beyssac et al., 2002) is applied here (§6) as the independent peak temperature estimate to be compared with those from THERMOCALC. It was calibrated as a geothermometer ($\pm 50^\circ\text{C}$) in the range 330-650°C. Relative, intersample uncertainties on temperature can be much smaller, around 10-15°C (Beyssac et al., 2004). Since the degree of organization of the carbonaceous material is irreversible, temperatures deduced from the Raman spectra represent peak temperature conditions reached by the rocks. RSCM was done on thin sections of graphite-bearing metavolcanoclasts oriented perpendicular to the foliation by focusing the laser beam beneath a transparent crystal. Raman spectra were obtained with a Renishaw INVIA Reflex Raman microspectrometer at the Laboratoire de Géologie of the Ecole Normale Supérieure, France. Spectra were excited at room

temperature with the 514.5 nm line of a 20 mW Ar Spectra Physics laser through a LEICA 100X objective (NA 0.90). Detail procedure of analysis follows that of Agard et al. (2006). We recorded at least 13 spectra for each sample to take into account the CM heterogeneities. The program Peak Fit 4.0 was then used to process the spectra.

3.3.5. Ti-in-Biotite Thermometry

An empirical Ti-in-biotite geothermometer (Henry et al., 2005) is also used here (§6) to serve as the independent temperature estimates for regional GS facies metamorphism recorded by biotite-bearing metavolcanoclasts. It was calibrated from rocks equilibrated at roughly 0.4-0.6GPa and 480-800°C with composition range of $X_{Mg} = 0.275-1.000$ and $Ti = 0.04-0.60$ apfu. Precision of the Ti-in-biotite thermometer is estimated to be $\pm 24^{\circ}C$ at the lower temperature range and improves to $\pm 12^{\circ}C$ at higher temperatures.

3.4. Radiometric Constraints

3.4.1. Zircon U-Pb Geochronology

Zircon grains of coesite-bearing eclogite samples (No. 11AT06, §4) were prepared by conventional crushing techniques and were hand-picked, mounted onto epoxy resin disks and polished with 0.25 μm diamond paste. The zircon grains and zircon standards (Plesovice, Peng Lai and Qing Hu zircon were used here as standards) were mounted in epoxy mounts and then polished to section the crystals in half. Assessment of zircon grains and the choice of analytical sites were based on the transmitted and reflected light microscopy and cathodoluminescence (CL) images. CL imaging was processed

on the LEO145VP scanning electron microscope with a Mini detector at the Institute of Geology and Geophysics, Chinese Academy of Sciences in Beijing (IGGCAS). The mount was vacuum-coated with high-purity gold prior to secondary ion mass spectrometry (SIMS) analyses. Measurements of U, Th and Pb were conducted using the Cameca IMS-1280 SIMS. U-Th-Pb ratios and absolute abundances were determined relative to the standard zircon 91500 (Wiedenbeck et al., 1995), analyses of which were interspersed with those of unknown grains, using operating and data processing procedures similar to those described by Li et al. (2009). A long-term uncertainty of 1.5% (1 RSD) for $^{206}\text{Pb}/^{238}\text{U}$ measurements of the standard zircons was propagated to the unknowns (Q.-L. Li et al., 2010) despite that the measured $^{206}\text{Pb}/^{238}\text{U}$ error in a specific session is generally around 1% (1 RSD) or less. Measured compositions were corrected for common Pb using non-radiogenic ^{204}Pb . Further details on instrument parameters, analytical method, calibration and correction procedures can be found in Li et al. (2010).

The U-Pb dating and trace element analysis of zircon grains in metabasite (No. 158, §6) was simultaneously conducted by LA-ICP-MS at the Wuhan SampleSolution Analytical Technology Co., Ltd., China. Detailed operating conditions for the laser ablation system and the ICP-MS instrument and data reduction are the same as description by Zong et al. (2017). Laser sampling was performed using a GeolasPro laser ablation system that consists of a COMPexPro 102 ArF excimer laser (wavelength of 193nm and maximum energy of 200mJ) and a MicroLas optical system. An Agilent 7700e ICP-MS instrument was used to acquire ion-signal intensities. Helium was

applied as a carrier gas. Argon was used as the make-up gas and mixed with the carrier gas via a T-connector before entering the ICP. A “wave” signal smoothing device is included in this laser ablation system (Hu et al., 2015). The spot size and frequency of the laser were set to 60 μ m and 6Hz, respectively, in this study. Zircon 91500 and glass NIST610 were used as external standards for U-Pb dating and trace element calibration, respectively. Each analysis incorporated a background acquisition of approximately 20-30s followed by 50s of data acquisition from the sample. An Excel-based software ICPMSDataCal was used to perform off-line selection and integration of background and analyzed signals, time-drift correction and quantitative calibration for trace element analysis and U-Pb dating (Liu et al., 2009). Concordia diagrams and weighted mean calculations were made using Isoplot/Ex_ver3 (Ludwig, 2003).

3.4.2. Sm-Nd Geochronology

Sm-Nd isotopic analyses were performed for the oriented sample of coesite-bearing eclogites (No. 11AT06, §4) and obtained at the Institute of Geology and Geophysics, Chinese Academy of Sciences, Beijing. 100 mg of samples were first mixed with ^{149}Sm - ^{150}Nd diluent, dissolved afterwards in a purified HF-HClO₄-HNO₃-mixture, and finally heated on an electric hot plate for a week. Separation and purification of bulk REE were conducted by a silica-column with an AG50W-X12 exchange resin (200–400 mesh, 2ml), those of Sm and Nd by a silica-column with Teflon powder (1 ml) as exchange medium. Isotopic ratios of Sm and Nd were measured using a Finnigan MAT-262 thermal ionization mass spectrometer. Nd isotopic data of unknowns were normalized to $^{146}\text{Nd}/^{144}\text{Nd}$ of 0.7219, and corrected

using Ames ($^{143}\text{Nd}/^{144}\text{Nd} = 0.512138$) as external standard. Errors in element concentrations and $^{147}\text{Sm}/^{144}\text{Nd}$ -ratios are less than 0.5% (2σ).

3.4.3. ^{40}Ar - ^{39}Ar Step-heating Geochronology

Selected samples were crushed and sieved (§6). Single grains phengite were handpicked under binocular microscope and cleaned in ultrasonic bath with acetone and distilled water. They were packaged in Al foils and irradiated for 40h in the core of the Triga Mark II nuclear reactor of Pavia (Italia) with several aliquots of the Fish Canyon sanidine standard (28.03 ± 0.08 Ma, Jourdan & Renne, 2007) as flux monitor. Argon isotopic interferences on K and Ca were determined by irradiation of KF and CaF_2 pure salts from which the following correction factors were obtained. Argon analyses were performed at Géosciences Montpellier, France with two analytical devices that each consist of: (a) an IR- CO_2 laser of 100kHz used at 5-15% during 60s, (b) a lenses system for beam focusing, (c) a steel chamber, kept at 10^{-8} - 10^{-9} bar, with a drilled copper plate, (d) an inlet line for purification of gases including two Zr-Al getters, (e) a multi-collector mass spectrometer (Argus VI from Thermo-Fisher). A custom-made software controls the laser intensity, the timing of extraction/purification and the data acquisition. To measure the Ar background within the system, one blank analysis was performed every three sample analyses. ArArCalc v2.5.2 was used for data reduction and plotting. The two-sigma errors reported on plateau, isochron and total gas ages include the error on the irradiation factor J. Atmospheric ^{40}Ar was estimated using a value of the initial $^{40}\text{Ar}/^{36}\text{Ar}$ of 295.5.

3.4.4. ^{40}Ar - ^{39}Ar In Situ Laser Ablation Probing Geochronology

The ^{40}Ar - ^{39}Ar in situ laser ablation technical procedure (§6) was first proposed by Schaeffer et al. (1977) and modified by Maluski & Monié (1988). Sample preparation and analysis (procedure as in Agard et al., 2002, 2006; Augier et al., 2005) were conducted at Géosciences Montpellier, France. The laser system consists of a continuous 6W argon ion laser, a beam shutter for selection of lasering exposure time, with typically 5ms pulses separated by 40ms, and a set of lenses for beam focusing. The number of pulses depends on the nature of the analyzed mineral, its K content and its presumed age. Argon extraction, purification and analyses are performed within three distinctive parts with the sample chamber where gas extraction is done, the purification line with hot getters and nitrogen liquid traps (cold) traps, and a MAP 215-50 noble gas mass spectrometer equipped with an electron multiplier. Rock sections 500 μm thick, which had been used to make the petrographic thin sections, were double polished within 1 μm tolerance. Whole section and detailed area photographs of both the rock section and corresponding thin section were taken for an accurate selection of favorable areas during lasering experiments. All samples were ultrasonically rinsed in ethanol and distilled water, wrapped in pure aluminum foils and then irradiated in the McMaster nuclear reactor (Canada) with several aliquots of the MMHb-1 international standard ($520.4 \pm 1.7\text{Ma}$, Samson & Alexander Jr, 1987). After irradiation, both the monitors and the sections were placed on a Cu holder inside the sample chamber and heated for 48h at 150-200°C.

For each age determination, argon was extracted from a $150 \times 300 \mu\text{m}$ surface corresponding to a mixture of several phengite grains, given grain size (Figs. 10b, S6). The crater is a $30\text{-}40 \mu\text{m}$ approximate hemisphere surrounded by a circular wall made of melted material. Incision of the sample did not exceed $10\text{-}20 \mu\text{m}$ deep depending on the three-dimensional orientation of the phengite crystals. Once the extraction was completed, about four minutes were required for gas cleaning of the line and 15 min for data acquisition by peak jumping from mass 40 to mass 36 (8 runs). For each experiment, ages have been obtained after correction with blanks, mass discrimination, radioactive decay of ^{37}Ar and ^{36}Ar and irradiation-induced mass interferences. They are reported with one sigma uncertainty (Table 4) and were evaluated assuming an atmospheric composition for the initially trapped argon (i.e., $(^{40}\text{Ar}\text{-}^{36}\text{Ar})^i \sim 295.5$).

4. P–T–time-isotopic evolution of coesite-bearing eclogites: Implications for exhumation processes in SW Tianshan

Tan, Z., Agard, P., Gao, J., John, T., Li, J.L., Jiang, T., Bayet, L., Wang, X.S., Zhang, X.X., 2017. P–T–time-isotopic evolution of coesite-bearing eclogites: Implications for exhumation processes in SW Tianshan. *Lithos* 278–281, 1–25. <https://doi.org/10.1016/j.lithos.2017.01.010>

Key words: *UHP metamorphism; eclogite; P-T path; pseudosection modeling; thermobarometry; zircon U-Pb; zircon oxygen isotope; exhumation pattern; Chinese Southwestern Tianshan;*

Authors:

Zhou Tan^{a,b,c}, Philippe Agard^{b,d}, Jun Gao^{a,c,}, Timm John^e, JiLei Li^a, Tuo Jiang^f, Léa Bayet^e, XinShui Wang^{a,c}, Xi Zhang^g*

- a. Key Laboratory of Mineral Resources, Institute of Geology and Geophysics, Chinese Academy of Sciences, 100029 Beijing, China
- b. Sorbonne Universités, UPMC Univ Paris 06, CNRS, Institut des Sciences de la Terre de Paris (ISTeP), 4 place Jussieu, 75005 Paris, France
- c. University of Chinese Academy of Sciences, 100049 Beijing, China
- d. Insitut Universitaire de France, F-75005, Paris, France
- e. Institut für Geologische Wissenschaften, Freie Universität Berlin, Malteserstr. 74–100, D-12449, Berlin, Germany
- f. Laboratory of Isotope Geochemistry, Wuhan Centre of China Geological Survey, 430205 Wuhan, China
- g. China Minmetals Corporation, 100010 Beijing, China

**corresponding author: Jun Gao, gaojun@mail.iggcas.ac.cn*

Abstract

The Chinese Southwestern Tianshan high- to ultra-high pressure low temperature (HP-UHP/LT) metamorphic belt exhibits well-preserved mafic layers, tectonic blocks/slices and boudins of different sizes and lithology embedded within dominant meta-volcanosedimentary rocks. Despite a wealth of previous studies on UHP relicts, P-T paths estimates and age constraints for metamorphism, controversies still exist on P-T-t assessments and regional exhumation patterns (i.e., tectonic *mélange* versus internally coherent “sub-belt” model). This study focuses on a group of coesite-bearing eclogite samples from a thick (~ 5 meters) layered metabasalt outcrop in order to unravel its detailed tectono-metamorphic evolution through space and time (both prograde, peak and exhumation). Using SIMS zircon U-Pb and oxygen isotope analyses, TIMS Sm-Nd multi-point isochron dating, in situ laser-ICP-MS trace-element analyses, classical thermobarometry and thermodynamic modeling, we link the multistage zircon growth to garnet growth and reconstruct a detailed P-T-time-isotopic evolution history for this UHP tectonic slice: from UHP peak burial $\sim 2.95 \pm 0.2$ GPa, 510 ± 20 °C around 318.0 ± 2.3 Ma to HP peak metamorphism $\sim 2.45 \pm 0.2$ GPa, 540 ± 20 °C at 316.8 ± 0.8 Ma, then, with eclogite-facies deformation $\sim 2.0 \pm 0.15$ GPa, 525 ± 25 °C at 312 ± 2.5 Ma, exhumed to near surface within ca. 303 to ca. 280 Ma. Our P-T-time-isotopic results combined to the compilation of regional radiometric data and P-T estimates notably point to the existence of a short-lived period of rock detachment and exhumation (< 10 Ma, i.e. at ca. 315 ± 5 Ma) with respect to subduction duration.

4.1. Introduction

Mechanisms and processes responsible for the occasional recovery of negatively buoyant, ocean-derived high- to ultra-high pressure low temperature (HP-UHP/LT) eclogites equilibrated along the subduction plate interface and for their juxtaposition as tectonic slices or blocks during exhumation remain a matter of debate (Agard et al., 2009; Burov et al., 2014; Chen et al., 2013; Federico et al., 2005; Gerya et al., 2002; Guillot et al., 2009; Klemd et al., 2011; Lü et al., 2012; Warren, 2013; Warren et al., 2008). The Southwestern Tianshan Akeyazi HP-UHP/LT metamorphic belt potentially provides an interesting test example, with well-preserved mafic horizons or tectonic blocks/slices/boudins of different sizes (from the cm- to km-scale) embedded in volumetrically dominant meta-volcanosedimentary rocks (Gao and Klemd, 2003; Gao et al., 1999; Meyer et al., 2016).

However, despite numerous previous works (on UHP relicts, detailed petrology, P-T estimates on isolated blocks/slices and time constraints on the timing of metamorphism; section 2), the area is still a matter of controversy as to (i) the exact P-T evolution and age of metamorphism, (ii) whether the metamorphic belt may be composed of two distinct HP and UHP slices and (iii) whether mafic bodies represent a tectonic *mélange* (Du et al., 2014; Gao et al., 1999; Klemd et al., 2011; Li et al., 2015; Meyer et al., 2016) or an assembly of km-scale tectonic slices (Lü et al., 2012).

Uncertainties partly arise from the fact that conclusions were drawn on spectacular but isolated samples (sometimes from loose scree and river beds) rather than on an extensive coverage of the area, and do not tightly enough link recrystallization

observations with P-T data. In order to contribute to clarifying these issues, we herein review and reappraise available P-T-t constraints for the area (Figure 16) and perform a combined P-T-radiometric-isotopic study on several eclogitic samples from a key location. Samples come from a thick (~ 5m) layered eclogite outcrop close to where UHP was previously reported (Lü and Zhang, 2012, Figure 16b) and were chosen to provide detailed constraints on their tectono-metamorphic and geochronological evolution (prograde, peak and exhumation stages) using SIMS high precision U-Pb isochron dating of zircon grains and whole-rock the TIMS Sm-Nd technique. Implications for recrystallization and exhumation processes are discussed and set back within the frame of the regional geodynamic evolution.

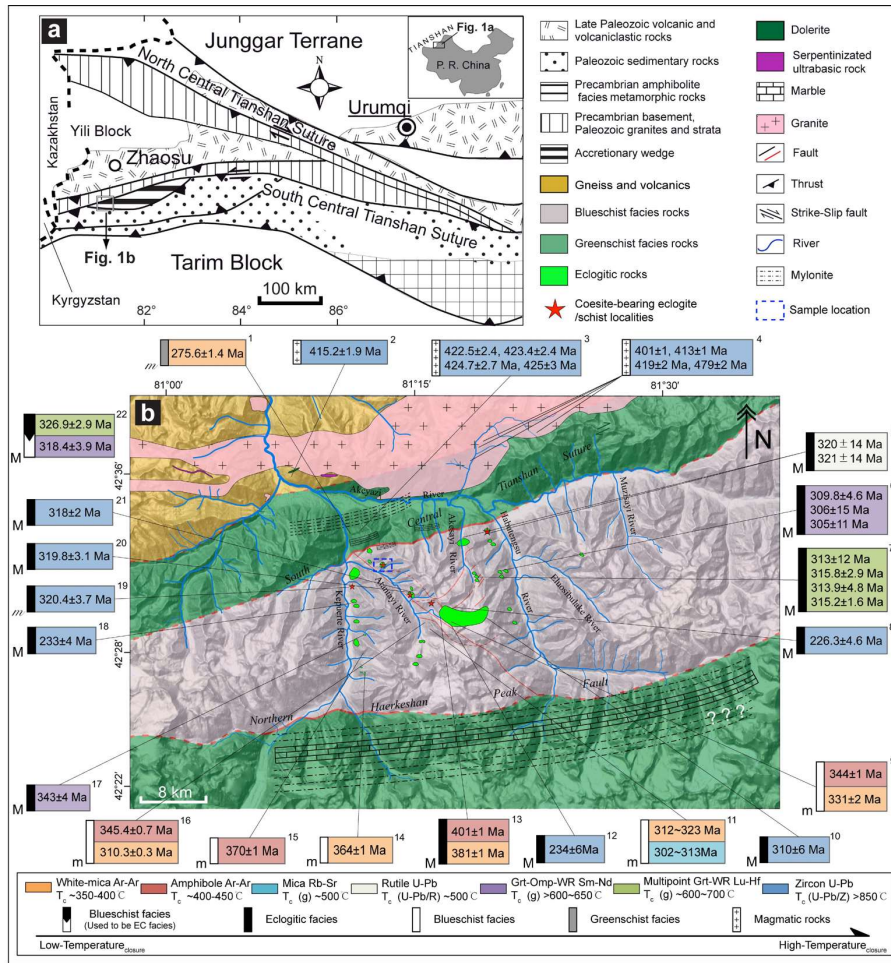


Figure 16: Simplified geological map of (a) the Chinese Western Tianshan and (b) close-up map for the area (modified after Gao et al. (1999) with tagged locality distribution of previous radio-chronological data. Red stars mark the location of UHP reports (the finding of coesite). Green overlays indicate the inferred distribution of eclogites based on literature data. The dashed blue box marks the sample location (Fig. 3) of this study. Letters on the lower-left corner of the age boxes refer to lithology: “M” for mafic (typical eclogite), “m” for matrix (mainly meta-volcanic sediment with abundant amphibole) and “m” for micaschist (mainly felsic). Numbers on the upper-right corner of the boxes correspond to publications listed in Table 2 and follow those of Figure 14 in chapter 2.

4.2. Geological setting

4.2.1. The Chinese Southwestern Tianshan HP-UHP/LT metamorphic complex

The Chinese Southwestern Tianshan high- to ultrahigh-pressure low-temperature metamorphic complex extends for about 200 km along the Southwestern Central Tianshan Suture Zone (SCTSZ; Figure 16). It is correlated with the Atbashi metamorphic complex in the Southwestern Tianshan Accretionary Complex (Hegner

et al., 2010) and the Fan-Karategin metamorphic belt (Volkova and Budanov, 1999). Gao et al. (1998) proposed that this HP-UHP/LT complex formed from the northward subduction of the South Tianshan ocean and subsequent collision between the already amalgamated Kazakhstan-Yili-Central Tianshan terrane, in the north, and the Tarim-Karakum plates in the south. Subduction polarity is still debated, however, with alternative suggestions of southward subduction (e.g. Lin et al., 2008).

The Southwestern Central Tianshan Suture Zone bounds to the north the Chinese section of the HP-UHP/LT metamorphic complex, known as the Akeyazi metamorphic complex. This contact, now a ~0.5 km wide sinistral strike-slip shear zone, was active from the late Permian to early Triassic (Gao et al., 1995; Gao and Klemd, 2000, 2003). To the north lies a LP-HT Palaeozoic active continental margin (Allen et al., 1993; Gao et al., 1998; Klemd et al., 2014), mainly made of amphibolite- and granulite-facies rocks, along with Late Silurian and Early Carboniferous continental arc-type volcanic and volcanoclastic rocks and granitoids (Gao and Klemd, 2003; Gao et al., 2009; Xia et al., 2014). The Akeyazi metamorphic complex (AMC) is overlain to the southwest by unmetamorphosed Palaeozoic sedimentary strata representing the northern, passive continental margin on margin of the Tarim plate (Allen et al., 1993; Carroll et al., 1995).

The Akeyazi metamorphic complex is predominantly composed of strongly schistosed meta-volcanosedimentary rocks hosting mafic metavolcanics, marbles and rare ultramafic rocks. Mafic metavolcanics are eclogites and/or blueschists showing gradual transitions or interlayering (Li et al., 2012). They are distributed as pods, boudins, thin layers or massive blocks in the host rocks (Gao and Klemd, 2003). The

AMC was interpreted by some as a tectonic mélangé and thought to have formed in a subduction accretionary wedge during subduction of the Southwestern Tianshan ocean (Gao and Klemd, 2003; Gao et al., 1999). Both the metavolcanics and the matrix meta-volcanosedimentary were variably retrogressed under blueschist and/or greenschist facies conditions.

Whole-rock geochemical data for the mafic metavolcanics suggest ocean basalt or arc-related affinities (Gao and Klemd, 2003; John et al., 2008; Klemd et al., 2005). A recent study indicated that some eclogite boundins also have a continental arc affinity protolith, possibly originating from the basement of a Palaeozoic continental arc setting (Liu et al., 2014a).

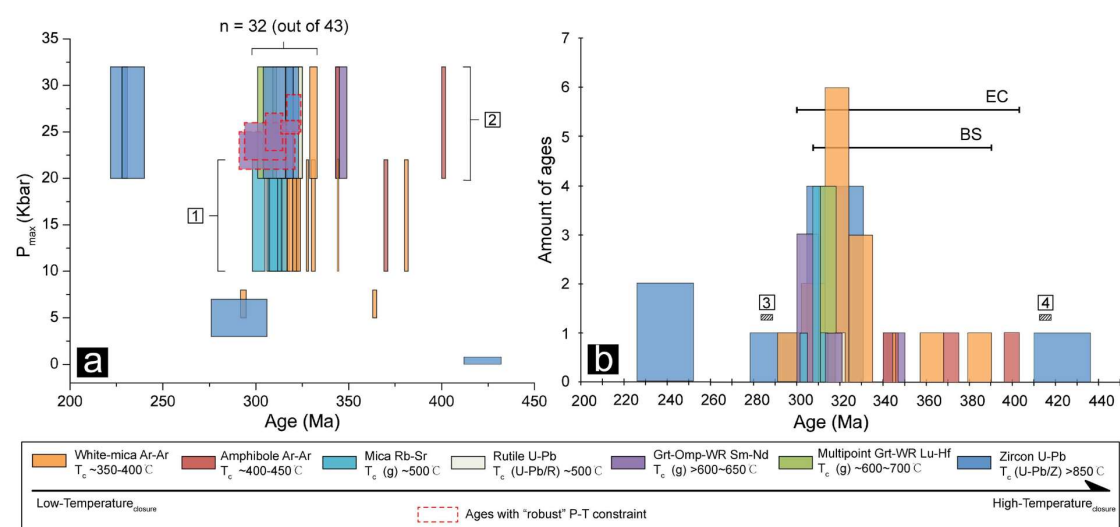


Figure 17: Compilation of age data (a) as a function of estimated P_{max} and (b) shown as a histogram (detail see Table 2). Sources listed in the captions of Figure 16 and Table 2. “1”: P_{max} range for previous “blueschist” ages lacking precise P - T constraint; “2”: same for eclogites; “3”: range of zircon U-Pb data from SP leucogranite dikes (Gao et al., 2011); “4”: range of zircon (inherited core) U-Pb data from regional rodingite (Li et al., 2010c).

4.2.2. Previous age constraints on the P - T evolution of tectonic slices/blocks

Most peak metamorphic estimates for eclogites and prograde blueschists (differences are largely controlled by lithology) yield eclogite-facies HP-LT conditions

within the range 480-580°C and 1.5-3.0 GPa (Beinlich et al., 2010; Gao et al., 1999; John et al., 2008; Klemd et al., 2002; Li et al., 2016; Meyer et al., 2016; Soldner et al., 2016; Wei et al., 2003). A range of P-T conditions of 570-630°C at 2.7-3.3 GPa was obtained for eclogite-facies micaschists (Wei et al., 2009; Yang et al., 2013), and 470-510°C at 2.4-2.7 GPa for eclogites (e.g. Meyer et al., 2016, see Table 2 for references). Evidence for UHP metamorphism comes from both relict coesite inclusions in garnet in several localities (stars in Figure 16b) and thermodynamic pseudosection modeling (Lü et al., 2008, 2009; Lü et al., 2012; Tian and Wei, 2013; Wei et al., 2009). The spread of P-T estimates (Du et al., 2011; Gao et al., 1995; Gao et al., 1999; Klemd et al., 2002; Li et al., 2015; Li et al., 2016; Li et al., 2012; Lü et al., 2009; Lü et al., 2012; Tian and Wei, 2013; Wei et al., 2003) may a priori arise from contrasting assumptions for thermodynamic modeling (and/or difficulties in determining Fe³⁺ content and assessing H₂O activity) or from the complexity of metamorphic evolutions in individual HP-UHP tectonic slices.

The exhaustive compilation of age data (location on Figure 16b), and the comparison of previous age data *versus* their assessed P_{max} estimates (Figure 17), evidence a considerable spread in ages too, with an overlap between eclogite and blueschist ages, whatever the protolith (Figure 17). The timing of peak metamorphic conditions falls in the range 325-305 Ma. Garnet growth by multi-point Lu-Hf isochron was dated at ca. 315 Ma (Klemd et al., 2011), for both eclogites and blueschists from a variety of valleys within AMC. U-Pb SIMS ages from metamorphic zircon rims in eclogites are indistinguishable within error, at 319 ± 3 Ma and 321 ± 2 Ma (Liu et al.,

2014a; Su et al., 2010) and similar to a U-Pb age of 318 ± 7 Ma obtained for eclogite-facies rutile (Li et al., 2011). Du et al. (2014) also reported a suite of relative consistent Sm-Nd isochron ages of 309 ± 4.6 Ma, 306 ± 15 Ma and 305 ± 11 Ma for eclogites from the Habutengsu river (Figure 16b). An age of 317 ± 5 Ma was obtained on high-pressure veins crosscutting a blueschist wall-rock, interpreted as the prograde dehydration-related transformation of blueschist to eclogite (Rb-Sr multi-point isochron, John et al., 2012). Recent Sm-Nd and Lu-Hf isochron ages of 318.4 ± 3.9 Ma and 326.9 ± 2.9 Ma on blueschists (Soldner et al., 2016) were interpreted as peak eclogite-facies and prograde metamorphism, respectively. Post-peak cooling was constrained by white mica K-Ar, Ar-Ar and Rb-Sr ages at around 310 Ma (Klemd et al., 2005). Ages < 280 Ma or > than ~325 Ma were considered by most authors as resulting from limitations of isotopic dating (e.g. excess Ar in Ar-Ar system; Nd disequilibrium in Sm-Nd system; difficulties to relate zircon U-Pb ages to metamorphic stages) or taken as evidence for distinct HP-UHP episodes.

4.2.3. Controversy on regional exhumation

The Akeyazi metamorphic complex is either interpreted as a tectonic mélangé or as made of two main units. In the first interpretation, mafic slices/blocks derived from different depths (UHP and HP conditions) were juxtaposed and mixed during exhumation in a meta-volcano-sedimentary subduction channel-like setting (Klemd et al., 2011; Li et al., 2016; Meyer et al., 2016). Despite, indications that rocks may have partly re-equilibrate with fluids in equilibrium with serpentinites (van der Straaten et al., 2008, 2012), serpentinites, which can act as buoyant material during exhumation

processes (Guillot et al., 2015), are extremely rare (Shen et al., 2015). Meta-volcanosedimentary rocks could also act as buoyant material and promote the exhumation of denser, negative-buoyant oceanic HP-UHP/LT rocks in a subduction channel (Gerya et al., 2002).

In contrast, the coherent sub-belt model (Lü et al., 2012), based on several individual UHP occurrences in the northern part of the AMC and the prevalence of blueschist facies rocks without UHP “signal” in the south, considers that the AMC consists of two internally coherent metamorphic “sub-belts”: a UHP in the north and a HP belt in the south, separated by a major fault contact (only inferred at present) and later juxtaposed during exhumation.

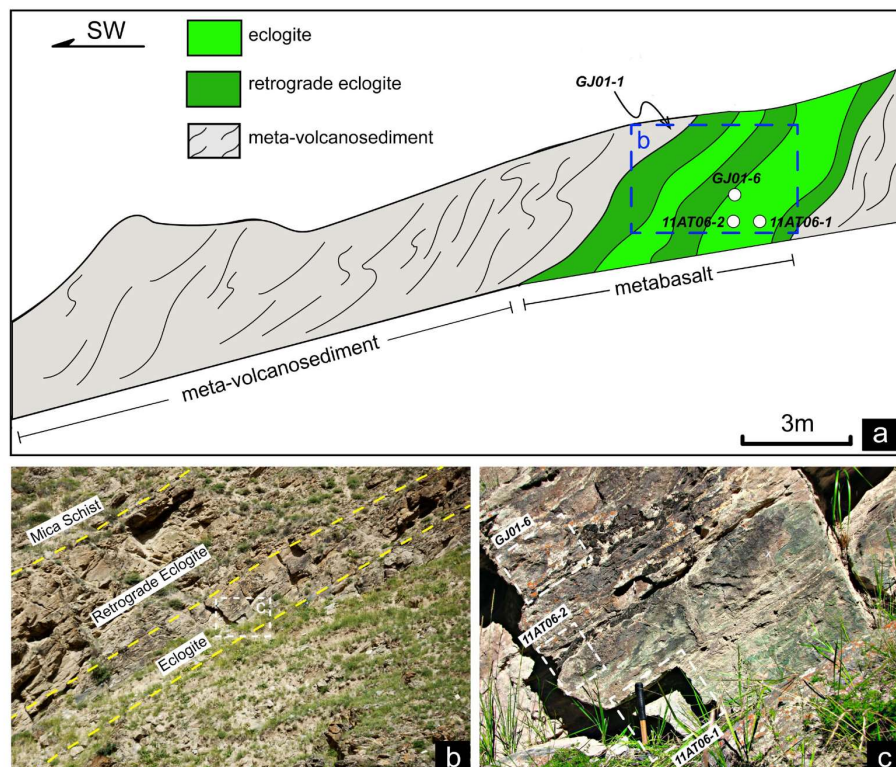


Figure 18: (a) Schematic outline of the studied outcrop; (b) field view of the sampling and (c) location of the samples in the layered eclogite.

4.3. Sample selection and whole-rock composition

Samples were collected from the second eastern tributary up the Atantayi valley (Figure 16b) in a ~six meter thick, layered eclogitic mafic slice. In order to detailedly reconstruct its tectono-metamorphic evolution (pro- and retrograde), three fresh eclogite samples were chose from the core of the thick-layered eclogite outcrop (Figure 18; oriented samples: GJ01-6, 11AT06-2; for geochemistry: 11AT06-1) and one garnet-clinopyroxene-quartz bearing micaschist from the meta-volcanosedimentary host-rock (GJ01-1). Considering the relative low Zr content (only ca. 50 ug/g) of the metabasalts (Table 4), about 100 kilograms of eclogite were sampled for the zircon study and approximately 500 zircon grains were collected and mounted (detailed processing is given in the Analytical methods in the Appendix).

Bulk- and trace-element geochemical data are shown in Table 4 and Figure 19. Loss on ignite on ranges between 1.8 and 3.3 wt. %, in agreement with modal abundances of hydrous mineral such as amphibole (5 to 8 vol%).

Chondrite- and primitive mantle-normalized (Sun and McDonough, 1989) rare earth element (REE) and trace-element patterns of the eclogites are similar to N-MORB (Figure 19), as further supported by a Th/Yb vs. Nb/Yb plot (Figure 19c) and by the $\epsilon_{\text{Nd}}(t)$ value of +8.5 ($t = \text{ca. } 312 \text{ Ma}$, Table. 7). They show a positive slope in LREEs to MREEs and flat in HREEs, with $(\text{La/Yb})_{\text{N}} = 0.542 - 1.097$, $(\text{La/Sm})_{\text{N}} = 0.524 - 0.666$, $(\text{Gd/Yb})_{\text{N}} = 0.999 - 1.536$ and a ΣREE concentration of 49.9 to 58.2 ppm (Table 4). Primitive mantle-normalized trace-element variations show moderate Rb, Ba, U and

Pb enrichments (Figure 19b) for these three eclogite samples. As expected for MORB type samples, there is no Nb-Ta depletion recorded.

The meta-volcanosedimentary rock is characterized by relatively high SiO₂ (~ 54.3 wt.%) and Al₂O₃ (~ 14.7 wt.%) contents. LREEs are enriched with La contents ~100 times higher than for chondrite, while HREE patterns are flat. REE and trace-element patterns for this meta-volcanosedimentary sample are close to that of the average upper continental crust (Fig. 4b, Rudnick and Gao, 2003) except for Rb.

Modal abundances of mineral assemblage in vol.%													
Samples	Grt	Omp	Amp	Ph	Pg	Ep/Zo	Qz	Ap	Rt	Ttn	Lws	Fe-Ti oxide	
<u>eclogite</u>													
11AT06-1	18	58	5	0.5	5.5	8	1	1	1.5	0.5	-	1	
11AT06-2	19	55	7	1	4	6	3	2	1	1	-	1	
GJ01-6	22	56	6	0.5	3.5	7	2	1	1	0.5	-	0.5	
GJ03-4a													
GJ03-4b													
Modeled abundances for Peak T condition (ca. 550°C+2.5GPa)	18.4	71	-	0.8	-	-	1	-	0.9	-	7.4	-	
<u>Wall-rock mica schist</u>													
GJ01-1	20	29	2	5	15	1	22	5	0.5	0.5	-	0.1	

Table 3: NOTES: Mineral modes were determined from the thin section by point counting on the basis of petrographic observations. The uncertainty of modal abundances of minerals was estimated to be less than 10% by repeating the same operations. Modeled abundances of mineral assemblage for peak T condition are calculated by pseudosection modeling with EBC-1.

Bulk rock major- and trace-element compositions						
Lithology	XRF data			EBC-1		EBC-2
	eclogite	Mica schist	eclogite	eclogite	eclogite	
Sample	11AT06-1	11AT06-2	GJ01-6	GJ01-1	11AT06-1	11AT06-1
Major elements (wt %)						
SiO ₂	47.97	47.62	46.92	54.33	50.63	52.47
TiO ₂	0.86	0.87	1.01	0.65	1.15	1.27
Al ₂ O ₃	14.87	14.55	15.23	14.65	14.62	14.06
MnO	0.23	0.14	0.14	0.14	0.10	0.05
MgO	7.22	6.38	6.75	4.03	6.28	6.65
CaO	10.05	11.75	10.69	7.18	11.53	12.15
Na ₂ O	4.15	4.60	5.10	3.96	5.31	5.92
K ₂ O	0.18	0.30	0.12	0.84	0.08	0.09
P ₂ O ₅	0.42	0.08	0.20	0.14	-	-
Fetot _a	11.88	10.23	10.68	9.09	-	-
FeO	8.72	7.28	7.80	-	8.23	5.87
Fe ₂ O ₃	2.19	2.14	2.01	-	2.06	1.47
LOI	1.86	3.34	2.68	4.86	-	-
Sum	99.69	99.86	99.52	99.87	100.00	100.00
Trace elements (ug/g)						
Li	33.2	34.8	34.5	21.7		
Be	0.537	0.370	0.480	0.680		
Sc	43.9	42.7	44.4	32.7		
V	263	263	273	179		
Cr	290	299	320	104		
Co	43.8	39.7	34.4	25.0		
Ni	137	128	103	86.6		
Cu	86.7	103	62.1	105		
Zn	172	144	156	94		
Ga	14.8	14.9	16.6	19.1		
Rb	6.28	5.51	6.50	19.6		
Sr	180	200	263	209		
Y	22.5	20.1	17.8	28.6		
Zr	59.3	48.1	50.0	106		
Nb	2.17	1.60	1.79	5.57		
Cs	1.03	0.610	0.580	1.53		
Ba	10.0	386	454	853		
La	2.47	1.73	2.57	18.6		
Ce	6.81	5.05	6.69	33.9		
Pr	1.18	0.980	1.27	4.29		
Nd	7.20	5.69	6.90	16.4		
Sm	2.46	2.13	2.49	3.89		
Eu	0.949	0.860	1.05	1.24		
Gd	3.08	2.89	3.12	4.20		
Tb	0.599	0.560	0.540	0.750		
Dy	4.08	3.81	3.40	4.78		
Ho	0.894	0.820	0.710	1.02		
Er	2.59	2.28	1.92	2.96		
Tm	0.396	0.350	0.280	0.450		
Yb	2.55	2.29	1.68	2.88		
Lu	0.391	0.360	0.260	0.460		
Hf	1.66	1.40	1.51	3.13		
Ta	0.156	0.120	0.120	0.430		
Tl	0.141	0.070	0.070	0.130		
Pb	14.9	8.44	8.79	3.90		
Bi	0.142	0.030	0.050	0.090		
Th	0.129	0.030	0.120	4.210		
U	0.232	0.240	0.310	0.940		
ΣREE	58.2	49.9	50.7	124.4		
(La/Yb) _N	0.695	0.542	1.10	4.62		
(La/Sm) _N	0.648	0.524	0.666	3.08		
(Gd/Yb) _N	1.00	1.04	1.54	1.21		
Nb/Ta	13.9	13.3	14.9	13.0		
Zr/Hf	35.7	34.3	33.1	34.0		
Th/Ta	0.827	0.250	1.00	9.79		
Ta/Hf	0.094	0.086	0.079	0.137		

Table 4: NOTES: "-" means do not detect or calculate; EBC means calculated effective bulk composition for pseudosection modeling; "Fetota" means the total amount of iron oxide analysed from XRF; The Fe₂O₃ content of bulk-rock is constrained from potassium permanganate titration method; The Fe₂O₃ and FeO contents of EBCs were calculated based on the constant ratio of Fe³⁺/Fe²⁺ from XRF data for evaluated composition;

4.4. Petrology

Mineral occurrences and modal abundances are given in Table 1. Mafic samples are true eclogites with > 70 vol. % of garnet and omphacite (Carswell, 1990). Mineral constituents of eclogite samples are garnet, omphacite, epidote-group minerals, paragonite, blue amphibole (rimmed in places by blue-green amphibole), quartz, as well as rutile/titanite, calcite and phengite (Figure 20a-f) in subordinate amounts. The fraction of hydrous minerals (especially amphibole) increases in the vicinity of the host-rock.

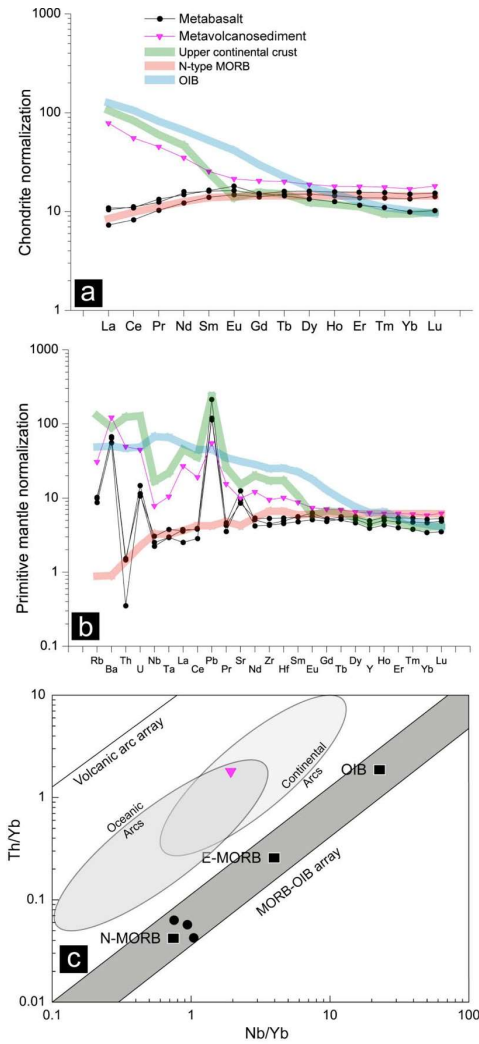


Figure 19: Whole-rock discrimination diagrams for the samples: (a) chondrite-normalized REE patterns, (b) primitive mantle-normalized spider diagram and (c) Th/Yb versus Nb/Yb diagram (Pearce, 2008). Reference curves for average N-MORB and OIB from Sun and McDonough (1989), and from Rudnick and Gao (2003) for upper continental crust.

of omphacite, quartz and rutile (Figure 20d). Blue amphibole is found as inclusions in some garnets (Figure 20h) and in the core of late-stage blue-green amphibole (Figure 20g). Rutile is present both in garnet porphyroblasts (Figure 20e), paragonite and amphibole grains as armored relicts, and in the matrix (Figure 20g), where it is replaced

Garnet in sample 11AT06 occurs as idioblastic porphyroblasts (~0.4 to 2.5 mm in diameter; Figure 20d, e) in a medium-grained omphacite matrix. The inclusion-rich cores (Figure 20e) host omphacite, epidote, chlorite, paragonite, quartz and glaucophane/barroisite (Figure 33). Box-shaped inclusions of aggregates of paragonite and epidote could represent pseudomorphs after lawsonite (Figure 34). Coesite inclusions (Figure 22b, c) were found in the garnet mantle (Figure 22d), where inclusions are much less than in the core.

Omphacite occurs as small subhedral-anhedral grains (~0.05 to 0.1 mm across), either as the main matrix phase or as inclusions in garnet, epidote and paragonite (Figure 20b, d, f, i). Epidote is subhedral and contains inclusions

by helicitic rims of titanite (Figure 33). Retrograde albite is rare and xenoblastic.

Chlorite replaces or cuts across garnet (Figure 20e).

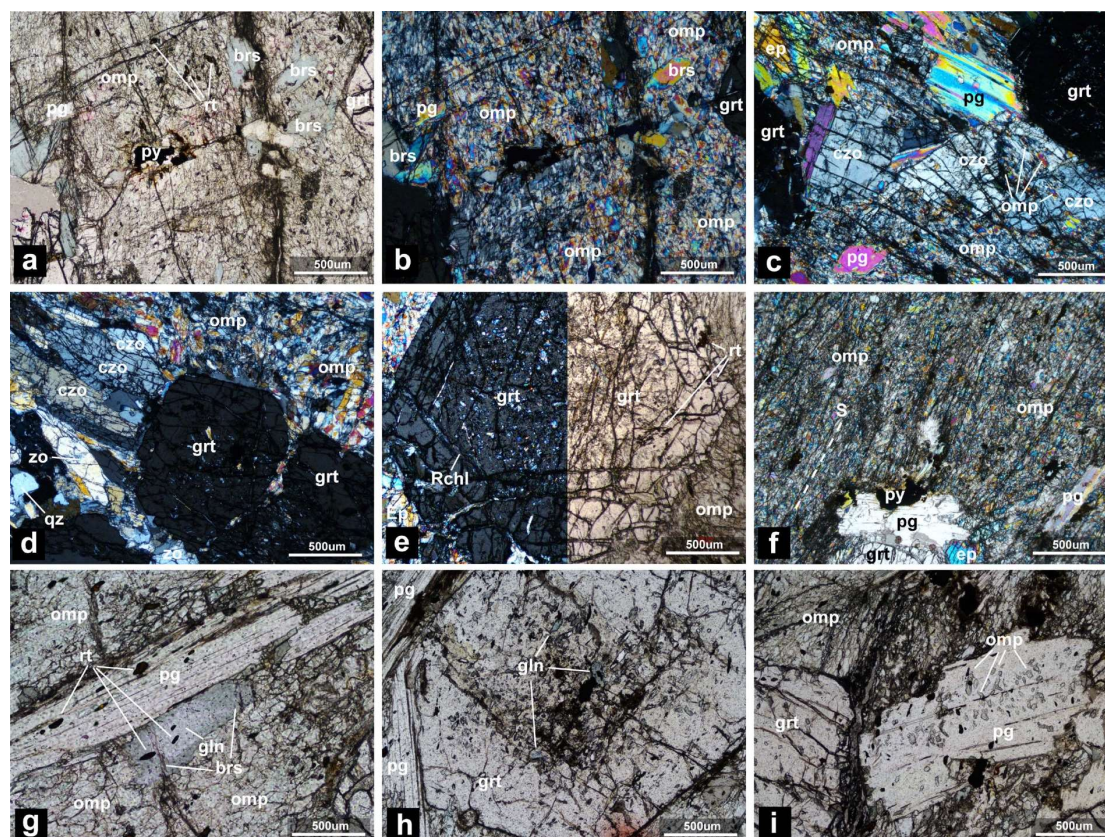


Figure 20: Mineral assemblages and microstructures of the studied eclogites. (a,b) Typical eclogitic facies mineral assemblages in sample 11AT06: subhedral-anhedral omphacite matrix grains (partially replaced by euhedral-subhedral amphibole porphyroblasts and subhedral paragonite grains), idioblastic garnet porphyroblasts and minor rutile grains in the omphacite matrix (cross-polar view). (c,d) Idioblastic garnet porphyroblasts partially replaced by subhedral epidote group minerals. (e) typical texture of studied garnet porphyroblast (same as in Figure 22a, d), with abundant mineral inclusions (showed both in cross polar and plane polar view) within the core-mantle domain and slightly replaced by chlorite. (f) Moderately foliated omphacite matrix in the oriented sample of the studied layered eclogite (cross polars). (g) Occurrence of rutile inclusions in paragonite porphyroblast. Note the amphibole with a glaucophane core (pale blue) and a more barroisitic greenish rim. (h) Glaucophane inclusions in the core of a garnet porphyroblast. (i) Omphacite inclusions in a paragonite porphyroblast. Mineral abbreviations: grt, garnet; omp, omphacite; brs, barroisite; gln, glaucophane; ph, phengite; pg, paragonite; ep, epidote; zo, zoisite; qz, quartz; rt, rutile; pyr, pyrite; chl, chlorite.

In oriented eclogite samples (11AT06-2 and GJ01-6), omphacite defines a weak to moderate foliation, and contain aggregates of epidote group minerals and paragonite aligned along the matrix foliation (Figure 20f, 21a-b). In the XZ plane of deformation,

σ -type garnet porphyroclasts with recrystallized aggregate tails made of epidote, omphacite and paragonite/phengite indicate top to NE shear senses.

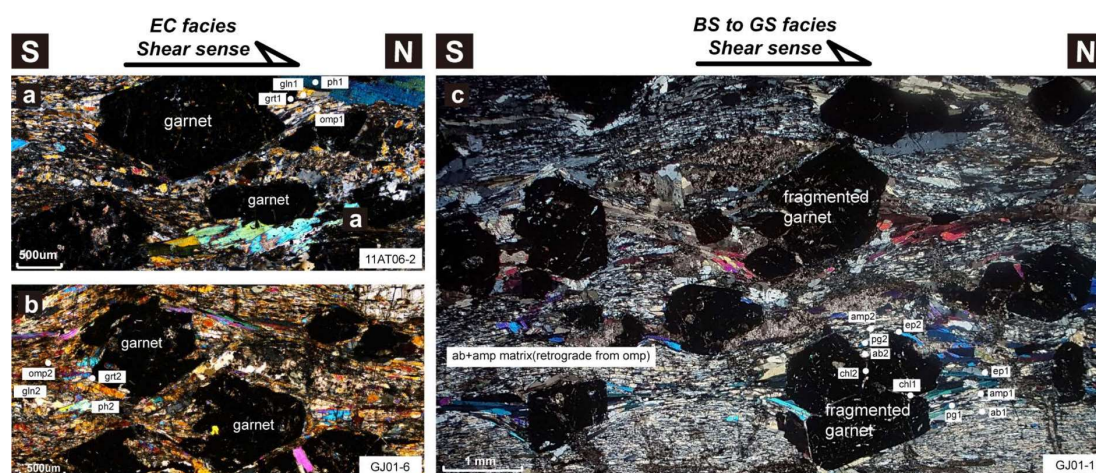


Figure 21: Thin-section scale shear senses in eclogite and greenschist facies for the UHP eclogite and its meta-volcano-sedimentary host-rock, respectively. (a, b) Foliated omphacite matrix and σ -type garnet porphyroclasts with epidote, omphacite and phengite recrystallized tails. (c) Foliated albite and amphibole matrix, and σ -type fractured porphyroclasts of garnet with quartz, albite, paragonite and amphibole recrystallized tails. Gray solid-circles show the location of EMPA analyses for Thermocalc averagePT calculations (see Table 10). Mineral abbreviations as for Figure 20.

The meta-volcanosedimentary sample GJ01-1 is strongly deformed and the foliation defined by lepidoblastic phengite/paragonite, albite and amphibole wraps around garnet porphyroclasts (Figure 21c). Garnet occurs as idioblastic to subidioblastic ~ 3.0 mm sized porphyroblasts in a fine- to medium-grained matrix, and contains inclusions of phengite/paragonite, epidote group minerals, quartz and chlorite. Matrix feldspar porphyroblasts contain numerous inclusions. Shear sense indicators, again top to the NE, correspond to retrograde greenschist/blueschist facies recrystallization.

4.5. Mineral chemistry

A selection of representative EPMA analyses is provided in Table 5. Mineral abbreviations are after Whitney and Evans (2010).

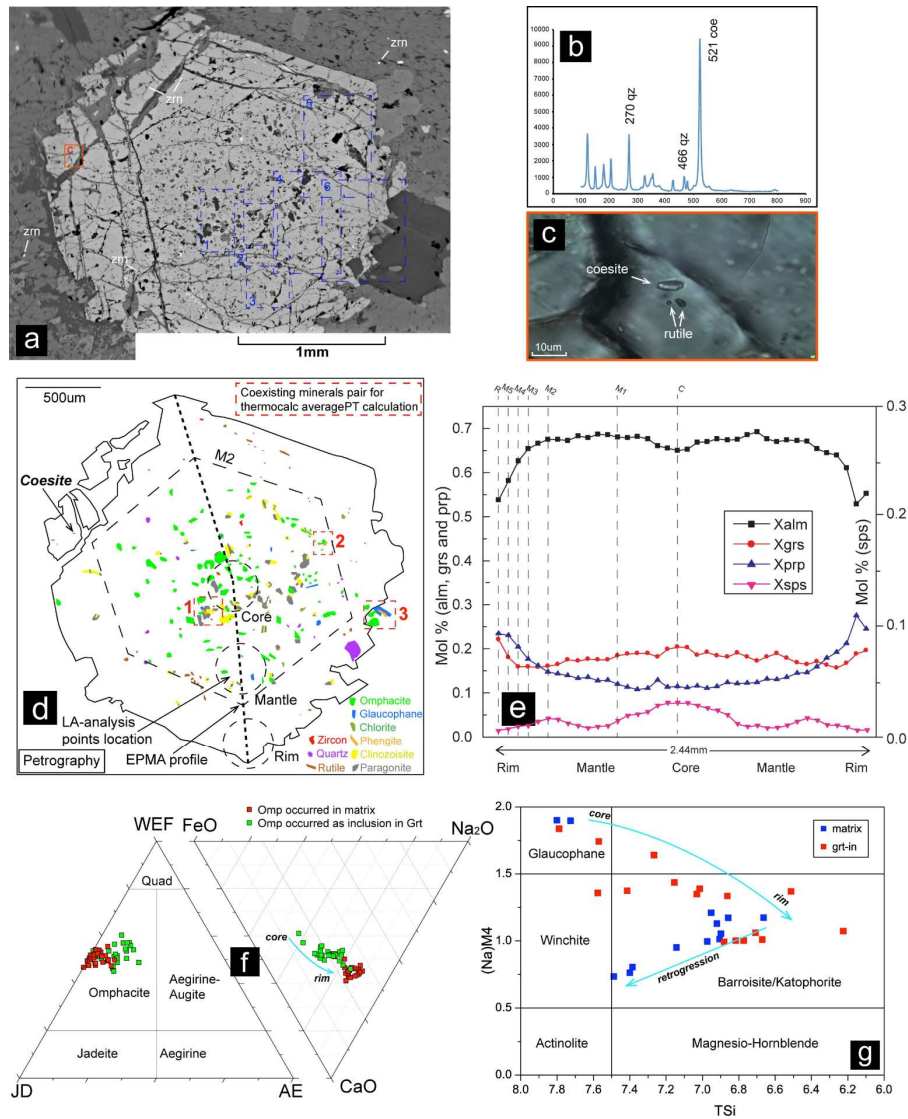


Figure 22: Garnet porphyroblast and mineral inclusions: (a) BSE imaging and location of mineral inclusions in the garnet core-mantle domain (dashed blue boxes shown in Fig. S2); (b) Raman spectrum of the analysed coesite inclusion; (c) Close-up view of the coesite inclusion in the garnet mantle domain; (d) Sketch of mineral inclusion distribution and location of analyses. Black dashed circles: laser-ICP-MS spots (see Fig. 9b); thick dashed line: EMPA profile (see Figure 22e; Table 5); red dashed rectangles: region with coexisting mineral inclusions chosen for thermocalc averagePT calculations; (e) Composition profile across the center of the studied garnet porphyroblast (Figure 22a, d); (f) composition of sodic clinopyroxene (Morimoto, 1988) outlining the distinct omphacite generations; (g) Chemical composition of amphiboles in studied eclogite after Hawthorne and Oberti (2006). Mineral abbreviations as for Figure 20.

4.5.1. Garnet

Garnet porphyroblasts in eclogite sample 11AT06-1 exhibit systematic compositional zoning (e.g., Figure 22e) with a core-mantle increase in pyrope (X_{prp})

and a slight decrease in spessartine and grossular content (X_{sps} and X_{grs}). The almandine (X_{alm}) profile is fairly constant from core to mantle then decreases steadily towards the outermost part of the rim (Figure 22e). Second-order fluctuations in X_{grs} and X_{sps} but also in X_{alm} can be observed (Figure 22e). Garnet profiles may show a rim-outer rim coeval increase in X_{alm} and decrease in X_{prp} , which is generally attributed to retrograde reequilibration by diffusion (Wei et al., 2009).

Garnet zoning in eclogite is highlighted by seven spots along the EMPA profile (Figure 22e), which are used in pseudosection modeling (section 8.2). Overall, garnet composition changes from core to mantle and rim from $\text{Alm}_{67}\text{Py}_{10}\text{Grs}_{20}\text{Sps}_4$ to $\text{Alm}_{70}\text{Py}_{12}\text{Grs}_{18}\text{Sps}_1$ to $\text{Alm}_{57}\text{Py}_{21}\text{Grs}_{22}\text{Sps}_{0.3}$ (Table 5). These average values correspond to the Grt-C, Grt-M1 to M2 and Grt-M5 to R zones defined in Figure 22d, and to the approximate location of the LA-ICPMS trace element analyses of the garnet core, mantle and rim.

4.5.2. Omphacite

Clinopyroxene is always omphacitic, but inclusions in garnet and matrix clinopyroxene show distinct compositional variations (Figure 22f). Inclusions have a lower jadeite content (31-45 mol.%, average 38 mol.%) and a higher total FeO content (4.3-12.9 wt.%, average 7.7 wt.%) than matrix omphacite (40-51 mol.% Jd and 2.5-6.5 wt.% FeO, respectively). Both have similar values of $\text{Na}_\text{N}/(\text{Na}_\text{N}+\text{Ca}_\text{N})$ (~0.48; Table 5). Omphacite inclusions in paragonite lie on the upper bound for jadeite content and $\text{Na}_\text{N}/(\text{Na}_\text{N}+\text{Ca}_\text{N})$ but on the lower bound for the total FeO content.

Mineral	Representative microprobe analyses																Czo	Ep	Chl-matrix	Rt	Tn				
	Grt-C	Grt-M1	Grt-M2	Grt-M3	Grt-M4	Grt-M5	Grt-R	Gln-in-grt	Gln-c-matrix	Bis-in-grt	Bis-r-matrix	Omp-in-grt-c	Omp-in-grt-m	Omp-in-pg	Omp-matrix	Ph-in-grt						Ph-matrix	Pg-in-grt	Pg-matrix	
SiO ₂	37.52	38.24	37.33	37.86	38.10	38.02	38.09	57.17	57.83	46.62	49.90	55.00	58.48	56.80	56.58	51.44	51.92	48.39	48.87	38.30	25.63	0.03	0.03	29.82	
TiO ₂	0.15	0.16	0.06	0.02	0.01	0.06	0.10	0.18	0.03	0.23	0.41	0.07	0.04	0.12	0.04	0.33	0.27	0.02	0.06	0.16	0.13	0.02	89.32	37.86	
Al ₂ O ₃	21.15	20.94	21.47	21.39	21.65	21.76	21.93	10.27	12.21	13.96	11.85	8.12	10.19	12.47	10.38	27.64	27.71	38.62	39.44	30.65	26.87	19.26	0.02	2.11	
Cr ₂ O ₃	0.73	0.00	0.21	0.06	0.03	0.09	0.01	0.02	0.05	0.08	0.04	0.02	0.08	0.02	0.00	0.05	0.04	0.09	0.07	0.00	0.00	0.06	0.19	0.03	
Fe ₂ O ₃	30.20	31.89	30.91	30.89	29.93	27.66	25.92	11.52	7.53	14.22	11.14	4.78	4.34	1.50	1.97	3.58	1.83	1.12	0.24	0.00	8.84	0.00	0.00	0.00	
MnO	1.48	0.70	0.81	0.52	0.48	0.39	0.21	0.10	0.04	0.15	0.02	0.08	0.05	0.04	0.03	0.01	0.04	0.04	0.00	0.00	0.09	0.21	0.00	0.02	
MgO	2.46	2.56	3.20	3.86	4.47	5.15	5.28	9.75	11.33	8.78	11.77	7.50	8.20	8.28	9.29	2.38	3.37	0.12	0.11	0.04	0.01	14.75	0.01	0.01	
CaO	6.88	6.09	5.41	5.42	5.44	6.25	7.76	1.51	1.14	7.15	7.95	13.32	11.62	12.51	13.58	0.10	0.01	0.29	0.29	23.03	23.00	0.13	0.08	29.11	
Na ₂ O	0.02	0.11	0.07	0.01	0.04	0.06	0.03	6.96	7.27	5.06	4.20	6.57	6.28	7.69	6.83	0.42	0.80	7.10	7.37	0.01	0.00	0.15	0.01	0.05	
K ₂ O	0.00	0.02	0.00	0.00	0.01	0.00	0.01	0.02	0.03	0.06	0.27	0.03	0.11	0.00	0.00	9.37	9.15	0.47	0.33	0.00	0.00	0.15	0.00	0.01	
Total	100.62	100.92	100.61	100.86	100.55	100.46	100.26	99.28	98.00	98.31	98.10	99.97	99.39	101.05	100.79	95.34	95.11	94.26	96.79	97.92	85.67	100.12	-	100.08	
O	12	12	12	12	12	12	12	23	23	23	23	6	6	6	6	11	11	11	11	13	13	14	2	5	
Si	2.879	3.024	2.958	2.980	2.889	2.967	2.964	7.854	7.849	6.773	7.099	1.995	2.069	1.980	1.989	3.421	3.431	3.004	3.060	3.025	3.011	2.903	0.000	0.978	
Ti	0.009	0.010	0.004	0.001	0.001	0.004	0.006	0.019	0.003	0.025	0.043	0.002	0.001	0.003	0.001	0.017	0.013	0.001	0.003	0.009	0.007	0.003	0.995	0.934	
Al	1.981	1.953	2.006	1.985	2.003	2.002	2.011	1.663	1.953	2.390	1.988	0.347	0.425	0.512	0.431	2.167	2.158	2.949	2.911	2.766	2.490	2.407	0.000	0.081	
Cr	0.002	0.013	0.003	0.004	0.002	0.006	0.000	0.002	0.005	0.009	0.005	0.001	0.002	0.000	0.000	0.003	0.002	0.005	0.004	0.000	0.000	0.010	0.000	0.000	
Fe ³⁺	0.044	0.000	0.078	0.049	0.023	0.060	0.054	0.184	0.055	0.219	0.058	0.122	0.000	0.041	0.054	0.000	0.000	0.000	0.000	0.259	0.523	0.000	0.005	0.000	
Fe ²⁺	2.006	2.109	2.049	2.034	1.964	1.805	1.687	1.323	0.854	1.728	1.326	0.145	0.128	0.045	0.059	0.199	0.101	0.061	0.013	0.000	0.000	2.088	0.000	0.029	
Mn	0.100	0.047	0.054	0.035	0.032	0.026	0.014	0.011	0.004	0.018	0.003	0.002	0.001	0.001	0.001	0.002	0.001	0.002	0.000	0.003	0.006	0.023	0.000	0.000	
Mg	0.292	0.302	0.378	0.453	0.523	0.599	0.612	1.996	2.291	1.901	2.495	0.406	0.432	0.430	0.487	0.236	0.332	0.012	0.000	0.004	0.001	2.408	0.000	0.000	
Ca	0.585	0.516	0.459	0.457	0.457	0.523	0.647	0.222	0.166	1.113	1.212	0.518	0.440	0.467	0.512	0.007	0.001	0.020	0.020	1.889	1.937	0.014	0.001	1.023	
Na	0.003	0.017	0.011	0.002	0.006	0.009	0.004	1.853	1.912	1.425	1.159	0.462	0.431	0.520	0.466	0.054	0.102	0.892	0.894	0.001	0.000	0.036	0.000	0.003	
K	0.000	0.002	0.000	0.000	0.001	0.000	0.001	0.003	0.005	0.011	0.049	0.001	0.005	0.000	0.000	0.696	0.771	0.038	0.027	0.000	0.000	0.022	0.000	0.001	
X(phase)	0.098	0.102	0.129	0.162	0.176	0.203	0.207	0.399	0.272	0.476	0.347	0.340	0.420	0.480	0.420	0.236	0.332	0.012	0.000	0.086	0.174	0.464	-	-	
Y(phase)	0.196	0.174	0.156	0.153	0.154	0.177	0.219	0.100	0.027	0.425	1.159	0.471	0.495	0.527	0.476	-	-	-	-	-	-	-	-	-	-

Table 5: NOTES: Microprobe data presented here are calculated from RAW data via AX_2 program (Holland); <http://www.esc.cam.ac.uk/research/research-groups/holland/ax/>; $X(grt) = X_{py} = Mg/(Fe^{2+} + Mn + Mg + Ca)$, $X(omp) = X_{jd}$, $X(omp) = X_{jd} / (Fe^{2+} + Mg)$, $X(Ph, pa) = Mg^{2+}$, $Y(grt) = X_{gr} = Ca / (Fe^{2+} + Mn + Mg + Ca)$, $Y(omp) = f(o) = Na / (Na + Ca)$, $Y(gln, ep, czo) = Fe^{3+} / (Fe^{3+} + AlIV)$, $Y(Brs) = (Na)M4$; c, core; m, mantle; r, rim; -in-phase: inclusion mineral in phase, -matrix: mineral in the matrix; "-" means did not calculate.

4.5.3. Amphibole

Amphibole in the layered eclogite is either glaucophane or barroisite (Figure 22g). Glaucophane occurs as euhedral porphyroblasts (~0.5 mm across) with barroisite rims (Figure 20g). Both glaucophane and barroisite appear as inclusions in garnet, with a wide range of compositions for the latter, across the magnesio-katophorite field (Leake, 1978) and a systematic decrease in $(\text{Na})_{\text{M4}}$ (Figure 20h). Glaucophane inclusions have higher $\text{Fe}^{2+}/(\text{Fe}^{2+}+\text{Mg})$ and $\text{Fe}^{3+}/(\text{Fe}^{3+}+\text{Al})$ ratios. Some amphibole grains have a clear zonation, with glaucophane in the core and barroisite in the rim, similar to the Tianshan garnet-omphacite blueschist samples described by Klemd et al. (2002).

4.5.4. White mica

Paragonite and minor phengite appear as matrix mineral and as inclusions in garnet. Paragonite flakes occur as subhedral fine grains (~0.05 mm across) or occasionally as porphyroblasts in the matrix (~0.5 to 2 mm across, Figure 20f-g, i). They are parallel or subparallel to the foliation (Figure 20f-g), contain omphacite and rutile inclusions (Figure 20g, i), and are interpreted to result from post-peak retrograde metamorphism. Phengite mainly occurs as subhedral fine grains in the matrix (~0.02 mm across) or as inclusions in garnet porphyroblasts (Figure 34). Both of them exhibit a similar Si content (~3.43 p.f.u.).

4.5.5. Epidote-group minerals

Epidote-group minerals occur as 0.5-0.7 mm large porphyroblasts or as subhedral grains close to garnet porphyroblasts (Figure 20c-e). Porphyroblasts are randomly

oriented in the matrix with mineral inclusions of omphacite and rutile (Figure 20c). The pistacite ($=\text{Fe}^{3+}/(\text{Fe}^{3+}+\text{Al})$) contents of epidote range from 0.09 to 0.17 (Table 5).

4.5.6. Chlorite

Chlorite appears as matrix minerals filled into the fractures of garnet porphyroblasts or as inclusions in garnet (Table 5).

4.5.7. Rutile/Titanite

Rutile appears as acicular or irregular crystals inclusions in paragonite (Figure 20g), glaucophane/barroisite (Figure 20g), garnet (Figure 34) and matrix minerals (Fig. S1). A titanite-armor around rutile is observed in both matrix omphacite (Figure 33a-b) and quartz (Figure 33c-d). The TiO_2 and Al_2O_3 contents of titanite are respectively about 37.9 wt % and 2.11 wt % (Table 5).

4.6. Trace-element pattern of zircon and garnet

Zircon in layered eclogite occurs as 30 to 50 μm grains in the matrix (Figure 22a) or in garnet (Figure 22a, 34). Cathodoluminescence images of zircon grains are used below as a proxy for variations in zircon chemistry (whereas trace-element patterns are discussed in next section). Zircon grains from eclogitic samples show two to four growth zones preserved (Figure 23, 34a-l). A dull-luminescent core domain is found in all zircon grains (Figure 23, 34a-l), with typical sector zoning. A large overgrowth is generally present and herein referred to as the 'mantle'. Complex zoning patterns (chaotic and wavy zoning) were also observed (Figure 23a, e and 34). A light-luminescent outer rim can also be distinguished in many grains (e.g., Figure 23 and

Figure 35). A metamorphic origin may be attributed to these zircon domains when considering the < 0.01 Th/U ratios and the presence of diagnostic HP minerals, such as omphacite and rutile, detected via Raman spectroscopy (with peaks at 682 cm^{-1} and 609 cm^{-1} , respectively; Figure 35m-n). Quartz was observed but never coesite.

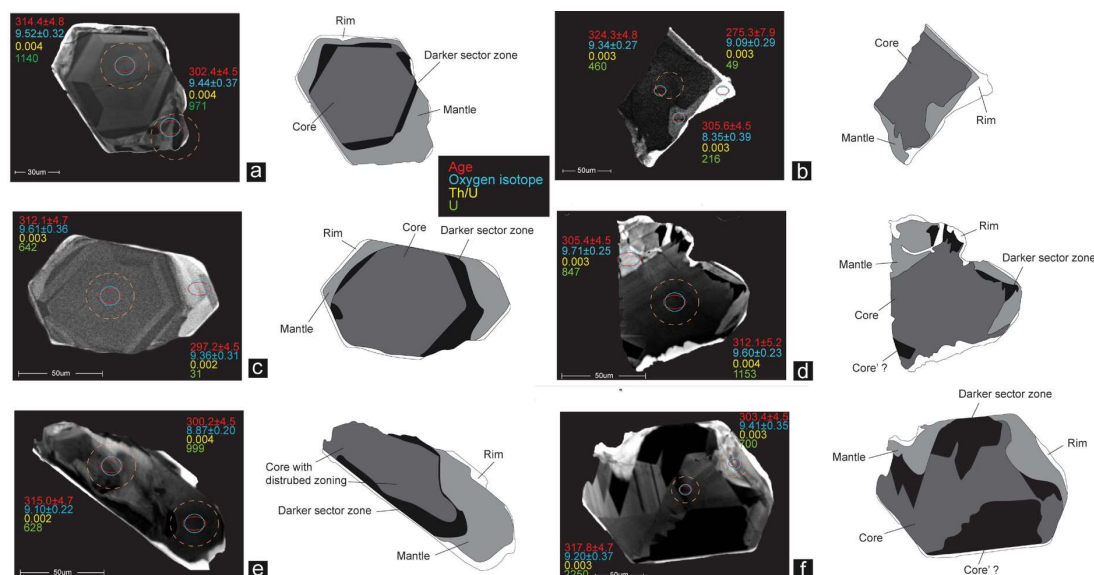


Figure 23: Cathodoluminescence imaging and sketches of analyzed zircon grains, showing multistage growth features. The location of U-Pb, REEs, $\delta^{18}\text{O}$ analyses is shown by red solid-ellipse ($10 \times 15\text{ }\mu\text{m}^2$ beam-size via SIMS), orange dash-circle (with $40 \times 40\text{ }\mu\text{m}^2$ beam-size via Laser-ICP-MS) and blue solid-circle (with $20 \times 20\text{ }\mu\text{m}^2$ beam-size via SIMS) respectively (see Table 7). Other zircon grains are shown in Figure 35.

4.6.1. Trace-element pattern and oxygen isotopes of zircon

Based on differences in cathodoluminescence (CL) images and chondrite-normalized REE patterns (and U-Pb chronology, which will be discussed in section 7.1), four zircon domains (or growth stages) have been defined from core to rim: respectively (1) the zircon core, (2) a zone enriched in HREE (with the same CL characteristics as the core, but more rarely preserved), (3) a mantle zone and (4) the zircon rim.

Chondrite-normalized REE patterns of zircon cores (Figure 24a) show a typically positive slope from LREE to MREE, a relative enrichment in HREE ($(\text{Lu}/\text{Sm})_{\text{N}} \sim$

22.94) and flat HREE patterns ($(\text{Lu}/\text{Tb})_N \sim 1.53$). This core is also characterized by low Th/U ratios (< 0.01), medium U (~ 980 ppm), low Th (~ 4 ppm) and moderate Y, Ti, P

Average Laser-ICP-MS trace-element compositions of various garnet and zircon domains.

Element	Garnet						Zircon							
	Core		Mantle		Rim		Core		Core high HREEs		Mantle		Rim	
	Average	Std(N=8)	Average	Std(N=9)	Average	Std(N=10)	Average	Std(N=30)	Average	Std(N=5)	Average	Std(N=4)	Average	Std(N=15)
P	53.5	31.9	117	155	13.9	2.84	27.2	9.92	34.6	10.4	-	-	21.2	6.27
Ti	681	152	1661	979	106	17.5	2.89	1.04	10.6	3.77	1.55	0.140	1.93	0.930
Nb	bd	bd	1.43	1.74	bd	bd	5.75	1.22	6.27	1.20	5.27	0.979	5.62	1.04
Y	81.2	17.6	47.4	11.5	49.8	5.42	89.1	17.2	231	57.7	44.6	8.57	47.6	19.3
La	bd	bd	0.471	0.356	bd	bd	bd	bd	bd	bd	bd	bd	bd	bd
Ce	0.181	0.204	1.63	1.35	bd	bd	0.121	0.060	0.123	0.064	bd	bd	bd	bd
Pr	0.042	0.015	0.314	0.214	bd	bd	bd	bd	bd	bd	bd	bd	bd	bd
Nd	0.308	0.249	2.36	1.16	bd	bd	bd	bd	bd	bd	bd	bd	bd	bd
Sm	0.746	0.245	1.77	0.590	bd	bd	0.336	0.051	0.420	0.269	bd	bd	bd	bd
Eu	0.882	0.281	1.13	0.360	0.278	0.060	0.284	0.115	0.294	0.137	0.325	0.248	bd	bd
Gd	5.14	1.38	5.18	1.63	1.83	0.401	2.81	0.905	2.87	0.873	2.34	1.09	0.648	0.135
Tb	1.69	0.301	1.24	0.328	0.926	0.125	1.23	0.299	1.96	0.578	0.705	0.291	0.192	0.093
Dy	13.9	2.74	8.91	1.95	8.46	0.772	10.5	2.14	24.0	6.72	4.91	1.80	2.03	1.32
Ho	3.38	0.788	1.89	0.458	1.89	0.208	2.40	0.539	6.70	1.86	1.01	0.411	0.913	0.603
Er	10.0	2.64	5.23	1.37	4.87	0.614	6.63	1.62	20.37	5.64	2.69	0.853	5.48	3.38
Tm	1.56	0.455	0.703	0.193	0.646	0.096	1.03	0.271	3.18	0.791	0.351	0.096	1.65	0.994
Yb	11.2	3.58	4.72	1.29	4.19	0.660	8.00	2.00	23.72	5.80	3.00	1.13	20.2	10.9
Lu	1.54	0.535	0.654	0.187	0.654	0.098	1.28	0.331	3.61	1.01	0.450	0.190	4.42	2.47
Ta	bd	bd	bd	bd	bd	bd	0.071	0.044	0.077	0.026	0.095	0.042	0.099	0.054
Hf	bd	bd	bd	bd	bd	bd	10127	366	10306	359	10553	317	10341	671
Th	bd	bd	bd	bd	bd	bd	3.59	3.00	5.39	5.27	2.88	1.57	0.174	0.107
U	bd	bd	bd	bd	bd	bd	982	860	982	657	740	255	30.6	34.9
Pb	bd	bd	bd	bd	bd	bd	232	158	229	141	170	60.6	16.3	12.8
(Lu/Sm) _N	12.4		2.23		-		22.9		51.7		-		-	
(Lu/Eu) _N	3.99		1.33		5.37		10.3		28.0		3.17		-	
(Lu/Tb) _N	1.35		0.779		1.04		1.53		2.71		0.940		33.9	

Table 6: Average Laser-ICP-MS trace-element compositions of various garnet and zircon domains. NOTES: "bd" means below detected; "-" do not calculated; Here the Std-dev is 1 sigma;

and Nb contents (~ 89 , 2670, 27 and 6 ppm, respectively; Table 6).

Some of the zircon cores show HREE contents 2-3 times higher ($(\text{Lu}/\text{Sm})_N \sim 51.72$; $(\text{Lu}/\text{Tb})_N \sim 2.71$; Y ~ 230 ppm; Figure 24a, 35i-l; Table 6). They are also distinct in terms of U-Pb isotopic composition (Figure 25), but have similar Th/U ratios (< 0.01), U and Th contents.

The zircon mantle domain (Figure 24b) shows a more gentle positive slope from LREE to MREE and a flat HREE distribution with lower HREE and Y absolute contents ($(\text{Lu}/\text{Eu})_N \sim 3.17$; $(\text{Lu}/\text{Tb})_N \sim 0.94$; Y content ~ 45 ppm; Table 6).

The REE pattern of zircon rims differ largely from that of the former three zones discussed above by a steeper MREE to HREE distribution (with $(\text{Lu}/\text{Gd})_N \sim 10$ and $(\text{Lu}/\text{Tb})_N \sim 34$, Table 6) and the absence of a HREE plateau. Its Y, P, Th and U contents are also much lower (i.e., respectively, ~ 48 , 21, 0.17 and 30 ppm). The Th and U contents are about 30 times less than in the other three zircon domains.

4.6.2. Trace-element pattern of garnet

Laser spots for the analysis of garnet core, mantle and rim corresponding to EPMA analyses of the C, M1 to M2 and M5 to R areas (shown in Figure 22b).

Chondrite-normalized REE patterns of garnet core, mantle and rim (Figure 24b) are broadly similar (and comparable to the REE distributions within zircon), with relatively high and flat HREE content and relative depletion in MREE and LREE. Garnet cores show the highest HREE enrichment with $(\text{Lu}/\text{Sm})_N \sim 12$, compared to the mantle domain ($(\text{Lu}/\text{Sm})_N \sim 2$). Garnet mantle shows the highest LREE and a slightly

SIMS zircon U-Pb isotopic data.													
Zircon core (n=31)	U (ug/g)	Th (ug/g)	Th/U	f_{206} (%)	^{207}Pb / ^{235}U	$\pm 1\sigma$	^{206}Pb / ^{238}U	$\pm 1\sigma$	ρ	^{207}Pb / ^{235}U	$\pm 1\sigma$	^{206}Pb / ^{238}U	$\pm 1\sigma$
11AT06-1a @10	631	1.69	0.003	0.33	0.36991	2.56	0.0505	1.50	0.5882	319.6	7.0	317.4	4.7
11AT06-1a @14	659	2.44	0.004	0.13	0.36494	2.68	0.0495	1.50	0.5614	315.9	7.3	311.2	4.6
11AT06-1a @15	750	2.94	0.004	0.23	0.36427	2.73	0.0496	1.50	0.5500	315.4	7.4	311.8	4.6
11AT06-1a @18	612	1.29	0.002	0.43	0.36714	2.53	0.0500	1.50	0.5956	317.5	6.9	314.7	4.6
11AT06-1a @2	746	1.94	0.003	0.03	0.36225	2.07	0.0507	1.50	0.7258	313.9	5.6	318.7	4.7
11AT06-1a @20	795	2.69	0.003	0.23	0.35596	2.91	0.0493	1.51	0.5199	309.2	7.8	310.0	4.6
11AT06-1a @28	653	1.57	0.002	0.09	0.37086	2.39	0.0509	1.54	0.6442	320.3	6.6	320.1	4.8
11AT06-1a @29	1114	4.02	0.004	0.11	0.37306	1.96	0.0506	1.50	0.7682	321.9	5.4	318.2	4.7
11AT06-1a @32	671	1.16	0.002	0.29	0.35594	2.25	0.0499	1.50	0.6686	309.2	6.0	313.9	4.6
11AT06-1a @36	870	4.55	0.005	0.22	0.37544	2.29	0.0505	1.50	0.6566	323.7	6.4	317.8	4.7
11AT06-1a @38	1034	3.46	0.003	0.21	0.36159	2.69	0.0493	1.51	0.5630	313.4	7.3	310.4	4.6
11AT06-1a @39	624	2.03	0.003	0.11	0.37371	2.64	0.0497	1.51	0.5699	322.4	7.3	313.0	4.6
11AT06-1a @6	731	3.47	0.005	0.19	0.37025	2.14	0.0509	1.51	0.7046	319.8	5.9	320.1	4.7
11AT06-1b @6	992	3.08	0.003	0.09	0.36843	1.82	0.0506	1.50	0.8259	318.5	5.0	318.4	4.7
11AT06-1c @2	642	2.00	0.003	0.00	0.35589	1.82	0.0496	1.55	0.8485	309.1	4.9	312.1	4.7
11AT06-1c @6	1021	3.93	0.004	0.48	0.37138	2.05	0.0506	1.67	0.8115	320.7	5.7	318.2	5.2
11AT06-1d @1	582	1.77	0.003	0.00	0.36228	1.86	0.0496	1.53	0.8221	313.9	5.0	312.0	4.7
11AT06-1d @33	180	0.45	0.003	0.82	0.36347	3.96	0.0499	1.51	0.3817	314.8	10.8	314.0	4.6
11AT06-1d @22	571	1.29	0.002	0.04	0.37170	1.86	0.0499	1.50	0.8071	320.9	5.1	314.1	4.6
11AT06-1d @6	1140	4.00	0.004	0.00	0.36469	1.72	0.0500	1.56	0.9084	315.7	4.7	314.4	4.8
11AT06-1d @19	439	0.65	0.001	0.06	0.36804	2.00	0.0506	1.50	0.7510	318.2	5.5	318.1	4.7
11AT06-1d @30	751	3.54	0.005	0.02	0.37868	2.13	0.0510	1.52	0.7131	326.1	6.0	320.6	4.8
11AT06-1d @7	460	1.19	0.003	0.20	0.37550	2.12	0.0516	1.50	0.7079	323.7	5.9	324.3	4.8
11AT06-1a @23	1347	3.37	0.002	0.03	0.37595	1.85	0.0514	1.50	0.8098	324.1	5.2	323.4	4.7
11AT06-1d @10	2250	6.57	0.003	0.01	0.37210	1.60	0.0505	1.52	0.9451	321.2	4.4	317.8	4.7
11AT06-1a @35	1051	4.76	0.005	0.04	0.37629	2.00	0.0505	1.50	0.7528	324.3	5.6	317.5	4.7
11AT06-1b @34	3354	25.69	0.008	0.15	0.37570	1.59	0.0509	1.51	0.9441	323.9	4.4	320.2	4.7
11AT06-1d @13	2740	11.91	0.004	0.24	0.37897	1.92	0.0515	1.53	0.8000	326.3	5.4	323.8	4.8
11AT06-1a @33	628	1.39	0.002	0.10	0.36444	2.48	0.0501	1.53	0.6188	315.5	6.7	315.0	4.7
11AT06-1d @14	573	1.72	0.003	0.00	0.37136	1.97	0.0503	1.51	0.7661	320.7	5.4	316.4	4.7
11AT06-1e @2	1153	4.64	0.004	1.60	0.37476	3.16	0.0496	1.51	0.4790	323.2	8.8	312.1	4.6
Zircon core with high HREEs (n=4)													
11AT06-1b @1	991	2.23	0.002	0.06	0.36720	1.71	0.0502	1.50	0.8780	317.6	4.7	315.9	4.6
11AT06-1d @29	476	1.01	0.002	0.02	0.38270	1.96	0.0506	1.50	0.7666	329.0	5.5	318.1	4.7
11AT06-1a @42	3392	14.14	0.004	0.03	0.37221	1.79	0.0510	1.50	0.8395	321.3	4.9	320.4	4.7
11AT06-1b @5	605	1.62	0.003	0.18	0.36372	1.79	0.0501	1.51	0.8451	315.0	4.9	315.3	4.7
Zircon mantle (n=7)													
11AT06-1a @1	971	4.00	0.004	{0.28}	0.35010	2.32	0.0480	1.52	0.6532	304.8	6.1	302.4	4.5
11AT06-1a @11	999	4.00	0.004	{0.30}	0.34716	2.98	0.0477	1.54	0.5181	302.6	7.8	300.2	4.5
11AT06-1a @21	700	2.00	0.003	{0.13}	0.35383	2.70	0.0482	1.52	0.5613	307.6	7.2	303.4	4.5
11AT06-1a @9	847	3.00	0.003	{0.19}	0.34857	3.15	0.0485	1.52	0.4813	303.6	8.3	305.4	4.5
11AT06-1a @37	661	3.00	0.004	{0.50}	0.35923	3.12	0.0488	1.50	0.4823	311.6	8.4	307.1	4.5
11AT06-1c @1	31	0.06	0.002	{0.00}	0.35326	6.18	0.0472	1.56	0.2519	307.2	16.5	297.2	4.5
11AT06-1d @8	216	0.58	0.003	{1.43}	0.31633	10.20	0.0486	1.51	0.1480	279.1	25.2	305.6	4.5
continued													
Zircon rim (n=8)	U (ug/g)	Th (ug/g)	Th/U	f_{206} (%)	^{207}Pb / ^{235}U	$\pm 1\sigma$	^{206}Pb / ^{238}U	$\pm 1\sigma$	ρ	^{207}Pb / ^{235}U	$\pm 1\sigma$	^{206}Pb / ^{238}U	$\pm 1\sigma$
11AT06-1a @13	665	1.64	0.002	{1.32}	22.149	1.58	0.05735	1.90	281.0	4.4			
11AT06-1a @31	287	1.66	0.006	{0.09}	22.896	1.51	0.05207	2.69	275.6	4.1			
11AT06-1a @7	187	0.66	0.004	{0.00}	22.241	1.57	0.05238	4.20	283.5	4.3			
11AT06-1d @31	8	0.03	0.004	{9.84}	19.487	9.29	0.14442	9.81	291.6	11.1			
11AT06-1e @3	5	0.02	0.004	{10.30}	19.625	9.667	0.10951	15.34	288.1	10.5			
11AT06-1e @4	1	0.01	0.009	{14.43}	19.656	10.210	0.08647	20.06	274.7	20.7			
11AT06-1d @9	49	0.15	0.003	{34.21}	15.081	3.06	0.29376	3.04	275.3	7.9			
11AT06-1d @34	6	0.05	0.009	{24.88}	16.306	5.14	0.20910	6.17	290.3	13.7			

Table 7: NOTES: f_{206} (%) is the percentage of common ^{206}Pb in total ^{206}Pb , calculated by ^{207}Pb -based; $t^{206}/^{238}\text{U}$ is ^{206}Pb - ^{238}U age calculated by ^{207}Pb -based common-lead correction; "*" means that the ratios are common Pb uncorrected;

negative slope for HREE. Garnet rims show the strongest depletion in MREE and a slightly lower HREE content compared to that of mantle.

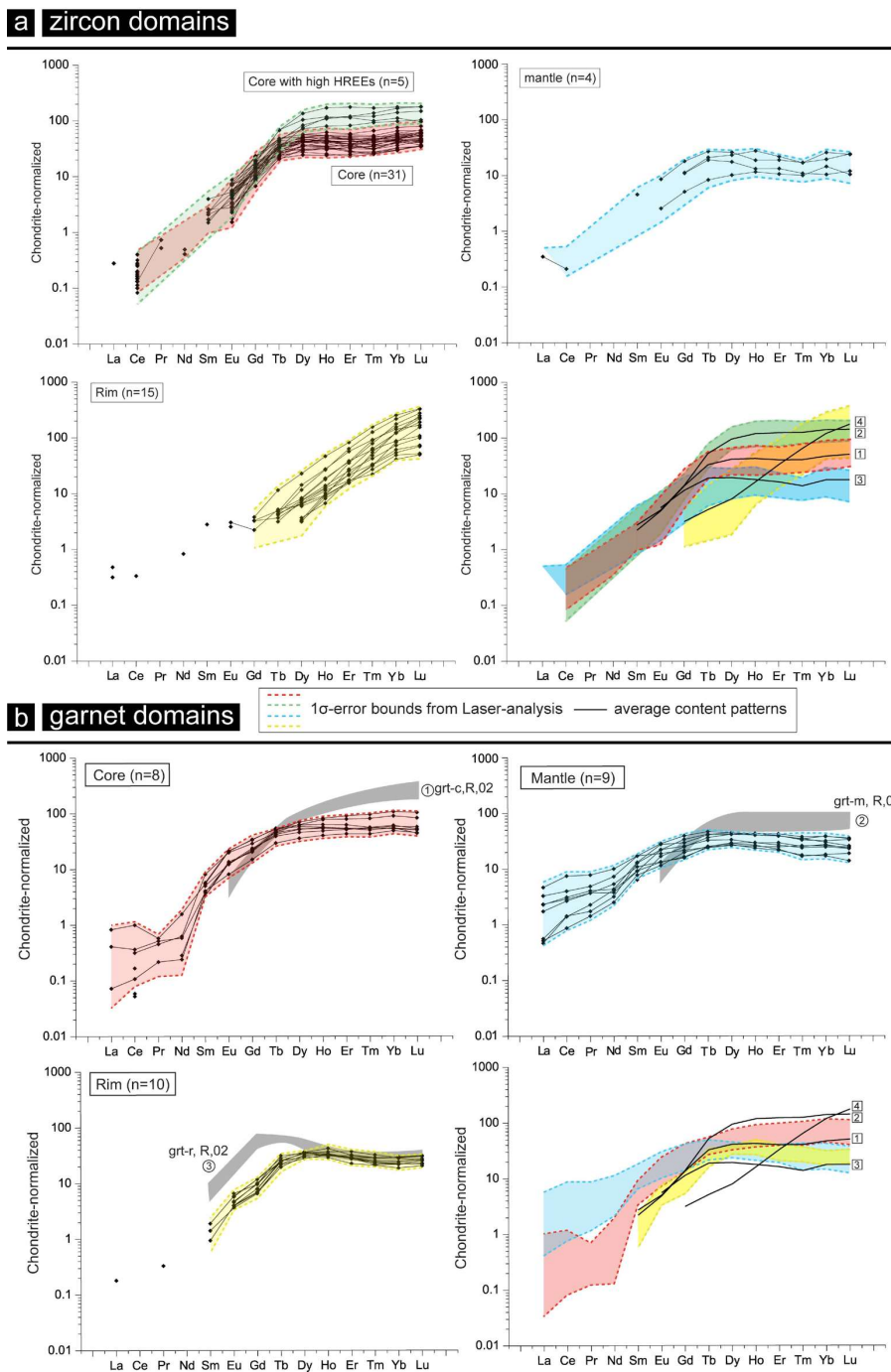


Figure 24: Chondrite-normalized (Sun and McDonough, 1989) REE abundances of the various zircon (a) and garnet domains (b) (Table 6). Overlays outline the compositional range of the various generations observed (taking into account the 1- σ uncertainty). For a better comparison of REEs patterns, average patterns of core, core with high HREEs, mantle and rim domains of zircon are labelled 1, 2, 3, 4. Circled numbers 1, 2, 3 in Figure 24b correspond to REE patterns of the core, mantle and rim of garnet (e.g. marked as grt-c, R, 02), identified as potentially coexisting with metamorphic zircon domain (rim), in the eclogite-facies micaschist of Rubatto (2002).

4.7. Geochronology and oxygen isotope

4.7.1. U-Pb dating and isotopes of zircon

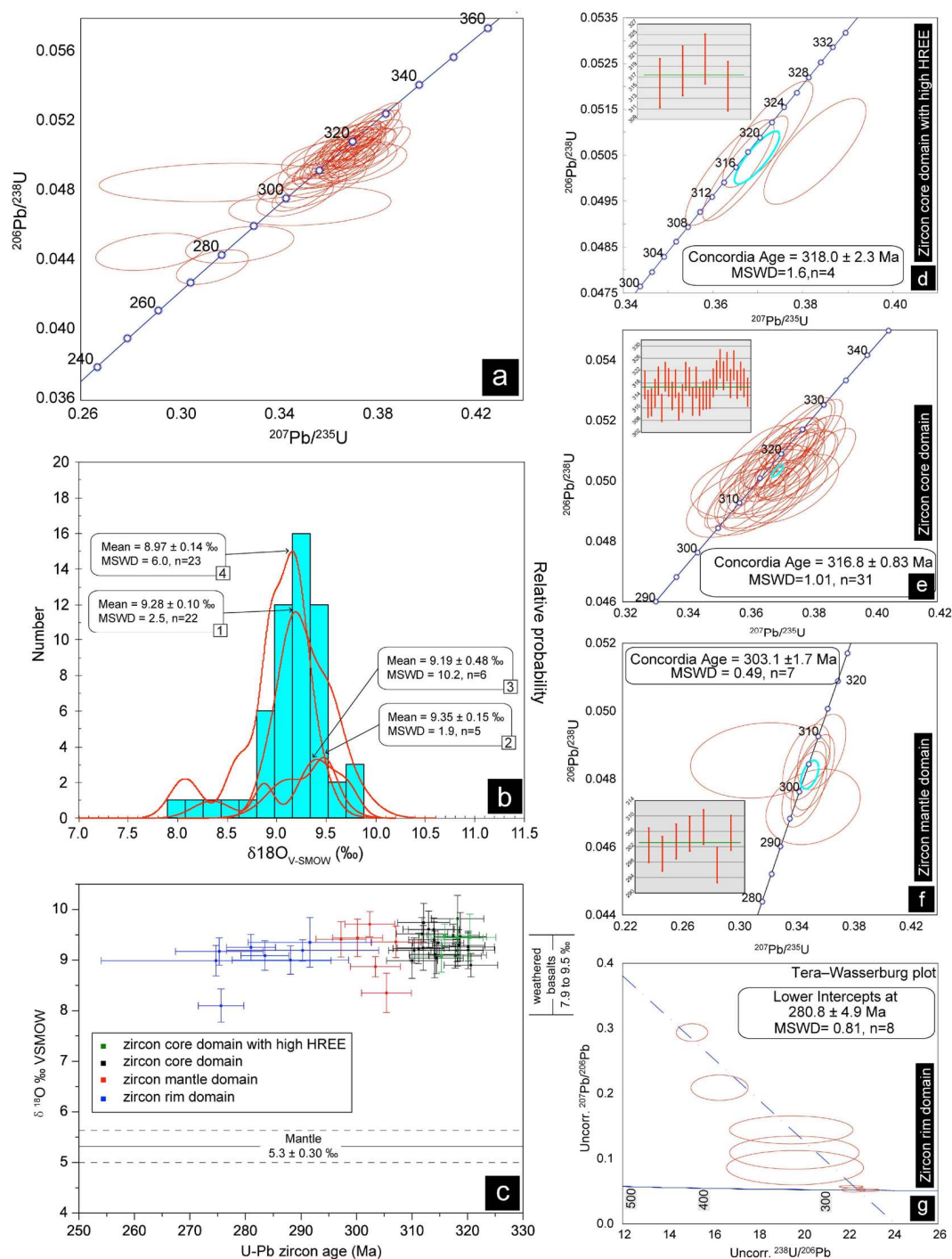


Figure 25: Results of SIMS U-Pb isotopic dating and $\delta^{18}\text{O}$ compositions for various zircon domains: (a, b) All SIMS analyses of the four zircon domains. (c) concentrations of $\delta^{18}\text{O}$ (‰) versus U-Pb ages of multistage zircon domains. The results of SIMS U-Pb age and $\delta^{18}\text{O}$ composition of, respectively, (d, number “1” with square in Figure 24b) zircon core domain with high HREEs content (corresponding to green contour in Figure 24a), (e, number “2” with square in Figure 25b) zircon core domain (corresponding to red contour in Figure 24a), (f, number “3” with square in Figure 25b) zircon mantle domain (corresponding to blue contour in Figure 24a) and (g, number “4” with square in Figure 25b) zircon rim domain (corresponding to yellow contour in Figure 24a) are listed in Table 7 and 8.

Fifty spots of twenty-seven zircon grains from eclogite sample 11AT06 have been analyzed to unravel the oxygen isotope composition and data the four growth domains (Table 7; Th/U ratios vary between 0.001 to 0.005). Core domains give apparent $^{206}\text{Pb}/^{238}\text{U}$ ages from 310.0 to 324.3 Ma, a mean Concordia age of 316.8 ± 0.83 Ma (MSWD = 1.01, n = 31) and a weighted mean age of 316.3 ± 1.6 Ma (MSWD = 0.71, n = 31) (Figure 25e). Similar results are found for the HREE enriched cores, with apparent $^{206}\text{Pb}/^{238}\text{U}$ ages varying from 315.3 to 320.4 Ma, a mean Concordia age of 318.0 ± 2.3 Ma (MSWD = 2.7, n = 4) and a weighted mean age of 317.4 ± 4.6 Ma (MSWD = 0.25, n = 4) (Figure 25d).

The mantle domain gives younger apparent $^{206}\text{Pb}/^{238}\text{U}$ ages, from 297.2 to 307.1 Ma, a mean Concordia age of 303.1 ± 1.7 Ma (MSWD = 0.49, n = 7) and a weighted mean age of 303.1 ± 3.3 Ma (MSWD = 0.58, n = 7) (Figure 25f).

Owing to the low U contents of the outer rims (5 of 8 analyzed spots have U contents mostly ranging from 1 to 49 ppm; Table 7), U-Pb results for this domain are presented on the Tera-Wasserburg plot and of poorer quality than the other domains. Common lead contents of the 8 analyzed spots are highly variable, with values of f_{206} between 0.09 % and 34.21 % (Table 7). The linear regression of the data points (MSWD = 0.81, n = 8) gives a lower intercept age of 280.8 ± 4.9 Ma and the upper intercept with $^{207}\text{Pb}/^{206}\text{Pb} = 0.381$ for the common Pb composition (Figure 25g). The weighted mean $^{206}\text{Pb}/^{238}\text{U}$ age of this rim domain is 280.5 ± 4.3 Ma (MSWD = 0.64, n = 8) using the ^{207}Pb -based common-lead correction (Williams, 1998) with the terrestrial Pb

isotope composition from Stacey and Kramers (1975), which is consistent with the lower intercept age within errors.

By contrast, oxygen isotope $\delta^{18}\text{O}$ compositions measured in the four zircon domains are very similar, with most values ranging between 8.9 ‰ and 9.5 ‰ (Figure 25b; mean value = 9.13 ± 0.09 ‰, MSWD = 5.6, n = 56; Table 8).

SIMS zircon oxygen isotopic data and modeled mineral & bulk-rock oxygen isotopic data at peak pressure conditions.					
Sample	$\delta^{18}\text{O}(\text{‰})_a$	$2\sigma(\text{‰})$	Sample	$\delta^{18}\text{O}(\text{‰})_a$	$2\sigma(\text{‰})$
zircon core			zircon rim		
11AT06-1a @10	9.49	0.22	11AT06-1a @13	9.25	0.26
11AT06-1a @14	9.23	0.30	11AT06-1a @31	8.10	0.33
11AT06-1a @15	9.52	0.32	11AT06-1a @7	9.09	0.29
11AT06-1a @18	9.34	0.27	11AT06-1d @31	9.35	0.49
11AT06-1a @2	9.46	0.48	11AT06-1e @3	9.00	0.28
11AT06-1a @20	8.99	0.35	11AT06-1e @4	8.99	0.30
11AT06-1a @28	9.20	0.37	11AT06-1d @9	9.17	0.27
11AT06-1a @29	9.82	0.46	11AT06-1d @34	9.19	0.21
11AT06-1a @32	9.60	0.23	11AT06-1e @6	9.19	0.20
11AT06-1a @36	9.08	0.24	11AT06-1e @7	8.06	0.29
11AT06-1a @38	9.19	0.25	11AT06-1e @8	8.93	0.15
11AT06-1a @39	9.61	0.36	11AT06-1e @9	9.02	0.33
11AT06-1a @6	9.26	0.28	11AT06-1e @10	9.43	0.28
11AT06-1b @6	9.29	0.31	11AT06-1e @11	8.88	0.28
11AT06-1c @2	9.74	0.38	11AT06-1e @12	9.16	0.40
11AT06-1c @6	9.10	0.22	11AT06-1e @13	9.22	0.28
11AT06-1d @1	9.24	0.44	11AT06-1e @14	9.10	0.35
11AT06-1d @33	9.40	0.36	11AT06-1e @15	8.94	0.24
11AT06-1d @22	9.11	0.46	11AT06-1e @16	9.27	0.29
11AT06-1d @6	9.04	0.31	11AT06-1e @17	9.22	0.36
11AT06-1d @19	9.19	0.22	11AT06-1e @18	8.55	0.22
11AT06-1d @30	8.90	0.23	11AT06-1e @19	8.91	0.44
			11AT06-1e @20	8.66	0.22
zircon mantle			zircon high HREEs		
11AT06-1a @1	9.71	0.25	11AT06-1b @1	9.49	0.22
11AT06-1a @11	9.44	0.37	11AT06-1a @42	9.45	0.46
11AT06-1a @21	8.87	0.20	11AT06-1b @7	8.98	0.47
11AT06-1a @9	8.35	0.39	11AT06-1d @29	9.44	0.38
11AT06-1a @37	9.36	0.31	11AT06-1e @5	9.08	0.32
11AT06-1c @1	9.41	0.35			
Modeled results	$\delta^{18}\text{O}(\text{‰})$	Assumed mode in P peak (vol %)	assumed end-member		
zircon	9.0000	1.00	zircon100%		
garnet	9.0995	20.00	alm60%.grs20%.prp20%		
omphacite	9.1144	70.00	Di50%.Jd50%		
coesite	9.1534	2.00	Stishovite100%		
bulk-rock	8.47	-	-		

Table 8: 'a', the $\delta^{18}\text{O}$ values have been corrected by the instrumental mass fractionation; Modeled results were calculated based on methods and relevant factors from Zheng (1991, 1993); P peak is setted on 530 °C.

4.7.2. Sm-Nd isotopic chronology

Whole rock, omphacite and garnet (including core and rim) Sm-Nd isotopic data of the oriented eclogite sample 11AT06-2 are given in Table 9. Sm and Nd concentrations of whole rock powder separates (1.68 and 4.26 ppm respectively) are in

good agreement with results obtained from whole-rock trace-elements analyses by ICP-MS (Table 5).

Whole rock and omphacite separates have $^{147}\text{Sm}/^{144}\text{Nd}$ ratios of 0.2841, 0.2452 and 0.2510 respectively. Garnet separates

have a Sm/Nd ratio of about 2.13 and $^{147}\text{Sm}/^{144}\text{Nd}$ ratios of 1.2828 and 1.2843, which are close to values reported for other SW Tianshan eclogites (Gao and Klemd, 2003). The WR-Omp-Grt isochron yields a Sm-Nd age of 312.1 ± 2.4 Ma (MSWD = 0.78, Figure 26), close to the Omp-Grt isochrone isochron (311.9 ± 2.6 Ma), with $\epsilon\text{Nd}(t)$ of $+ 8.5$ ($t = \text{ca. } 312$ Ma, Table 9).

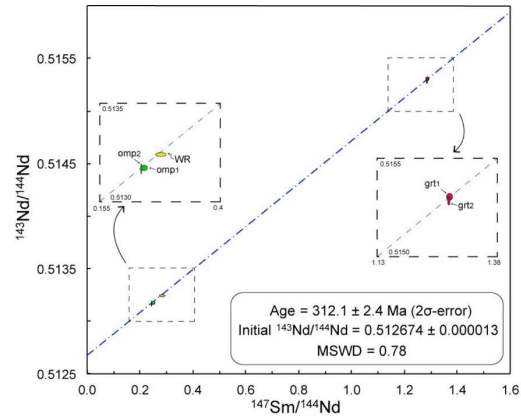


Figure 26: WR-garnet-omphacite Sm-Nd isochron age for the oriented sample (11AT06-2; Table 9)

TIMS Sm-Nd isotopic data

Sample	Mineral	Sm (ppm)	Nd (ppm)	$^{147}\text{Sm}/^{144}\text{Nd}$	$^{143}\text{Nd}/^{144}\text{Nd}$	$^{143}\text{Nd}/^{144}\text{Nd}$	errogrt-omp-WR age (Ma)	grt-omp age (Ma)	$\epsilon\text{Nd}(t)$
11AT06-2	WR	1.680	4.260	0.2841	0.513251	0.000008	312.1 ± 2.4	311.9 ± 2.6	8.5
	grt1	0.621	0.292	1.2843	0.515307	0.000014			
	grt2	0.624	0.294	1.2828	0.515286	0.000018			
	omp1	0.287	0.692	0.2510	0.513186	0.000011			
	omp2	0.290	0.714	0.2452	0.513180	0.000022			

Table 9: NOTES: WR means the whole rock, the absolute errors of $^{143}\text{Nd}/^{144}\text{Nd}$ and isochron ages are given in 2σ ; $\lambda = 6.54 \times 10^{-12} \text{ year}^{-1}$; $^{147}\text{Sm}/^{144}\text{Nd}_{\text{CHUR}} = 0.1967$, $^{147}\text{Sm}/^{144}\text{Nd}_{\text{DM}} = 0.2137$, $^{143}\text{Nd}/^{144}\text{Nd}_{\text{CHUR}}(0) = 0.512638$, $^{143}\text{Nd}/^{144}\text{Nd}_{\text{DM}}(0) = 0.513151$ are used for the calculation.

4.8. Pressure-Temperature estimates

4.8.1. Multi-equilibrium thermobarometry

P-T estimates for prograde equilibrium stages (using mineral inclusion pairs within garnet porphyroblast cores of sample 11AT06-1; Figure 22d), peak eclogitic-facies and retrograde blueschist- to greenschist-facies recrystallizations (e.g., recrystallized tails of σ -type porphyroclasts in oriented samples 11AT06-2, GJ01-6 and GJ01-1; Figure 21a, b, c), are constrained using THERMOCALC average PT multi-

equilibrium thermobarometry (Holland and Powell, 1998, 2011; version 3.33 with updated database tc-ds55). Average PT results and used representative mineral compositions are given in Table 10.

P-T estimates of 495 ± 20 °C and 2.75 ± 0.05 GPa were derived assuming equilibrium between garnet cores and inclusions of omphacite and amphibole (i.e., red square #1 in Figure 22d). Equilibrating omphacite inclusions and the garnet mantle (red square #2 in Figure 22d), in the vicinity of coesite inclusion, yield higher P-T estimates of 520 ± 15 °C and 3.0 ± 0.75 GPa but with considerable pressure uncertainties. Lower P but higher T values, around 570 ± 35 °C and 2.4 ± 0.3 GPa, are obtained for garnet rims, considering an omp-grt-ph-amp equilibrium assemblage (i.e., red square #3: Figure 22d; Table 10). Quartz (or coesite) was assumed to be present in all calculations and water activity was set to 1.0. Lowering the water activity (e.g. $a_{\text{H}_2\text{O}} = 0.8$) only results in a minor decrease in temperature (≤ 15 °C) and pressure (≤ 0.05 GPa).

P-T estimates obtained for the garnet rim, omphacite-amphibole-epidote± phengite assemblage marking the foliation of both sheared eclogitic samples (Figure 21a-b; GJ01-6 and 11AT06-2) are 525 ± 25 °C & 2.0 ± 0.15 GPa.

P-T conditions for the retrograde, blueschist- to (or) greenschist-facies equilibration stages associated with top-to-NNE shear senses (Fig. 6c, GJ01-1) were estimated from the mineral assemblage amphibole + paragonite + epidote + chlorite + feldspar (albite) at 380 ± 50 °C and 1.0 ± 0.2 GPa, and 420 ± 25 °C & 0.9 ± 0.1 GPa.

4.8.2. Phase equilibrium modeling

Pseudosection modeling for sample 11AT06-1 was performed in the system MnNCKFMASHTO (Tables 3, 4, 5), with excess SiO₂ (i.e., quartz or coesite). TiO₂ must be considered due to the presence of rutile and/or titanite in the matrix or as inclusions in porphyroblasts. The fluid phase is assumed to be pure H₂O and was set in excess. CO₂ was neglected as only small amounts of carbonate occur as thin secondary veins. Fe₂O₃ was set at 22.5 mol% of total FeO according to XRF data (Table 4).

In order to take into account the sequestration of elements induced by the growth zoning of garnet porphyroblast, effective bulk compositions were adjusted from XRF compositions by removing part of the garnet modal abundance, following the method of Carson et al. (1999). For the modelling of prograde and peak conditions (EBC-1), half of the modal abundance of zoned garnet (Warren and Waters, 2006; Wei et al., 2009) was removed from the XRF composition. For the retrograde path (EBC-2), garnet porphyroblasts were subtracted from the bulk-rock composition (see Table 4 for XRF, EBC-1 and EBC-2 compositions).

The P-T pseudosections were calculated using the software *Perple_X* 6.68 (Connolly, 1990, 2005) and an internally consistent thermodynamic dataset (*hp02ver.dat*, Connolly and Kerrick, 2002; Holland and Powell, 2003) based on the effective recalculated bulk rock composition (EBC-1 and EBC-2; Table 4). Mineral solid-solution models are Gt(HP) for garnet (Holland and Powell, 1998), Omph(GHP) for omphacite (Green et al., 2007), Amph (DP) for amphibole (Diener et al., 2007), Mica(CHA) for white mica (Coggon and Holland, 2002), Chl(HP) for chlorite (Holland

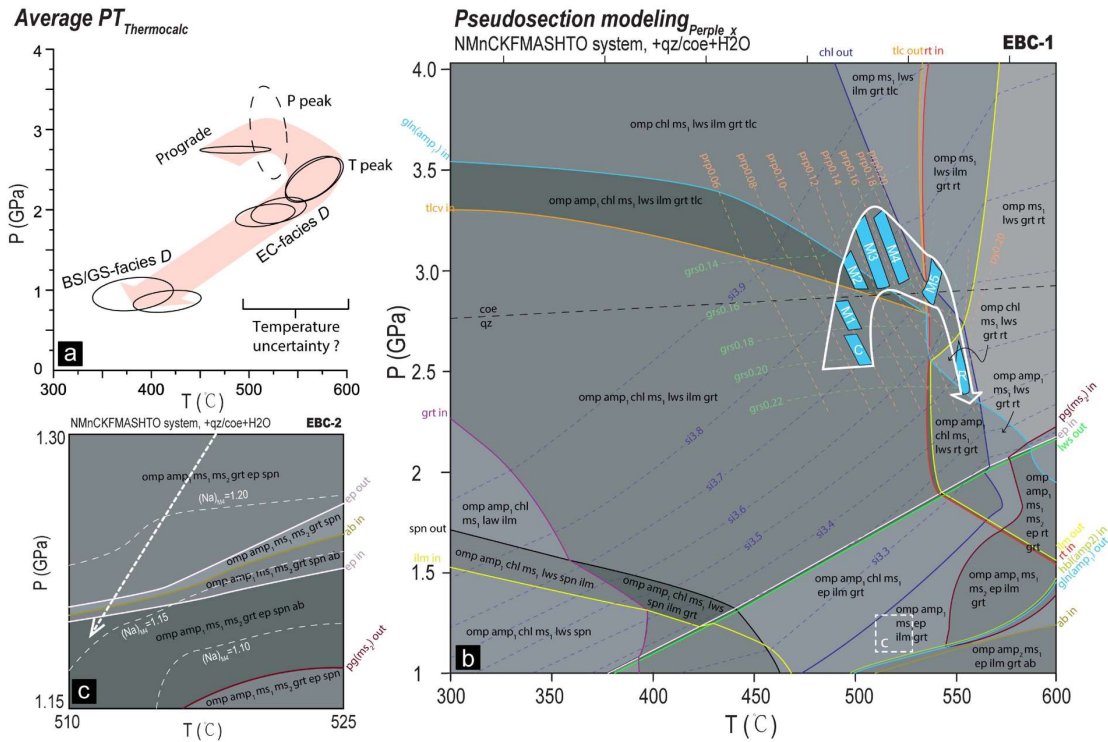


Figure 27: P-T estimates for the studied UHP eclogites, inferred from Perple_X pseudosection modeling and Thermocalc averagePT calculation: (a) compilation of Thermocalc averagePT results (Table 10); the pink arrow features the estimated trajectory, taking into account the uncertainties from avPT calculations. (b) P-T pseudosection in the system NMnCKFMASH for the studied UHP eclogite (effective bulk composition in Table 4). Seven spots across the core-rim EMPA profile (Figure 22e; Table 5) were used to estimate PT conditions based on calculated isopleths. Blue boxes also consider ca. 5 %-calculated uncertainties. White arrow: estimated P-T trajectory from pseudosection modelling; dashed box: estimation of retrograde P-T conditions from the (Na)M4 content of matrix amphibole. Mineral abbreviations as in Figure 20.

and Powell, 1998), Ep(HP) for epidote/clinozoisite (Holland and Powell, 1998), and H₂O-CO₂ fluid solution model is from Connolly and Trommsdorff (1991).

The pseudosection for sample 11AT06-1 is shown in Figure 27. It is dominated by tri- and quadrivariant fields with a few di- and quini-variant fields. P-T conditions were further constrained by comparing predicted garnet isopleths with measured garnet compositions (boxes on Figure 27b incorporate typical uncertainties on EMPA analyses, ca. 3% to 5%, Lifshin and Gauvin, 2001; Williams and Jercinovic, 2006).

Stage I, as defined by core-mantle zoning (i.e., garnet zoning from Grt-C to Grt-M3 in Figure 22e; see compositions in Table 5), is marked by an increase in both T and

P, from 2.55~2.70 GPa and 495~505°C to 2.95~3.30 GPa and 500~520°C. Peak pressure (P_{\max}) is constrained by using the garnet mantle compositions (corresponding to Grt-M2 to Grt-M4) which have the lowest X_{grs} content, and coincide with the location of coesite inclusions (Figure 22a-d).

Stage II is constrained by the mantle-rim zoning (corresponding to Grt-M4, Grt-M5 and Grt-R in Figure 22d, Table 5) and the mineral assemblage omp-amp₁(gln)-mica₁(ph)-lws-grt-rt. It is marked by a slight increase in T at 550~560°C and a pressure decrease at 2.35~2.60 GPa, further constrained by the Si content of phengite included in garnet (3.43 p.f.u.; Table 5). Later retrograde re-equilibration, based on the EBC-2 whole-rock composition, is estimated from measured $(\text{Na})_{\text{M4}}$ contents in amphibole and $(\text{Na})_{\text{M4}}$ isopleths modeled from pseudosection (Figure 27c) at ca. 1.20 GPa and 548°C.

4.9. Discussion

4.9.1. Nature of the protolith and P-T-(fluid) constraints

The studied mafic eclogites show LREE-depleted and HREE-flat N-MORB patterns (Sun and McDonough, 1989), with enrichments in Rb, Ba, U, Pb, and Sr. $\delta^{18}\text{O}$ values for multistage zircons ($\sim 9.13 \pm 0.09$ ‰; Figure 25b) with modelled bulk-rock $\delta^{18}\text{O}_{\text{P peak}}$ of ca. 8.47 ‰ (Table. 6, oxygen fractionation factors from Zheng, 1991, 1993) are similar to those of typical altered ocean crust (AOC, ~ 7.9 to 9.5 ‰ from Cocker et al., 1982; Miller and Cartwright, 2000), suggesting that the metamorphic zircons may have inherited the composition of the bulk (e.g., Rubatto and Angiboust, 2015) Some characteristic element patterns (e.g., in Rb vs K, Nb/U vs U, K/Th vs Ba/Th

and Ba/Nb vs U/Nb diagrams, Bebout, 2007, 2013) suggest that the N-MORB protolith was later slightly enriched in LILE during metamorphism. By contrast, the meta-volcanosedimentary host rock yields an Upper Continental Crust-like trace-element and REE-distribution pattern, with notable Nb and Ta anomalies (Figure 19).

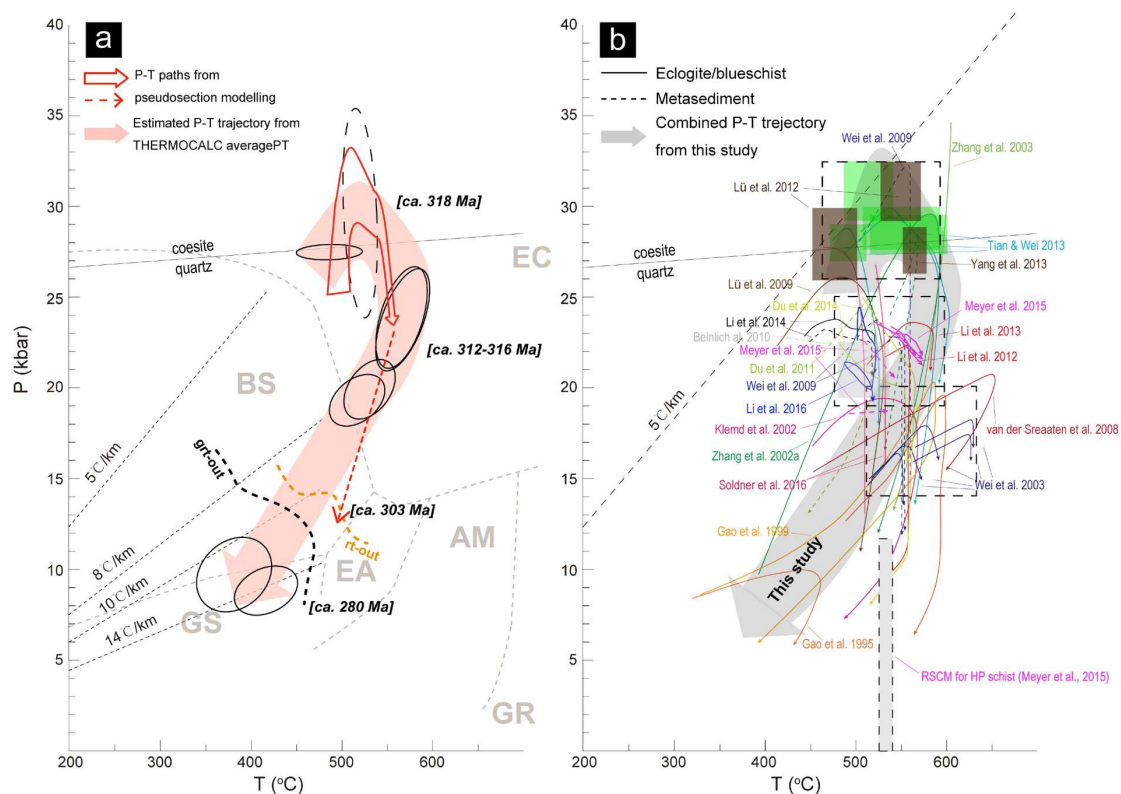


Figure 28: P-T trajectory estimates from this study (a) and previous works (b). See text for details. Brown boxes mark: estimates of peak metamorphism for UHP mica schist (Wei et al. (2009) Yang et al. (2013)). Light-green box: peak metamorphic UHP conditions for metabasite from Tian and Wei (2013). Ages shown in Figure 28a are discussed in §4.9.3.

The $\delta^{18}\text{O}$ values of the various zircon domains are remarkably constant despite considerable multistage growth from ca. ~ 318 to 280 Ma. This suggests that the rock system remained essentially closed over \sim ca. 40 Ma, during metamorphic re-equilibration, with respect to potential external fluid infiltration, at both the cm- and m-scale (zircon grains were collected from rock fragments from different parts of the outcrop), and/or that fluids were derived from (or equilibrated with) a similar source. External fluids derived from subduction-related lithologies would indeed have likely

shifted the $\delta^{18}\text{O}$ signature (unaltered slab mantle and oceanic crust ~ 5.7 ‰, serpentized slab mantle $\sim 1-8$ ‰, metasediment $\sim 12-29$ ‰ from van der Straaten et al., 2012). We therefore hypothesize that external fluid infiltration was limited and/or $\delta^{18}\text{O}$ was internally buffered (Martin et al., 2006; Martin et al., 2008).

The P-T evolution followed by mafic eclogites (Figure 27) is characterized by burial along a typical subduction gradient ($\sim 7^\circ\text{C}/\text{km}$) with a moderate heating (up to $50-80^\circ\text{C}$) during decompression. This is consistent with recent results of thermodynamic modeling (Li et al., 2015; Li et al., 2016; Lü et al., 2009; Tian and Wei, 2013; Wei et al., 2003), though in contrast to some early claims of counterclockwise (Lin and Enami, 2006) or hairpin-shaped P-T trajectories (Gao et al., 1999).

Thermodynamic modelling of successive re-equilibration stages yield P-T estimates within ~ 0.2 GPa and 20 °C (1σ -error, see also discussion by Li et al., 2016), considering uncertainties on solid solution models and thermodynamic properties (Dachs et al., 2012; Worley and Powell, 2000), effective bulk composition (Carson et al., 1999; Evans, 2004) and microprobe analyses (Lifshin and Gauvin, 2001; Williams and Jercinovic, 2006). Conventional thermobarometry give consistent and robust P-T results (Figure 28a) but with larger uncertainties for the pressure peak (Figure 27a, Table S1). When considering these uncertainties, most previous published P-T paths in fact will overlap (Figure 28b, except for Li et al., 2015; Li et al., 2016; van der Straaten et al., 2008; Wei et al., 2003). Most studies concord on T_{max} conditions for peak burial in the range $510-570$ °C (Figure 28b). Our results ($520 \pm 30^\circ\text{C}$ for UHP peak burial and $550 \pm 30^\circ\text{C}$ for the temperature peak) are consistent with the recent independent results

obtained by Raman spectroscopy of carbonaceous matter (ca. $540 \pm 30^\circ\text{C}$, Meyer et al., 2016).

Future studies should help clarify their contrasts in P_{max} estimates, which cluster in three distinct groups (dashed boxes; Figure 28b): 1) a UHP group ranging from ca. 2.7 to 3.3 GPa (e.g., Tian and Wei, 2013; Wei et al., 2009; Yang et al., 2013) (and this study), 2) a HP group in the range of ca. 1.8-2.5 GPa (e.g., Beinlich et al., 2010; Du et al., 2014; Li et al., 2015; Li et al., 2016 ; Li et al., 2014; Meyer et al., 2016; Soldner et al., 2016) and 3) a blueschist-facies group ranging from ca. 1.3 to 1.9 GPa (e.g., Gao et al., 1999; Klemd et al., 2002; van der Straaten et al., 2008; Wei et al., 2003).

4.9.2. Linking garnet with zircon growth

This section attempts to link the potential of garnet as thermobarometer (e.g., Konrad-Schmolke et al., 2008) with that of zircon as geochronometer (e.g., Rubatto, 2002) to closely tie U-Pb ages to metamorphic conditions and finally derive a precise P-T-time path.

Figure 24b shows that REE patterns for successive garnet and zircon metamorphic growth are almost parallel, except for the zircon rim. Partitioning data for REE between zircon and garnet (Rubatto, 2002; Rubatto and Hermann, 2003) suggest that zircon preferentially sequesters Y and HREE over garnet, with D-values of $\sim 2-4$ (Figure 29a). Data show that only the zircon high HREE core and/or core domains (and not the zircon mantle and rim) have higher HREE contents than garnet (Figure 29b, Table 6) and may therefore have equilibrated with it.

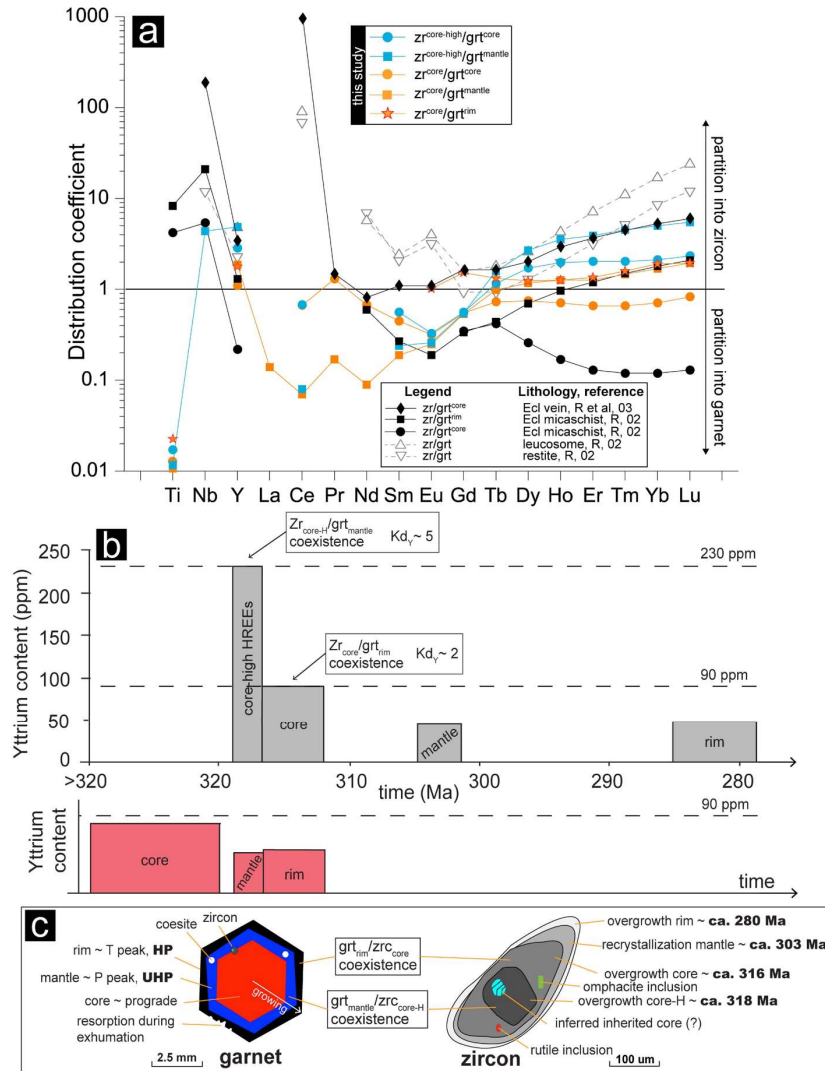


Figure 29: (a-b) Patterns of trace element distribution coefficients between various possibly coexisting zircon and garnet domains. (c) sketch summarizing the various growth zones observed in zircon and garnet.

Zircon high-HREE cores may have co-crystallized either with the garnet core or mantle domains (Figure 29b), but the $D^{Y+HREEs}_{zrn/grt}$ pattern of the second option is more similar to the one reported in eclogite vein by Rubatto and Hermann (2003). For the zircon core domain, the most likely candidate would be the garnet rim. We thus tentatively propose (Figure 29c, 30) that zircon high-HREE core grew in equilibrium with the garnet mantle at ~ ca. 318 Ma at UHP conditions (~ ca. 2.6-3.1 GPa; Grt-M1 to M2 stages with coesite inclusions; Figure 22), while zircon core grew in equilibrium with the garnet rim at ~ ca. 316 Ma (~ ca. 2.3-2.7 GPa; Grt-M5 to R stage).

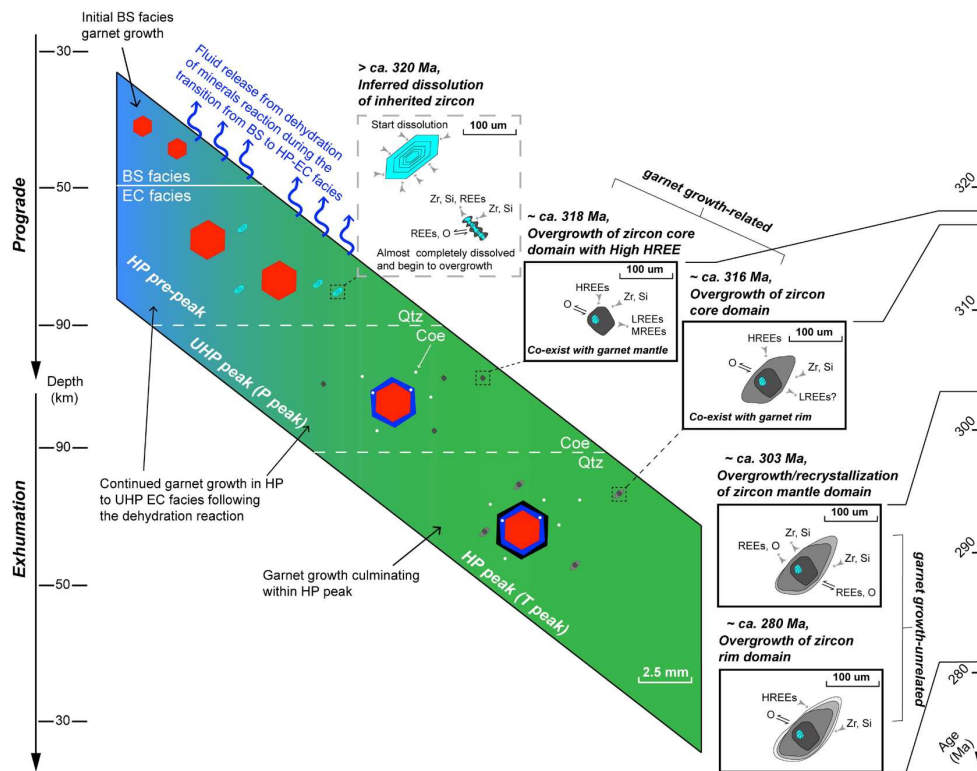


Figure 30: Sketch depicting the petrologic evolution of mineral growth within metabasalts and inferred mobility of elements (mainly REEs) within the garnet-zircon-matrix metamorphic system during subduction and exhumation.

The zircon mantle domain (~ ca. 303 Ma, Figure 25f), with similar but lower HREE patterns (Figure 24a), could have inherited its HREE content from the partial resorption of garnet (and/or zircon cores, i.e., Degeling et al., 2001), while garnet abundance was still buffering the HREE budget. By contrast, the different REE pattern of the last zircon rim overgrowth (~ ca. 280 Ma, Figure 25g), hints to the breakdown of another Zr-bearing mineral during greenschist/blueschist-facies exhumation, possibly rutile (Kohn et al., 2015; Lucassen et al., 2010). Similar multi-stage zircon growth from the Dabie mountain (but with zircon from separate eclogite and quartz vein, Liu et al., 2014b; Zheng et al., 2007) was interpreted as a witness of channelized fluid flow during exhumation.

4.9.3. Age constraints and regional-scale tectonic implication

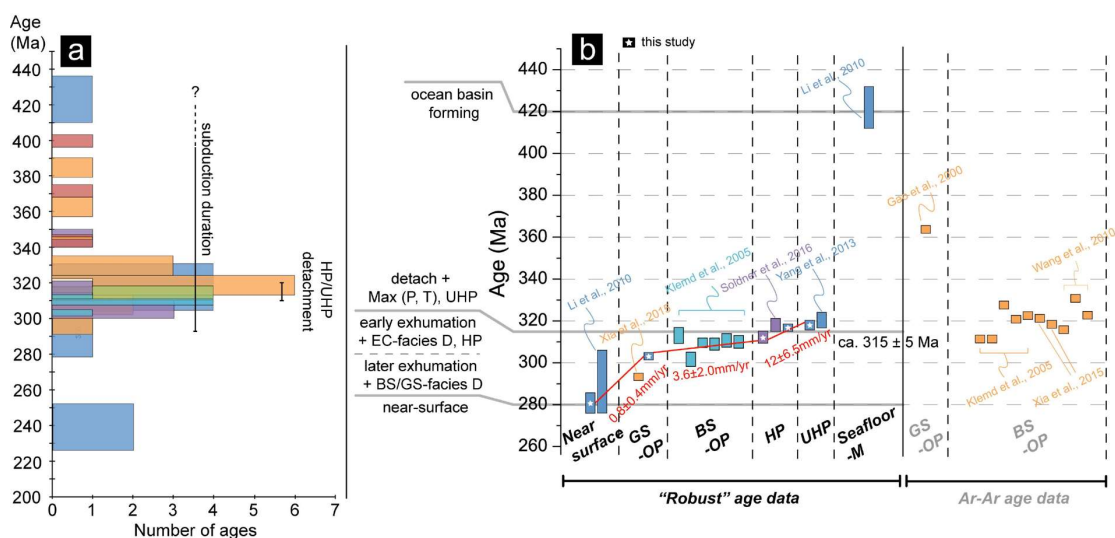


Figure 31: Previous radiometric data (see Table 2) and results from this study place constraints on the main tectonic stages for the area (i.e., detachment, exhumation, etc), as well as on exhumation rates.

Based on garnet-zircon equilibrium, ages of \sim ca. 318 and ca. 316 Ma can be ascribed to the peak burial (UHP) and peak temperature (HP) metamorphic stages, respectively (Figure 29c, 30). Whole rock-grt-omp and grt-omp Sm-Nd isochrons give additional, consistent age constraints at $\sim 312 \pm 2.5$ (Figure 26; Table. 7). Although experimentally determined closure temperatures for Nd diffusion differ in garnet (~ 500 - 850°C , Li et al., 2000) and omphacite ($\sim 1050^\circ\text{C}$, Sneeringer et al., 1984), questioning Nd equilibrium between these phases at a peak temperature of $530 \pm 30^\circ\text{C}$, consistent mineral pair and whole rock Sm-Nd isochron were reported for similar fine-grained eclogites from distinct localities in the Dabie mountains (Li et al., 2000).

This WR-garnet-omphacite Sm-Nd age of ca. 312 Ma (Figure 26, Table 9) can therefore be treated as constraining the post-peak eclogite-facies deformation event coeval with omphacite growth in the matrix (Figure 21a-b), slightly after or coeval with the growth of zircon cores in equilibrium with garnet rims (i.e., \sim ca. 316 Ma). These age constraints are broadly consistent with a recent Sm-Nd WR-grt-omp age of ~ 307

± 11 Ma interpreted as dating the timing of HP metamorphism (Du et al., 2014) and a Sm-Nd WR-grt-gln age of 318.4 ± 3.9 Ma for a blueschist equilibrated close to HP peak metamorphism (Soldner et al., 2016). Ages between 318 and 312 Ma are also consistent with the 320.4 ± 3.7 Ma zircon-rim U-Pb age obtained on coesite-bearing meta-volcanosedimentary rocks (Yang et al., 2013) and with the 315.2 ± 1.6 Ma garnet-multi-point Lu-Hf age obtained for eclogites (Klemd et al., 2011).

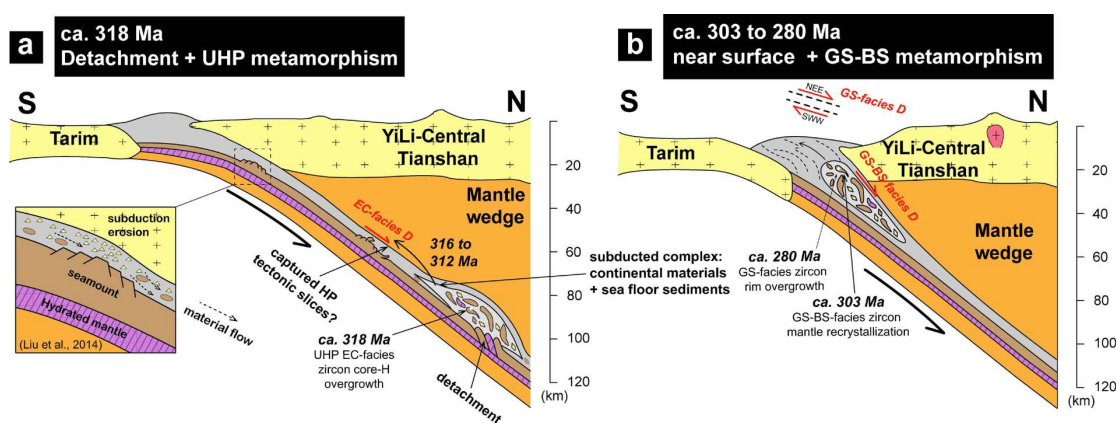


Figure 32: Simplified geodynamic cartoon setting back the studied samples and the overall time constraints inferred from this study within the evolution of the Chinese Southwestern Tianshan HP-UHP/LT metamorphic belt.

Overall, the present study allows to conclude that 315 ± 5 Ma can be taken as a reliable value for the attainment of HP to UHP conditions in the Chinese Southwestern Tianshan UHP-HP/LT metamorphic complex. The dispersion of Ar/Ar ages (Fig. 16b, Gao et al., 2000; Klemd et al., 2005; Wang et al., 2010; Xia et al., 2015) may therefore be due to a problem of excess argon, at least in some eclogite/blueschist samples. Indeed the same outcrop yielded very distinct Ar-Ar plateau ages (e.g., 401 ± 1 and 364 ± 1 Ma by Gao et al., 2000) versus ca. 320 Ma by Klemd et al. (2005), and similar ages were obtained for Rb/Sr and Ar/Ar ages by Klemd et al. (2005), for which white mica closure temperatures (if strictly under fluid-assisted recrystallization-free assuming)

differ by 100 °C or more (Li et al., 1994; Ruffet et al., 1997; Villa, 1998; Villa and Puxeddu, 1994).

The 303 Ma age derived from zircon mantle recrystallization (Figure 25f) is here taken as a minimum age for the garnet-free or garnet resorption greenschist-facies metamorphism. This conclusion is strengthened by a greenschist-facies Ar-Ar plateau age of $\sim 293.1 \pm 1.7$ Ma reported by Xia et al. (2015). Later recrystallization of zircon rims at ~ 280 Ma, though of poor quality (Figure 25g) could correspond to the late exhumation movements, as similar ages were reported for the extensive ductile strike-slip deformation of the Southwestern Central Tianshan Suture zone (i.e., de Jong et al., 2009; Laurent-Charvet et al., 2003). Note that late, post-exhumation rodingitization was constrained at 291 ± 15.0 Ma (Li et al., 2010c) and that crosscutting, undeformed leucogranites were dated at $\sim 284.9 \pm 2.0$ Ma (Gao et al., 2011).

These age constraints point to decreasing exhumation velocities, from ca. 12.0 ± 6.5 mm/yr for early UHP to HP exhumation (if < 2 Ma) to 3.6 ± 2.0 mm/yr for blueschist-facies exhumation (within ca. 13 Ma) and 0.8 ± 0.4 mm/yr for greenschist-facies exhumation (within ca. 22 Ma). The average exhumation rate, ca. 2.6 mm/yr, falls within the range of 1-5 mm/yr for exhumed oceanic rocks worldwide (Agard et al., 2009). Importantly, the timing of HP-UHP metamorphism appears very restricted (at 315 ± 5 Ma; i.e., < 10 Ma) compared to the likely duration of active subduction (> 50 -100 My, since an oceanic domain existed in the region from at least $\sim 422 \pm 10$ Ma to ca. 280-300 Ma, Li et al., 2010c).

Although this study focuses on a single key exposure, a simple geodynamic reconstruction is provided (Figure 32) to set back our results in a tentative evolution of the Chinese Southwestern Tianshan metamorphic complex. HP-UHP/LT rocks were detached or exhumed after their peak burial only at about 315 ± 5 Ma (Figure 31) and brought back to the surface to greenschist-facies conditions between ca. 310 and 300 Ma (Figure 32b). Pervasive north-trending shear senses deduced from eclogite-, blueschist- and greenschist-facies recrystallizations (this study, Fig. 6, see also in Lin et al., 2008; Wang et al., 2010) are interpreted to result from southwest-trending extrusion of the AMC (Figure 32b).

At present, thorough large-scale structural studies and/or extensive P-T(-t) mapping across the whole HP/UHP complex are still missing to assess whether the punctuated exhumation at 315 ± 5 Ma is associated with chaotic block-in-matrix mixing, with heterogeneous P-T and/or fluid conditions (e.g., extremely complex zoning of both garnet and amphibole, Li et al., 2016) or to accretion of tectonic slices of volcanosedimentary material hosting stripped pieces from the seafloor (i.e., mafic meta-volcanics).

4.10. Conclusions

This study provides P-T-radiometric-isotopic constraints on several eclogitic samples from a key coesite-bearing location in the Chinese Southwestern Tianshan UHP-HP/LT metamorphic complex. Together with an exhaustive review of available P-T (-time) constraints for the area, the following conclusions can be drawn from these new data:

- (1) Mafic eclogites have slightly LILE-enriched N-MORB like features with $\delta^{18}\text{O}_{\text{zircon}}$ values of \sim ca. 9.0 ‰ typical of an AOC protolith. The constant $\delta^{18}\text{O}$ values for the successive zircon growths suggest a metamorphic system closed (or very limited) to external fluid infiltration.
- (2) Thermodynamic modeling permits a complete recovery of their P-T trajectory from pre-peak burial to UHP conditions ($\sim 2.95 \text{ GPa} \pm 0.2$ and $510^\circ\text{C} \pm 20$) and later exhumation. REE partitioning between multistage zircon and garnet growth domains allows for a critical assessment of the P-T-time path: the ca. 318 Ma and 316 Ma zircon ages are tied to UHP and HP metamorphism, respectively, along with a consistent ca. 312 Ma Sm-Nd age for HP eclogite-facies deformation. Thus, peak burial can be constrained at about 315 ± 5 Ma. These P-T-t constraints point to decreasing exhumation velocities, from ca. 12.0 ± 6.5 mm/yr for early UHP to HP exhumation to 3.6 ± 2.0 mm/yr for blueschist facies exhumation and 0.8 ± 0.4 mm/yr for greenschist facies exhumation.
- (3) The comparison of P-T (-time) estimates between this study and the compilation of previous works outlines the existence of a short-lived detachment of subducted eclogites (< 10 Ma) with respect to the “long-term” subduction duration (> 50 -100 Ma).

ACKNOWLEDGMENTS

This study was essentially funded by the National Natural Science Foundation of China (41390440, 41390445, 41025008). Additional support was provided by project “Zooming in between plates” (Marie Curie International Training Network) to Prof. Philippe Agard. We would like to thank the editor Prof. Marco Scambelluri and anonymous reviewers for their constructive comments that greatly helped in improving the article. We further thank He Li and Bingyu Gao for helping the major and trace elements analysis, Qian Mao and Reiner Klemd for helps and data processing during microprobe analyses, Qiuli, Li, Yu Liu, Guoqiang Tang and Jiao Li for helps during SIMS zircon U-Pb dating and oxygen analyse, Yueheng Yang for help during zircon and garnet in situ trace elements analyse, and Zhuyin Chu for help during Sm-Nd isotope analyse.

APPENDIX

Analytical methods

Bulk-rock analyses

Four bulk-rock chemical analyses were performed at the Institute of Geology and Geophysics, Chinese Academy of Sciences (IGGCAS) on three samples from one eclogite outcrop (see location in Fig. 4; 11AT06-1, 11AT06-2 and GJ01-6), and one sample from the wall-rock mica schist ~3 meters away (GJ01-1). Major oxides were determined by a PHILLIPS PW1480 X-ray fluorescence spectrometer (XRF) on fused glass discs. Loss on ignition (LOI) was measured after heating to 1,000 °C.

Uncertainties for most major oxides are ca. 2%, for MnO and P₂O₅ ca. 5%, and totals are within 100 ± 1 wt.%. Whole rock Fe₂O₃ content is constrained by potassium permanganate titration. Trace element concentrations were analyzed by inductively coupled plasma mass spectrometry (ICP-MS) using a Finnigan MAT ELEMENT spectrometer at the IGGCAS. The detailed analytical procedure is identical to that used by Qian et al. (2006). Relative standard deviations (RSD) are within ±10% for most trace elements but reach ± 20% for V, Cr, Co, Ni, Th and U according to analyses of rock standards. Detail major and trace elements analyses are presented in Table 4.

Mineral major elements

In situ major element compositions of garnet and inclusion minerals were obtained from polished thin sections by electron microprobe analyses at the IGGCAS with the use of JEOL JXA 8100. Quantitative analyses were performed using wavelength dispersive spectrometers with an acceleration voltage of 15 kV, a beam current of 15 nA, a 3 µm beam size and 30 s counting time. Natural minerals and synthetic oxides were used as standards, and a program based on the ZAF procedure was used for data correction. Representative microprobe analyses for pseudosection modeling and for Thermocalc averagePT calculations are presented in Table 5 and Table 10, respectively.

Mineral trace elements

In situ trace element analyses of zoned garnet and zircon were performed by LA-ICP-MS at the IGGCAS with a single collector quadrupole Agilent 7500a ICM-MS, equipped with an UP193Fx argon fluoride New Wave Research Excimer laser ablation system. The glass reference material NIST SRM 610 and NIST SRM 612 were used as

standards for external calibration. LA-ICP-MS measurements were conducted using a spot size diameter of 40 to 60 μm , a laser frequency of 15 Hz and 0.63 GW/cm² and a fluence of 3.32 J/cm². Acquisition time was 20 s for the background and 120 s for the mineral analyses. The Ca-content of garnet determined by EMP analyses and the Si-content of zircon constrained by standard zircon 91500 were used as internal standards. Reproducibility and accuracy, which were determined for NIST SRM 610 and NIST SRM 612, are usually < 8 % and < 6 %. Trace element concentrations were then calculated using GLITTER Version 3 (Van Achterbergh et al., 1999). Representative average trace element data of the relevant garnet and zircon domains are given in Table 6.

Raman analyses

In order to identify coesite inclusions in garnet or small high-pressure mineral inclusions in zircon (e.g. omphacite or rutile), Raman spectroscopy was performed at IGGCAS using a Renishaw Raman MKI-1000 system equipped with a CCD detector and an Ar ion laser. The laser beam with a wavelength of 514.5 nm was focused on the coesite inclusion through 50 \times and 100 \times objectives of a light microscope. The laser spot size was focused to 1 μm . The reproduction of spectra for the same spot is better than 0.2 cm⁻¹.

Sm-Nd isotope chronology analyses

Sm-Nd isotopic analyses were obtained at the Institute of Geology and Geophysics, Chinese Academy of Sciences, Beijing. 100 mg of samples were first mixed with ¹⁴⁹Sm-¹⁵⁰Nd diluent, dissolved afterwards in a purified HF-HClO₄-HNO₃-

mixture, and finally heated on an electric hot plate for a week. Separation and purification of bulk REE were conducted by a silica-column with an AG50W-X12 exchange resin (200–400 mesh, 2ml), those of Sm and Nd by a silica-column with Teflon powder (1 ml) as exchange medium. Isotopic ratios of Sm and Nd were measured using a Finnigan MAT-262 thermal ionization mass spectrometer. Nd isotopic data of unknowns were normalized to $^{146}\text{Nd}/^{144}\text{Nd}$ of 0.7219 and corrected using Ames ($^{143}\text{Nd}/^{144}\text{Nd} = 0.512138$) as external standard. Errors in element concentrations and $^{147}\text{Sm}/^{144}\text{Nd}$ -ratios are less than 0.5% (2σ). Sm-Nd data for the studied sample is shown in Table 9.

U-Pb isotope chronology and Oxygen isotope of zircon

For the preparation of zircon study, and considering the relative low Zr content (only ca. 50 ug/g) of this N-MORB type meta-basalt (Table 4), about 100 kilograms eclogite were sampled from outcrop (detailed sampling locations are shown in Figure 18a, c. 11AT06-1, ca. 40 kg, sampled in 2011; 11AT06-2, ca. 60 kg, sampled in 2013), and approximately 500 zircon grains were collected and mounted in three different epoxy mounts. Fifty point analyses on different zircon domains from grains selected via CL images were chosen for investigating the U-Pb isotopic chronology and Oxygen isotopic composition of the potential multistage growth of zircon.

Zircon grains of sample 11AT06 were prepared by conventional crushing techniques and were hand-picked, mounted onto epoxy resin disks and polished with 0.25 μm diamond paste. The zircon grains and zircon standards (Plesovice, Peng Lai and Qing Hu zircon were used here as standards) were mounted in epoxy mounts and

then polished to section the crystals in half. Assessment of zircon grains and the choice of analytical sites were based on the transmitted and reflected light microscopy and cathodoluminescence (CL) images. CL imaging was processed on the LEO145VP scanning electron microscope with a Mini detector at the Institute of Geology and Geophysics, Chinese Academy of Sciences in Beijing (IGGCAS). The mount was vacuum-coated with high-purity gold prior to secondary ion mass spectrometry (SIMS) analyses. Measurements of U, Th and Pb were conducted using the Cameca IMS-1280 SIMS. U-Th-Pb ratios and absolute abundances were determined relative to the standard zircon 91500 (Wiedenbeck et al., 1995), analyses of which were interspersed with those of unknown grains, using operating and data processing procedures similar to those described by Li et al. (2009). A long-term uncertainty of 1.5% (1 RSD) for $^{206}\text{Pb}/^{238}\text{U}$ measurements of the standard zircons was propagated to the unknowns (Li et al., 2010a) despite that the measured $^{206}\text{Pb}/^{238}\text{U}$ error in a specific session is generally around 1% (1 RSD) or less. Measured compositions were corrected for common Pb using non-radiogenic ^{204}Pb . Further details on instrument parameters, analytical method, calibration and correction procedures can be found in (Li et al., 2010b). Results of U-Pb isotopic chronology of zircon for sample 11AT06 are listed in Table 7.

Oxygen isotope analyses at the exact locations of U-Pb isotope zircon were also processed with the use of the Cameca IMS-1280 SIMS at IGGCAS. After U-Pb dating, the mount was carefully repolished for the O isotope analyses. The Gaussian focused Cs^+ ions are used as a primary beam to sputter zircon for O-isotope analyses. The primary beam size is ~ 10 μm in diameter, and 2.5-3 nA in intensity. The ^{16}O and ^{18}O

ions are detected simultaneously by two Faraday cups, and the currents are amplified by 10^{10} ohms and 10^{11} ohms resistors, respectively. Each spot analysis consists of pre-sputtering, beam centering in apertures, and a signal collecting process. A single spot analysis lasts 3 mins, including 2 mins for pre-sputtering and centering the secondary beam, and 1 min to collect 16 cycles of ^{16}O and ^{18}O signals. Oxygen isotopes were measured using the multi-collection mode. The instrumental mass fractionation (IMF) was corrected using an in-house zircon standard Penglai with $\delta^{18}\text{OVSMOW} = 5.31 \pm 0.10\text{‰}$ (Li et al., 2010d). The measured $^{18}\text{O}/^{16}\text{O}$ ratios were normalized to the VSMOW composition, then corrected for IMF as described in (Li et al., 2010b): $\text{IMF} = \delta^{18}\text{O}_M - \delta^{18}\text{O}_{\text{Standard}}$, and $\delta^{18}\text{O}_{\text{Sample}} = \delta^{18}\text{O}_M + \text{IMF}$, where $\delta^{18}\text{O}_M = [({}^{18}\text{O}/{}^{16}\text{O})_M / 0.0020052 - 1] \times 1000$ (‰) and $\delta^{18}\text{O}_{\text{Standard}}$ is the recommended $\delta^{18}\text{O}$ value for the zircon standard on the VSMOW scale. Corrected $\delta^{18}\text{O}$ values are reported in the standard per mil notation with 2σ errors. Analytical conditions, instrumentation and operation conditions are similar to Li et al. (2010d); Tang et al. (2015), and the results of oxygen isotope for zircon in sample 11AT06 are listed in Table 8.

Supplementary Figures and Tables:

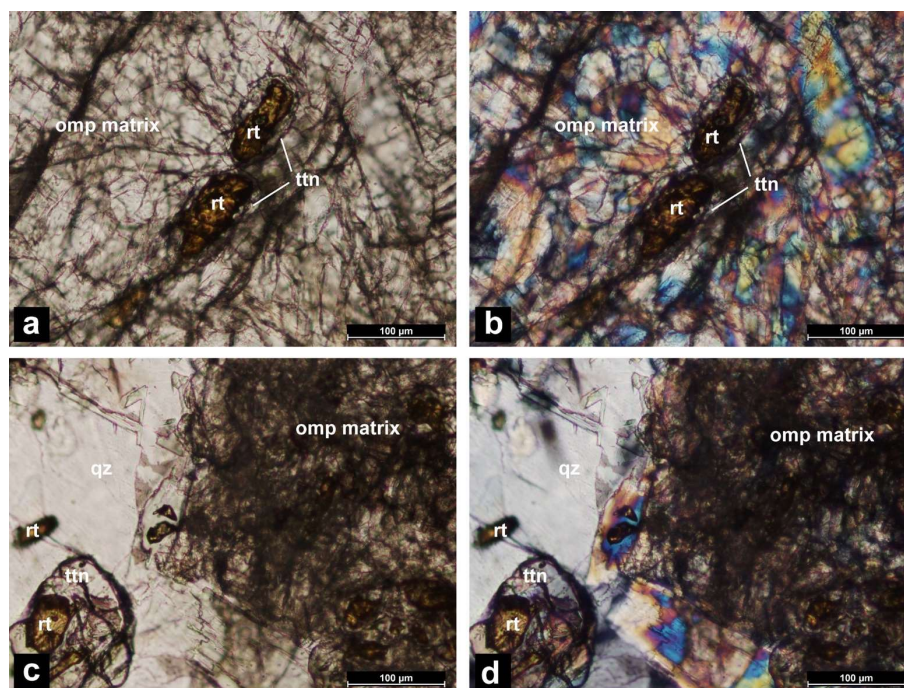


Figure 34: Rutile armored by sphene in both omphacite matrix (a, b) and later stage retrograde-growth quartz (c, d). Rutile-breakdown (and the absence of ilmenite) could be tied to the growth of the last zircon rim generation (Figure 23, 25, 35).

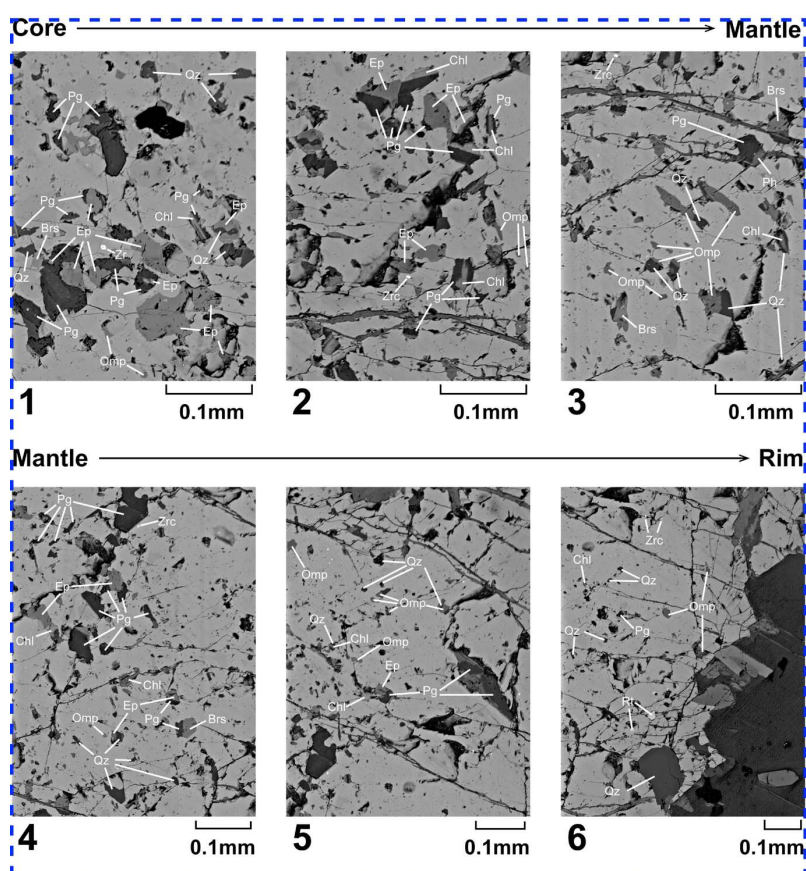


Figure 33: BSE imaging of mineral inclusion distribution in the studied garnet porphyroblast. Location correspond to dark blue dashed-line rectangles in Figure 22a, also schematically shown in Figure 22b).

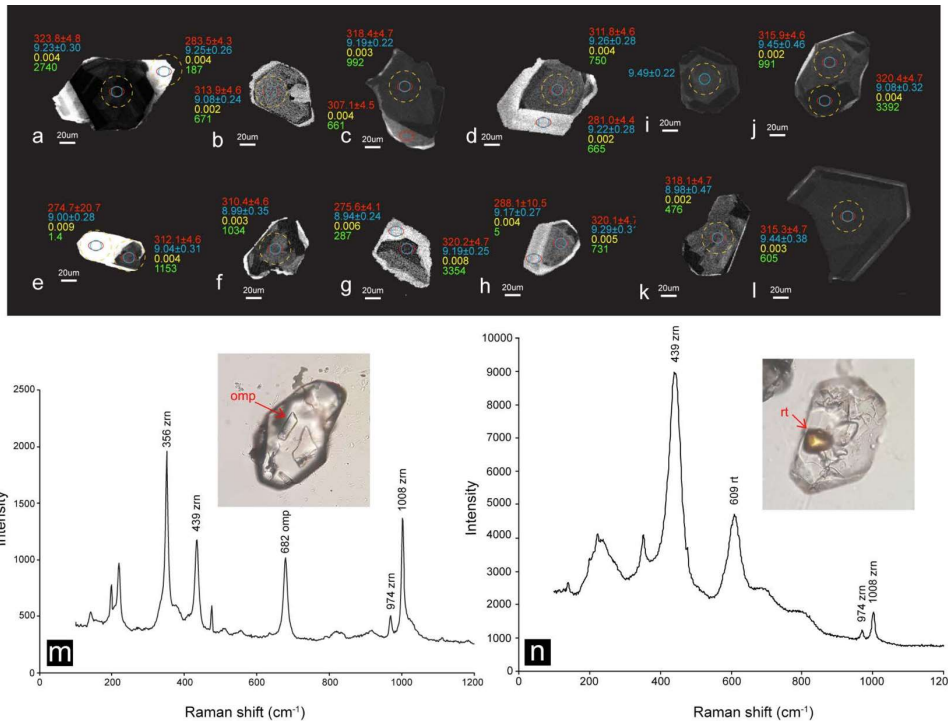


Figure 36: Continued from Figure 23: (a-i): cathodoluminescence images of other studied zircon grains; (m-n): typical HP (or UHP) metamorphic minerals (omphacite and rutile) revealed from Raman analyses.

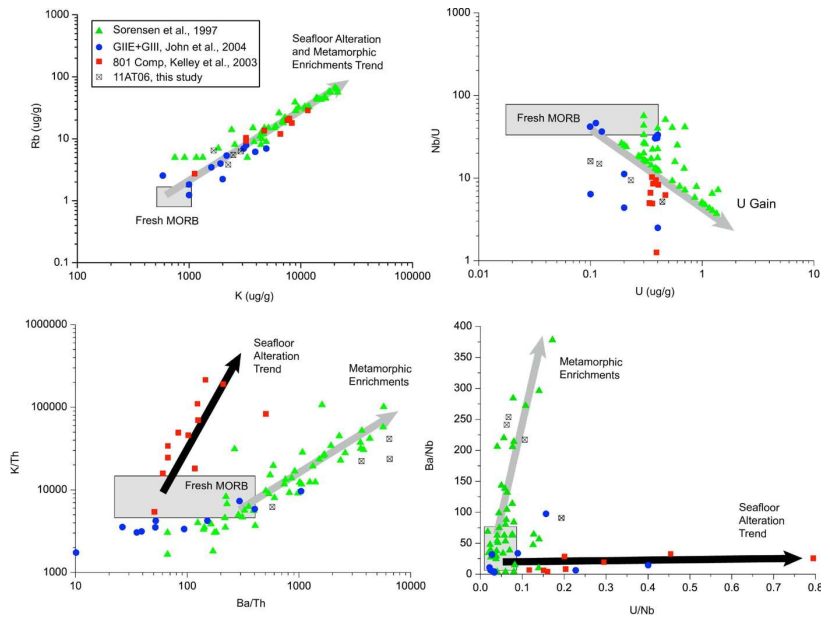


Figure 35: Rb vs K, Nb/U vs U, K/Th vs Ba/Th and Ba/Nb vs U/Nb diagrams (Bebout, 2007, 2013) for discriminating between LILE enrichment by metamorphism and seafloor alteration. 1: eclogite/blueschist/amphibolite (Sorensen et al., 1997); 2: eclogite/gabbro/metagabbro (GIIe+GIII, John et al., 2004); 3: typical altered oceanic crust rocks from ODP Sites 801 (Kelley et al., 2003).

Sample	11AT06-1										11AT06-2										GUM-1									
	Prognoze		Amphibole		Oxide		P peak		T peak		Oxide		P peak		T peak		Oxide		P peak		T peak		Oxide		P peak		T peak			
SiO ₂	Al ₂ O ₃	FeO	CaO	MgO	SiO ₂	Al ₂ O ₃	FeO	CaO	MgO	SiO ₂	Al ₂ O ₃	FeO	CaO	MgO	SiO ₂	Al ₂ O ₃	FeO	CaO	MgO	SiO ₂	Al ₂ O ₃	FeO	CaO	MgO	SiO ₂	Al ₂ O ₃	FeO	CaO	MgO	
190	51.83	38.36	46.71	58.55	57.87	57.27	38.60	52.67	57.83	56.54	38.82	52.90	57.79	57.93	50.29	51.92	39.00	57.39	49.72	52.55	38.75	26.42	66.32	48.87	47.05	33.81	27.72	69.45	48.80	51.68
200	0.06	0.16	0.27	0.05	0.09	0.08	0.05	0.03	0.03	0.02	0.00	0.16	0.02	0.02	0.31	0.27	0.05	0.09	0.15	0.30	0.19	0.04	0.01	0.11	0.09	0.06	0.12	0.09	0.00	0.14
300	11.18	21.29	12.12	12.37	11.34	10.07	27.08	11.72	22.67	27.53	22.44	10.90	11.11	27.70	22.18	11.98	12.18	27.39	26.02	18.58	19.70	38.75	11.30	29.08	19.90	19.99	39.20	9.33	0.00	0.08
400	0.00	0.03	0.05	0.00	0.04	0.05	0.00	0.00	0.04	0.04	0.00	0.00	0.04	0.12	0.03	0.04	0.04	0.03	0.06	0.05	0.01	0.11	0.12	0.05	0.03	0.04	0.01	0.10	0.08	
500	12.01	31.20	19.39	8.22	4.00	27.05	2.27	4.00	26.49	2.27	25.89	3.33	10.30	1.83	26.86	2.28	11.84	2.45	1.80	1.92	1.18	22.22	0.00	0.00	13.80	0.05	24.16	0.00	0.17	9.12
600	0.24	0.84	0.13	0.02	0.03	0.01	0.04	0.00	0.38	0.01	0.35	0.02	0.07	0.01	0.31	0.01	0.04	0.04	0.09	0.25	0.06	0.00	0.25	0.06	0.00	0.11	0.00	0.00	0.05	0.05
700	0.49	2.61	3.20	11.63	7.83	4.45	3.32	7.67	5.37	3.28	3.37	4.81	8.09	11.04	3.24	23.62	0.12	0.58	0.15	0.76	23.95	0.05	0.23	0.33	8.58	0.00	0.00	0.00	0.00	0.00
800	11.90	8.40	8.28	5.41	1.34	12.57	8.11	0.02	1.14	11.88	7.92	0.03	7.42	13.01	8.50	0.01	8.09	12.93	8.17	0.02	0.04	0.15	0.09	0.41	0.32	0.00	0.04	0.32	0.15	
900	0.00	0.00	0.00	0.00	0.00	0.00	0.00	0.00	0.00	0.00	0.00	0.00	0.00	0.00	0.00	0.00	0.00	0.00	0.00	0.00	0.00	0.00	0.00	0.00	0.00	0.00	0.00	0.00	0.00	
1000	99.94	101.65	98.02	99.07	101.32	100.86	95.70	97.94	100.06	101.70	99.26	101.08	101.49	99.22	95.11	101.38	101.84	98.86	96.13	96.02	83.26	99.64	95.73	97.51	94.27	89.25	101.94	96.49	98.12	
Structural formula																														
Si	3.01	3.01	2.99	3.46	7.79	2.00	2.99	3.46	7.85	2.00	2.86	3.46	2.96	2.02	7.08	3.43	3.00	3.45	3.00	3.00	3.04	2.90	2.50	3.09	6.89	3.04	2.84	2.88	3.07	7.29
Al	0.48	1.96	2.11	0.43	1.96	0.47	2.02	2.10	1.95	0.49	2.05	2.12	2.04	0.45	1.84	2.16	2.01	0.49	2.03	2.12	2.41	2.41	1.03	2.89	1.95	2.68	2.40	1.01	2.90	1.55
Fe ³⁺	0.00	0.00	0.01	0.01	0.00	0.00	0.00	0.00	0.00	0.00	0.00	0.00	0.00	0.00	0.00	0.00	0.00	0.00	0.00	0.00	0.00	0.00	0.00	0.00	0.00	0.00	0.00	0.00	0.01	0.01
Fe ²⁺	0.00	0.00	0.00	0.00	0.00	0.00	0.00	0.00	0.00	0.00	0.00	0.00	0.00	0.00	0.00	0.00	0.00	0.00	0.00	0.00	0.00	0.00	0.00	0.00	0.00	0.00	0.00	0.00	0.00	0.00
Mg	0.01	0.05	0.05	0.00	0.08	0.05	0.00	0.00	0.08	0.06	0.02	0.00	0.04	0.02	0.18	0.00	0.00	0.04	0.00	0.00	0.00	0.00	0.00	0.00	0.00	0.00	0.00	0.00	0.00	0.00
Mn	0.00	0.00	0.00	0.00	0.00	0.00	0.00	0.00	0.00	0.00	0.00	0.00	0.00	0.00	0.00	0.00	0.00	0.00	0.00	0.00	0.00	0.00	0.00	0.00	0.00	0.00	0.00	0.00	0.00	0.00
Ca	0.47	0.54	1.31	0.46	0.47	0.47	0.67	0.00	0.17	0.45	0.65	0.00	0.61	0.32	0.42	0.65	0.44	2.69	0.33	0.42	2.41	0.03	0.01	2.40	0.02	2.61	0.00	0.01	2.84	0.00
Na	0.01	0.03	0.19	0.01	0.01	0.01	0.01	0.01	0.01	0.01	0.01	0.01	0.01	0.01	0.01	0.01	0.01	0.01	0.01	0.01	0.01	0.01	0.01	0.01	0.01	0.01	0.01	0.01	0.01	0.01
K	0.00	0.00	0.00	0.00	0.00	0.00	0.00	0.00	0.00	0.00	0.00	0.00	0.00	0.00	0.00	0.00	0.00	0.00	0.00	0.00	0.00	0.00	0.00	0.00	0.00	0.00	0.00	0.00	0.00	0.00
Independent set																														
reactors from																														
averagePT calculation																														
independent set																														
cut value of each																														
PT	P = 27.5 kbars, sd = 0.4, cor = 0.233, sigfl = 1.97																													
Average T = 493.0, sd = 22.																														
P = 2.89 kbars, sd = 7.6, cor = 0.021, sigfl = 0.24																														
T = 520.0, sd = 16.																														
P = 29.8 kbars, sd = 2.4, cor = 0.720, sigfl = 1.97																														
T = 572.0, sd = 29.																														
P = 24.0 kbars, sd = 2.9, cor = 0.686, sigfl = 2.44																														
T = 627.0, sd = 35.																														
P = 19.9 kbars, sd = 1.3, cor = 0.724, sigfl = 1.83																														
T = 530.0, sd = 25.																														
P = 8.7 kbars, sd = 1.2, cor = 0.740, sigfl = 1.77																														
T = 518.0, sd = 25.																														
P = 9.7 kbars, sd = 1.1, cor = 0.768, sigfl = 0.51																														
T = 419.0, sd = 26.																														
P = 6.9 kbars, sd = 1.1, cor = 0.768, sigfl = 0.51																														
T = 380.0, sd = 49.																														
P = 8.7 kbars, sd = 2.0, cor = 0.569, sigfl = 1.72																														
T = 419.0, sd = 26.																														
P = 6.9 kbars, sd = 1.1, cor = 0.768, sigfl = 0.51																														

Table 10: NOTES: All the EMPA data are re-calculated by AX program under conditions with $T=530\text{ }^{\circ}\text{C}$ & $P=2\text{ GPa}$ except data for GS/BS deformation (with $T=400\text{ }^{\circ}\text{C}$ & $P=1.2\text{ GPa}$); The entire avPT calculations are processing with setting $x(\text{H}_2\text{O})=1.0$.

5. Concordant pulse in Mn, Y and HREEs concentrations during UHP eclogitic garnet growth: transient rock dynamics along a cold subduction plate interface

EPSL, under review

Key words: *UHP oceanic eclogite; garnet zoning; Zr-in-rutile thermometry; diffusion modeling; cold subduction regime; Chinese SW-Tianshan;*

Authors: *Tan Zhou^{a,b,c}, Agard Philippe^b, Gao Jun^{a,c,*}*

- h. Key Laboratory of Mineral Resources, Institute of Geology and Geophysics, Chinese Academy of Sciences, 100029 Beijing, China
- i. Sorbonne Université, CNRS-INSU, Institut des Sciences de la Terre de Paris, ITeP UMR 7193, F-75005 Paris, France
- j. University of Chinese Academy of Sciences, 100049 Beijing, China

Corresponding author: **Gao Jun, gaojun@mail.iggcas.ac.cn*

Abstract

The detailed petrological study of ultrahigh-pressure low-temperature oceanic eclogites from a fragment of the fossil Devonian-Carboniferous subduction plate interface (SW-Tianshan) reveals a strikingly concordant Mn, Y and HREEs garnet zoning. Zr-in-rutile thermometry, thermodynamic modelling and diffusion-controlled garnet growth modeling suggest that this type of zoning results from a short-lived thermal pulse of ~80 °C (from 490 to 570 °C) rather than from mineral breakdown. This event is estimated to have lasted ~300 Kyr, assuming a prograde to peak burial of 5 Myrs. Such a garnet zoning is observed for grains sampled meters apart (Figure 37d),

and was detected in other eclogites in the region. This transient thermal excursion is tentatively tied to the fast movement of detached UHP oceanic slices towards the hotter mantle wedge.

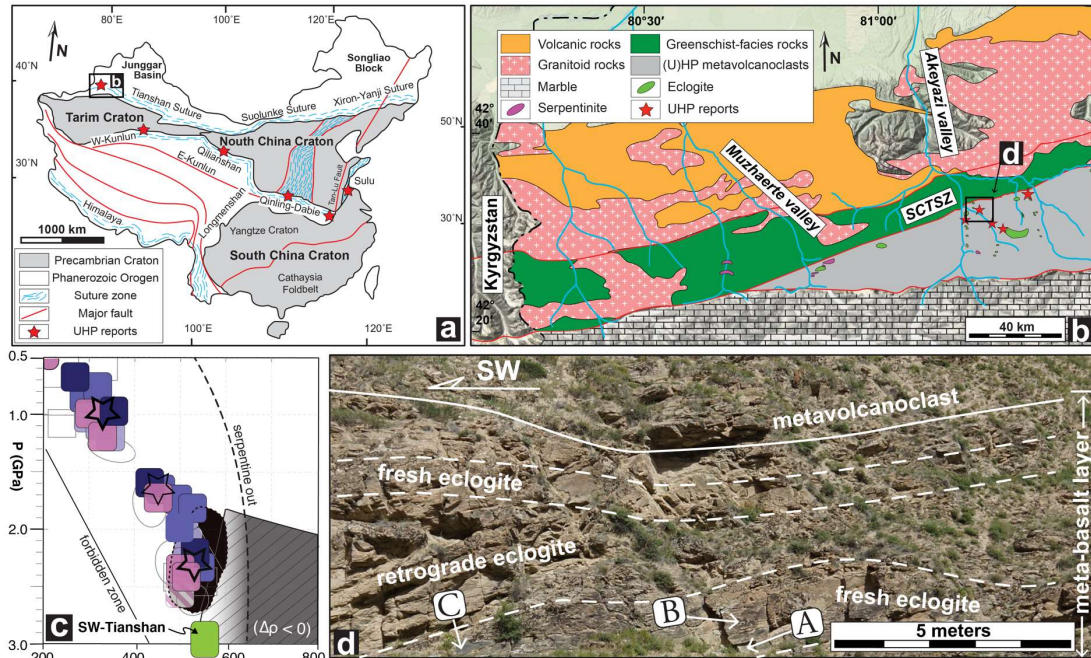


Figure 37: Geological background of the SW-Tianshan LT-HP/UHP metamorphic complex. (a) Location of the research area with respect to other key UHP reports in China; (b) Close-up view showing the regional geological setting and sampling location: previous UHP reports based on coesite inclusions in garnet are highlighted by red stars (modified after Tan et al., 2017). SCTSZ: South Central Tianshan Suture Zone; (c) Comparison of the P-T conditions experienced by SW-Tianshan metavolcanics with those of exhumed oceanic rocks worldwide (modified after Agard et al., 2009; Plunder et al., 2015) highlighting the provenance of these rocks from a deep, cold subduction zone (i.e., ~100 km, ~5 °C/km); (d) Location of samples on the outcrop.

5.1. Introduction

Garnet plays an ultimate role in disclosing mechanical and thermal processes at plate boundaries, by constraining complex pressure-temperature-time histories (e.g., Baxter et al., 2017; Caddick and Kohn, 2013, and references therein) and kinetics of metamorphic processes (e.g., Angiboust et al., 2012; Berg et al., 2013; King et al., 2004; Moore et al., 2013; Prior et al., 2002; Skora et al., 2006; Yang and Rivers, 2003). Garnet also yields unique information about nucleation and growth (Carlson, 2011), fluid-

infiltration events (King et al., 2004; Li et al., 2013) and timescales of peak metamorphic heating, burial/exhumation and retrogression (Caddick et al., 2010; Skora et al., 2009).

In particular, crucial information can be retrieved by studying special garnet compositional zoning, e.g. (i) oscillatory/rhythmic zoning of major elements recording fluid infiltration or subtle P-T path perturbations (García-Casco et al., 2002; Li et al., 2013; Schumacher et al., 1999), (ii) healed fracture zoning in major elements related to subduction zone seismicity (Angiboust et al., 2012), (iii) Y+REEs secondary peak zoning revealing major or accessory mineral breakdown (King et al., 2004; Pyle and Spear, 1999; Yang and Rivers, 2003) or diffusion-controlled dynamic growth (Skora et al., 2006).

This study focuses on the evolution of deeply subducted, coesite-bearing oceanic eclogites from the SW-Tianshan UHP metamorphic complex, whose P-T-time evolution was recently reappraised (Tan et al., 2017). In some rocks we noted an unusual garnet zoning with concordant, annular enrichment in Mn, HREEs and Y (Figure 38a-c), but not in other major (Fe, Ca, Mg) or key trace elements (L/MREEs, Ti, Sr, Zr, Sc, Rb and P; Figure 39). Based on Zr-in-rutile thermometry and detailed petrology, geochemical diffusion and thermodynamic modeling, we show that a ~80°C short-lived (~300 kyrs) thermal pulse is required to account for this joint Mn, HREEs & Y enrichment. We then discuss implications for element mobility and transient rock dynamics along a deep cold subduction plate interface.

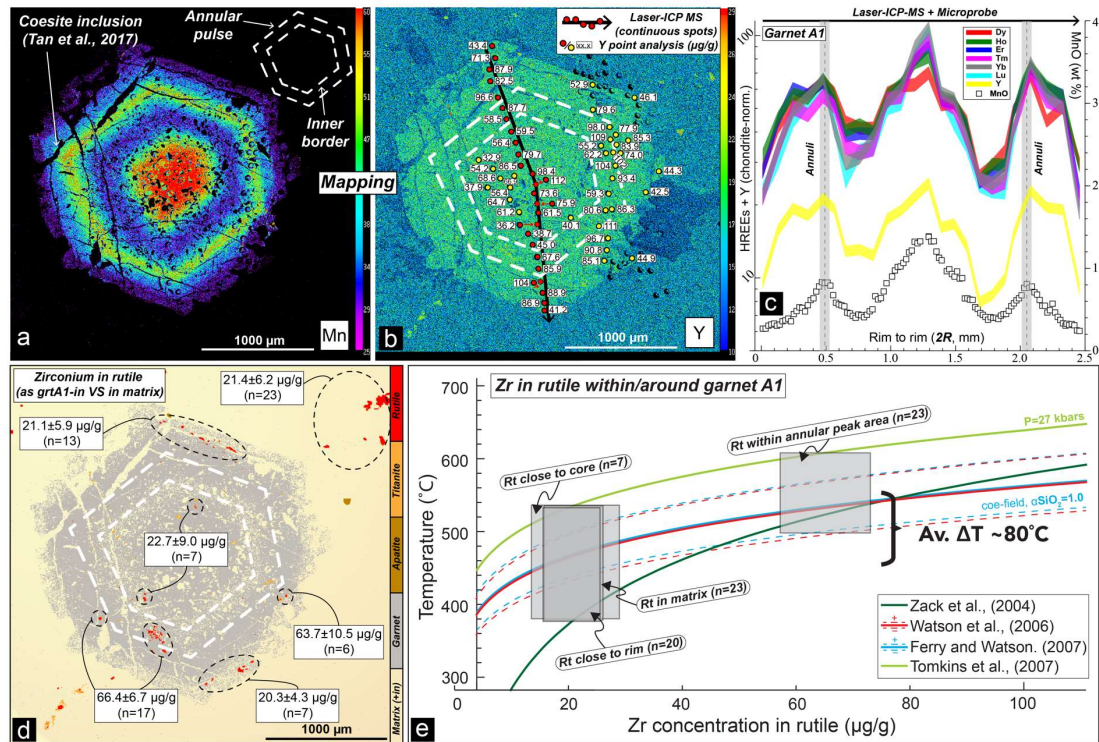


Figure 38: Key features of the specific garnet zoning investigated here, exemplified by garnet A1: (a) Manganese mapping reveals a euhedral annular Mn-rich zone in the mantle of garnet A1, which hosts coesite in its outer rim (Tan et al., 2017); (b) Yttrium laser-ICP-MS points and profile (superimposed on Y mapping, fogged by microprobe detect limitation); (c) Superimposed microprobe and laser-ICP-MS profiles of garnet A1 reveal concordant concentration pulses in Mn, Y and HREEs; (d) Spatial variations of Zr content in rutile grains located within different garnet domains (i.e., inclusions in the core, annular pulse, rim or in the matrix). Skeleton map exported from matrix data of Mn, Y, Ti and P mapping via XMapTools (Lanari et al., 2014); (e) Results of Zr-in-rutile thermometry (Table 13) using four different calibrations, pointing to a ~80 °C thermal pulse.

5.2. Geological setting

The Chinese Southwestern Tianshan HP/UHP-LT metamorphic complex extends for about 200 km along the Southwestern Central Tianshan Suture Zone (SCTSZ; Figure 37a-b). It is correlated with the Atbashi metamorphic complex in the Southwestern Tianshan Accretionary Complex (Hegner et al., 2010) and the Fan-Karategin metamorphic belt (Volkova and Budanov, 1999). The SCTSZ bounds to the north the Chinese section of the HP-UHP/LT metamorphic complex, known as the Akeyazi metamorphic complex (AMC). To the north lies a LP-HT Palaeozoic active

continental margin (Gao et al., 1998), mainly made of amphibolite- and granulite-facies rocks, along with Late Silurian and Early Carboniferous continental arc-type volcanic and volcanoclastic rocks and granitoids (Gao et al., 2009). To the south the AMC is overlain by unmetamorphosed Palaeozoic sedimentary strata, which also represent the northern, passive continental margin of the Tarim plate (Carroll et al., 1995).

The AMC is predominantly composed of strongly schistosed metavolcanoclastics hosting mafic metavolcanics, marble horizons (Bayet et al., 2018) and rare ultramafic rocks as pods, lenses, boudins, thin layers or massive blocks (Gao and Klemd, 2003). The AMC was mainly interpreted as a tectonic *mélange* and thought to have formed in a subduction accretionary wedge during norward subduction of the Southwestern Tianshan Ocean (Gao et al., 1999; Klemd et al., 2014). Whole-rock geochemical data for the mafic metavolcanics suggest oceanic basalt or arc-related affinities (Gao and Klemd, 2003; John et al., 2008).

According to our compilation of regional P-T-time constraints (Tan et al., 2017), most peak metamorphic estimates for eclogites and prograde blueschists yield eclogite-facies HP-LT conditions within the range 480-580°C and 1.5-3.0 GPa. A range of P-T conditions of 450-570°C at 2.7-3.3 GPa was obtained for eclogite-facies micaschists. Evidence for UHP metamorphism comes from both relict coesite inclusions in garnet from several localities (stars in Figure 37b) and thermodynamic calculation. The timing of peak metamorphism falls at 315 ± 5 Myrs, i.e. in a very restricted range with respect to a ~100 Myr-long subduction (Tan et al., 2017; their figures 13, 16). Metavolcanoclastic rocks from SW-Tianshan preserve P-T conditions slightly higher

than most exhumed HP/UHP oceanic units (Agard et al., 2009; Plunder et al., 2015; Figure 37c).

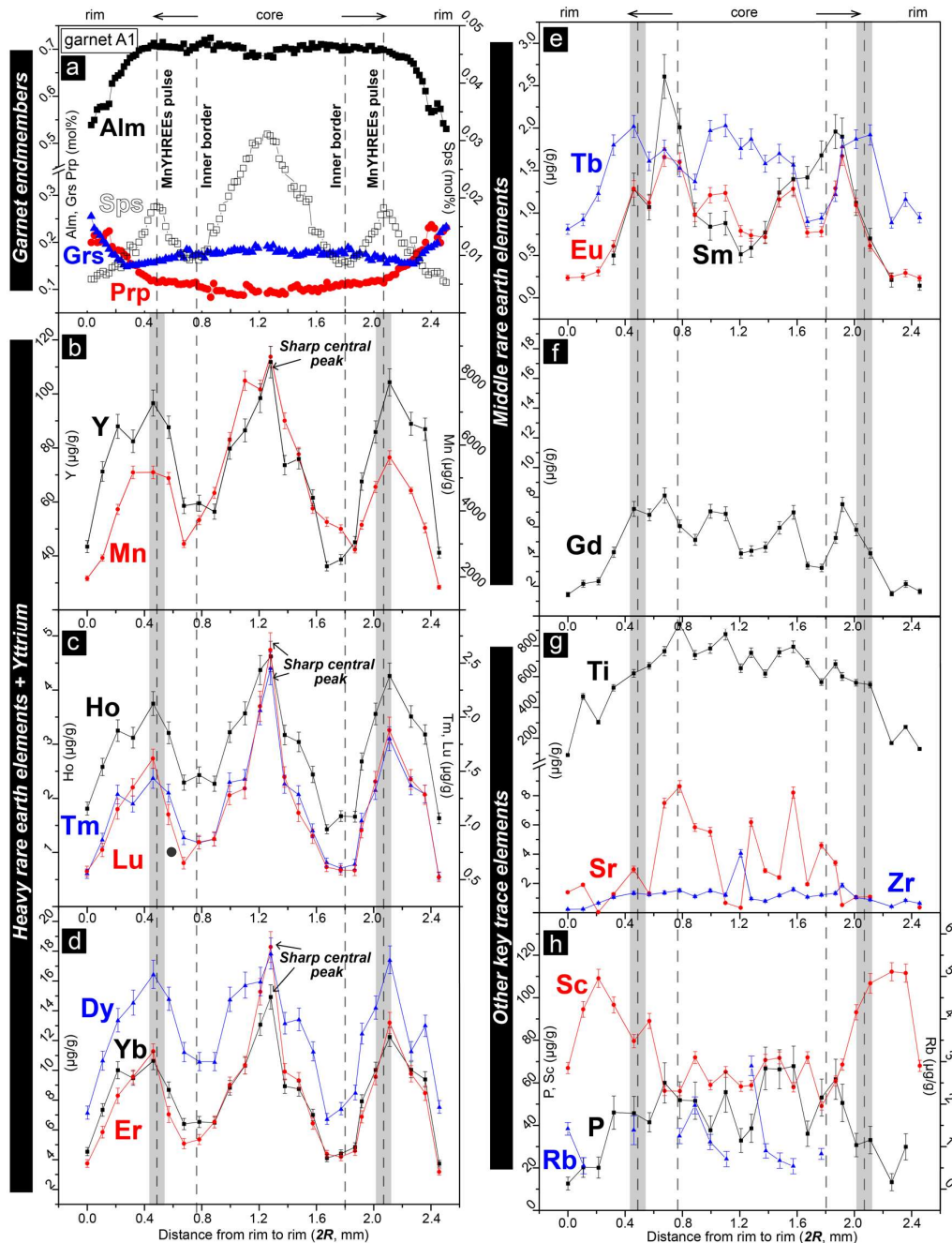


Figure 39: Variations in the concentrations of (a) major divalent cations, (b-d) HREEs and Yttrium, (e-f) MREEs and (g-h) other key trace elements for garnet A1, along the profile shown in Figure 38b. These variations outline the existence of a concordant MnYHREE garnet zoning. Grey vertical overlays mark the location of the secondary peak in Mn concentration (taking into account uncertainties on spot location, ~0.12 mm, during LA-ICP-MS measurement).

5.3. Sample description

Three fresh samples of coesite-bearing UHP eclogite (A, B, C; Figure 37d, 46, 48) were collected from a hm-scale eclogitic mafic slice (in the second eastern tributary up the Atantayi valley; Figure 37b), along adjacent meter thick fresh eclogite layers (Figure 37d; N42°31'57", E81°12'37"; Tan et al., 2017). They mainly consist of garnet, omphacite, glaucophane, phengite/paragonite, epidote/clinozoisite and rutile/titanite in variable amounts (Figure 46, 48). Their N-MORB type bulk-rock compositions, together with analysed $\epsilon\text{Nd}(t) \sim +8.5$ ($t=312$ Ma) and modeled bulk-rock $\delta^{18}\text{O} \sim -8.47\%$, suggest that the protolith was a piece of altered oceanic crust (Tan et al., 2017). Peak burial conditions, in part recorded by garnet compositions, is in the range 470-550 °C, 2.7-3.2 GPa, similar to other reported UHP slices in the region (Tan et al., 2017; their figure 13b).

Garnet occurs as idioblastic porphyroblasts with radius ~ 0.12 -1.58 mm (Figure 46, 48) in the fine-grained omphacite matrix. Garnet size distribution was systematically surveyed for each sample (Figure 48; see Appendix A for details). Garnet cores are generally inclusion-rich and host tiny crystals (~ 5 to 50 μm in diameter, Figure 40c) of omphacite, epidote, chlorite, paragonite, quartz and glaucophane/barroisite (as exemplified by garnet A1; Figure 40c, 46a). Box-shaped inclusions of aggregates of paragonite+epidote (\pm chlorite) are interpreted as pseudomorphs after lawsonite (Tan et al., 2017). Coesite in the mantle of garnet A1 (Figure 38a, 40c) is located immediately outside the annular, concordant MnYHREE pulse (Figure 38a-c). Omphacite occurs as subhedral-anhedral fine grains (~ 0.05 to 0.1 mm across), either as the main matrix

phase or as inclusions in garnet (Figure 40c). Blue-green amphibole is found as glaucophane inclusions in garnet (Figure 40c) and barroisite with glaucophane cores in the matrix. Rutile (Figure 38d, 45a) is present both in garnet porphyroblasts as armored relicts and in the matrix, where partly replaced by titanite. Chlorite is included in or cuts across garnet (Figure 40c, 46a).

5.4. Mineral geochemistry

Systematic major and trace element analyses were performed for garnet of all sizes, for relevant inclusions hosted in garnet (i.e., A1) and for matrix minerals. Representative data are shown in Table 12.

5.4.1. Garnet compositional profile and mapping

Microprobe major element composition profiles and mapping were conducted for eight garnet porphyroblasts representative of the size distribution in the studied eclogites (Figure 46-48). Additional high-resolution mapping for key elements (Mn, Y, Ti and P; Figure 38a-b, 46) and LA-ICP-MS trace element profiles were performed on one coesite-bearing garnet grain (i.e., A1, Figure 38).

4.1.1. Concordant, annular zoning in Mn, Y and HREEs

Garnet growth zoning reveals a concordant pulse in Mn, Y and HREEs concentrations, as shown for garnet porphyroblast A1 in Figure 38, 46, 48. This similarity between Mn, Y and HREEs compositional profiles (Figure 38c, 39) is not observed, however, for the rest of major and trace elements (Figure 39a, e-h).

In detail, Mn, Ho and Dy present relatively wide central peaks ($\sim 1/3$ of garnet diameter, Figure 39b-d; Mn $\sim 6072 \pm 1269 \mu\text{g/g}$; Ho $\sim 3.38 \pm 0.788 \mu\text{g/g}$; Dy $\sim 13.9 \pm 2.74 \mu\text{g/g}$; Table 12) compared to the rest of HREEs (i.e., Tm, Er, Lu and Yb) and Y ($\sim 1/9$ of the diameter; Figure 39b-d; Tm $\sim 1.56 \pm 4.55 \mu\text{g/g}$; Er $\sim 10.0 \pm 2.64 \mu\text{g/g}$; Lu $\sim 1.54 \pm 0.535 \mu\text{g/g}$; Yb $\sim 11.2 \pm 3.58 \mu\text{g/g}$, Table 12). A secondary peak is observed at a rather constant $\text{core}_{\text{peak}}\text{-secondary}_{\text{peak}}$ distance ($\sim 0.77 \pm 0.06$ mm for garnet A1, considering uncertainties from LA-ICP-MS analyses spots interval ca. 0.12 mm; Figure 38c) before the outermost rim is depleted again to approximately $1/5$ to $1/3$ of the absolute concentrations with respect to their core peaks (Figure 39, Table 12). Note that only punctual Y concentrations determined by LA-ICP-MS analyses are shown in Figure 38b since concentrations of ~ 40 to $110 \mu\text{g/g}$ are too low to be detected by microprobe analyses.

In contrast, neither central nor secondary peaks can be observed on the profiles and mapping of other garnet major components (i.e., Fe, Mg and Ca; Figure 39a, 45c-d). The X_{grs} (mol % of grossular) gradually decreases from $0.18\sim 0.20$ to $0.15\sim 0.16$ then increases to $0.22\sim 0.24$ in the outermost rim, while the X_{prp} monotonously increases from $0.09\sim 0.10$ to $0.22\sim 0.23$ but shows minor oscillations at the outermost rim (Figure 39). The X_{alm} evolution is quite simple with almost constant values from core to mantle (i.e., $0.67\sim 0.7$), then gradually decreases to $0.54\sim 0.57$ at the outermost rim (with a small near-edge plateau; Figure 39).

Compositional profiles of MREEs and key trace elements (most LREEs analyses are below detect limitation; Table 12) also largely differ from the MnYHREE zoning

(Figure 39e-h). None of the central peaks can be identified (e.g., Sm and Eu are even depleted in the core; Figure 39e). Secondary peaks can be noticed among the profiles of some elements (e.g., Sc, Sm), but their position varies for each element. Ti and P mapping (Figure 45a-b) suggests joint growth of garnet with Ti- and P-bearing phases.

4.1.2. Concordant Mn pulse among diverse size garnets

Eight representative garnet grains from samples A-B-C were selected for detailed compositional investigations (garnets A1-2-3, B1-2-3-4, C1, ranging from 0.35 to 1.58 mm in radius), based on an extensive garnet size survey (Figure 48). Mn profiles vary with respect to garnet radius (Figure 40a-b): (i) large garnet grains (A1 ~1.22mm; A2 ~1.11mm; B1: ~1.58mm; B2: ~0.90mm; C1: ~1.12mm) show marked central peaks and symmetrical secondary peaks; (ii) middle-size garnet grains of (A3: ~0.42mm; B3: ~0.51mm) show depleted cores with moderate secondary peaks yet Mn concentrations comparable to the large ones (c_{Mn} ~0.66 to 0.72 wt%); (iii) the small garnet B4 (R ~0.35mm) shows a central peak with Mn concentration comparable to secondary peaks of larger garnets (c_{Mn} ~0.75 wt%). $Core_{peak}$ - $secondary_{peak}$ distances are remarkably similar among large garnets at $\sim 0.77 \pm 0.04$ mm ($n=7$, 1σ). Mn secondary peaks coincide with a euhedral garnet growth zone (Figure 38a, 47).

These relationships between garnet size and Mn zoning suggest that large garnets nucleated almost simultaneously, before middle and then small garnets, explaining a different record of yet similar MnYHREE enrichment. The fact that this is observed for samples meters apart (Figure 37d) suggests the existence of an external control (at outcrop- or km-scale) on diffusion-controlled nucleation and growth mechanism.

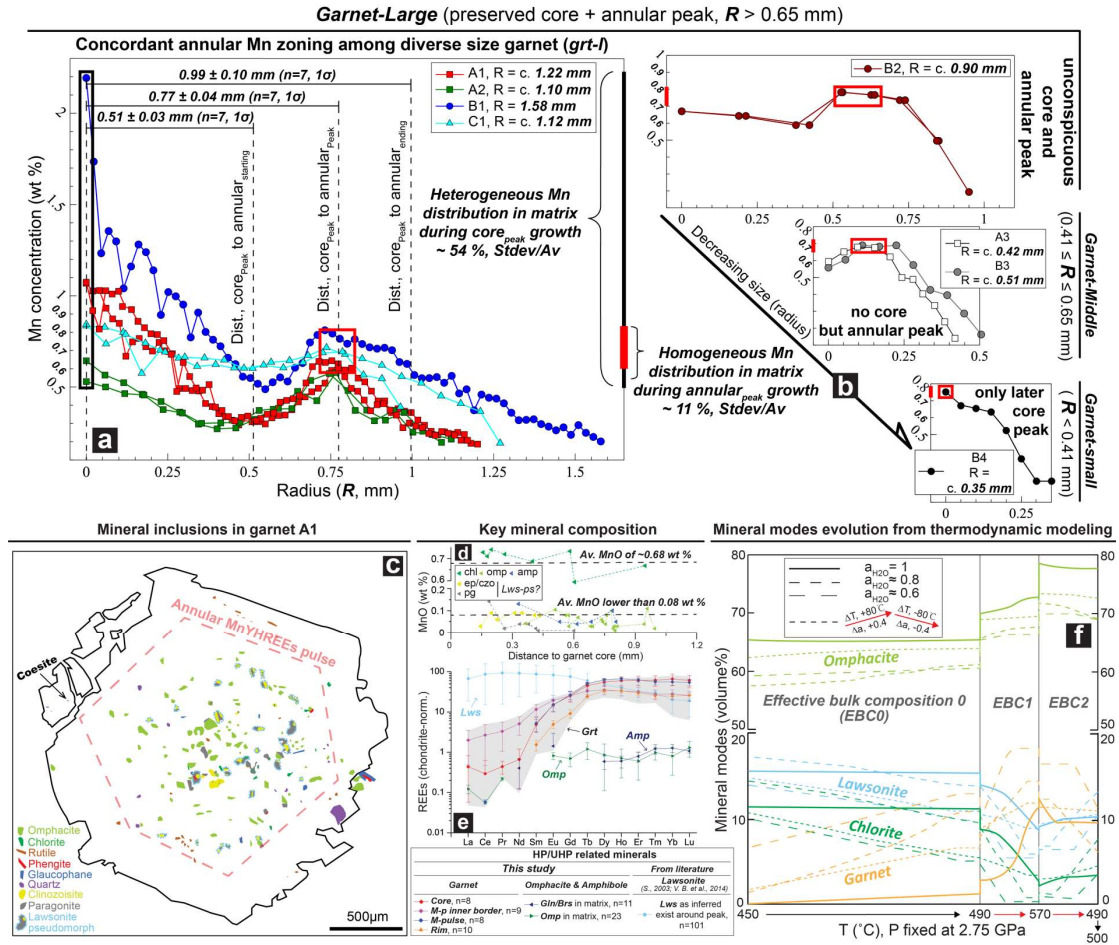


Figure 40: (a-b) Mn concentration profiles for diverse sized garnets. Large garnet grains display a variably high Mn core peak and an annular secondary peak (except B2), with similar corepeak-annularpeak distance ($R_p \sim 0.77 \pm 0.04$ mm; $n=7$, 1σ). Middle size garnet grains (A3, B3) display an annular peak with depleted core, and small garnet grains (e.g., B4) only a core peak. These patterns are more readily observed in element maps (Figure 47); (c) Map of inclusions hosted in garnet A1; (d-e) MnO concentrations and REEs patterns of key mineral inclusions in garnet A1, showing that chlorite and lawsonite represent potential budgets of Mn and HREEs; (f) Evolution of mineral modes predicted by *Perple_X* thermodynamic modeling on stepwise fractionated effective bulk rock compositions (EBCs, Figure 49, Table 11) along different activity and/or temperature paths. Modelling shows that garnet growth coincides with a certain amount of chlorite and/or lawsonite breakdown. Major and trace elements composition of lawsonite were cited from literature (Spandler et al., 2003; Vitale Brovarone et al., 2014).

5.4.2. Major/trace elements composition of associated minerals

In order to assess the potential mass contribution of Mn, Y and HREEs from associated minerals to investigated unusual garnet zonation, major and trace elements analyses were performed for minerals either included in garnet A1 (i.e., omphacite,

amphibole, chlorite, rutile and box-shape paragonite + epidote; Figure 40c) or in the adjacent matrix. Representative compositions are listed in Table 12.

Chlorite inclusions show the highest average MnO concentrations, ~0.68 wt% (n=8, Figure 40d, Table 12), i.e. ~60% of garnet core values (Table 12). Other minerals show variable but insignificant MnO amounts <0.08 wt% (Figure 40d, Table 12).

Since omphacite and amphibole inclusions are too small for LA-ICP-MS analyses (~5 to 50 μ m in diameter, Figure 40c), trace element compositions for them are those of matrix minerals. Due to the lack of fresh lawsonite in our samples (fresh lawsonite in the region appears as inclusions in, e.g., quartz and pyrite. Du et al., 2011; Du et al., 2014; Li et al., 2013), literature data are used here (Spandler et al., 2003; Vitale Brovarone et al., 2014).

Lawsonite and analysed garnet domains (i.e., core, mantle-pulse inner border, mantle-pulse and rim domains) show similar HREEs enrichments patterns, with a notable plateau ($(\text{Lu/Tb})_N \sim 0.32\text{-}1.35$, Table 12) forty to eighty higher than that of chondrite ($\sum\text{HREEs}+\text{Y} \sim 69.5\text{-}123$, Figure 40e, Table 12). Lawsonite, however, has much higher concentrations of LREEs, and to a lesser extent MREEs, than garnet. Omphacite and amphibole display REEs patterns quite comparable to chondrite in HREEs and Y (Figure 40e).

5.4.3. Trace elements composition of rutile and Zr-in-rutile thermometry

Rutile is either found as anhedral inclusions in garnet (ca. 5 to 30 μ m in diameter) or armored by omphacite in the matrix (Figure 38d, 45a). Concentrations of Zr, V, Cr, Nb, Si, Fe and Al were estimated by EPMA following the procedure of Zack et al.

(2004), avoiding potential relicts of pre-existing Zr-rich phases along grain margins (e.g., ilmenite, Austrheim et al., 2008) and contamination from host minerals (i.e., Si concentrations >200 $\mu\text{g/g}$ were discarded). Results are listed in Table 13. Average concentrations of V, Cr and Nb in rutile grains show no correlation with garnet zoning and fall broadly within the range reported for eclogites of the same region (i.e., 1000~2200, 250~1000 and 30~110 $\mu\text{g/g}$; Chen et al., 2012; Li et al., 2013; Zhang et al., 2016).

By contrast, concentrations of Zr in rutile show a specific trend with respect to garnet zoning (Figure 38d). Concentrations close to the core and rim of garnet A1 and in matrix are approximately the same, respectively 22.7 ± 8.96 (n=7), 20.3 ± 5.93 (n=20) and 21.4 ± 6.19 (n=23) $\mu\text{g/g}$, while inclusions within (or close to) the annular domain of MnYHREE enrichment yield almost three-times higher values, of 66.4 ± 6.71 (n=17) and 63.7 ± 10.5 (n=6) $\mu\text{g/g}$.

Four commonly applied calibrations (Ferry and Watson, 2007; Tomkins et al., 2007; Watson et al., 2006; Zack et al., 2004) were used to estimate temperatures from Zr concentrations in rutile (Table 13). Assumptions of $P=27$ kbars (for the calibration of Tomkins et al., 2007) and $a_{\text{SiO}_2}=1$ (Ferry and Watson, 2007) are justified by P-T estimates and the presence of coesite inclusions next to the mantle garnet A1 (Fig. 2a; Tan et al., 2017). Temperature estimates (Figure 38e) for core, rim and matrix range from ca. 380 to 540 $^{\circ}\text{C}$, while rutile grains adjacent to the annular MnYHREE pulse yield ~ 80 $^{\circ}\text{C}$ higher temperature estimates, whatever the calibration (Figure 38e).

5.5. Thermodynamic modeling

Thermodynamic modelling was used to predict the evolution of mineral modes during garnet growth (notably chlorite and lawsonite; Figure 40d-e) and evaluate their impact as a source and/or local buffer on the Mn, Y and HREEs budget of the rock. In order to account for element fractionation during garnet growth, three pseudosections were calculated based on evolving effective bulk rock compositions (EBC0-1-2; Figure 40f, Table 11). The evolution of relevant mineral modes was calculated along a pressure-constant heating path (Figure 40f), starting from 450 °C to 490 °C, followed by a transient 80 °C T pulse (to 580 °C), then later heating to 500°C, broadly consistent with regional $T_{\max} \sim 500\text{-}600$ °C by Zr-in-rutile and RSCM thermometers (Bayet et al., 2018; Chen et al., 2012; Meyer et al., 2016). Details on effective bulk rock compositions (EBCs), K_D^E estimates and related pre-settings are given in Appendix A (see also Table 11 for EBCs).

Calculations were performed for different water activity scenarios. Under water-saturated conditions (i.e., $\alpha_{\text{H}_2\text{O}} = 1$), moderate amounts of chlorite and lawsonite (~ca. 4-5 vol %) break down during the T pulse (for similar eclogite-facies dehydration see Groppo and Castelli, 2010; Martin et al., 2014; Tsujimori and Ernst, 2013; Vitale Brovarone et al., 2014). For a lower water activity of 0.8, chlorite and lawsonite breakdown increases slightly to ca. 6-7 vol %. Additional chlorite and lawsonite could break down before the T pulse for a water activity down to ~0.6. In the scenario where the T pulse coincides with a change in $\alpha_{\text{H}_2\text{O}}$ (i.e., from 0.6 to 1.0 on heating, and 1.0 to

0.6 on cooling), the extent of chlorite and lawsonite breakdown can be quite limited around 1-1.5 vol % (Figure 40f).

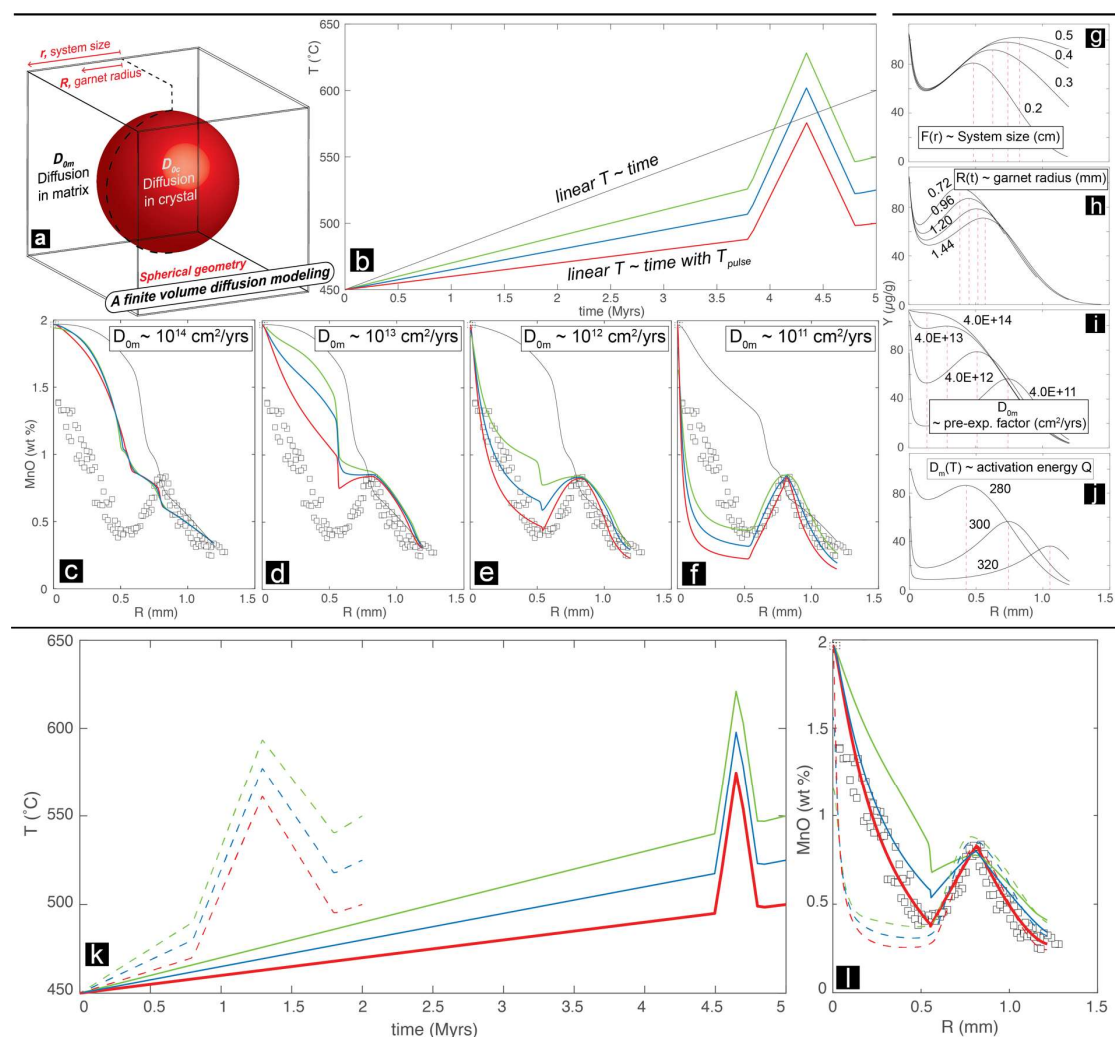


Figure 41: Influence of key parameters on diffusion-controlled garnet growth. (a) Sketch depicting the spherical geometry, finite system size and diffusion in both the crystal and matrix considered by Hesse (2012), after which modelling is performed (see App. B for details). (b) Linear (black) or pulse-like (color) T -time paths with variable T_{final} . (c-f) Tests exploring the range of plausible pre-exponential D_{0m} values needed to match the Mn garnet concentration profile. (g-j) Influence of key parameters on the possibility to produce secondary concentration pulse (Y is here taken as example), along a linear T -time path (black line in Figure 42b). (k-l) Modelled Mn concentration profiles for different T -time paths and durations for fixed D_{0m} ($\sim 10^{12}$ cm²/yrs). The best-fit is obtained for a transient thermal excursion of ~ 0.3 Myrs (out of 5 Myrs; red-line). Parameters and details are given in Table 14.

5.6. Diffusion modeling

Diffusion modeling (Figure 41) is herein used to evaluate the conditions required to match the concordant MnYHREE enrichment during the $\sim 80^\circ\text{C}$ T pulse revealed by petrological data. Details of diffusion modeling are presented in Appendix B.

Skora et al. (2006) explained the existence of central peaks or annular maxima in garnet (for both Y and HREEs, but spatially discordant) by thermally accelerated diffusion REE uptake in the surrounding matrix, assuming a constant crystal growth rate and a non-linear T increase. Similar crystal diffusion modelling was performed with a prescribed interface velocity/growth rate, instead of calculated as part of the solution (Alexander, 2011; Ketcham and Carlson, 2012; Watson and Müller, 2009). However, porphyroblast growth rate depends on the exact growth mechanism (Ague and Carlson, 2013; Carlson, 1989) and on the competition between crystals interacting during diffusion-controlled growth, suggesting time-dependent growth rates with an important stochastic component (Carlson, 2011; Hesse, 2012). A time- dependent growth rate (see App. B) is therefore applied throughout the diffusion modeling (except for the parametric study performed with a linear T-t path and growth rate: Figure 41b, g-j).

5.6.1. Influence of key parameters (for a linear T-t path)

The key input parameters, i.e. system size (r), garnet radius (R_f), pre-exponential factor (D_{0m}) of diffusion coefficient in matrix and activation energy (Q_m), were first tested along a linear T-time path (450 to 600 °C in 5 Myrs: black line in Figure 41b) to evaluate their impact on the existence and location of trace element peaks, using Y as a reference (Figure 41g-j; Table 14).

Increasing system size (r) from 0.2 to 0.5 cm (Figure 41g) can lead to an outward shift of the annular Y peak of ~0.35 mm (i.e. ~1/4 of fixed garnet radius, Table 14). Increasing the garnet radius (R_f) from 0.72 to 1.44 mm (Figure 41h) will also produce

an outward shift of ca. 0.20 mm. However, changing the pre-exponential factor (D_{0m}) and activation energy (Q_m) results in larger shifts around 0.60-0.65 mm (1/2 of fixed garnet radius, Table 14), for $D_{0m} \in [4.0 \times 10^{11} \text{ to } 4.0 \times 10^{14} \text{ cm}^2/\text{yrs}]$ or $Q_m \in [320 \text{ to } 280 \text{ kJ/mol}]$.

More importantly, these diagrams illustrate the large shifts in peak location predicted from linearly $T \sim \text{time}$ path (with linear $R \sim \text{time}$ growth law; i.e., $n=1$ for Eq. (7a) in App. B.), depend on modeled system/crystal scales (i.e., r and R_f) and intrinsic differences of D_{0m} and Q_m thermodynamic properties among elements (e.g. Mn, HREEs+Y). As a result, chances of producing spatially concordant pulses in Mn, Y and HREEs among diverse size garnets and distinct samples are very limited (Figure 38, 39).

5.6.2. Parameter space and boundary conditions

Diffusion-controlled garnet growth modeling was performed with the following assumptions and boundary conditions (see Appendix B for further details):

— garnet radius (R_f) strictly follows the measurements of the four large garnets (A1, A2, B1, C1) preserving the whole MnYHREE pulse.

— system size (r) controls the overall element mass balance. Estimating it is difficult because it requires 3D investigation of the nucleation and growth history of the nearest neighbors (Carlson, 2011; Skora et al., 2006). Element accessibility for the earliest-grown (and largest) garnets suggests an initially large system size, decreasing with time as new (relative smaller) garnets nucleate in the vicinity of pre-existing porphyroblasts (Skora et al., 2006). According to our garnet survey (in 2D), the distance

between the nearest neighbors and the large garnet B1 is ca. 0.52 cm (red line in Figure 48), suggesting that the half-distance from center to center to the nearest neighbor is a reasonable estimate for its system size (~ca. 0.26 cm); a similar assumption was made for all garnets.

— the garnet growth rate used here is expressed as a function of the final garnet radius (R_f) and time duration of the various steps of T-t path (t_n , t_p and t_n'). It is neither a linear nor square root function of time, contrary to previous studies (e.g., Baumgartner et al., 2005; Skora et al., 2006; Weare et al., 1976). This assumption allows to reproduce $core_{peak}$ to $secondary_{peak}$ distance and to fit the joint annular MnYHREE pulse observed in any given garnet and the similar Mn zoning among diverse size garnets (taking place at $R_p = 0.077 \pm 0.004$ cm, Figure 40).

— initial element concentrations in the matrix are those of the unfractionated bulk rock composition (i.e., EBC0, calculated by normalized XRF+ICP-MS data, Table 11).

— the activation energy (Q_k) and pre-exponential diffusion factor D_{0k} are theoretically covariant for each element in both the porphyroblast (Q_g , D_{0g} , garnet) and matrix (Q_m , D_{0m} , mainly clinopyroxene) but generally poorly constrained (Brady and Cherniak, 2010) or missing (e.g., in the P-T window considered here, UHP and $T_{max} < 500-600^\circ\text{C}$). For the sake of simplicity, the activation energy is here fixed at ~300 kJ/mol ($Q_g = Q_m$), following experiments for Mn, HREEs & Y diffusivities in garnet/diopside (at ~ca. 1000 °C) giving Q_k ~ca. 220 to 480 kJ/mol (Carlson, 2006; Carlson, 2012; Chu and Ague, 2015; Dimanov and Sautter, 2000; Dimanov and Wiedenbeck, 2006; Van Orman et al., 2001; Van Orman et al., 2002). Similarly, D_{0g}

is set at a fixed 1×10^6 cm²/yrs for Mn, HREEs and Y diffusivities in garnet (yet, at ~ ca. 1000 °C, experiments yield estimates one order of magnitude smaller; Carlson, 2006; Carlson, 2012; Chu and Ague, 2015; Van Orman et al., 2002).

— by contrast, we vary the pre-exponential diffusion factor D_{0m} in the matrix to fit the observed garnet zonation profiles. The fitted D_{0m} hence represents the bulk diffusive response of the matrix to a “sink” or source term for a specific divalent/trivalent cation, and serves as a macroscopic effective property of each sample (i.e., it includes potential effects of the structure of grain boundaries, of porosity, as well as of the conceivable contribution of the trace elements’ accumulation on the grain boundaries and intra-grain diffusion; e.g., Dohmen and Chakraborty, 2003; Ganguly, 2010; Hiraga et al., 2004).

— the duration of investigated garnet A1 growth is set at 5 Myrs, broadly agree with an estimated duration of garnet growth (t_f) of 7.6 ± 6.8 Myrs, inferred from the gap between Lu-Hf and Sm-Nd ages of regional blueschists (Soldner et al., 2016). Relevant boundary conditions for each modeling round are listed in Table 14.

Three distinct T-t trajectories with fixed T_0 (at 450°C; Figure 41b-f) and variable T_f associated with a 80°C T pulse of 1 Myr were tested to evaluate the impact of different T_f (500 to 550°C) and pre-exponential diffusion factors in matrix D_{0m} (8×10^{10} to 8×10^{13} cm²/yrs). The Mn profile of garnet A1 is taken as reference (Figure 41c-f; modeling *Runs 16 to 27*, Table 14). The linear T-t path within 5 Myrs from 450 to 600°C (without 80 °C T pulse in anytime) is used for comparison.

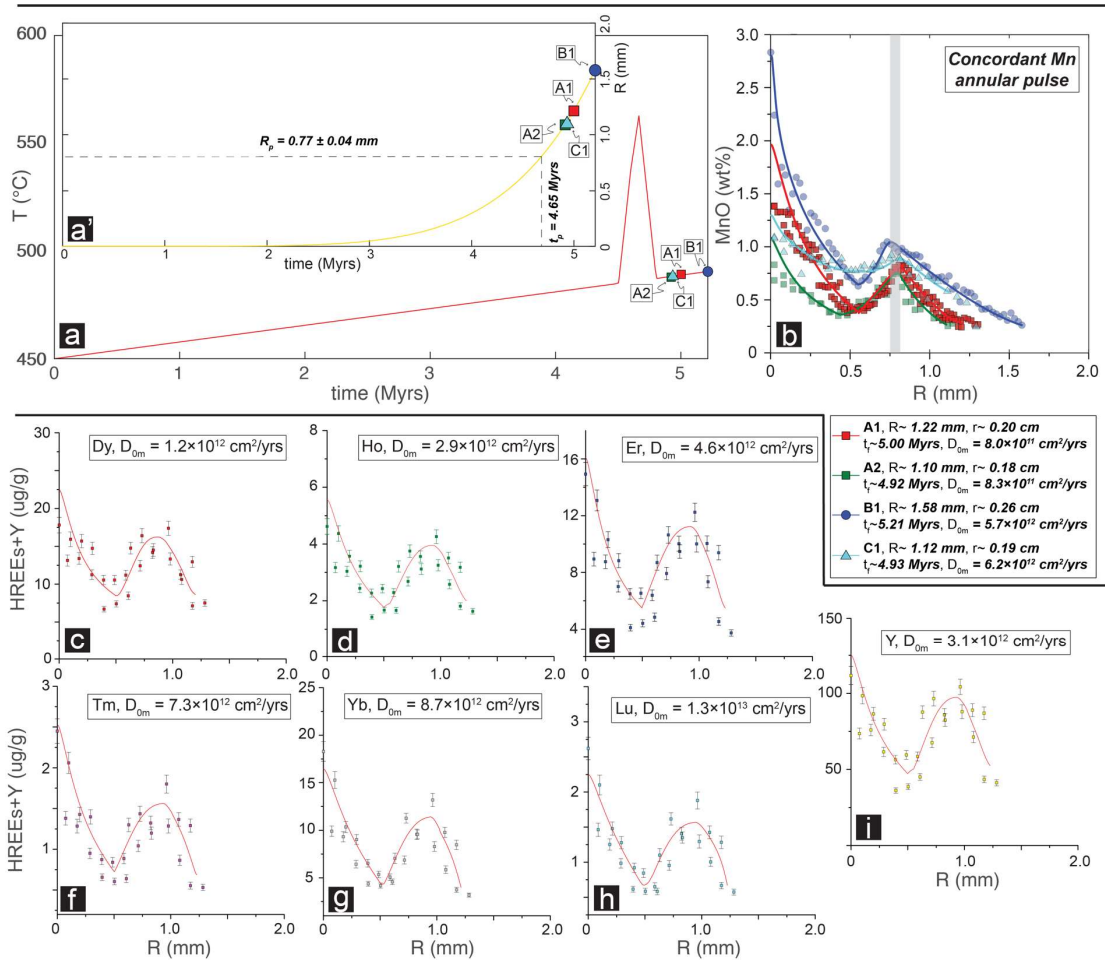


Figure 42: Modelling of the concordant MnYHREE garnet zoning for diverse size garnets and in garnet A1 (Runs 30, 34-36 for a-b; Runs 37-43 for c-i; Table 14). See text for details.

With a relatively fast $D_{0m} \sim 8 \times 10^{13}$ cm²/yrs (Fig. 5c; i.e., a value comparable to experimental constraints at ca. 1000°C for Mn diffusivity in natural diopside, converted with applying $Q_m = 300$ kJ/mol; Dimanov and Sautter, 2000; Dimanov and Wiedenbeck, 2006), no secondary peak is produced, whatever the T-t path and with or without T pulse. All profiles resemble a classical “Rayleigh fractionation” pattern (e.g., Hollister, 1966; Otamendi et al., 2002). Decreasing D_{0m} by one to three log₁₀ units in magnitude (Figure 41d-f) reduces the gap between modeled and observed profiles, especially for the Mn secondary peak (Figure 41e-f). However, depending on D_{0m} , the early part of the modeled Mn profiles, before the secondary peak, may largely deviate from the observed profile. The best fit is observed for D_{0m} of 8×10^{11} cm²/yrs. Further tests

explore the duration of garnet growth (t_f) versus that of the T pulse (t_p ; Figure 41k-l; Runs 28 to 33, Table 14). At fixed $D_{0m} \sim 8 \times 10^{11}$ cm²/yrs, a transient t_p of 0.3 Myrs (t_f set as 5 Myrs) fits measured profiles much better than a longer lived t_p of 1 Myr (t_f set as 2 Myrs).

Overall, the best-fit (red profile in Fig. 41l) is obtained with conditions of $T_f = 500^\circ\text{C}$, $D_{0m} = 8 \times 10^{11}$ cm²/yrs and ~ 5 Myrs t_f accompanied by transient (\sim ca. 1/20 of t_f) $\sim 80^\circ\text{C}$ T pulse (Run 30; Table 14).

5.6.3. Modeling garnet zoning with a transient thermal pulse

Further tests were performed to try and reproduce 1) annular Mn zonation among diverse size garnets and 2) annular joint MnYHREE pulse in garnet A1 under the same scenario.

In order to account for differences in radius and grain distribution in the different samples (i.e., garnets A1-2, B1, C1, Figure 42a), some minor adjustment of the t_f and D_{0m} (for Mn) parameters is needed with respect to those used to best fit Mn zoning in garnet A1 (Figure 41), allowing D_{0m} to vary by less than one order of magnitude only. Best-fit results and fitting parameters are presented in Figure 42a-b. Noteworthy, the similar distance to the annular Mn pulse in the different large garnets (i.e., $R_p \sim 0.77$ mm; Figure 40a, 42a') and timing (i.e., ≈ 4.65 Myrs, based on garnet A1 radius and a 5 Myrs growth duration) logically implies slight different growth durations of diverse size garnets (Figure 42a'; Table 14).

Potential differences in diffusion rate of HREEs and Y in the matrix need to be considered to account for the concordant MnYHREE zoning, since experiments show

that differences in ionic radius amongst the HREEs impact diffusivity in diopside, from Dy to Lu, by $\sim 1 \log_{10}$ unit (converted into $Q = 300 \text{ kJ/mol}$, Van Orman et al., 2001). Additional tests, increasing diffusion rates by about one \log_{10} unit with decreasing ionic radius (Dy to Lu), were therefore applied to obtain best-fit value of D_{0m} for each HREE and Y profile (see Figure 42c-i and Table 14; *Run 37 to 43*).

5.7. Discussion

5.7.1. Interpretation of petrological patterns

Garnet with secondary peak zoning in Mn and/or HREEs (\pm Y) was previously reported in a few studies: 1) partial correlation (with asymmetric peaks) of Mn, Ca, Sc, Zr, Y and M/HREEs attributed to Mn-rich epidote breakdown and/or resorption of garnet (W-Labrador metapelite; Yang and Rivers, 2003); 2) correlated Y, HREEs and Hf peaks in Cignana UHP eclogite attributed to clinozoisite + titanite breakdown (King et al., 2004); 3) positive or negative Ca, Fe and Mg anomalies coincident with (disordered) secondary peaks of MREEs, attributed to element sequestration into garnet cores combined with changes in major garnet-forming reactions (UHP eclogites, WGR Norway; Konrad-Schmolke et al., 2008); 4) oscillatory zoning of Mn decoupled from Fe due to slight fluctuations in decompression rate and P-T path (Schumacher et al., 1999); 5) Mn, Y and REEs multi-secondary peaks possibly linked to externally derived fluids (Franciscan blueschist; Moore et al., 2013). Skora et al. (2006) interpreted their discordant MREE/HREEs mantle maxima garnet zoning in Zermatt-Saas Fee eclogites

as reflecting the interplay between growth and intergranular diffusion rates, hence departing from Rayleigh fractionation.

Yet, none of the specific Mn, HREEs and Y garnet patterns shown here, namely (i) concordant annular zoning in Mn, HREEs & Y (e.g., garnet A1; Figure 38, 39) and (ii) similar Mn zoning amongst diverse sized garnets (Figure 40, 47), was reported so far. Whether this zoning results from a change in source (fluid-mediated or not) and/or in P-T conditions (i.e., a change in diffusion or incorporation properties) needs to be assessed.

The main carriers of L/MREEs (\pm HREEs), Sc, and Sr in blueschists/eclogites (i.e., within the “subduction factory”) are epidote group minerals and lawsonite. Apatite, ilmenite, titanite, rutile and zircon, respectively, serve as important carriers of P + Mn + HREEs, Ti + Mn + REEs, Ti + HREEs and Zr + HREEs (Spandler et al., 2003; Spandler and Pirard, 2013). The lack of corresponding secondary peaks of MREEs and key trace elements (Ti, Sr, Zr, Sc, Rb, P; Figure 39e-h) essentially allows to discard mineral breakdown as a major cause. Furthermore, no breakdown of apatite and titanite/rutile is observed together with garnet growth, as shown by Ti and P mapping (Figure 45a-b).

Predicted amounts of chlorite and lawsonite breakdown accompanying garnet growth along a temperature pulse such as revealed by Zr-in-rutile data (Figure 48d), lie in the range 1.5-7.0 vol % (lws) and 1.0-6.0 vol % (chl), whatever the $a_{\text{H}_2\text{O}}$ value (Figure 40f). Their breakdown predicts a joint supply of major and trace elements with a 40/35/30 wt% increase in L/M/HREEs and 21% in CaO (for lawsonite) and a 11/3/22

wt% increase in MnO, MgO and FeO for chlorite. These joint enrichments conflict, however, with the decoupled trends observed for Fe, Mg, Ca and Mn, HREEs, Y in the various garnet profiles/maps (Figure 38, 39, 47). We therefore conclude that this specific garnet zoning cannot be ascribed to the breakdown of potential Mn- and/or REE-rich major minerals (i.e., epidote, lawsonite, chlorite, apatite, Ti-rich phases). The observation that the metamorphic system remained isotopically closed (Tan et al., 2017) also indicates minimum external fluid infiltration.

Zr concentrations found in rutile grains (Figure 38e, Table 13) match those reported in nearby eclogites (Chen et al., 2012; Li et al., 2013; Zhang et al., 2016). Given the relatively moderate regional T_{\max} (<500-600°C), these Zr signatures can probably be considered as pristine and not affected by later intracrystalline diffusive resetting (Cherniak et al., 2007; Kohn et al., 2016; Penniston-Dorland et al., 2018), thereby providing a faithful record of the temperature evolution. An alternative interpretation could be that the lower Zr concentrations of matrix rutile grains (e.g., ~20 $\mu\text{g/g}$ Zr, Figure 38d-e, Table 13) result from retrograde reequilibration, implying exsolution of high Zr-phases to produce lower-Zr rutile during cooling (Penniston-Dorland et al., 2018). No Zr-bearing phase was however found rimming investigated rutile grains (e.g., zircon, very bright in BSE image, than rutile, Figure 45e-f), strengthening the view that the estimated T pulse of ~80°C is real.

Diffusion-controlled garnet growth under transient thermal excursion

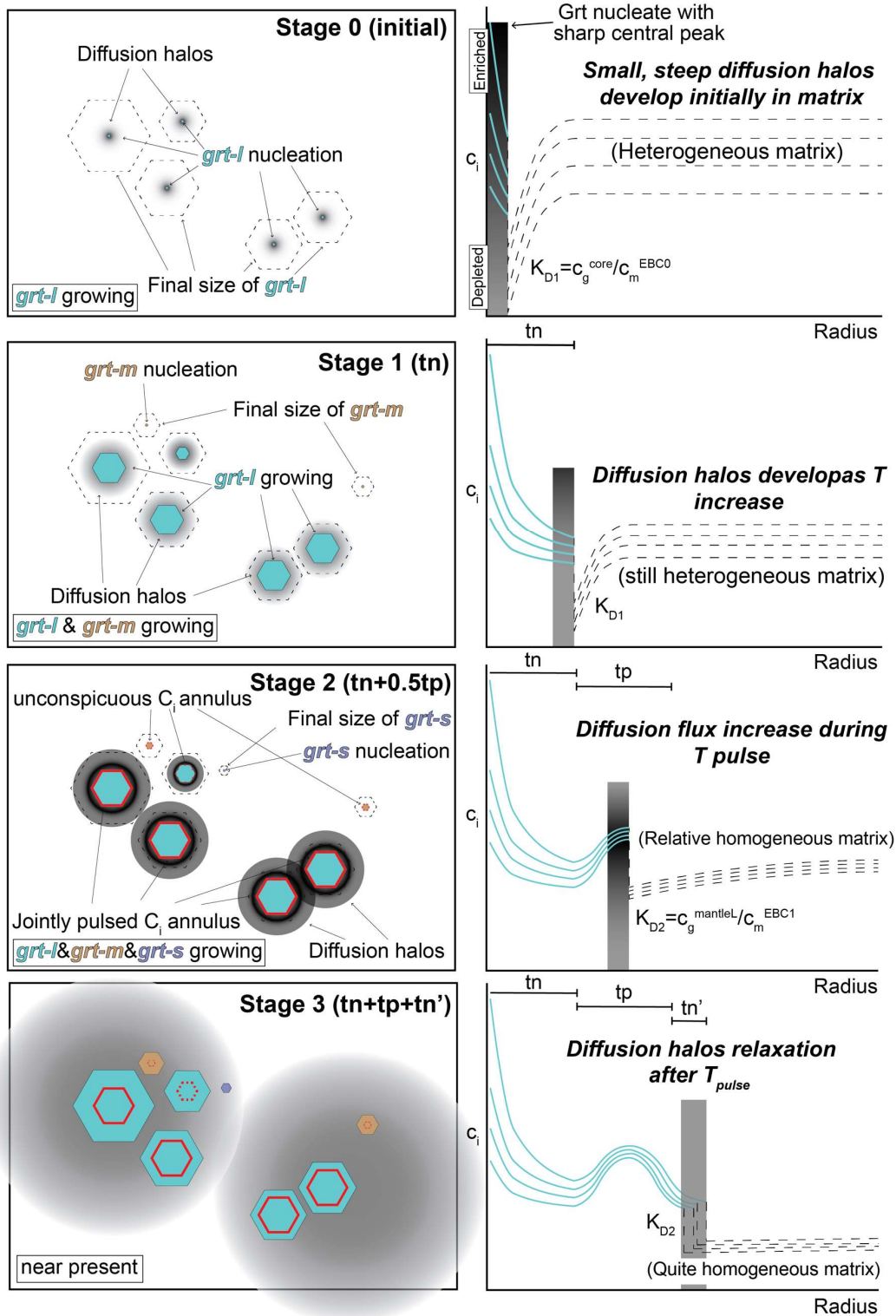


Figure 43: Simplified sketches depicting the impact of diffusion-controlled garnet growth (here during a transient thermal pulse). Left column: growth of diverse size garnets at thin-section scale. The concordant MnYHREE pulse is highlighted as the red-zone. Grey overlays indicate the respective sizes of diffusion halos. Right column: evolution of concentrations as a function of time (or garnet radius).

5.7.2. *Necessity of a transient thermal pulse and implications for thermodynamic modeling*

Control on Y+REEs concentrations in garnet by diffusion through the intergranular medium was first proposed by Skora et al. (2006) and reappraised by Hesse (2012) and Moore et al. (2013). This predicts, however, that the location of Y+REEs (mantle) peaks will differ for each element (Skora et al., 2006; this study; Figs 5g-j) owing to the significant dependence of uptake on competing rates of crystal growth ($R(t)$, Eq. (7)), intergranular diffusion ($D_m(T)$, Eq. (8), Figure 41i), changes in system size (r , Figure 41g), crystal radius (R_f , Figure 41h) and activation energy (Q , Figure 41j).

We herein show that this zoning can nevertheless develop if a specific T-time pulse modifies the rate of intergranular diffusion. T-time paths with a transient ΔT of $\sim 80^\circ\text{C}$ (*Run 16 to 27*, Table 14) indeed allow to satisfactorily model Mn profiles (color lines in Figure 41c-f) at moderate D_{0m} ($8.0 \times 10^{11} \text{cm}^2/\text{yrs}$). Tests were performed for different values of grain size (R_f), growth (t_f) and T pulse durations (t_p) with constant concentration pulse position ($R_p = 0.77 \text{mm}$), range of temperatures (T_f) and pre-exponential diffusion factors (D_{0m}) for intergranular diffusivity. Tests evaluating the interplay of t_f and t_p (Figure 41k-l) argue for the necessity of a transient T pulse with duration $t_p \sim 300 \text{Kyr}$ ($\sim 1/20$ of t_f set as 5 Myrs) to best-fit the observed Mn profile of garnet A1 (*Run 30*, Table 14; red-line, Figure 41l). By contrast, no secondary peaks can be retrieved, even for small D_{0m} (Figure 41f), by applying a linear T-time path with identical growth rate derived from fixed R_p (Eq. (7b)).

The zoning patterns described here reveal an increase in Mn concentration coincident with a temperature increase, which goes against usual thermobarometric inferences (e.g., Baxter et al., 2017; Caddick and Kohn, 2013). Diffusion-controlled garnet growth is generally not considered when applying thermobarometry, however, and this study suggests that care should be taken in directly relating major element zoning with T and P evolutions. The lack of significant zoning in Ca, Fe and Mg associated with the thermal pulse is also surprising: this may indicate that the thermal pulse may have been too short to effectively modify the diffusion of these cations in the system.

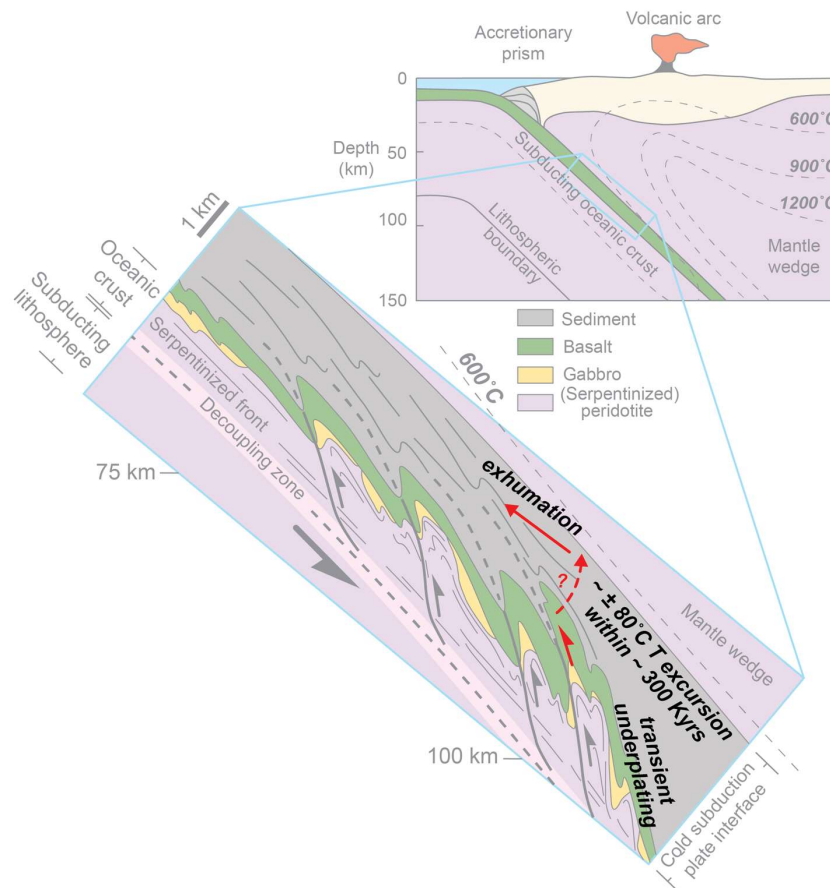


Figure 44: Tentative interpretation of the thermal excursion recorded by the UHP volcanoclastics in terms of rock dynamics along a deep cold subduction plate interface.

5.7.3. Geodynamic significance of a transient thermal pulse

The existence of a transient thermal pulse is identified based on (i) variations in Zr concentration in rutile grains accompanying garnet growth (i.e., $\Delta T \sim 80^\circ\text{C}$) and (ii) modeling of the specific annular MnYHREE zoning through a T-time pulse. This chemical zoning is observed for garnet grains from samples meters apart (Figure 37d), demonstrating that this thermal pulse is at least an outcrop-scale phenomenon. Its spatial extension is in fact probably much larger, since a similar concordant MnYHREE zoning can be observed in eclogites and mafic schists in two adjacent valleys ~ 10 km apart (Klemd et al., 2011: samples FTS9-2 and FTS5-15, their figures 2a-c, 2k-i; annular Mn garnet zoning was also documented in eclogitic mafic boudins ~ 12 km to the east: samples 11-06-5 and 11-06-6, their figures 4d, 4g in Meyer et al., 2016).

Further evidence can thus probably be gathered from the STMB. However, preservation/formation of this type of zoning requires an almost closed system behaviour (which is probably not the case for most samples across the region, as shown by the distributed blueschist/eclogite veins arguing for efficient fluid circulation; e.g., Gao et al., 2007; John et al., 2008; Li et al., 2013), since final patterns of garnet Mn profiles are extremely sensitive to the variation of D_{0m} (Figure 41c-f). Any external supply of Mn, HREEs and Y could similarly boost intergranular diffusivities, thereby hindering the formation of a pulse and producing a monotonic profile (i.e., Rayleigh Fractionation. Hollister, 1966; Otamendi et al., 2002) or oscillatory zoning (Li et al., 2013; Moore et al., 2013).

Several possible explanations can be envisioned for such a thermal transient during deep cold oceanic subduction ($\sim 5^\circ\text{C}/\text{km}$, peak $T < 500\text{-}600^\circ\text{C}$, Bayet et al., 2018; Tan et al., 2017): (i) heat advection from pervasive fluid flow (Ague and Baxter, 2007; Baxter et al., 2002; but magmas are relatively rare during the fate of SW-Tianshan ocean from ca. 320 to 300 Myrs; Gao et al., 2009; Gao et al., 2006; Long et al., 2011) and/or radioactive decay could in principle modify thermal patterns along the subduction interface but are likely $< 30^\circ\text{C}$ (Penniston-Dorland et al., 2015; Royden, 1993); (ii) metamorphic hydration reactions may supply additional energy (Lyubetskaya and Ague, 2009; Penniston-Dorland et al., 2015), but dehydration reactions (of lawsonite and chlorite) are instead predicted across the temperature range (i.e., 490 to 570°C); (iii) shear heating, which is proportional to velocity times rock strength, could in principle modify the thermal budget along the subduction thrust by up to $\sim 200^\circ\text{C}$ (Mako and Caddick, 2017; see discussion in Penniston-Dorland et al., 2015) but will be small in fluid-rich environments. Furthermore, no mylonites/ultramylonites advocating for high strain are observed (but only fine-grained omphacite at the margin of the studied UHP eclogitic slices. Tan et al., 2017) and lattice preferred orientations of omphacite in strained eclogites from exposures ~ 1 km away (Soldner et al., 2016) advocate for maximum strain around peak to early exhumation, hence rather after peak garnet growth. The duration of shear heating would also probably exceed that of the modeled thermal pulse (i.e., ~ 300 Kyrs across 5 Myrs).

Convective motion of subducted material along the plate interface has been proposed based on thermomechanical numerical modeling (e.g., Gerya et al., 2002) and

petrological observations (e.g., Blanco-Quintero et al., 2011). Although tectonic slices rather than mélangé formation characterize the STMB (Bayet et al., 2018; Tan et al., 2017), any fast translation of UHP slices nearer to a relatively hotter mantle wedge (for example following detachment from the slab; Figure 44) might trigger a transient thermal excursion. To match a $\sim 80^{\circ}\text{C}$ thermal pulse a ca. 1-5 cm/yr up-dip movement of detached UHP slices would be required, considering a ~ 3.5 km wide plate interface with a $\sim 150^{\circ}\text{C}$ temperature difference across (Abers, 2005; Gerya et al., 2002; Ruh et al., 2015). So far the (few) estimates for the duration of garnet growth point to Myr scale: 7.55 ± 0.52 Myrs for a single 2.7 cm radius garnet grain by Sm-Nd dating (Austrian Alps; Pollington and Baxter, 2010) and ca. 7 Myrs for a millimeter-scale garnet in HP rocks by combined Sm-Nd and Lu-Hf geochronology (Dabie orogen, Cheng et al., 2008; SW-Tianshan, Soldner et al., 2016), although a geologically surprising 30-40 Myrs duration for UHP eclogitic garnet growth (Lago di Cignana, W-Alps) was inferred by Skora et al. (2009). A transient 1-5 cm/yr movement of UHP eclogitic slices exceeds the average exhumation rate of (U)HP oceanic rocks worldwide ($\sim 1\text{-}5\text{mm/yr}$, Agard et al., 2009) but resembles that of (U)HP continental rocks ($\geq \text{cm/yr}$, Ernst, 2001; Green, 2005; Rubatto and Hermann, 2001). Some numerical models of oceanic crust subduction with fast convergence and steep cold slab show $\sim \text{cm/yr}$ movements during early detachment which could match our observations (12 cm/yr, 60° angle. Ruh et al., 2015).

5.8. Conclusion

Detailed petrological investigations on major and trace elements geochemistry of garnet highlight a concordant annular Mn, Y and HREEs zoning, visible at the outcrop- and probably km-scale, in a representative UHP oceanic eclogitic slice in SW-Tianshan. This pattern coincides with a transient ~ 80 °C increase in temperature revealed by Zr-in-rutile thermometry. Mineral compositions together with thermodynamic modeling indicate that mineral breakdown cannot account alone for this unusual garnet zonation. Diffusion-controlled garnet growth modeling supports the necessity of a ~ 300 kyr transient thermal excursion to reproduce the observed garnet zonation (assuming a 5 Myr duration for the overall garnet growth). Such a transient thermal excursion is tentatively tied to the fast movement of detached UHP oceanic slices towards the hotter mantle wedge. This study also highlights the necessity of considering diffusion-controlled garnet growth whenever assigning major element zoning to specific P-T conditions.

Acknowledgements

This study was essentially funded by the National Natural Science Foundation of China (No. 41390440, 41390445, 41025008) to Prof. Jun Gao and the International Training Network ZIP (Marie Curie Actions, Zooming In-between Plates, REA grant agreement No. 604713) to Prof. Philippe Agard. We would like to thank the editor Prof. Michael James Bickle and anonymous reviewers for their constructive comments that greatly helped in improving the article. We greatly benefitted from discussions with L.

Labrousse, Y. Chen, J-J. Yang, J-L. Li, M. Locatelli and G. Bonnet. We further thank Y. Chen for the support of microprobe mapping in IGGCAS and M. Fialin & N. Rividi for the help of rutile trace elements microprobe analyses in ISTeP.

Appendix A. Thermodynamic modeling for the estimate of mineral modes evolution and effective partition coefficient

Garnet size distribution (Figure 48) was investigated to derive effective bulk rock compositions (EBCs, Figure 49, Table 11), i.e. taking into account progressive garnet fractionation from the whole-rock composition, and to evaluate the evolution of mineral mode (Figure 40f) under a specific P-T loop (i.e., T pulse, Figure 40f). This allows estimating dynamic effective partition coefficient K_D^E of specific elements during the modeling of diffusion-controlled garnet growth (App. B.).

Garnet size distribution (Figure 48) was estimated using Photoshop manual coloring (for each garnet grain) and assuming euhedral garnet ranges from pentagon- to octagon-shape to derive radius (and corresponding uncertainties). Modal proportions of each garnet group (large, middle and small; see main text for grouping strategy and Figure 40a-b, 48) are used to infer approximate volume proportions for EBC calculation.

Using major elements profiles (Figure 40a-b) and mapping (Figure 47), estimates of effective bulk rock compositions are first conducted by defining:

$$V_g = aR_g \tag{1a}$$

$$a = \frac{V_{grt-x}^{measured}}{R_{grt-x}^{max}} \tag{1b}$$

where V_g represents the volume % of garnet during growth, R_g is the radius of garnet (the same as defined in App. B.), while a is the corresponding ratio constant for different garnet groups and will be respectively calculated by $a = V_{grt-x}^{measured} / R_{grt-x}^{max}$ ($grt-x$ subscript refers to the three garnet groups, $V_{grt-x}^{measured}$ is the measured approximate values mentioned above and R_{grt-x}^{max} is the maximum radius of each garnet group; Figure 40, 48). Element concentrations along garnet profiles (i.e., microprobe and laser-ICP-MS results) are converted to volume concentrations and described via polynomial fitting (Figure 49):

$$C_g = f(V_g) \quad (2)$$

where $f_c(V_g)$ represent the fitted polynomial equations for given element concentration profile as a function of V_g . The fractionated mass C_g from the matrix, as a result of garnet growth, can be calculated by integrating $f_c(V_g)$ within the relevant range $V \in [0, V_g]$:

$$C_g = \sum_{V_{grt-x}}^{x=L,M,S} \int_0^{V_{grt-x}} f(V_g) dV \quad (3)$$

Successive fractions were thus subtracted XRF bulk rock composition to account for the growth of garnet core, mantle and rim and estimate EBCs used for thermodynamic and diffusion modelling. Calculated EBCs are shown in Table 11.

Thermodynamic modeling was performed with `Perple_X` (Connolly, 1990, 2005) using successively the unfractionated bulk-rock composition (i.e., EBC0, Table 11) and garnet-fractionated effective bulk rock compositions (EBC1-2, Table 11) to estimate minerals modes along the near-peak prograde path. Pressure is fixed at 2.75 GPa for simplification, and temperature increases from 450 to 500 °C, with a short-lived ~80

°C T excursion. The database and solid solutions are the same as in Tan et al. (2017). Different values of $\alpha_{\text{H}_2\text{O}}$ (Figure 40f), as well as a temperature-dependent change in $\alpha_{\text{H}_2\text{O}}$, were applied via T- $\alpha_{\text{H}_2\text{O}}$ pseudosections to test its influence on the predicted mineral modes.

Generally, garnet central peak concentrations (of given element) of the profiles were compared to the bulk rock composition to estimate the bulk distribution coefficient K_D (Hollister, 1966), assuming that the effective matrix concentration during garnet growth equals that of the bulk rock composition (Skora et al., 2006). K_D is treated as constant at a given temperature and pressure, for a sufficiently dilute trace component between two phases (e.g., Hesse, 2012; Skora et al., 2006). Two values of effective K_D^E , before and after the concordant pulse in concentrations, were considered (Figure 43):

$$K_D^E = \left(\frac{c_{g-c}^i}{c_{EBC0}^i}; \frac{c_{g-ml}^i}{c_{EBC1}^i} \right) \left(\frac{v_g^i}{v_{EBC0,1}^i} \right)_{(P,T)} \quad (4)$$

where c_{EBC0}^i , c_{EBC1}^i and c_{g-c}^i , c_{g-ml}^i are the concentration of element i , respectively, in effective bulk rock composition and corresponding position from garnet profiles with respect to the representative Mn, Y and HREEs annular zoning of garnet A1 (Figure

40, 49). For simplification, the variable of $\left(\frac{v_g^i}{v_{EBC0,1}^i} \right)_{(P,T)}$, which describe the ratio

between P-T dependent activity coefficients v_g^i and $v_{EBC0,1}^i$, is treated to approach unity. Calculations of initial K_D (i.e., $\frac{c_{g-c}^i}{c_{EBC0}^i}$) will be particular sensitive to

uncertainties in the location of the central cuts with respect to garnet cores. Potentially

missed central peaks of some garnets were estimated in proportion of the sharp central peak pattern of the largest garnet B1 (for Mn) and relative smaller garnet A1 (for Y, Tm, Lu, Yb and Er). Values of K_D^E for each element are listed in Table 14.

Appendix B. Finite volume diffusion modeling

The finite volume method from Hesse (2012), with spherical geometry in a uniform matrix, is used to compute the diffusion and partitioning of trace elements during porphyroblast growth (Figure 41a). Diffusion on both sides of the moving crystal–matrix interface are explicitly considered in this study (i.e., intragranular and matrix diffusion), whereas most previous studies only consider diffusion in the matrix (e.g., Castro et al., 2008; Skora et al., 2006; Skora et al., 2008; Watkins et al., 2008) or inside the growing porphyroblast (e.g., Alexander, 2011). The motion of the crystal–matrix interface and the thermal evolution are prescribed as time functions. The appropriate conditions for the diffusion flux across the crystal–matrix interface are derived from discrete mass conservation.

The evolution of the concentration profiles is controlled by:

$$\frac{\partial}{\partial t}(r^2 \mathbf{c}_g) + \frac{\partial}{\partial r}(r^2 \mathbf{F}_g(\mathbf{c}_g)) = 0, \text{ on } \Omega_g \in [r_{\min}, R] \times [0, t_f] \quad (1a)$$

$$\frac{\partial}{\partial t}(r^2 \mathbf{c}_m) + \frac{\partial}{\partial r}(r^2 \mathbf{F}_m(\mathbf{c}_m)) = 0, \text{ on } \Omega_m \in [R, r_{\max}] \times [0, t_f] \quad (1b)$$

Where $r^2 \mathbf{c}_k$ and \mathbf{F}_k represent the accumulation and the diffusive flux of the trace element in the k-phase. The phase subscript g refers to garnet and m to the matrix.

The exponential factor 2 on r reflects the radial dependence of volume and area in spherical coordinates. The Diffusive flux \mathbf{F}_k in k-phase is defined by:

$$F_k = -D_k \frac{\partial C_k}{\partial r} \quad (2)$$

Where D_k is the diffusion coefficient in k-phase, and initial conditions in each spatial domain are given by:

$$c_g(r, 0) = c_g^0, \text{ on } \Omega_g \in [r_{\min}, R] \quad (3a)$$

$$c_m(r, 0) = c_m^0, \text{ on } \Omega_m \in [R, r_{\max}] \quad (3b)$$

Four boundary conditions are required. Two are at the internal interface R (i.e., garnet radius, Figure 41a) and the other two are at the outer boundaries of the domain r (i.e., system size, Figure 41a). Hesse (2012) assumed that concentration profiles are symmetric across the center of the porphyroblast and that the matrix surrounding it acts as a closed system, so that:

$$F_g(r_{\min}) = F_m(r_{\max}) = 0 \quad (4)$$

At the moving internal boundary during modeling, the diffusive flux F_l across the porphyroblast interface is continuous while the concentration profile is discontinuous because of the partitioning of trace elements, controlled by the effective partition coefficient $c_g = K_D^E c_m$ (also see App. A. for the definition and estimates of K_D^E). The conditions at the interface are therefore described as:

$$\lim_{r \rightarrow R^-} F_g(r) = \lim_{r \rightarrow R^+} F_m(r) = F_l(R) \quad (5a)$$

$$\lim_{r \rightarrow R^-} c_g(r) = K_D^E \lim_{r \rightarrow R^+} c_m(r) \quad (5b)$$

While $T(t)$ and $R(t)$ are described by power-laws functions with preset exponential factors by Hesse (2012), these were modified here to test the impact of a thermal pulse on MnYHREE garnet zoning. $T(t)$ is therefore computed as:

$$= \frac{(T_f - T_0)t}{t_n + t_p + t_n} + T_0, t \in [0, t_n] \quad (6a)$$

$$= \left(\frac{T_f - T_0}{t_n + t_p + t_{n'}} + \frac{2\Delta T_p}{t_p} \right) t + T_0 - \frac{2\Delta T_p t_n}{t_p}, \quad t \in [t_n, t_n + \frac{1}{2}t_p] \quad (6b)$$

$$= - \left(\frac{T_f - T_0}{t_n + t_p + t_{n'}} + \frac{2\Delta T_p}{t_p} \right) t + T_0 + \frac{2(T_f - T_0)(t_n + t_p)}{t_n + t_p + t_{n'}} + \frac{2\Delta T_p(t_n + t_p)}{t_p}, \quad t \in [t_n, t_n + t_p] \quad (6c)$$

$$= \frac{(T_f - T_0)t}{t_n + t_p + t_{n'}} + T_0, \quad t \in [t_n + t_p, t_n + t_p + t_{n'}] \quad (6d)$$

Where T_0 and T_f represent the initial and final value at $t = 0$ and $t = t_n + t_p + t_{n'}$, respectively. ΔT_p represents the absolute change of temperature during the thermal pulse and is fixed at a constant 80°C following estimates of Zr-in-rutile thermometry (Figure 38, 45, Table 13; Table 14). t_n , t_p and $t_{n'}$ are the variable on different modeling runs for constraining the time duration of processes before (t_{normal}), during (t_{pulse}) and after (t_{normal}) the T pulse. To account for the concordant Mn zoning among diverse size garnets (i.e. at $R_p = 0.77 \pm 0.04$ mm; Figure 40), the garnet growth rate $R(t)$ is computed using a polynomial power-law equation with variable exponent n :

$$R(t) = R_0 + (R_f - R_0) \left(\frac{t}{t_n + t_p + t_{n'}} \right)^n, \quad t \in [0, t_n + t_p + t_{n'}] \quad (7a)$$

$$n = \log_{\left(\frac{t_n + 0.5t_p}{t_n + t_p + t_{n'}} \right)} \left(\frac{R_p - R_0}{R_f - R_0} \right) \quad (7b)$$

Where $R_0 = 0$, and R_f are 1.22, 1.10, 1.58 and 1.12 mm respectively (for A1-2, B1 and C1 garnets; Figure 40, 46). R_p , in contrast, was set constant at 0.77 mm (Figure 40a), except for test calculations performed along an ordinary T-t path (Figure 41b, g-j) for which $R(t)$ follows a linear evolution. Since all garnet growth rates are the same and set to follow that of garnet A1 (i.e., in Eq (7a); $n=6.34$), slight to moderate differences are predicted for their total growth duration.

The diffusion coefficient of divalent/trivalent cations in matrix and growing porphyroblast is expressed as a function of temperature T by Arrhenius equation:

$$D_k = D_{0k} \exp\left(\frac{-Q_k}{UT}\right) \quad (8)$$

Where D_{0k} is the pre-exponential factor, Q_k is the constant activation energy, U is the universal gas constant, and k is the phase subscript (herein, represent garnet porphyroblast and matrix respectively). In this study, the constant activation energy Q_k will be fixed at 300 kJ/mol (except for benchmarks tests for varying Q_k , Table 14) for simplification since the finite volume model from Hesse (2012) is mostly sensitive to variations on Q_k (Figure 41j). The interested reader is referred to (Hesse, 2012) for further modelling details.

Appendix C. Analytical methods

Major elements electron microprobe analyses and mapping

Most major element compositions of garnet, mineral inclusions and matrix minerals, as well as relevant profiles and mapping analyses, were obtained by electron microprobe analyses at IGGCAS with JEOL JXA 8100 under presettings of wavelength dispersive spectrometers with an acceleration voltage of 15 kV, a beam current of 15 nA, at 1 to 3 μm beam size and 30 s counting time. Additional high resolution Mn, Y, P and Ti mapping for key garnet grain (A1, Figure 38a-b, 45) with 15 kV acceleration voltages and 200 nA beam current under 60 ms dwell time was conducted on CAMECA SX Five FE at IGGCAS. Natural minerals and synthetic oxides were used as standards,

and a program based on the ZAF procedure was used for data correction. Average compositions for mineral chemistry of studied UHP eclogite are presented in Table 12.

Laser-ablation ICP-MS trace elements analyses

In situ trace element point and profile (Figure 38b-c, 39) analyses of zoned garnet and associated matrix mineral were performed by LA-ICP-MS at IGGCAS with a single collector quadrupole Agilent 7500a ICM-MS, equipped with an UP193Fx argon fluoride New Wave Research Excimer laser ablation system. Glass reference material NIST SRM 610 and NIST SRM 612 were used as standards for external calibration. LA-ICP-MS measurements were conducted using a spot size diameter of 60 μm with a laser frequency of 15 Hz and 0.63 GW/cm² and a fluence of 3.32 J/cm². Acquisition time was 20 s for the background and 120 s for the mineral analyses. The Ca-content of garnet determined by EMPA was used as internal standard. Reproducibility and accuracy, which were determined for NIST SRM 610 and NIST SRM 612, are usually <8% and <6%. Trace element concentrations were then calculated using GLITTER Version 3 (Van Achterbergh et al., 1999). Average trace element composition of the relevant garnet domains and associated minerals are given in Table 12, following their microprobe data.

Zirconium contents of rutile electron microprobe analyses

Concentrations of Zirconium in rutile were determined by electron microprobe following the method outlined by Zack et al. (2004), since the size of most rutile euhedral inclusions in garnet A1 (Figure 38d) were too small (ca. 5 to 30 μm in dia., Figure 38d, 45) to be analysed by LA-ICP-MS. All analyses were conducted with a

CAMECA SX Five in ISteP, Sorbonne Université, France. EMPA conditions were optimised so that detect limits on Zr could be improved by four times (20 µg/g compared with 80 µg/g). Acceleration voltage was set at 20 kV with 120 nA beam current and 5 µm beam diameter. A H-type spectrometer was chosen for measuring Zr-L α because of its highest sensitivity for this element. Detailed settings for spectrometers followed the Table 2 of Zack et al. (2004). Every 10 analyses of unknown rutile were bracketed by 2 analyses of synthetic rutile standard for true zero-concentration count rates on the peaks and to exclude any machine drift. Summary of rutile measurements with respect to their location is presented in Table 13.

Supplementary figures and tables

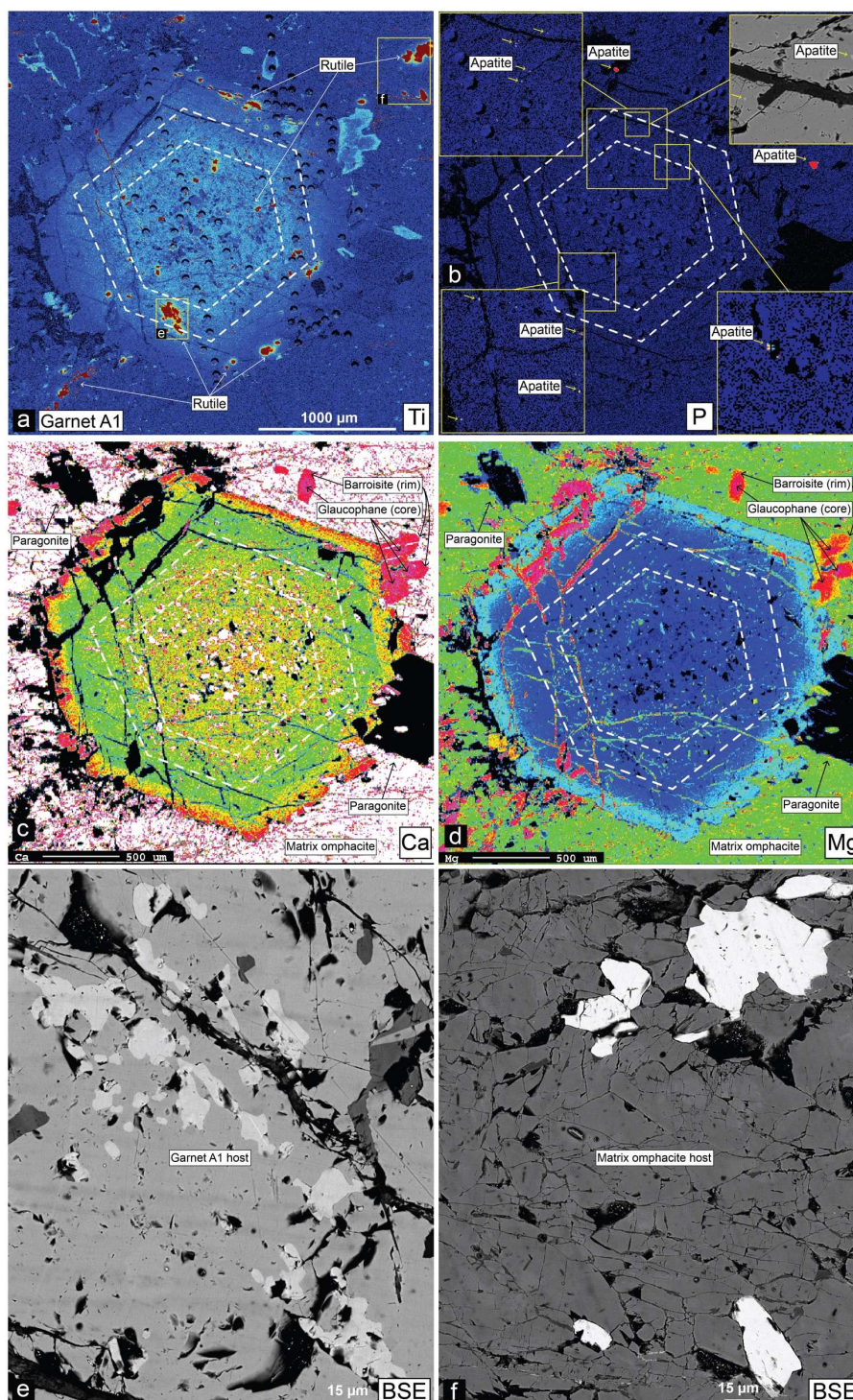


Figure 45: (a) Ti, (b) P, (c) Ca and (d) Mg mapping reveal the relationships between garnet A1 and associated Ti, P, Ca, Mg-bearing inclusion/matrix minerals. The white dash-lines highlight the location of the MnYHREE pulse, after Figure 38a; (e-f) close-up SEM-BSE image of measured rutile grains (corresponding to areas marked by yellow rectangles in Figure 45a) hosted in garnet A1 (e) and in matrix (f). These images indicate that measured rutile grains are mainly host by Zr-free phases (i.e., garnet and omphacite, Table 12), and that no Zr-rich phase can be found rimming rutile (e.g., no zircon, which would be very bright in the BSE image).

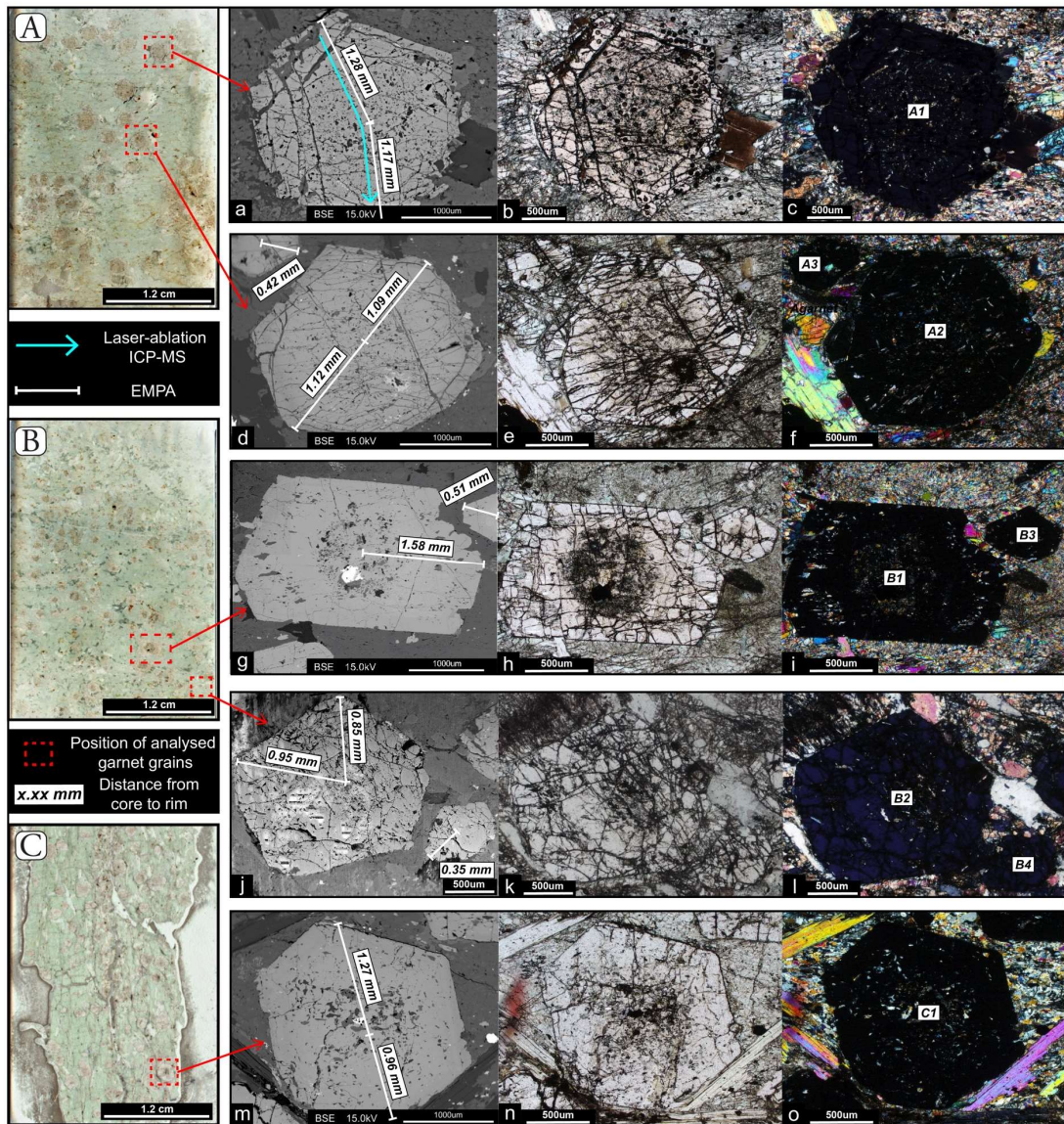


Figure 46: EMPA-BSE, transmitted light and cross-polarized light images of investigated garnet grains (A1-3, B1-4, C1), sampled from different parts of the outcrop (Figure 37d).

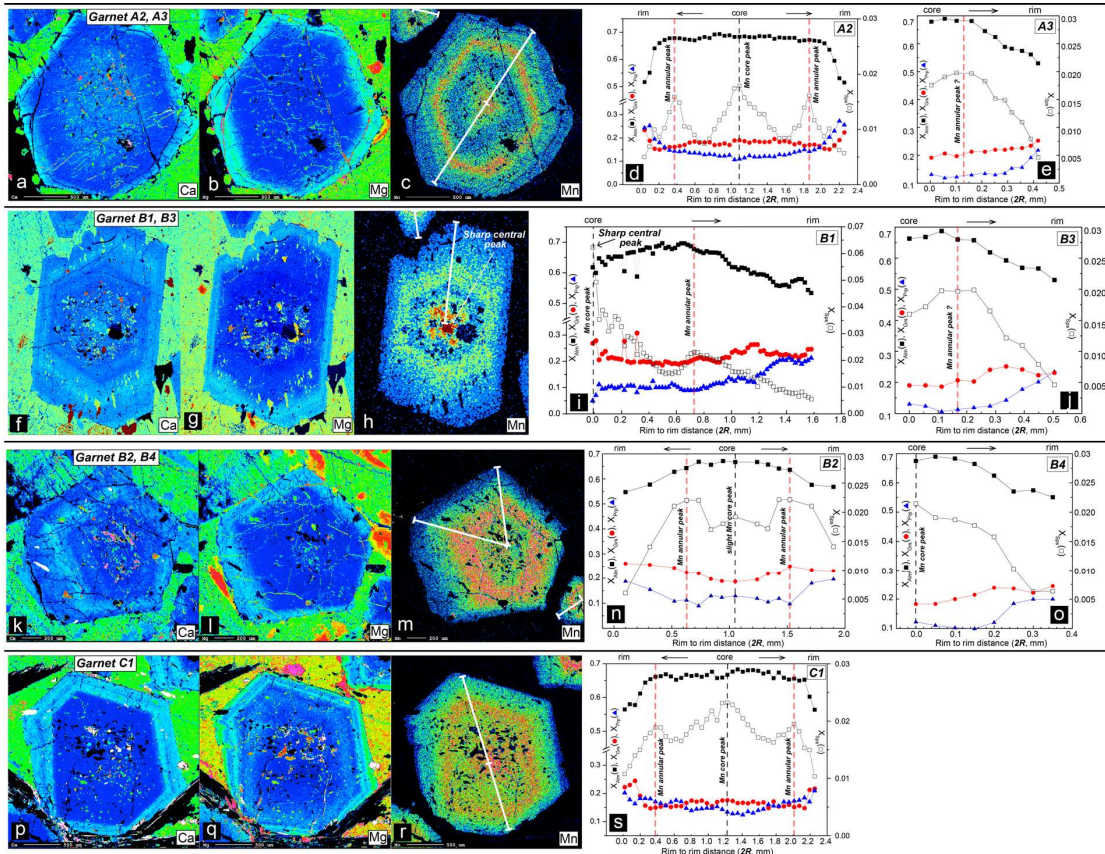


Figure 47: The Ca, Mg and Mn mapping as well as corresponding compositional profiles of the rest of investigated garnet grains (except garnet A1, shown in Figure 38).

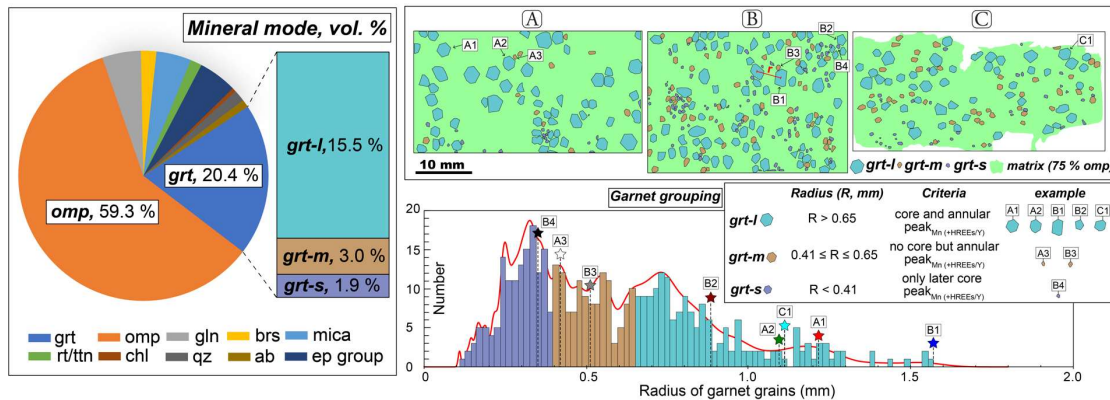


Figure 48: Systematic garnet size survey. The three main groups and estimated mineral modes (vol %) for investigated UHP eclogite samples are shown. See main text for details.

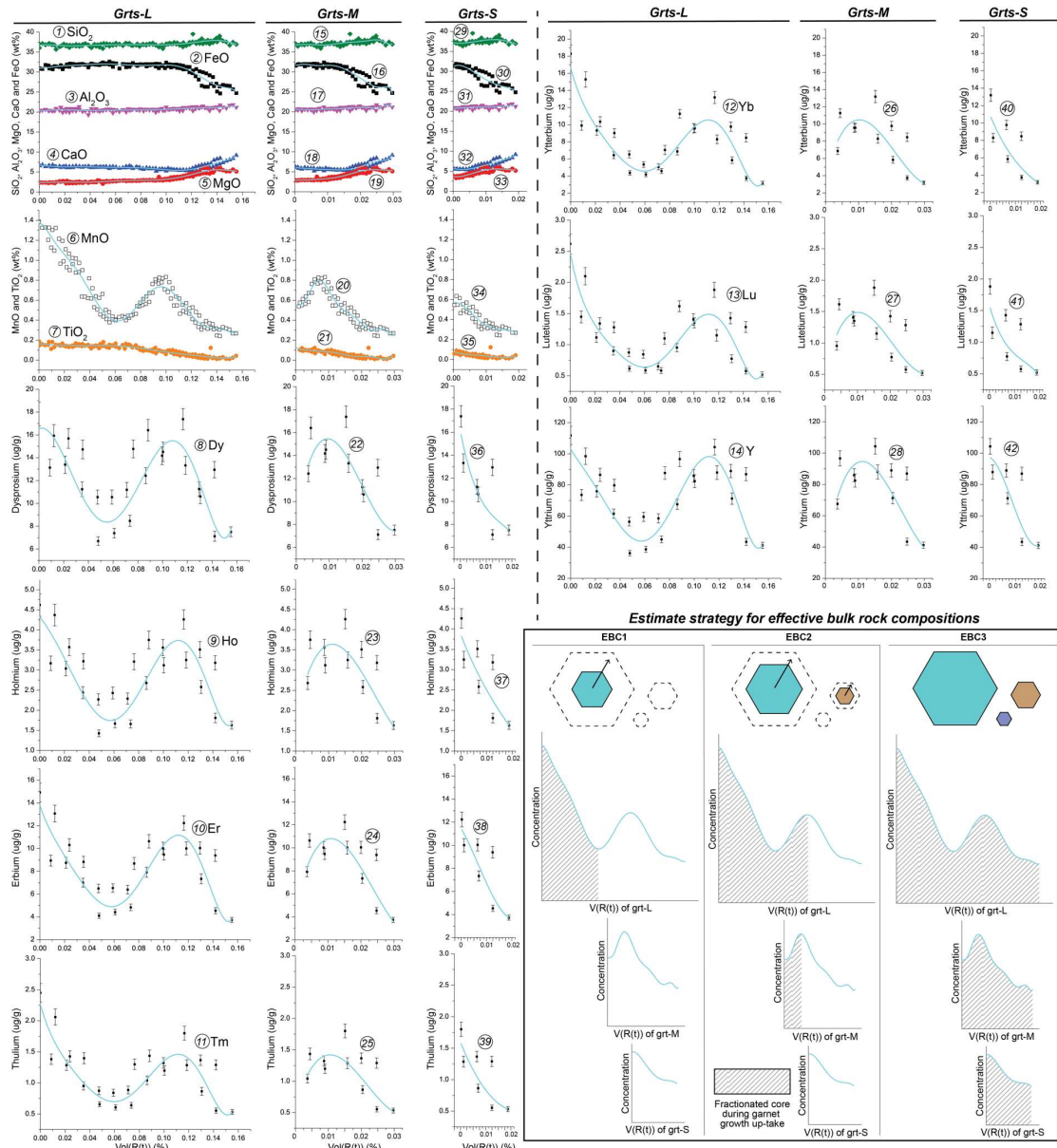


Figure 49: Polynomial fitting for estimating effective bulk rock compositions during garnet growth (and uptake of major elements, HREEs and Y). See Appendix A.

Measured and calculated, fractionated, effective bulk rock compositions								
Lithology		UHP oceanic eclogite AT06						
Method Strategy	XRF+ICP-MS		Effective bulk-rock compositions					
	Bulk-rock composition		For thermodynamic modeling					
	Av.	Std. (n=3)	EBC0	EBC1	EBC2	EBC3		
Major oxides (wt %)	SiO ₂	47.9	0.3	49.9	51.1	52.0	54.1	
	TiO ₂	0.913	0.084	0.951	1.02	1.06	1.19	
	Al ₂ O ₃	14.4	0.527	15.0	14.7	14.4	13.8	
	Fe _{tot}	10.9	0.849	-	-	-	-	
	FeO	7.96	0.726	8.28	6.57	5.40	2.69	
	Fe ₂ O ₃	2.10	0.113	2.18	1.73	1.43	0.710	
	MnO	0.167	0.055	0.173	0.125	0.102	0.062	
	MgO	6.69	0.464	6.96	7.33	7.56	7.96	
	CaO	11.18	0.981	11.64	12.10	12.43	13.24	
	Na ₂ O	4.46	0.272	4.65	5.02	5.27	5.93	
	K ₂ O	0.263	0.072	0.274	0.296	0.311	0.350	
	P ₂ O ₅	0.177	0.212	-	-	-	-	
	LOI	2.63	0.741	-	-	-	-	
	Sum	99.8	0.087	100	100	100	100	
	Trace elements (µg/g)	Li	33.1	0.871	-	-	-	-
		Be	0.440	0.085	-	-	-	-
Sc		40.4	0.875	-	-	-	-	
V		279	5.59	-	-	-	-	
Cr		280	15.1	-	-	-	-	
Co		49.7	4.73	-	-	-	-	
Ni		150	17.4	-	-	-	-	
Cu		115	20.6	-	-	-	-	
Zn		162	14.2	-	-	-	-	
Ga		13.8	1.02	-	-	-	-	
Rb		5.90	0.519	-	-	-	-	
Sr		113	43.5	-	-	-	-	
Y		19.1	2.36	19.1	14.8	12.0	5.15	
Zr		51.5	6.02	-	-	-	-	
Nb		2.26	0.289	-	-	-	-	
Cs		0.640	0.252	-	-	-	-	
Ba		403.0	45.2	-	-	-	-	
La		1.73	0.460	-	-	-	-	
Ce		3.68	0.983	-	-	-	-	
Pr		0.740	0.148	-	-	-	-	
Nd		4.02	0.798	-	-	-	-	
Sm		1.40	0.200	-	-	-	-	
Eu		0.590	0.095	-	-	-	-	
Gd		2.14	0.123	-	-	-	-	
Tb		0.500	0.030	-	-	-	-	
Dy		3.57	0.343	3.57	2.79	2.30	1.21	
Ho		0.790	0.093	0.790	0.610	0.503	0.234	
Er		2.23	0.337	2.23	1.71	1.40	0.636	
Tm	0.350	0.058	0.350	0.272	0.231	0.130		
Yb	2.29	0.447	2.29	1.74	1.46	0.755		
Lu	0.360	0.068	0.360	0.284	0.244	0.143		
Hf	1.57	0.130	-	-	-	-		
Ta	0.150	0.021	-	-	-	-		
Tl	0.080	0.041	-	-	-	-		
Pb	3.73	3.64	-	-	-	-		
Bi	0.010	0.060	-	-	-	-		
Th	0.190	0.055	-	-	-	-		
U	0.230	0.043	-	-	-	-		
ΣHREEs+Y	28.72	3.71	28.7	22.2	18.2	8.26		

Table 11: NOTES: "-" means do not detect or calculate; EBC means calculated effective bulk composition for pseudosection modeling; "Fe_{tot}" means the total amount of iron oxide analysed from XRF; The Fe₂O₃ content of bulk-rock is constrained from potassium permanganate titration method; The Fe₂O₃ and FeO contents of EBCs were calculated based on the constant ratio of Fe³⁺/Fe²⁺ from XRF data for evaluated composition; The bulk rock compositions listed here will be used during thermodynamic modeling for the estimate of mineral modes evolution, and for evaluating effective partition coefficients (K^{eD}) during diffusion modeling.

Trace element data of rutile analysed in garnet and in the matrix. Calculated temperatures via different calibrations are indicated

Occurrence	As inclusions in garnet											
	Close to core		Within annular peak		Within annular peak		Close to rim		Close to rim		In matrix	
	Av. (n=7)	Std.	Av. (n=17)	Std.	Av. (n=6)	Std.	Av. (n=7)	Std.	Av. (n=13)	Std.	Av. (n=23)	Std.
Elements (µg/g)												
Zr	22.7	8.96	66.4	6.71	63.7	10.5	20.3	4.25	21.1	5.93	21.4	6.19
V	1579	535	1825	382	2054	185	1539	533	1896	321	1886	335
Cr	690	390	1116	576	1274	385	696	446	858	307	1118	535
Nb	75.4	41.5	64.2	23.0	68.2	17.6	76.3	39.6	65.1	21.5	65.3	20.0
Si	99.6	43.0	114	50.7	95.2	54.2	119	46.5	126	34.3	130	61.3
Fe	2931	634	2444	879	1993	439.0	3237	778	3769	1106	2784	996
Al	134	86.1	97.7	54.4	176	97.7	102	60.1	199	108	174	118
T estimates												
Zack et al. (2004)	389	53.4	526	13.2	521	23.6	375	28.2	379	39.0	381	40.9
Watson et al. (2006)	472	22.2	534	6.51	532	11.4	466	11.6	467	16.0	468	16.7
Tomkins et al. (2007)	540	24.2	608	7.08	605	12.4	533	12.6	535	17.4	536	18.2
Ferry and Watson (2007)	474	22.1	536	6.45	534	11.3	468	11.5	470	15.9	471	16.6

Table 14: Notes: * marked calibrations with specific preassumed parameters, e.g., activity of SiO₂ or pressure value input. Check figure. 2c-d and relevant context for detail.

List of parameter values considered for each diffusion modeling calculation

Diffusion modeling		Modeling system parameters				Arrhenius parameters			T (time)					R (time)	Mass Balance		
Var.	Runs/Units	Sys. size	Grt size - R _r	C _{om}	E _{K_D}	D _{om}	D _{og}	Q	T ₀	ΔT _p	T _r	t _n	t _p	t _r	n	wt% or ug/g	
		cm	wt% or ug/g	-	-	cm ² /yr	kJ/mol	°C	°C	°C	Myrs	Myrs	Myrs	Myrs	PL-exponent	wt% or ug/g	
System size	R1	0.5															
	R2	0.4															
	R3	0.3				4.0E+12		300									
	R4	0.2															
Q	R5																
	R6	0.122				4.0E+11		280									
	R7							300									
D _{om}	R8			7.27 (Y)	15.4*/14.4	4.0E+11				600	5.000			5.000	1		
	R9					4.0E+12											
	R10					4.0E+13											
	R11					4.0E+14											
Grt size - R(t)	R12		0.072														
	R13		0.096														
	R14		0.12			4.0E+12											
	R15		0.144														
Various T _r versus distinct D _{om}	R16					8.0E+11				550						2.90E-17	
	R17					8.0E+11				525						7.15E-18	
	R18					8.0E+11				500						3.36E-18	
	R19	0.2				8.0E+12				550						3.20E-16	
	R20					8.0E+12				525						8.01E-17	
	R21					8.0E+12				500						2.90E-17	
	R22					8.0E+10	1.0E+06	450		550	3.800	1.000	0.200	5.000	3.05	4.02E-18	
	R23					8.0E+10				525						1.54E-18	
	R24					8.0E+10				500						4.39E-19	
	R25	0.122			10.5*/4.3	8.0E+13				550						2.56E-15	
	R26			0.17 (Mn)		8.0E+13		300		525						8.04E-16	
R27					8.0E+13				500						3.15E-16		
Short L _p	R28									80						1.27E-17	
	R29									525	4.500	0.300	0.200	5.000	6.34	4.05E-18	
	R30									500						3.53E-18	
Comparable L _p and L _r	R31					8.0E+11				550						3.37E-17	
	R32									525	0.800	1.000	0.200	2.000	1.07	1.07E-17	
	R33									500						3.97E-18	
Divers e size grts	R34	0.18	0.110		6.3*/5.1	8.3E+11				500	4.500	0.300	0.119	4.919	6.34	7.27E-18	
	R35	0.19	0.112		8.4*/6.6	6.2E+12				500	4.500	0.300	0.133	4.933	6.34	4.11E-17	
	R36	0.26	0.158		13.9/7.5	5.7E+12				500	4.500	0.300	0.408	5.208	6.34	3.41E-16	
HREEs profiles within A1	R37			1.43 (Dy)	12.4/12.2	1.2E+12										5.51E-18	
	R38			0.391 (Ho)	11.8/11.1	2.9E+12										7.19E-18	
	R39			1.01 (Er)	14.8*/12.8	4.6E+12										3.09E-17	
	R40	0.2	0.122		0.171 (Tm)	13.2*/11.7	7.3E+12			500	4.500	0.300	0.200	5.000	6.34	7.47E-18	
	R41				1.36 (Yb)	12.1*/11.3	8.7E+12										8.82E-17
	R42				0.221 (Lu)	11.1*/9.78	1.3E+12										1.97E-17
	R43			7.27 (Y)	15.4*/14.4	3.1E+12											2.23E-18

Table 13: Notes: * marked estimated initial K_D for garnet grains whose concentration central peak of given elements were probably missed during EMPA. Check App. A for detail estimate strategy.

6. Contrasting P-T-deformation-time evolutions in the SW-Tianshan (Akeyasi HP/UHP complex, China): implications for Late Carboniferous subduction dynamics

Key words: *UHP/HP metamorphism; P-T-deformation-time histories; ^{40}Ar - ^{39}Ar in situ laser ablation analyse; Juxtaposition; Cold subduction regime; Subduction dynamics; Chinese SW-Tianshan;*

Authors: *Tan Zhou ^{a,b,d}, Agard Philippe ^{b,e}, Monié Patrick ^f, Wan Bo ^{c,d}, Gao Jun ^{a,d,*}, John Timm ^g, Bayet Léa ^g, Jiang Tuo ^h, Wang Xin-Shui ^a, Hong Tao ^a*

- k. Key Laboratory of Mineral Resources, Institute of Geology and Geophysics, Chinese Academy of Sciences, 100029 Beijing, China
- l. Sorbonne Université, CNRS-INSU, Institut des Sciences de la Terre de Paris, ISTeP UMR 7193, F-75005 Paris, France
- m. State Key Laboratory of Lithospheric Evolution, Institute of Geology and Geophysics, Chinese Academy of Sciences, 100029 Beijing, China
- n. University of Chinese Academy of Sciences, 100049 Beijing, China
- o. Institut Universitaire de France, F-75005 Paris, France
- p. Geosciences Montpellier, UMR5243, Université Montpellier 2, CNRS, Place E. Bataillon, F-34095 Montpellier CEDEX 05, France
- q. Institut für Geologische Wissenschaften, Freie Universität Berlin, Malteserstr. 74-100, D-12449 Berlin, Germany
- r. Laboratory of Isotope Geochemistry, Wuhan Centre of China Geological Survey, 430205 Wuhan, China

* *Corresponding author: Gao Jun, gaojun@mail.iggcas.ac.cn*

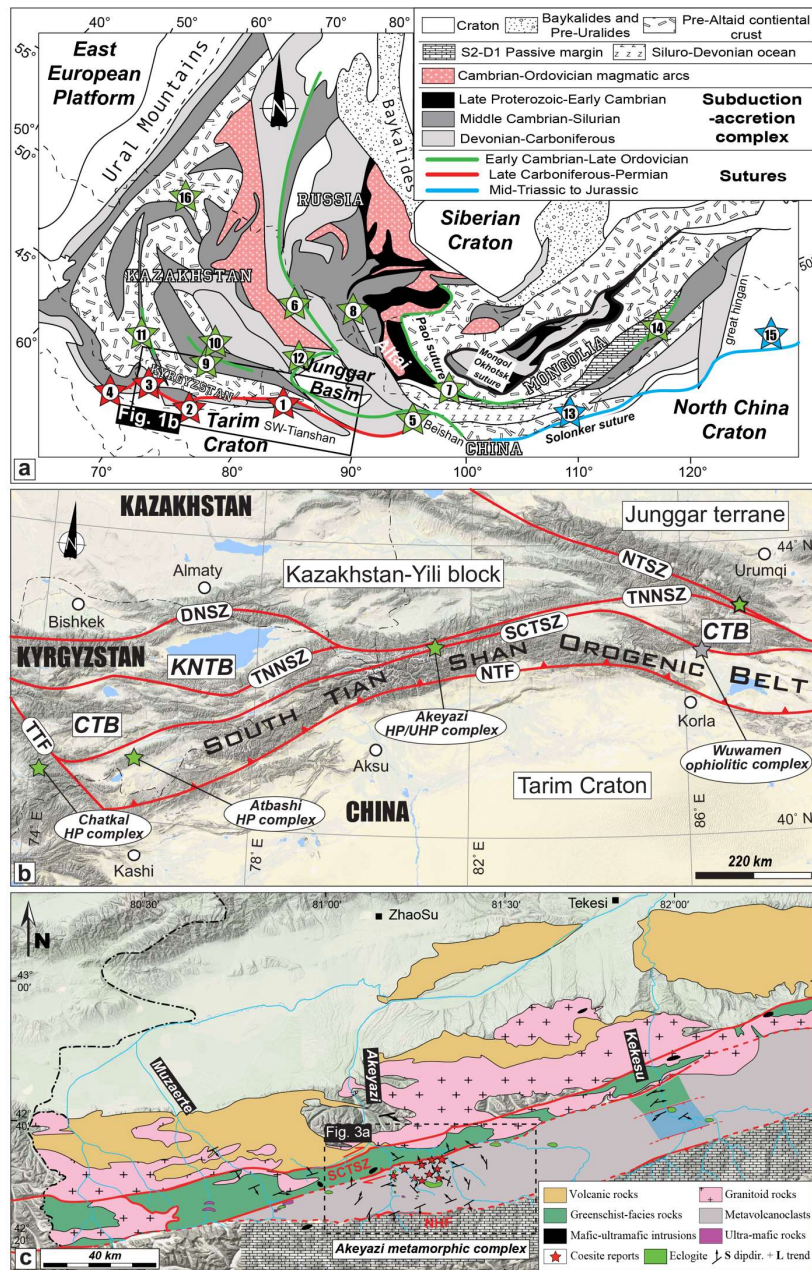


Figure 50: (a) Tectonic sketch showing the middle to western segments of the Central Asian metallogenic domain, modified after Gao et al. (2017), Soldner et al. (2017) and Xiao et al. (2015). Colored stars with number marked the occurrence of high (ltra-high) pressure/low temperature metamorphic rocks (see Gao et al. (2017) and references therein): 1. Akesayi, ~320 Ma; 2. Atbashi, ~320 Ma; 3. Chatkal, ~301 Ma; 4. FanpKarategin, ?; 5. Beishan, ~465 Ma; 6. Chara Zone, ~445 Ma; 7. SW Mongolia, ~540 Ma; 8. Gony Altai, ~630 Ma; 9. Aktyuz, ~460-470 Ma; 10. Chu-Yili, ~490 Ma; 11. Makbal, ~475-500 Ma; 12. Barleik, ~492-504 Ma; 13. Central inner Mongolia, <235 Ma; 14. Toudaoqiao, ~490-510 Ma; 15. Yilan, ~180-210 Ma; 16. Kokchetav, ~524-537 Ma. (b) Simple sketch showing the relationship between main contacts and tectonic units in the South Tianshan Orogen and adjacent region. CTB = Central Tianshan Block, KNTB = Kyrgyzstan North Tianshan Block, NTSZ = North Tianshan Suture Zone, TNNSZ = Terskey-North Nalati Suture Zone, SCTSZ = South Central Tianshan Suture Zone, DNSZ = Djalair-Naiman Suture Zone, NTF = North Tarim Fault, TTF = Talas-Fergana Fault. (c) Geological map of the Southwestern Tianshan HP/UHP metamorphic belt (STMB). The structural data was plotted according to the measurement from this study, Bayet et al. (2018), Gao et al. (1998), Lin et al. (2008) and Soldner et al. (2017). The location of coesite reports follows the compilation of Tan et al. (2017) and Bayet et al. (2018).

Abstract

We present the first comprehensive P-T-deformation-time and kinematic constraints for HP/UHP eclogite, blueschist and greenschist-facies metavolcano-sedimentary rocks cropping out in the SW-Tianshan metamorphic wedge (within the ~30 km wide N-S Akeyazi-Kebuerte area). We reappraise this HP/UHP “mélange”, which should be divided into three main tectonic units, from north to south, according to their discrepant lithologies and P-T-time-deformation histories. These three units crop out in a tectonic window beneath greenschist-facies metavolcanics. P-T estimates point out to 1) UHP-LT conditions around 2.7-2.8 GPa at ~520 °C for the metavolcano-sedimentary rocks of the northern HP/UHP unit, 2) HP-LT conditions of 1.8-2.1 GPa and ~500 °C for the central blueschist horizon and 3) lower-blueschist facies conditions of 1.0-1.5 GPa at ~485 °C for the southern ultramafic-mafic unit. In situ laser probe Ar-Ar age constraints (with textural control) on recrystallized phengites from the HP/UHP unit cluster within 315 to 325 Ma. Phengite ages from the central blueschist horizon are 15-20 Ma older, at ~325-345 Ma. Laser-ICP-MS U-Pb dating on zircon from the south ultramafic-mafic unit yield ages around ~360 Ma for metamorphic overgrowths. In contrast, step-heating Ar-Ar phengite age constraints for the greenschist-facies metavolcano-sediments fall within 280-300 Ma. These new field and P-T-time data disclose an episodic exhumation of the three main tectonic slices, respectively from ~85 km, ~65 km and ~45 km depths. Final juxtaposition, at ~20 km was probably achieved around 300 Ma, prior to collision.

6.1. Introduction

Mechanisms and processes responsible for the occasional recovery of ocean-derived high- to ultra-high pressure low temperature (HP-UHP/LT) metavolcanics/metavolcanoclastics equilibrated along the subduction plate interface (Agard et al., 2009) are essential to constrain subduction dynamics and gain insights on the meter- to hectometer-scale constitution of the plate boundary (Bachmann et al., 2009; Stöckhert, 2012; Agard et al., 2018 and references therein). The diversity of subducted material, either from the downgoing plate (generally the uppermost section, i.e. pelagic sediments with basaltic oceanic crust and/or seamounts) or upper plate derived (i.e., ashes from arc-volcanism and/or detrital sediments in the accretionary wedge, and/or basement material if basal erosion occurs), is likely to influence viscosity, density and thus buoyancy, and to control chemical and mechanical behaviors within the plate interface (Bebout, 2007, 2013; Yamato et al., 2007; Krebs et al., 2011).

Regardless of their origin, subducted material transported on top of the subducting plate may be stripped from the slab as *mélange* (e.g., Blanco-Quintero et al., 2011; Wakabayashi, 2011, 2015) or tectonic slices (e.g., Angiboust et al., 2013; Bonnet et al., 2018; Locatelli et al., 2018) and later juxtaposed during exhumation. To unravel the fate of deeply subducted material (down to ~80 km depth), the Chinese South Tianshan Metamorphic Belt (STMB) is a potentially important example. It is indeed characterized by an unusually thick (~5km) pile of well-preserved HP/UHP metavolcanoclastics (Bayet et al., 2018) wrapping eclogite boudins/slices with numerous coesite findings (e.g., Bayet et al., 2018; Lü & Zhang, 2012; Tan et al., 2017).

However, despite numerous studies providing detailed petrological, geochemical evolutions or geochronology data (e.g., Gao et al., 2007; John et al., 2008; Klemd et al., 2011; van der Straaten et al., 2012; Tan et al., 2017 and references therein), the internal structures and tectonic evolution of the STMB remain poorly constrained: why is it so thick so deep, and what can we learn from this exceptional example across a depth range critical for mechanical coupling (~80 km; Syracuse et al., 2010; Wada & Wang, 2009)? The present study provides for the first time a detailed, fully coupled tectono-metamorphic-radiometric study across the STMB, combining a composite ~30 km long cross-section, average PT estimates for each domain and in-situ Ar-Ar dating (together with zircon U-Pb and step-heating measurements) to provide age constraints with deformation control. Results allow to discuss the conditions of recovery, exhumation rates and implications for subduction processes and regional geodynamics.

6.2. Geological Setting of SW-Tianshan Accretionary Complex

The Chinese Southwestern Tianshan high- to ultrahigh-pressure low-temperature (HP/UHP-LT) accretionary complex constitutes the eastern part of the Kazakhstan collage system (Gao et al., 2017; and references therein) within the Altaids (also called the Central Asian Orogenic Belt; Figure 50a). It extends for about 200 km along the Southwestern Central Tianshan Suture Zone (SCTSZ, Figure 50b), and correlates with the Atbashi (Hegner et al., 2010; Loury et al., 2018; Simonov et al., 2008), Chatkal (Loury et al., 2016; Mühlberg et al., 2016) and Fan-Karategin (U)HP metamorphic complexes (Volkova and Budanov, 1999) in the Kyrgyzstan part of the South Tianshan

Orogenic Belt (STOB). The SCTSZ bounds to the north the Chinese section of the HP-UHP/LT metamorphic complex, known as the Akeyazi metamorphic complex (AMC, Figure 50c). This contact, now a ~0.5 km-wide dextral strike-slip shear zone, was active from the Early Permian to Early Triassic (Gao & Klemd, 2003; Laurent-Charvet et al., 2003). To the north lies a LP-HT Palaeozoic active continental margin (Allen et al., 1993; Gao et al., 1998; Klemd et al., 2015), mainly made of amphibole- and granulite-facies rocks, along with Late Silurian and Early Carboniferous continental arc-type volcanic, volcanoclastic rocks and granitoids (Gao et al., 2009a; Xia et al., 2014). To the south the AMC is overlain by unmetamorphosed and/or low grade Palaeozoic sedimentary strata, which also represent the northern, passive continental margin of the Tarim plate (Carroll et al., 1995).

The AMC is predominantly composed of strongly schistosed metavolcanoclastics hosting mafic metavolcanics as pods, lenses, boudins, thin layers or massive blocks (Gao & Klemd, 2003) and marble horizons (Bayet et al., 2018), as well as very rare ultramafic rocks (Li et al., 2010; Shen et al., 2014). Whole-rock geochemical data for the mafic metavolcanics suggest oceanic basalt or arc-related affinities (Gao & Klemd, 2003; John et al., 2008; Liu et al., 2014; Meyer et al., 2016; Tan et al., 2017) while the metavolcanoclastics have characteristics similar to upper continental crust and trench sediments (Liu et al., 2014; Meyer et al., 2016; Tan et al., 2017).

Previous work mostly focused on individual HP/UHP rocks/outcrops for the reconstruction of P-T-(time) histories (e.g., Li et al., 2016; Lü et al., 2012; Tan et al., 2017), fluid-rock interaction processes and/or geochemical budgets (e.g., Beinlich et

al., 2010; John et al., 2012; van der Straaten et al., 2008). A recent compilation of regional P-T (-time) constraints (Tan et al., 2017) indicates that most peak metamorphic estimates for eclogite and prograde blueschist yield eclogite facies (EC facies) HP-LT conditions within the range 480-580°C and 1.5-3.0 GPa. A range of P-T conditions ~450-570°C at 2.7-3.3 GPa was obtained for some EC facies metavolcanoclastics. Evidence for UHP metamorphism comes from both coesite relics in garnet (from several localities: stars in Figure 50c, 51a, d, 52a, 69) and thermodynamic calculation. The spread of regional P-T estimates (Tan et al., 2017, their Figure 13) could a priori arise from contrasting assumptions for thermodynamic modeling (e.g., difficulties in determining effective bulk rock composition and Fe³⁺ content and/or assessing H₂O activity) or from the complexity of metamorphic evolutions in individual HP-UHP tectonic slices (Bayet et al., 2018).

Our recent compilation of previous P-T-time works (Tan et al., 2017) suggests that the timing of peak HP/UHP metamorphism falls within 315 ± 5 Ma, i.e., in a restricted range with respect to a ~100 Ma-long subduction (also see Table 22 and Figure 69 for the compilation), in support of a Late Carboniferous accretionary system (Gao et al., 2009b). Some controversy exists, however, to the east of SCTSZ, in the Beishan arc terrane of South Tianshan Orogenic Belt: some workers propose that accretion may have lasted until the Early Triassic (Tian et al., 2014), while others suggest a Permian collision (e.g., Xiao et al., 2004). Regional ages <280 Ma (e.g., Zhang et al., 2007) or > 325 Ma (e.g., Gao et al., 1995, 2000, 2006) were previously considered as either resulting from intrinsic limitations of isotopic dating (e.g., excess Ar, Nd disequilibrium

in Sm-Nd system; difficulty to link zircon U-Pb ages to precise metamorphic stages) or taken as evidence for distinct HP-UHP episodes (Tan et al., 2017).

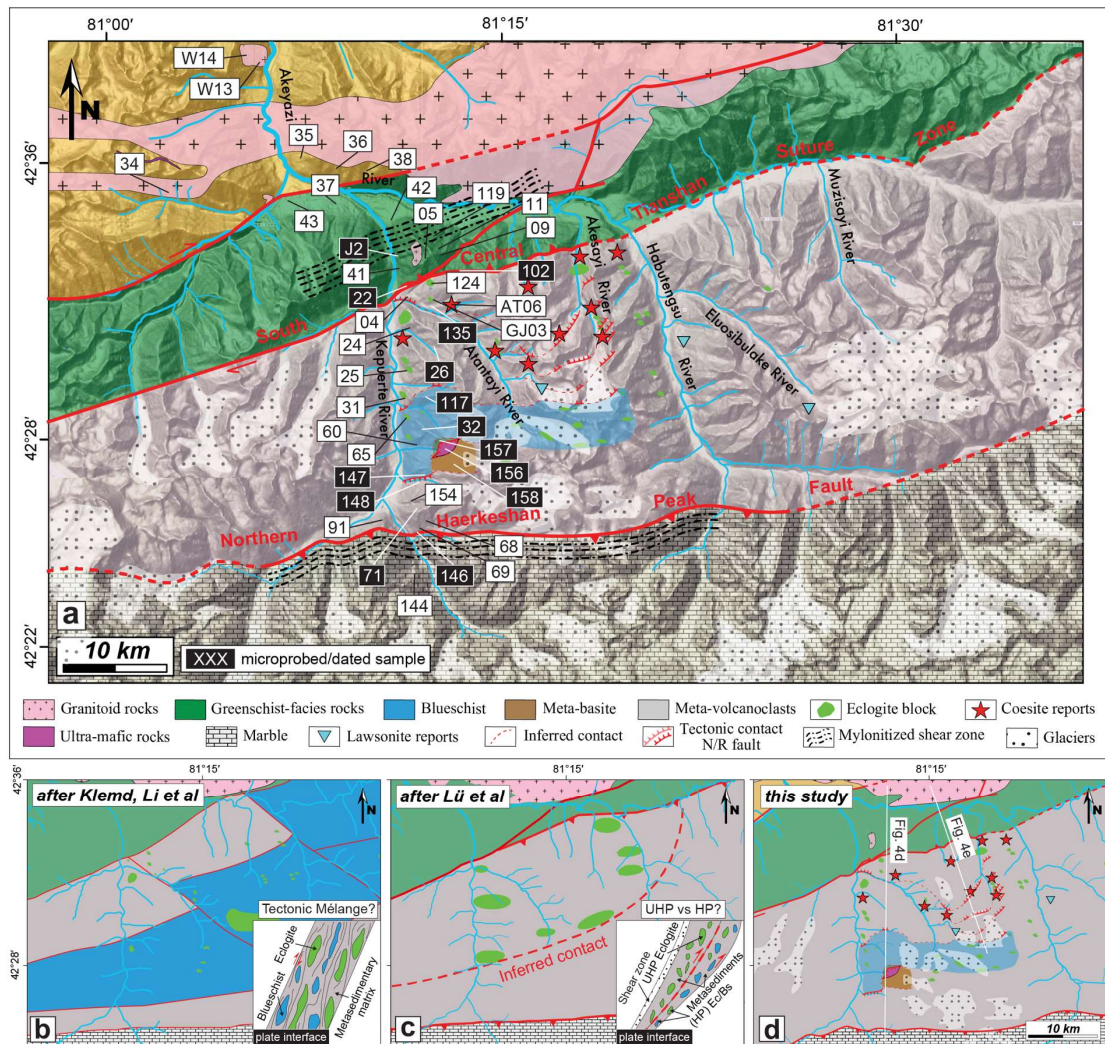


Figure 51: (a) Close-up views of the Akesayi metamorphic complex (AMC) showing sampling localities and reappraised tectonic sub-units & contacts. The location of coesite reports follows the compilation of Tan et al. (2017) and Bayet et al. (2018). The location of lawsonite reports were cited from Li et al. (2013), Du et al. (2011) and Du et al. (2014). Samples with black frame were studied with the electron probe microanalysis (Table 15). (b, c) Simple sketches showing the controversy about the regional geodynamic model: Tectonic mélange (e.g., Klemd et al., 2011; Li et al., 2016) versus UHP/HP sub-belts (e.g., Lü et al., 2012). (d) Reappraisal geological map of the AMC (this study).

6.3. Structural Data

Structural information for the SW-Tianshan Metamorphic Belt is scarce (Gao et al., 1999), with only few recent reports for the Akesayi Metamorphic Complex (Bayet et al., 2018; Lin et al., 2008; Soldner et al., 2017; Tan et al., 2017) and for the nearby

Kekesu valley (~60km to the east, Figure 50c. Gao et al., 1995). Based on the new investigations in this study and previous regional structural works, a revised structural map is proposed for the area (Figure 51a-d).

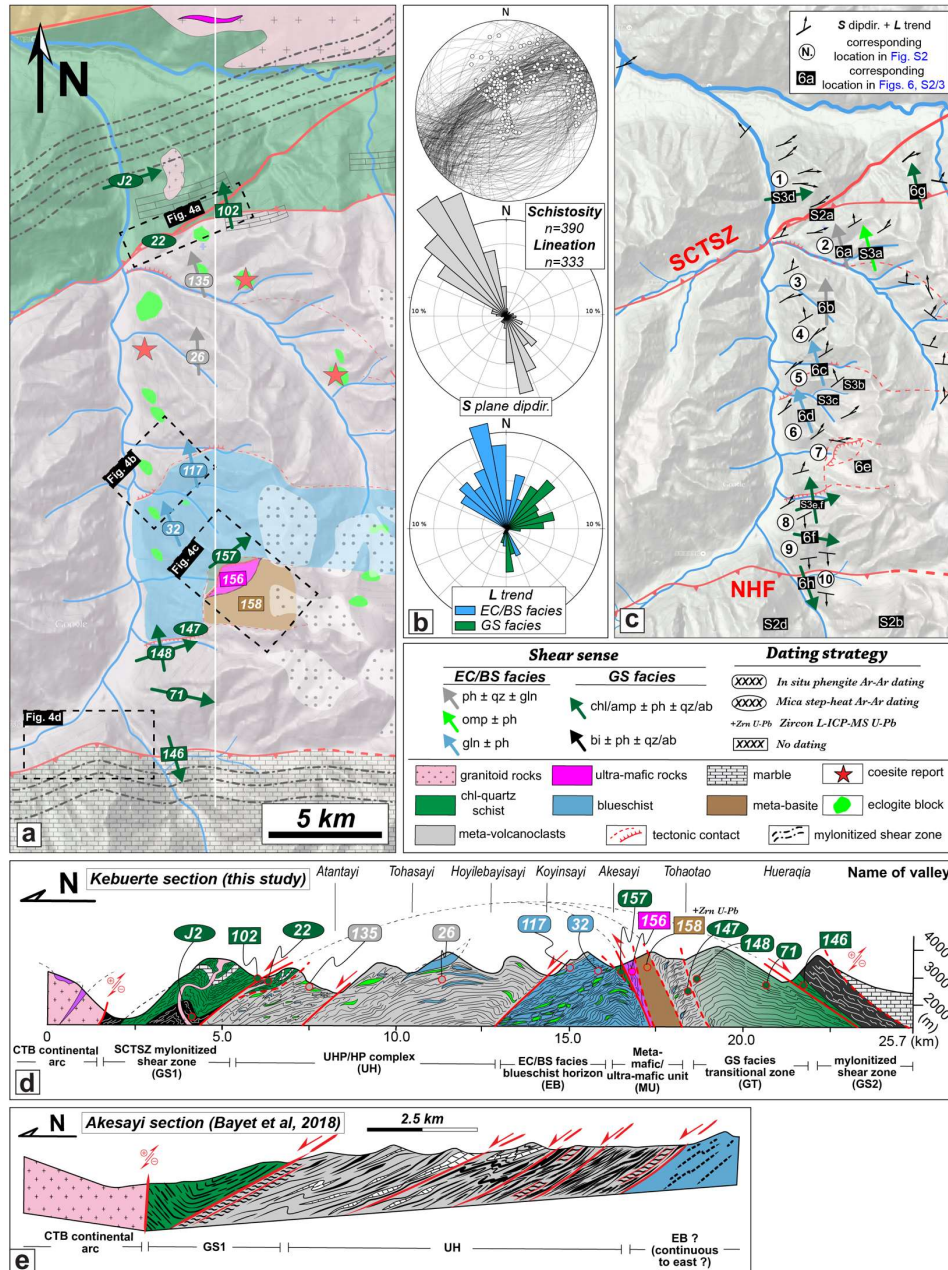


Figure 52: (a) Close-up view of the area along the Kebuerte valley showing sampling sites, measured shear senses and the location of field observations (Figure 53). (b) The summary of the pattern of regional schistosity and lineation. Detail data with respect to measurement location are presented in Figure 54. (c) Simple map with the plots of structural element showing the location of field observations corresponding to those in Figures 55, 64 and 65. (d) Approximately N-S ~30km-long section constructed, along the Kebuerte valley, across the previous so-called HP/UHP mélangé (e.g., Klemd et al., 2011; Li et al., 2016) and further touch to the South margin of the STMB around the Northern Haerkeshan Fault (NHF), with detailed sample sites and analysis strategy. (e) The Akesayi section from recent work (Bayet et al., 2018) was also cited for comparison.

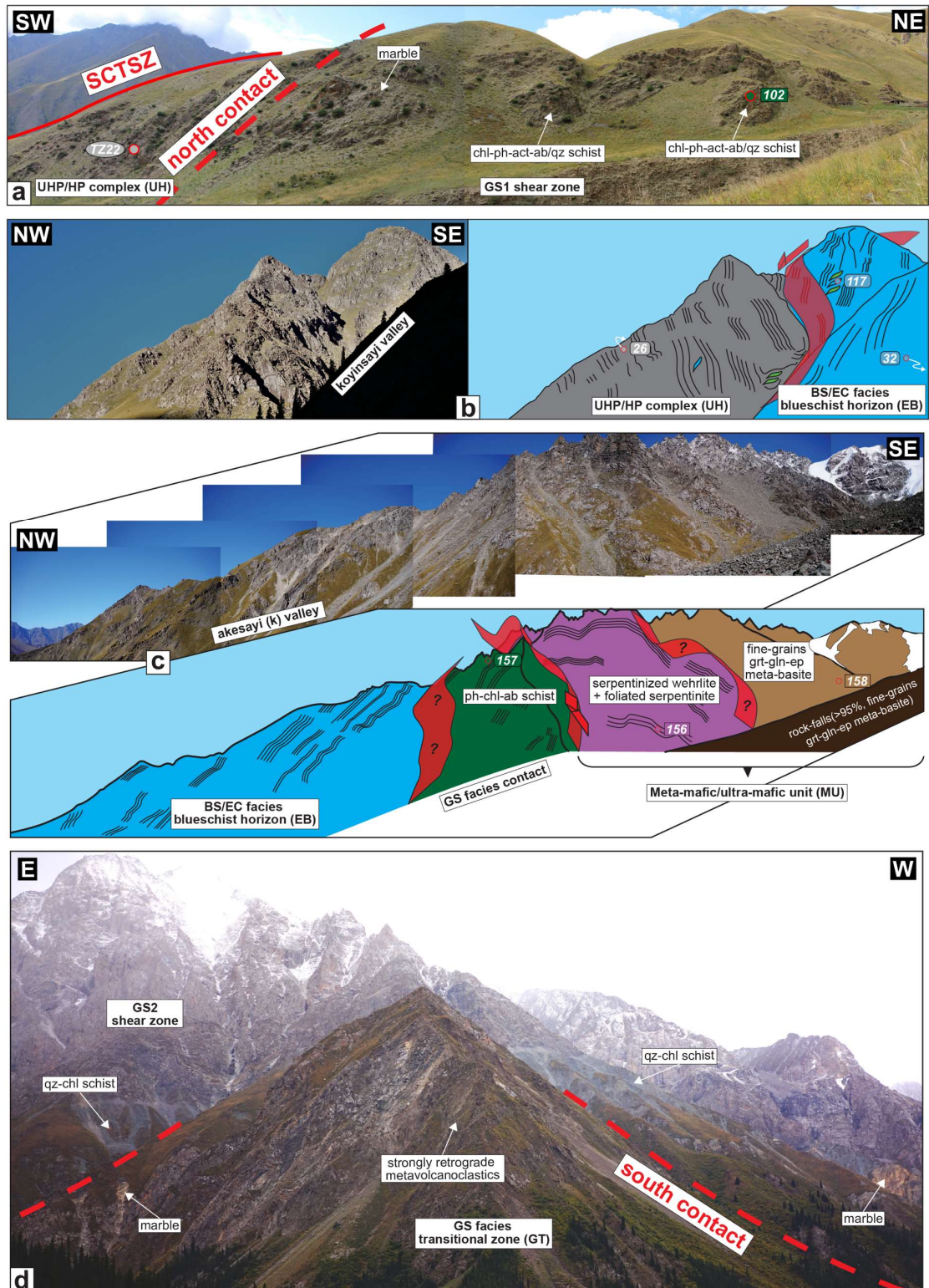


Figure 53: Panoramic views of the main sub-units and contacts in the AMC, with representative sample localities. Also check Figure 63 for the rest panoramic pictures.

6.3.1. Overall structural organization of the Akeyasi Metamorphic Complex

An approximately 30 km-long N-S cross-section was constructed along the Kebuerte valley (Figure 51d, 52a, d). It cuts across the whole South Tianshan Orogenic Belt, namely, from north to south: the south margin of Central Tianshan continental arc, the AMC, and the unmetamorphosed to low grade Palaeozoic sedimentary strata bounded by the North Haerkeshan Peak Fault (NHF). A recently published cross-section along the adjacent Akesayi valley (Bayet et al., 2018) is shown for comparison (Figure 52e).

In the study area, the AMC is a metamorphic dome structure (Figure 52d) that can be further divided into six sub-units bounded by hm-/km-scale contacts (Figure 53, 63) on the basis of petrological, lithological and structural characteristics (e.g., Figure 52-54):

1) Unit GS1: this ~3 km-wide GS facies unit (Figure 52a, d, 53a, 63a) separates the CTB continental arc from the HP/UHP exposures (e.g., Klemd et al., 2011; Li et al., 2016, Figure 51b). It consists of strongly schistosed chl-phengite-biotite-quartz schist (Figure 64d, 65a) and actinolite-epidote-chlorite-quartz/albite schist (Figure 55g, 65b), with few garnet-bearing, significantly retrograded metapelites (Figure 56h), m-/hm-scale marble horizons and magmatic intrusions (Pu et al., 2011). Mylonitic horizons are found in places;

2) Unit UH: this corresponds to the so-called HP/UHP metamorphic 'mélange' (e.g., Klemd et al., 2011; Li et al., 2016, Figure 51b), host to most previous P-T-time(-fluid) works (Table 22; Figure 69) and coesite reports (Figure 50c, 51a, d; Bayet et al., 2018; Lü et al., 2009; Lü & Zhang, 2012; Tan et al., 2017; Yang et al., 2013). This unit crops

out for ~9km along section (Figure 51a, d, 52a, d) and is separated by two normal shear sense faults (Figure 52, 53a-b, 63a) from the GS1 unit to the north and a EC/BS facies blueschist unit to the south. Noteworthy, Bayet et al. (2018) identified several internal, km-scale individual tectonic slices in this unit (Figure 51a, d, 52e). It is predominantly composed of strongly schistosed meta-pelitic/-psammitic volcanoclastics (Figure 55a-b, 56a, 65c) hosting mafic metavolcanics as pods, lenses, boudins, thin layers or massive blocks (e.g., Figure 55a; Soldner et al., 2017; Tan et al., 2017) as well as some marble horizons (Figure 52e; Bayet et al., 2018);

3) Unit EB: this ~4km-large EC/BS facies unit (Figure 51a, d, 52a, d-e) occupies the central and lowermost portion of the AMC on this transect. It lies structurally below the UH unit to the north (Figure 53b), and is overthrust on its southern side by a meta-mafic/-ultramafic unit (MU, Figure 53c) through a GS facies contact zone. It is characterized by relatively homogeneous, moderately schistosed blueschist horizons (Figure 55c-d, 56b-c) hosting lenses and/or pillow-shaped eclogite/blueschist blocks (Figure 55c).

4) Unit MU: this unit comprises metamorphosed mafic and ultramafic rocks (Figure 53c), which is the first report of meta-ultramafic rocks within the AMC. Similar lithologies have so far been reported only in the Changawuzi-Muzaerte valley (~40 km to the west, Figure 50c; Gao et al., 1999; Li et al., 2007). To the north, the meta-ultramafic rocks are closely associated with a GS facies, weakly schistosed phengite-chlorite-quartz/albite schist shear zone (Figure 64e, 65d) and overthrust by a ~1km-wide metabasic slice to the south (Figure 53c, 55e, 56e-g). The mutual relationships

between the MU and UH units (both overlie the EB unit) cannot be ascertained due to glacial coverage (Figure 52a, 54a, c), but the attitude of schistosity and aerial views suggest that MU overlies UH.

5) Unit GT: this ~5km-wide GS facies transitional zone (Figure 52a, d, 53d, 63d) is located at the southern side of the MU. The boundary between GT and MU could be more complex than the simple contact drawn on Figure 52d. GT is overthrust by a strongly retrograded meta-mafic slice (Figure 65g), which could represent the southern margin of the MU or a local small sub-unit. The GT unit is bounded by a km-scale normal shear zone to the south (Figure 53d, 63b-c). The GT mainly consists of moderately to strongly schistosed GS facies chlorite-phengite-quartz schist ± garnet relics or pseudomorphs (Figure 55f, 56i, 64g-h, 65g-i), with few blueschist blocks previously reported close to its northern margin (Figure 69, Gao et al., 2000);

6) Unit GS2: this unit shows lithologies and structural patterns very similar to those of the GS1 unit, with mainly strongly deformed phengite-chlorite-albite/quartz (Figure

Parageneses of the Main Samples Studied in Chinese SW-Tianshan HP/UHP-LT accretionary complex														Tectonic affinity	Data	Coordinates				
Sample	Qz	Grt	Ph	Pg	Bi	Cpx	Amp	Ep/Czo	Chl	Ctd	Rt	Ttn	Fsp/Ab				Carb	Srp		
J2	x		x		x				x								GS facies Shear Zone (GS1)	P+R+D _{in}	N42°33'11.3"	E81°10'53.7"
102	x		x				x	x										P+R	N42°32'37.9"	E81°12'17.3"
22	x	x	x		x		x		x		x	x	x				UHP/HP Complex (UH)	P+R+D _{in}	N42°32'18.5"	E81°11'49.0"
135	x	x	x	x		x*	x	x	x		x	x	x					P+R+D _{in}	N42°31'55.0"	E81°12'12.7"
26	x	x	x						x				x	x				P+R+D _{in}	N42°30'47.5"	E81°12'10.6"
117	x	x	x	x			x		x		x	x	x		x		EC/BS facies blueschist horizon (EB)	P+R+D _{in}	N42°29'1.9"	E81°12'0.9"
32	x	x	x	x	x		x	x	x	x	x	x	x		x			P+R+D _{in}	N42°28'25.9"	E81°11'56.9"
157	x		x												x	x	Contact between EB and MU	P+R+D _{in} st	N42°28'8.4"	E81°12'27.3"
156-1									x*			x					Meta-ultramafic/mafic unit (MU)	P	N42°27'39.5"	E81°12'52.5"
156-2			x*						x									P	N42°27'36.9"	E81°12'52.4"
156-3									x*									P	N42°27'38.8"	E81°12'50.2"
158	x	x	x				x*	x	x				x	x	x			P+D _z	N42°27'32.2"	E81°13'28.5"
147	x	x	x	x	x		x	x	x		x	x			x		GS facies transitional zone (GT)	P+R+D _{in}	N42°26'51.6"	E81°11'23.5"
148	x	x	x	x	x				x		x	x			x			P+R+D _{in}	N42°26'40.9"	E81°11'26.9"
71	x		x						x					x			GS facies Shear Zone (GS2)	P+R+D _{in}	N42°26'8.7"	E81°11'16.1"
146	x		x						x		x	x		x				P+R	N42°25'8.4"	E81°11'37.3"

Table 15: Notes: Abbreviation for Data column, P: petrological investigation (e.g., microprobe); R: RSCM thermometer; Dst, Din and Dzu respectively mean age dating via phengite/biotite Ar-Ar step-heating, in situ phengite Ar-Ar probing and zircon U-Pb technology. Mineral abbreviations: Qz, quartz; Grt, garnet; Ph, phengite; Pg, paragonite; Bi, biotite; Cpx, clinopyroxene; Amp, amphibole; Ep/Czo, epidote/clinozoisite; Chl, chlorite; Ctd, chloritoid; Rt, rutile; Ttn, titanite; Fsp/Ab, feldspar/albite; Carb, carbonate; Srp, serpentine. The x means that the mineral is present. The x* marks the samples with special mineral composition compared with the others: Grt in sample 156-2 is grossular (Grs); Cpx in samples 135 and 158 is omphacite (Omp), but in samples 156-2 and 156-3 is diopside; Chl in samples 156-1 and 156-2 is Mg-rich chlorite (MgChl).

55h, 63c, 65j) and phengite-biotite quartz schists (Figure 52a, d, 53d). It is bounded to the south by a major EW-trending fault, the North Haerkeshan Peak Fault (NHF; Figure 52a, d, 53d, 63b, d).

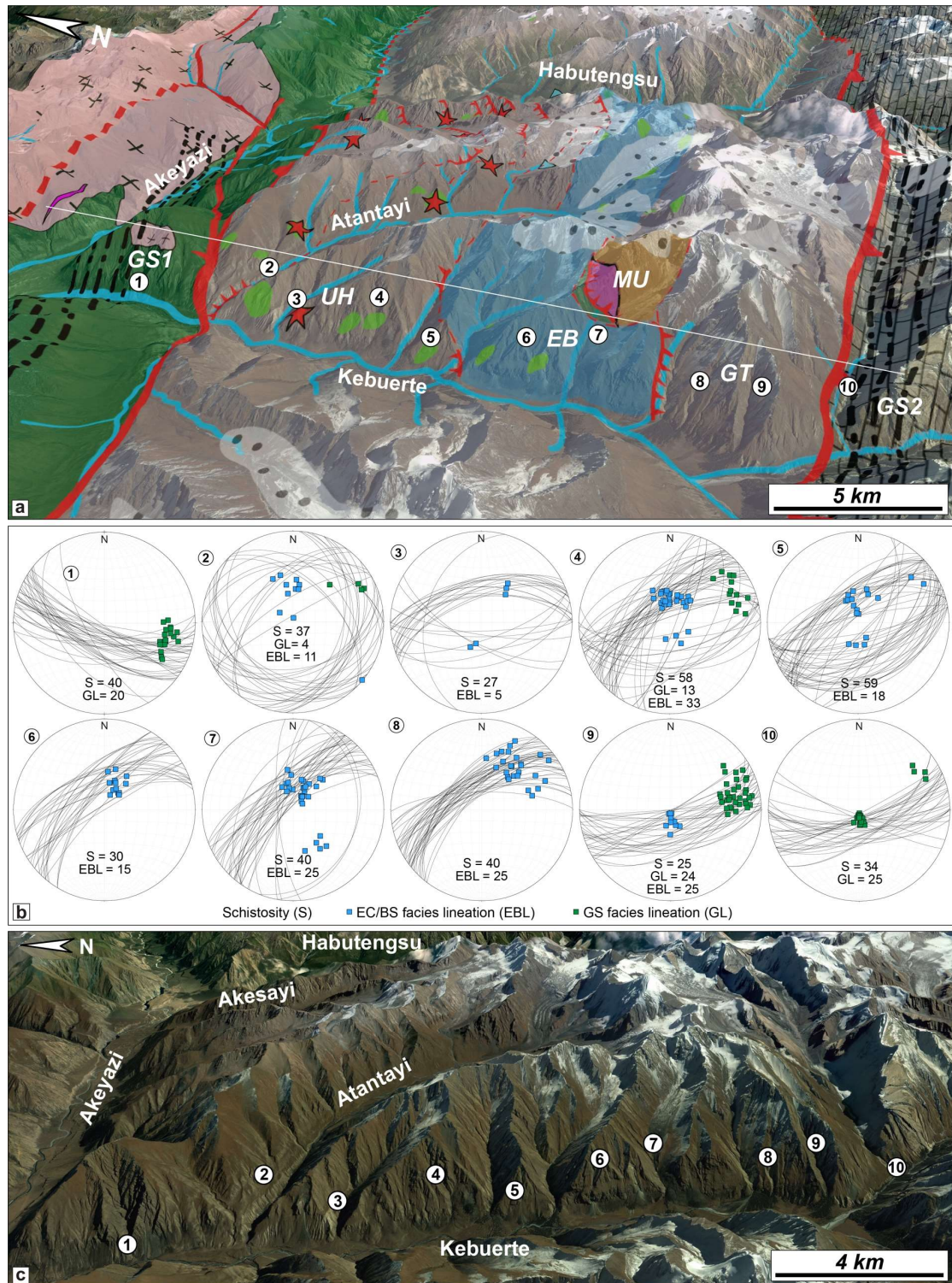


Figure 54: (a) The structural sketch showing the extension on E-W of the revised AMC, with (b, c) the detail data of field structural measurements for the schistosity and lineation.

6.3.2. Deformation stages and deformation patterns

Deformation stages are herein essentially defined based on textures and mineralogy. The main schistosity (noted S_2 in the north of the study area by Soldner et al., 2017) most commonly corresponds to a blue amphibole bearing, blueschist facies schistosity (S_1 is only seldom preserved in eclogitic or eclogite to blueschist facies boudins, in UH or EB units for example, Figure 64a; Soldner et al., 2017; Tan et al., 2017). This schistosity is in fact composite, depending on the extent of retrogression and exhumation-related deformation, and may encompass a range of P-T conditions, from late eclogite to incipient blueschist and even down to a transitional blueschist to greenschist facies. A detailed mapping of regional schistosity by facies should in principle be feasible but was not performed here, in part because eclogite and/or blueschist facies schistositities may correspond to diachronous events in the different sub-units. Crenulation of the dominant schistosity is also evidenced in several exposures (as in Bayet et al., 2018) and more strongly developed in the GS1 and GS2 units. For the sake of comparison with thin-sections and radiometric constraints, deformation are hereafter termed D_e , D_b and D_g . White micas analyzed in situ by laser ablation (for Ar-Ar dating) were denoted S if following the schistosity and C along shear planes.

The dominant schistosity and various stretching lineations are reported in Figure 50c, 52a-c, and 54. The schistosity varies from place to place but dominantly strikes NW-

SE (Figure 52b-c, 54), whatever the lithologies. Some differences are observed for the GS1 and GS2 units, where schistosity is more E-W (Figure 52b-c, 54).

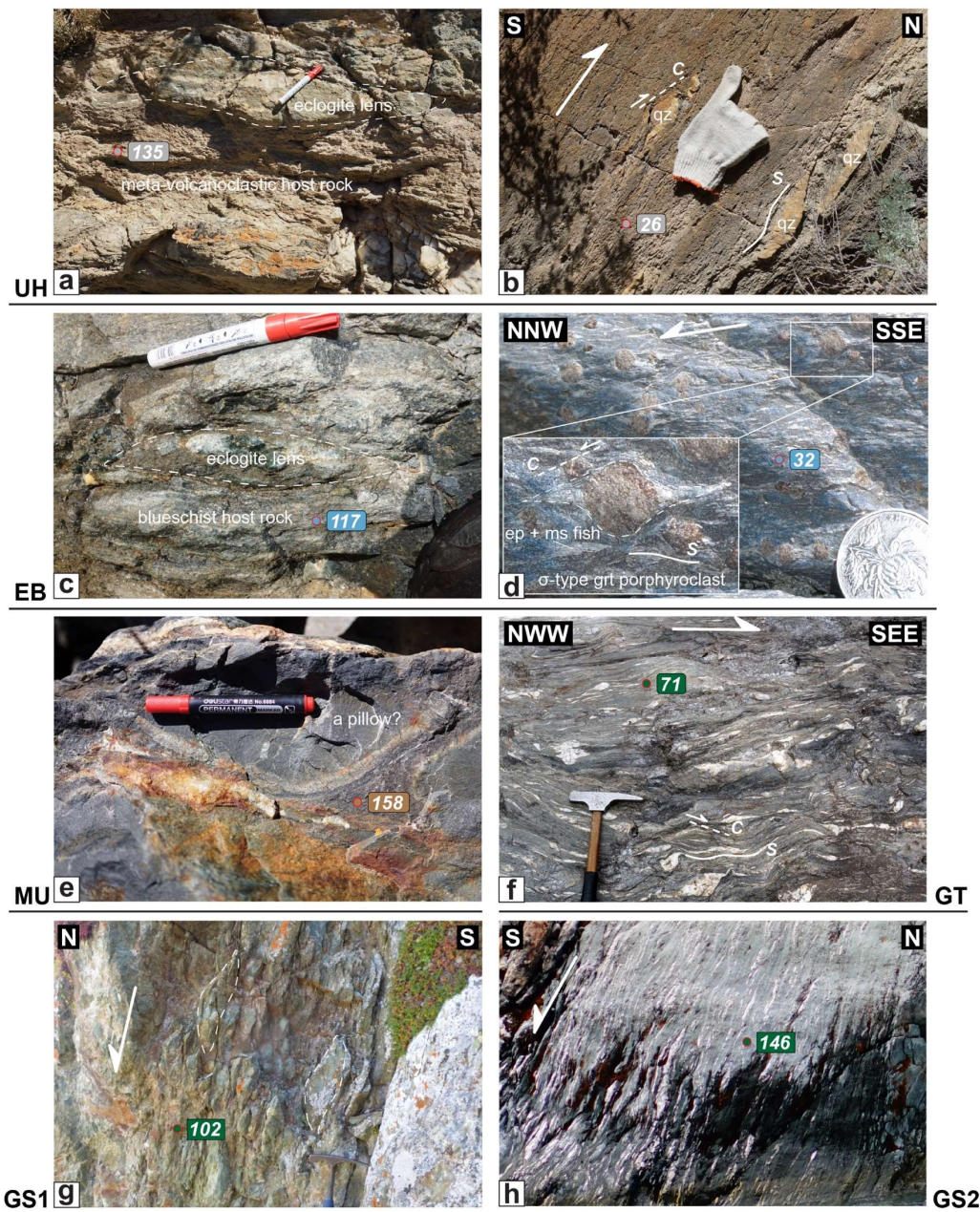


Figure 55: Outcrop observation of representative samples in this study. The letter of sub-figures corresponds to the localities marked in Figure 52c. (a) Metavolcanoclastics (sample, 135) matrix hosting eclogite lens in the UHP/HP complex (UH unit). (b) Stretched quartz veins in metavolcanoclastics (sample, 26) from the UH unit advocating for non-coaxial shearing (top to N). (c) Blueschist matrix (sample, 117) hosting eclogite lens in the EC/BS facies blueschist horizon (EB unit). (d) σ -type garnet porphyroclast in blueschist (sample, 32) from the EB unit indicating a top to NNW shear sense. (e) Specious pillow structure in the metamafic slice (sample, 158) from the Metamafic/ultra-mafic unit (MU unit). (f) Stretched quartz veins in metavolcanoclastics (sample, 71) from the GS facies transitional unit (GT unit) indicating a top to SEE shear sense. (g) Stretched chlorite-quartz assemblage in the GS facies metavolcanoclast (sample, 102) from the North SCTSZ mylonitized shear zone (GS1 unit) advocating for a top to N shear sense. (h) Stretched chlorite-quartz assemblage in the GS facies metavolcanoclast (sample, 146) from the South SCTSZ mylonitized shear zone (GS2 unit) indicating for a top to S shear sense. Also check Figure 64 for the rest of outcrop observations.

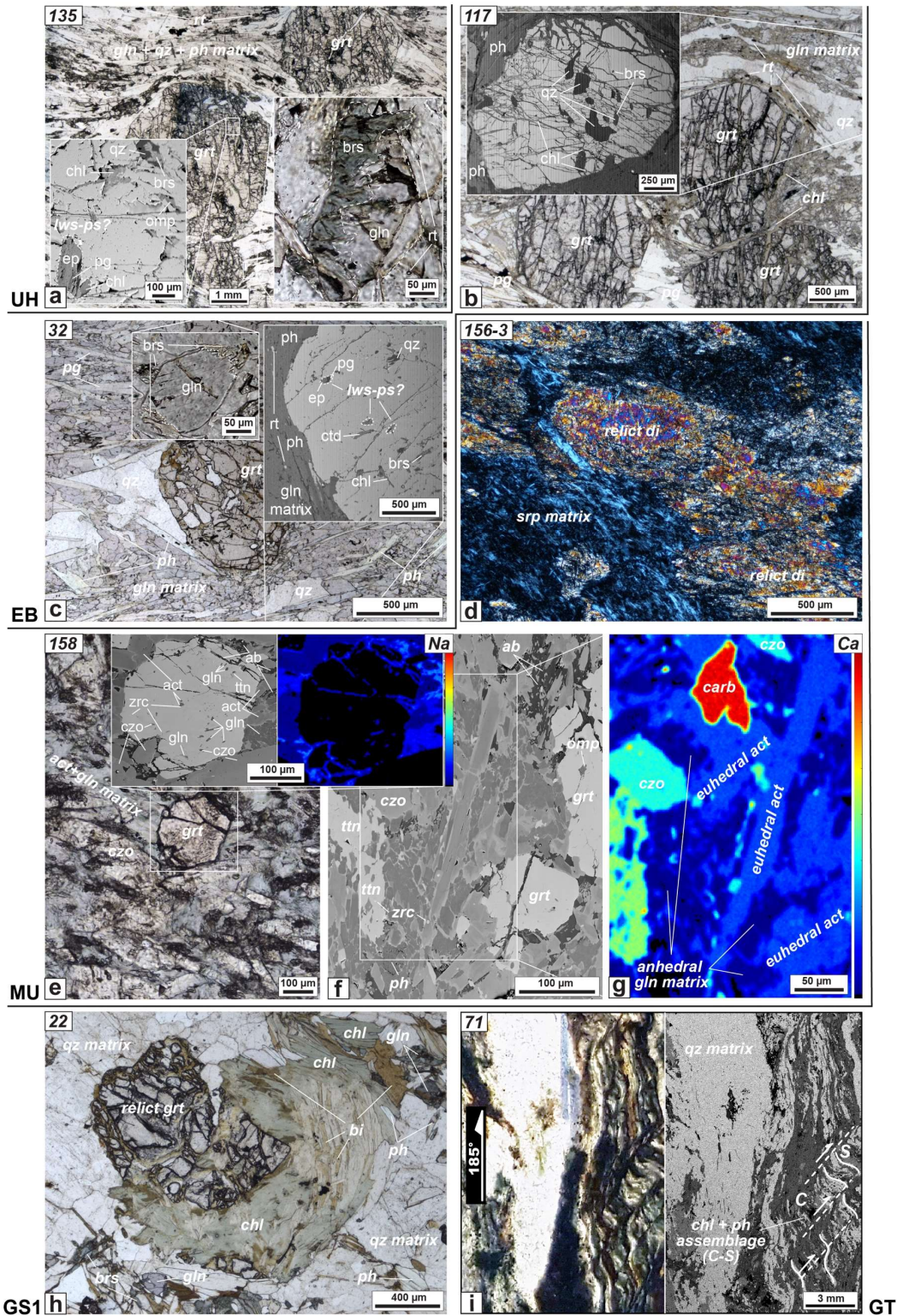


Figure 56: Microphotographs of some of the samples investigated in the present study. Mineral abbreviations are Qz, quartz; Grt, garnet; Ph, phengite; Pg, paragonite; Bi, biotite; Di, diopside; Omp, Omphacite; Gln, Glaucophane; Brs, barroisite; Act, Actinolite; Ep/Czo, epidote/clinozoisite; Chl, chlorite; Ctd, chloritoid; Rt, rutile; Ttn, titanite; Fsp/Ab, feldspar/albite; Carb, carbonate; Srp, serpentine. (a, b, c) Grt-Ph-Amp-Qz-Rt±Cpx±Ep±Chl±Ttn±Ctd±Pg±Bi assemblages and relevant garnet inclusion patterns in metabasalts from the UH and EB units. (d) Serpentinized ultra-mafic rock (sample, 156-3) with relict diopside. (e) Grt-Act-Gln-Brs-Ep-Ttn±Cpx±Pg±Qz±Chl±Ab±Carb assemblage and relevant garnet inclusion pattern in metamafic sample 158 from the MU unit. (f, g) The pattern of the appearance of amphiboles, with euheedral actinolite columnar crystals rounded by anhedraal glaucophane matrix then both partly replaced by barroisite rim, in sample 158 is distinct compared with those in samples from the UH and EB units (normally gln replaced by brs rim), further indicating contrasting P-T (-time) experiences. (h) Strongly retrograded metabasalt (sample, 22) located in the GS1 unit with relict glaucophane and garnet replaced by chlorite+biotite assemblage. (i) S-C structure constructed by chlorite+phengite+quartz assemblage in GS facies metabasalt (sample, 71) from the GT unit indicating a top to E shear sense. Also check Table 15 for the detail of mineral assemblage of each sample and Figure 65 for the rest of microphotographs.

Eclogite to blueschist facies lineations are indicated by elongated omphacite or glaucophane-quartz and/or phengite, respectively (Figure 55a-d, 60b, 64a-c, 66). They cluster along a NNW-SSE strike at \sim N160 (Figure 52a-c, 54). By contrast, GS facies stretching marked by oriented crystals of amphibole, quartz or albite (and more rarely phyllosilicates, i.e. phengite, chlorite, or biotite; Figure 55f-h, 56i, 60b, 64d-e, g-h, 65a-b, d, h-j, 66) lies dominantly along a NEE-SWW trend, around N \sim 040 (Figure 52a-c, 54). GS facies lineations (Figure 55g-h, 63c, 65b, j) observed close to the north and south boundaries of the AMC are nevertheless aligned along a more N-S trend (Figure 52a-c, 54).

Despite ample evidence for recumbent folding and flattening (e.g., Figure 64b-c), regional deformation is relatively non-coaxial, as exemplified by pervasive S-C structures (Figure 55, 56i, 60b, 64-66) and asymmetric folding (although less conspicuous in the EB unit). Shear senses associated with EC/BS and GS facies metamorphism, whether at outcrop scale or in thin-section, are very consistent throughout the area, and respectively top to NNW and top to NEE (Figure 52a-c).

6.4. Sampling strategy and sample description

Sample selection (Figure 51a, 52) was intended at providing samples for average PT comparison between the different sub-units (rather than detailed individual trajectories by thermodynamic modelling; e.g., Tan et al., 2017), ideally for each of the metamorphic equilibration stages, seeking enough textural control on deformation and/or recrystallisation stages that in-situ Ar-Ar dating could be used to provide age

constraints with deformation control. Sampling strategy, geographic coordinates and parageneses are given in Table 15. A brief sample description is given below:

— UH unit:

#135 is a strongly schistosed pelitic metavolcanoclastic rock hosting eclogite lens (Figure 55a) with well-preserved eclogitic paragenesis of Grt-Gln-LwsPs-Omp-Ph-Qz-Rt±Ttn±Brs±Chl (Figure 56a, 60b) and clear top to N shear sense as indicated by elongated glaucophane, phengite and quartz along the schistosity and shear band (Figure 60b, 66). Omphacite was detected both as inclusion in garnet (Figure 56a) and as relict in the gln+qz matrix. Fresh Lawsonite was not found but only pseudomorphs in garnet (Ep+Pg, Figure 56a). This sample represents the host rock of the coesite-bearing HP/UHP eclogite (Figure 51, 52, 69; Tan et al., 2017) and is taken here to represent D_e .

#26 is a strongly schistosed felsic metavolcanoclastic rock with Grt-Ph-Qz-LwsPs-Chl-Rt±Ttn±Carb (Figure 65c), sampled close to the coesite-bearing felsic metapelite of Yang et al. (2013) (Figure 51, 52, 69). Top to N sense of shear is indicated by stretched recrystallized quartz (Figure 55b) and elongated phengite along the schistosity and shear band (Figure 66). As for sample #135, no fresh lawsonite was detected but only pseudomorphs in garnet (Ca-Grt+Pg, Figure 65c). It is also representative of the metavolcanoclastic matrix host rock of the UH unit.

— EB unit:

#117 is a strongly to moderately schistosed pelitic metavolcanoclast hosting eclogite lens (Figure 55c) with Grt-Gln/Brs-Ph-Qz-Rt±Ttn±Chl assemblage (Figure 56b, 66)

and relatively obvious top to N shear sense (Figure 66) as indicated by elongated glaucophane, phengite and quartz along the along the schistosity and shear band. It locates close to the north margin of the EB unit, as representative lithology of the blueschist horizon.

#32 is a strongly schistosed pelitic metavolcanoclastic rock with Grt-Gln/Brs-Qz-Ctd-Rt±Ttn±Chl assemblage (Figure 56c, 60b, 66) and clear top to N shear sense (Figure 60b, 66) as indicated by elongated glaucophane, phengite and quartz along the along the schistosity and shear band. No fresh lawsonite was detected but pseudomorph in garnet (Ep+Pg; Figure 56c). It locates at the central part of the EB unit, as representative lithology of the blueschist horizon (Figure 55d).

— MU unit:

#157 is a moderately to weakly schistosed felsic metavolcanoclastic rock with GS facies Ph-Chl-Ab-Qz assemblage (Figure 65d, 66) and relatively obvious top to NE shear sense from outcrop observation (Figure 64e). It locates at the north margin of the MU unit associated with the meta-ultramafic rock and probably represents an individual contact between the EB and MU units (Figure 53c). Both in situ and step-heating ⁴⁰Ar-³⁹Ar radiometric analyses were performed for this sample.

#156-1 is a moderately to strongly schistosed metamafic/ultramafic schist with MgChl-Ttn assemblage (Figure 65e). It is associated with the serpentinite slice in the MU unit as vein or thin layers (Figure 64f).

#156-2 is a metaultramafic (rodingite?) vein with Grs-Di-Chl assemblage (Figure 65f). It locally crosscuts the serpentinite slice in the MU as vein (Figure 64f).

#156-3 is the mainly representative lithology of the serpentinite slice in the MU unit, with Srp-Di assemblage (Figure 56d). It was strongly schistosed but no sense of shear can be observed (Figure 64f). It is locally closely associated to south with the metabasite slice with inferred contact (Figure 53c). As for the other two former samples, only microprobe work was performed for this sample.

#158 is more mafic than typical samples from the EB unit. It was sampled next to probably former pillows (Figure 55e). It shows a complex mineral assemblage with Grt-Czo-Gln/Brs/Act±Ph±Ttn±Omp±Ab±Chl (Figure 56e-g). Elongated euhedral actinolite is wrapped by a relatively anhedral glaucophane matrix, and both are replaced by later barroisite. Phengite and omphacite are rare and only found as relic in the matrix (Figure 56f-g) or as inclusion in epidote. Zircon separation was performed for LA-ICPMS trace elements and U-Pb measurements for this sample.

— GT unit:

#147 is a weakly schistosed, relatively mafic rock with a Grt-Ph-Pg-Chl-Ab-Qz-Ep±relict Gln±Carb±Bi assemblage (Figure 65g). The appearance of relict glaucophane implies it probably experienced lower BS facies metamorphism prior to the regional GS facies overprinting marked by the significant replacement of garnet/phengite by biotite+chlorite (Figure 65g). No clear shear sense could be found on the outcrop, and only ^{40}Ar - ^{39}Ar step-heating was performed for this sample.

#148-1 is a strongly schistosed felsic metavolcanoclastic rock with Grt-Ph-Chl assemblage (Figure 65h, 66). Top to NEE sense of shear was observed as indicated by stretched recrystallized quartz vein (Figure 64g) and mica “fish” (Figure 65h, 66). It

locates at the central part of the GT unit. The sample was prepared for in situ phengite ^{40}Ar - ^{39}Ar radiometric, specifically testing whether the large mica “fish” (~3mm across; Figure 65h, 66) recorded potential excess Ar.

#148-2 is a strongly schistosed felsic metavolcanoclastic rock with Grt-Ph-Chl assemblage (Figure 65i, 66), sampled close to #148-2 but with contrasting sense of shear in the GT unit. Top to N shear sense was indicated by relict σ -porphyroblast, elongated phengite and quartz along the schistosity and shear band (Figure 65i, 66).

#71 is a strongly schistosed pelitic metavolcanoclastic rock with Ph-Chl-Qz \pm Ab assemblage (Figure 56i, 60b, 66) sampled close to the southern margin of the GT unit. Top to S sense of shear was indicated by stretched recrystallized quartz vein (Figure 55f) and phengite+chlorite+quartz along the schistosity and shear plane (Figure 56i, 66).

— GS1 and GS2 units:

#J2 is a strongly schistosed pelitic metavolcanoclastic rock with Ph-Bi-Chl-Qz assemblage (Figure 65a). It locates at the central part of the GS1 unit. Top to NEE sense of shear was indicated by stretched recrystallized quartz vein (Figure 64d) and phengite+quartz along the schistosity and shear plane (Figure 65a).

#102 is a moderately to strongly schistosed pelitic metavolcanoclastic rock (Figure 55g) from the south margin of GS1, close to the UH unit with Act-Ep-Chl-Ph-Qz \pm Ab \pm Ttn \pm Carb assemblage (Figure 65b). Top to N sense of shear was indicated by sigmoidal (Figure 55g) and chlorite+phengite+quartz along the schistosity and shear plane (Figure 65b). Only microprobe analyses were performed for this sample.

#22 is a weakly schistosed metavolcanoclastic rock located in the GS1 unit adjacent to the north margin of the UH unit, with Grt-Ph-Bi-Chl-Qz±relict Gln/Brs assemblage (Figure 56h). Relictual glaucophane/barroisite hints to BS facies metamorphism prior to the regional GS facies. No clear sense of shear can be found on outcrop/sample-scale, therefore phengite grains were picked up only for ^{40}Ar - ^{39}Ar step-heating radiometric analysis.

#146 is a strongly schistosed pelitic rock from the northern margin of GS2, close to the GT unit (Figure 55h), with Chl-Ph-Qz±Ab±Ttn assemblage (Figure 65j). Top to S sense of shear was indicated by stretched recrystallized quartz vein (Figure 55h) and chlorite+phengite+quartz along the schistosity and shear plane (Figure 65j).

Mineral habits, textural relationships and microstructural location were used to select minerals for multiequilibrium calculations. In general, the following deformation-crystallization relationships were observed:

— In the schistosed garnet-bearing metavolcanoclastic samples (e.g., *samples 135, 26, 117, 32, 148*), relative euhedral or relictual garnet appears as millimeter to centimeter-sized σ -type porphyroblast in textural equilibrium with recrystallized blue amphibole-phengite-quartz tails (Figure 55d, 56a-c, 65c, h-i).

— In the schistosed garnet-free metavolcanoclastic samples (e.g., *samples J2, 102, 157, 71, 146*), biotite/phengite-chlorite±green amphibole±epidote appear as matrix minerals in textural equilibrium around albite/quartz porphyroblasts constituting synkinematic structures with clear shear senses along millimeter-sized shear bands (Figure 55f-h, 56i, 64d-e, 65a-b, d, j).

— In the weakly schistosed metavolcanoclastic and metavolcanics samples (e.g., *samples 22, 147, 148*), although garnet is significantly replaced by chlorite-biotite/phengite and displays irregular rims, textural equilibrium with matrix phengite-quartz/albite±chlorite±relict blue amphibole is preserved in places (Figure 56h, 65g-i).

— In the undeformed metavolcanics sample (sample, *158*), a complex metamorphic history is recorded by multistage green/greenish blue/blue amphibole growth together with garnet±epidote±omphacite±phengite±albite (Figure 56e-f).

Minerals involved in the same microstructural domain (e.g., S-C structures, Figs. 60b, 66) and in close contact were considered to have crystallized coevally. In parageneses involving garnet, mineral inclusions (e.g., Figure 56a-c, e, 65c) were assumed to be in equilibrium with the corresponding garnet core/mantle compositions. Minerals recrystallized as tails around σ -type porphyroblast were assumed to be in equilibrium with the garnet rim compositions. Detail of selected mineral assemblages for P-T estimates is listed in Figure 59c and Table 17.

6.5. Analytical Methods

6.5.1. Whole-rock chemistry

Analyses were performed at the Institute of Geology and Geophysics of the Chinese Academy of Sciences (IGGCAS), using ICP-MS with a Finnigan MAT ELEMENT spectrometer and Institut des Sciences de la Terre de Paris (ISTeP), Sorbonne Université, France with ICP-MS 8800 Triple Quadrupole. Relative standard deviations (RSD) are within $\pm 10\%$ for most trace elements but reach $\pm 20\%$ for V, Cr,

Co, Ni, Th and U according to analyses of rock standards. Relevant data is plotted in Figure 57 and listed in Table 19.

6.5.2. Mineral Chemistry

Mineral analysis was performed on key minerals preserved from retrogression, as inclusions within garnet and/or in the matrix, using a CAMECA SX FIVE electron probe at ITeP, Sorbonne Université (15Kv, 10nA, WDS), France using Fe₂O₃ (Fe), MnTiO₃ (Mn, Ti), diopside (Mg, Si), Cr₂O₃ (Cr), orthoclase (Al, K), anorthite (Ca) and albite (Na) as standards. Data is shown in Figure 58 and representative analyses are listed in Table 16.

6.5.3. Thermobarometry

6.5.3.1. THERMOCALC average P-T

The internally consistent thermodynamic dataset (tc-ds55) and the program THERMOCALC v3.33 (Holland and Powell, 1998, 1990) were applied for multiequilibrium P-T estimates. Structural formulae and end-member activities were calculated with the AX program (<ftp://www.esc.cam.ac.uk/pub/minp/AX/>). Only P-T estimates passing the equilibrium test criteria (e.g., sigfit, hat; Holland & Powell, 1998) have been considered in this study (Figure 59). Precision of P-T estimates is generally on the order of 0.05-0.2GPa for pressure and 10-30°C for temperature. The merely present end-members (e.g., Fe-celadonite/celadonite for some phengite, Figure 58c)

yielding a large uncertainty on the results were removed during calculation (check Table 17 for detail).

6.5.3.2. Raman Spectroscopy of Carbonaceous Material Thermometry

The Raman spectroscopy of carbonaceous material (RSCM, calibrated in the range 330-650°C; Beyssac et al., 2002) is used here to obtain peak temperature estimates independent from those of THERMOCALC. While absolute calibration is $\pm 50^\circ\text{C}$, intersample comparison allows detecting much smaller temperature differences, around 10-15°C (Beyssac et al., 2004). RSCM was done on thin sections of graphite-bearing metavolcanoclastics oriented perpendicular to the foliation by focusing the laser beam beneath a transparent crystal. Raman spectra were obtained with a Renishaw INVIA Reflex Raman microspectrometer at the Laboratoire de Géologie of the Ecole Normale Supérieure, France. Spectra were excited at room temperature with the 514.5 nm line of a 20 mW Ar Spectra Physics laser through a LEICA 100X objective (NA 0.90). At least 13 spectra were collected for each sample, to take into account the CM heterogeneities, and processed with the program Peak Fit 4.0. Temperature estimates are given in Table 17.

6.5.3.3. Titanium in Biotite Thermometry

An empirical Ti-in-biotite geothermometer (Henry et al., 2005), calibrated in the range 0.4-0.6 GPa and 480-800°C, for compositions of $X_{\text{Mg}} = 0.275-1.000$ and $\text{Ti} = 0.04-0.60$ apfu, is used to derive temperature estimates for regional GS facies metamorphism recorded by biotite-bearing metavolcanoclastics (Table 17). Precision

of the Ti-in-biotite thermometer is estimated to be $\pm 24^{\circ}\text{C}$ at the lower temperature range and improves to $\pm 12^{\circ}\text{C}$ at higher temperatures.

6.5.4. Radiochronology

Eleven samples for which P-T-kinematic constraints were collected (§ 5 and 6) were selected from different tectonic sub-units (Figure 52d, 60a). Seven of them with syntectonic textural features (Figure 60b, 66) were dated by the ^{40}Ar - ^{39}Ar in situ laser ablation technique on phengite grains from rock slices already analysed by microprobe. ^{40}Ar - ^{39}Ar step-heating analyse on phengite (Figure 67) was performed for four weakly to moderately schistosed samples (Figure 56h, 65a, d, g). Additional radiometric constraints by zircon U-Pb isotopic analysis were obtained for one metamafic sample from the MU unit (Figure 56e-g, 67). Age results are presented in Figure 60 together with representative examples of ^{40}Ar - ^{39}Ar in situ dating. Further details are given in Figure 60b, 66 and 67, and data are listed in Table 18, 20 and 21.

5.4.1 ^{40}Ar - ^{39}Ar In Situ Laser Ablation Analysis

The ^{40}Ar - ^{39}Ar in situ laser ablation technical procedure was first proposed by Schaeffer et al. (1977) and modified by Maluski & Monié (1988). Sample preparation and analysis (procedure as in Agard et al., 2002, 2006; Augier et al., 2005) were conducted at Géosciences Montpellier, France. The laser system consists of a continuous 6W argon ion laser, a beam shutter for selection of lasering exposure time, with typically 5ms pulses separated by 40ms, and a set of lenses for beam focusing. The number of pulses depends on the nature of the analyzed mineral, its K content and

its presumed age. Argon extraction, purification and analyses are performed within three distinctive parts with the sample chamber where gas extraction is done, the purification line with hot getters and nitrogen liquid traps (cold) traps, and a MAP 215-50 noble gas mass spectrometer equipped with an electron multiplier. Rock sections 500 μm thick, which had been used to make the petrographic thin sections, were double polished within 1 μm tolerance. Whole section and detailed area photographs of both the rock section and corresponding thin section were taken for an accurate selection of favorable areas during laser experiments. All samples were ultrasonically rinsed in ethanol and distilled water, wrapped in pure aluminum foils and then irradiated in the McMaster nuclear reactor (Canada) with several aliquots of the MMHb-1 international standard ($520.4 \pm 1.7\text{Ma}$, Samson & Alexander Jr, 1987). After irradiation, both the monitors and the sections were placed on a Cu holder inside the sample chamber and heated for 48h at 150-200°C.

For each age determination, argon was extracted from a 150 \times 300 μm surface corresponding to a mixture of several phengite grains, given grain size (Figure 59b, 68). The crater is a 30-40 μm approximate hemisphere surrounded by a circular wall made of melted material. Incision of the sample did not exceed 10-20 μm deep depending on the three-dimensional orientation of the phengite crystals. Once the extraction was completed, about four minutes were required for gas cleaning of the line and 15 min for data acquisition by peak jumping from mass 40 to mass 36 (8 runs). For each experiment, ages have been obtained after correction with blanks, mass discrimination, radioactive decay of ^{37}Ar and ^{36}Ar and irradiation-induced mass interferences. They are

reported with one sigma uncertainty (Table 18) and were evaluated assuming an atmospheric composition for the initially trapped argon (i.e., $(^{40}\text{Ar}/^{36}\text{Ar})^i \sim 295.5$).

5.4.2 $^{40}\text{Ar}/^{39}\text{Ar}$ Step-Heating Analysis

Selected samples were crushed and sieved. Single grains of phengite were handpicked under binocular microscope and cleaned in ultrasonic bath with acetone and distilled water. They were packaged in Al foils and irradiated for 40h in the core of the Triga Mark II nuclear reactor of Pavia (Italia) with several aliquots of the Fish Canyon sanidine standard (28.03 ± 0.08 Ma, Jourdan & Renne, 2007) as flux monitor. Argon isotopic interferences on K and Ca were determined by irradiation of KF and CaF₂ pure salts from which the following correction factors were obtained. Argon analyses were performed at Géosciences Montpellier, France with two analytical devices that each consist of: (a) an IR-CO₂ laser of 100kHz used at 5-15% during 60s, (b) a lenses system for beam focusing, (c) a steel chamber, kept at 10^{-8} - 10^{-9} bar, with a drilled copper plate, (d) an inlet line for purification of gases including two Zr-Al getters, (e) a multi-collector mass spectrometer (Argus VI from Thermo-Fisher). A custom-made software controls the laser intensity, the timing of extraction/purification and the data acquisition. To measure the Ar background within the system, one blank analysis was performed every three sample analyses. ArArCalc v2.5.2 was used for data reduction and plotting. The two-sigma errors reported on plateau, isochron and total gas ages include the error on the irradiation factor J. Atmospheric ^{40}Ar was estimated using a value of the initial $^{40}\text{Ar}/^{36}\text{Ar}$ of 295.5.

5.4.3 U-Pb dating and trace element analysis of zircon by LA-ICP-MS

U-Pb dating and trace element analysis of zircon were simultaneously conducted by LA-ICP-MS at the Wuhan SampleSolution Analytical Technology Co., Ltd., China. Detailed operating conditions for the laser ablation system and the ICP-MS instrument and data reduction are the same as in Zong et al. (2017). Laser sampling was performed using a GeolasPro laser ablation system that consists of a COMPexPro 102 ArF excimer laser (wavelength of 193nm and maximum energy of 200mJ) and a MicroLas optical system. An Agilent 7700e ICP-MS instrument was used to acquire ion-signal intensities. Helium was applied as a carrier gas. Argon was used as the make-up gas and mixed with the carrier gas via a T-connector before entering the ICP. A “wave” signal smoothing device is included in this laser ablation system (Hu et al., 2015). The spot size and frequency of the laser were set to 60 μ m and 6Hz, respectively, in this study. Zircon 91500 and glass NIST610 were used as external standards for U-Pb dating and trace element calibration, respectively. Each analysis incorporated a background acquisition of approximately 20-30s followed by 50s of data acquisition from the sample. An Excel-based software ICPMSDataCal was used to perform off-line selection and integration of background and analyzed signals, time-drift correction and quantitative calibration for trace element analysis and U-Pb dating (Liu et al., 2009). Concordia diagrams and weighted mean calculations were made using Isoplot/Ex_ver3 (Ludwig, 2003).

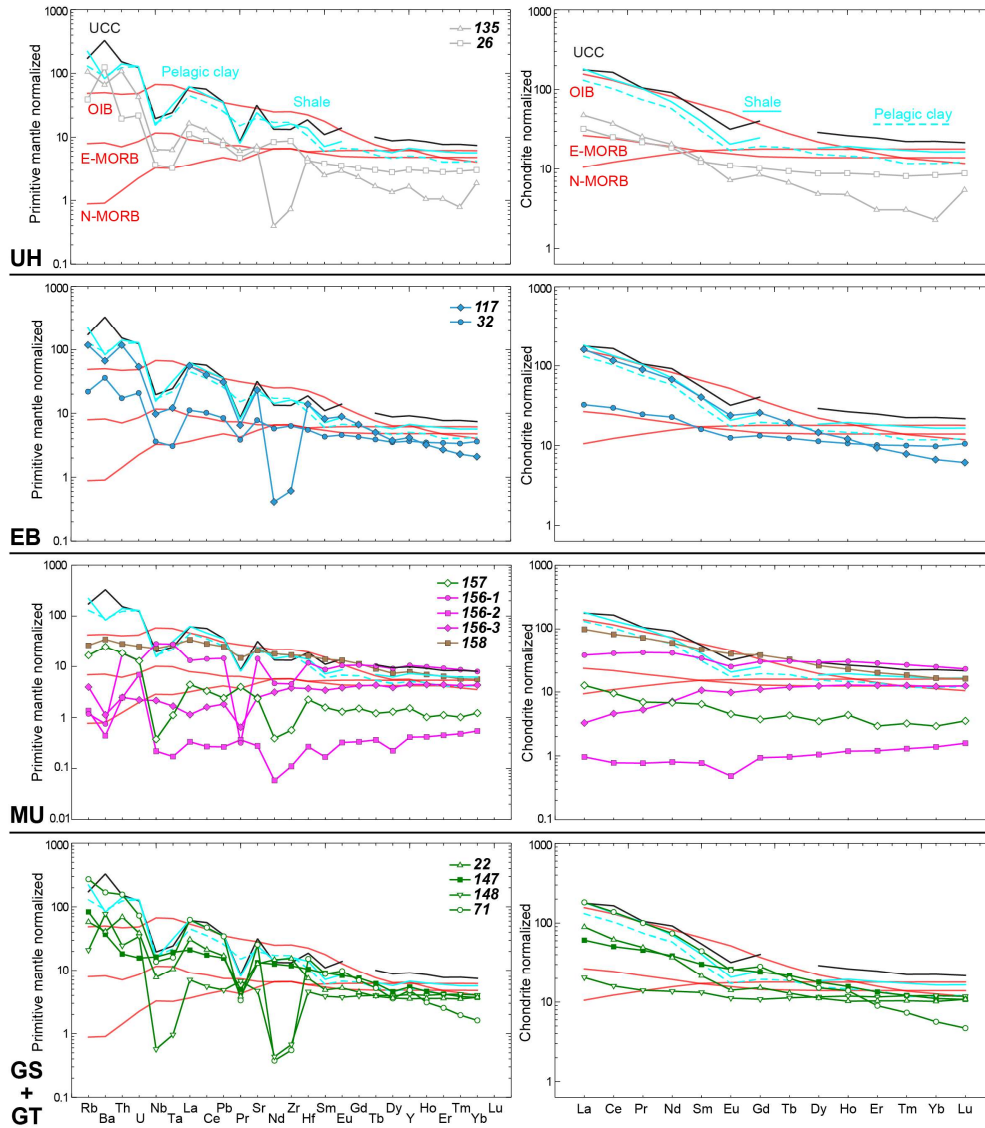


Figure 57: Primitive mantle-normalized spider diagram and chondrite-normalized REE pattern for samples in this study (Table 19).

6.6. Results

6.6.1. Bulk chemistry of major lithologies

The protolith lithologies of samples in this study mainly correspond to metavolcanoclastics, metavolcanics and meta-ultramafic rocks.

— The metavolcanoclastic samples locally contain mud/silty/sand components that either resemble metapelite or quartz-rich metagraywacke as reflected by the main

parageneses, which comprise Grt-Ph-Amp-Qz-Rt±Cpx±Ep±Chl±Ttn±Ctd±Pg±Bi (e.g., *samples 22, 135, 117, 32*; abbreviations after Table 15), Grt-Ph-Qz-Chl-Rt±Pg±Ab±Ttn (e.g., *sample 26*) and Ph-Qz-Chl-Ab±Grt±Pg±Ttn±Amp±Carb±Bi±Ep (e.g., *samples J2, 102, 157, 148, 71, 146*). They uniformly show significant Rb/Ba/Th/U/Pb enrichments and notable Nb-Ta depletions in primitive mantle-normalized (PM) trace element pattern and a steep negative slope ($(La/Yb)_N = 1.69-32.2$, Table 19) in chondrite-normalized REEs pattern (Figure 57), similar to that of the average upper continental crust (UCC, Rudnick & Gao, 2003) or trench sediment (Li & Schoonmaker, 2003; Plank & Langmuir, 1998). These lithologies are found in all sub-units, without significant differences, except in MU.

— The metavolcanics are dominantly mafic, as reflected by Grt-Amp-Ph-Ep-Rt-Ttn±Cpx±Pg±Qz±Bi±Chl±Ab±Carb parageneses (e.g., *samples 158, 147*). They were here only sampled in units MU and GT. Their moderate Rb/Ba/Th/U/Pb enrichments and lack of detectable Nb-Ta depletions in primitive mantle-normalized trace element pattern, and a moderately negative slope ($(La/Yb)_N = 5.51-5.95$, Table 19) in chondrite-normalized REEs pattern (Figure 57) fall into the range between that of ocean island basalt and enriched mid-ocean ridge basalt (OIB, E-MORB, Sun & McDonough, 1989).

— The meta-ultramafic rocks are serpentinized and/or metasomatized with parageneses consisting of MgChl-Ttn (e.g., *sample 156-1*), Grs-Cpx-Chl (e.g., *sample 156-2*), Srp-Cpx (e.g., *sample 156-3*). They present Rb/Ba/Th/U/Pb comparable to PM and a slightly positive slope ($(La/Yb)_N = 0.27-1.53$, Table 19) in chondrite-normalized REEs pattern (Figure 57).

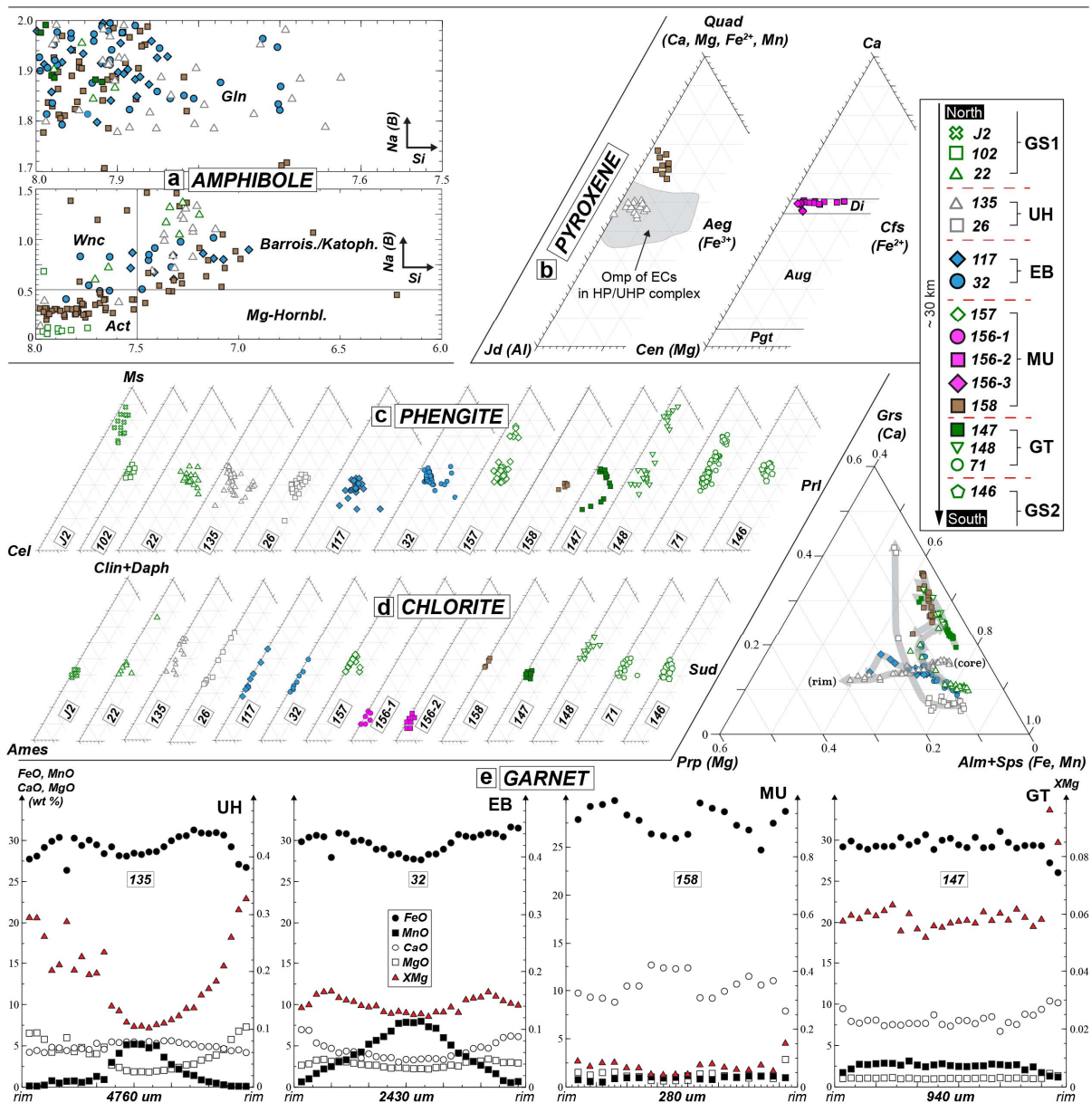


Figure 58: Mineral plots of compositions determined with the electron probe microanalysis (check Table 16 for detail data). XMg is herein after taken as $Mg/(Mg+Fe^{2+})$. (a) Na (site B) versus Si content in all the AMC amphiboles analyzed in this study. Compositions mainly cluster in the glaucophane field and around a composition intermediate between actinolite and barroisite but almost span the entire range. Terminology is after Hawthorne & Oberti (2006). (b) Composition of sodic and calcic clinopyroxenes (Morimoto, 1988). (c) Phengite composition variations, which are mostly parallel to the muscovite-celadonite (Ms-Cel) joint. The variations are dominated by the tschermak substitution exchange vector $Si(Mg, Fe)-2Al$ as for most metavolcanoclastics and metavolcanics. Note that phengite in sample 135 and 26 from the UH unit reach exceptionally high tschermak values ($Si^{4+} > 3.6$, Table 16). (d) Chlorite plot mostly along the amesite-clinocllore (Ames-Clin) joint as a result of the tschermak substitution. (e) Triangular plot for garnet composition expressed as a function of their grossular, pyrope and almandine (+spessartite) content. Thick gray arrows indicate core to rim evolution of the composition observed in the garnet profiles of each sample. Garnet profile patterns of representative samples from different sub-units are also present as examples.

6.6.2. Mineral compositions

6.6.2.1. Phengite

White mica compositions are mostly phengitic with variations along the tschermak Si (Fe, Mg) = AlAl exchange vector between muscovite and celadonite, as shown by Figure 8c. The deviation from the purely phengitic substitution trend (Figure 58c) is observed for all samples, which suggests that a certain amount of ferric iron is present. Phengite is the main matrix mineral in most metavolcanoclastic samples (Figure 56, 60b, 65, 66), showing several distinct generations with respect to porphyroblasts and/or C-S structures (see § 4). Microprobe images also reveal complicated multistage growth structure (e.g., Figure 68) or contamination by biotite growth (Figure 56h, 65g). The Si content of samples from the UH unit (3.38-3.66) is higher than that from the EB (3.34-3.50), MU (3.35-3.45), GS1/2 (3.07-3.45) and GT units (3.05-3.38), especially with a few crystals with high Si content in sample 26 (Si = 3.66). Larger variations of compositions are observed in samples 148 and 71 (GT), 135 (UH) and 117 (EB), and partial clusters in 157 (MU) and 148 (GT). These variations are compared below to age constraints, in particular in situ analyses.

6.6.2.4. Amphibole

Blue or blue-green amphiboles were detected either as inclusion or matrix mineral in most garnet-bearing samples (samples 22, 135, 117, 32, 158, 147, Figure 56a-c, e-h, 65g) with compositions varying largely and ranging from glaucophane to barroisite to actinolite (Figure 58a). Barroisite replaces glaucophane in many of the high grade metavolcanoclastics (samples 135, 117, 32, Figure 56a-c), as a consequence of

retrogression, but the opposite evolution is documented in sample *158*, with euhedral actinolite rimmed by an anhedral glaucophane matrix (Figure 56e-g).

6.6.2.3. Clinopyroxene

Omphacitic clinopyroxene (Figure 58b) is common in metavolcanic rocks and true eclogites of the UH unit (e.g., Gao et al., 1999; Tan et al., 2017). In the selected metavolcanoclastic samples, it was only found as small crystals in garnet and/or in the matrix of samples *135* and *158* (~100 μm , Figure 56a, e-f, 68a), with average compositions between ~48% jadeite and ~6% acmite end-members (and ~46% diopside) for the former and between ~30% jadeite and ~5% acmite end-members (and ~65% diopside) for the latter, which is out of the common area of omphacite from regional eclogites (unpublished compilation). Diopside (Figure 58b) appears as a relict mineral wrapped by serpentine matrix or vein crosscutting grossular matrix in metaultramafic rocks (samples, *156-1 to -3*, Figure 56d, 65e-f).

6.6.2.4. Chlorite

Chlorite compositions are mainly ferrous and range between clinochlore/daphnite and amesite along the tschermak exchange vector (Figure 58d), with $X_{\text{Mg}} \sim 0.16\text{-}0.50$. It either appears as the main matrix mineral in the low to intermediate grade metavolcanoclastics (Figure 56i, 65a-b, d, j) or retrograde mineral rimming/cutting porphyroblasts (Figure 56a-c, h, 65g-i). Significantly magnesium-rich chlorite, with $X_{\text{Mg}} \sim 0.55\text{-}0.88$, is found only as prograde mineral inclusion in garnet (Figure 56b, 65c) or matrix mineral in metaultramafic samples (Figure 65e-f). Deviation toward sudoite is very limited.

6.6.2.5. Garnet

Garnet is dominantly ferrous (FeO ~23.7-34.8wt%), with X_{Mg} values ranging from 0.04 to 0.24 (Figure 58e). The evolution of garnet zoning is characterized by a Mn decrease with a Ca, Fe and Mg fluctuation toward rim in samples from the UH and EB sub-units (Figure 58e), with limited reequilibration on the garnet rims. In detail, diverse patterns (Figure 58e) are encountered for metavolcanoclastic (e.g., samples *135*, *32*) and metavolcanic rocks (e.g., samples *158*, *147*) from the different sub-units.

6.6.2.6. Others

No fresh lawsonite was found but only box-shaped pseudomorphs (epidote +albite/paragonite±chlorite assemblages, Figure 56a, c, 65c) in the garnet of samples *135*, *26*, *32*. Coesite was assumed to appear at or near the metamorphic peak of UH samples since i) sampling locations (i.e., samples *135*, *26*, Figure 51a, 52a) are very close to previous UHP reports of coesite, ii) the UH unit was confirmed as a UHP unit with ubiquitous coesite (Figure 50c, 51a, d; Bayet et al., 2018). Epidote appears as matrix mineral (Figure 56e-g, 66b, g) and inclusion (occasionally within the box-shaped lawsonite pseudomorphs; Figure 56a, c), with a pistacite composition varying between 0.12 and 0.58 but broadly constant in each sample. Biotite either appears as the main mineral making up the schistosity in sample *J2* (Figure 66a) or replaces garnet/phengite (Figure 56h, 66g) in samples *22*, *32* and *147*. Its composition lies along the tschermak substitution trend between eastonite and phlogopite/annite with Si ~2.75-2.91, X_{Mg} ~0.34-0.58 and Ti ~0.06-0.10apfu. Plagioclase is purely albitic in composition in all relevant samples.

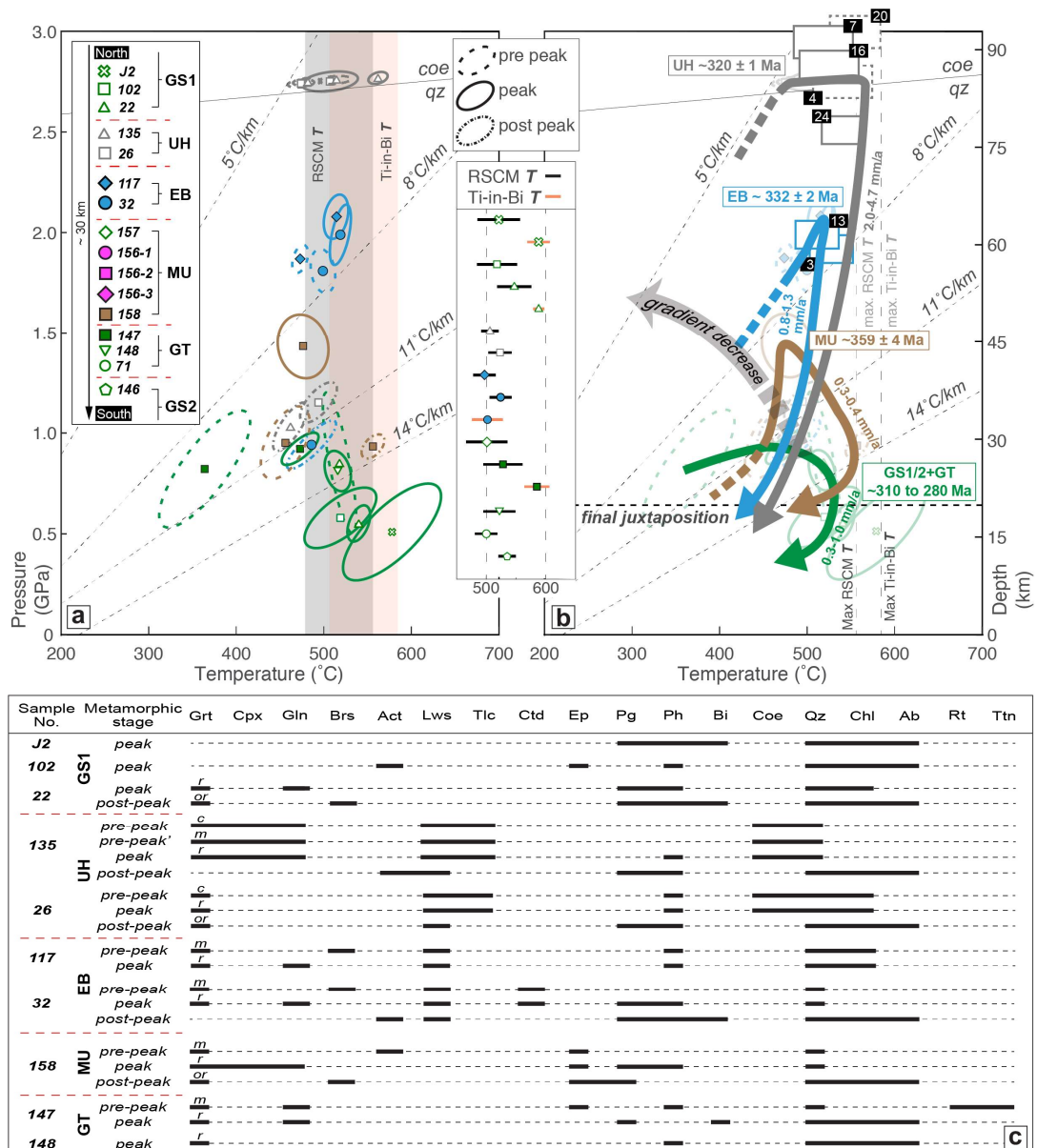


Figure 59: P-T plot showing the results of our P-T estimates using THERMOCALC (Holland & Powell, 1990) together with estimates of metamorphic temperature by the Raman spectroscopy of carbonaceous material (RSCM, Beyssac et al., 2002; Beyssac et al., 2004) and Ti-in-biotite geothermometry (Henry et al., 2005). Ellipses indicate confidence intervals obtained with THERMOCALC. Ellipses with nondense dash-, solid- and dense dash-lines respectively correspond to P-T estimates for pre-peak, peak and post peak metamorphism. (a) Results without further interpretations. (b) Results plotted with synthetic P-T paths, radiometric indications and geodynamic implications (e.g., exhumation velocities) for different sub-units. Colored rectangles (solid-line: metavolcanics, dash-line: metavolcanoclastics) showing previous works, which belong/close to the same sub-units as redefined in this study Figure 69, Table 22), with relatively precise P-T estimates tied to comparable age constraints. Numbers in black boxes correspond those in Table 22, for the detail compilation of regional P-T-time works. Notes that average peak P-T estimates correspond to a metamorphic P-T gradient decrease for rocks exhumation from different depths: the UH ~5, Eb ~7, MU ~10 and GT ~12°C/km. The maximum burial conditions of each sub-units were reached at the timing broadly as their index minerals (i.e., phengite or zircon) recorded and revealed by in situ Ar-Ar or U-Pb technique (Figure 60, 66): the UH ~320, EB ~330, MU ~360 and GT ~310 Ma. The final juxtaposition of these sub-units could take place around 280-300 Ma, as echoed by the dominance of ages within this range probed from moderately substituted phengite in samples amongst all those four sub-units (Figure 60, 66). (c) List of selected mineral assemblages of each sample for the THERMOCALC average P-T calculation. Also check Table 16 for corresponding mineral compositions.

Calculations Performed With THERMOCALC ^a Average P-T and RSCM & Ti-in-biotite Thermometers																											
Minerals involved in the Paragenesis ^b																											
Sample	Metamorphic stage	Qz	Coe	Grt	Ph	Pg	Bl	Cpx	Amp	Ep/Czo	Chl	Cld	Others	Mod ^c	THERMOCALC average P-T					RSCM T.		Ti-in-biotite T.					
															P (GPa)	dP	T (°C)	dT	cor.	Fit	Fit ^c	T _{max} (°C)	dT	n	T (°C)	dT	n
J2	peak	+	-	-	ph4	+	bi3	-	-	-	chl5	-	fsp	cel, ann, feel	0.51	0.24	578	56	0.74	0.7	2.0	521	36	15	588	19	10
GS1	peak	+	-	-	ph3	-	-	-	act6	ep4	chl4	-	fsp	ames, cel, fact	0.58	0.15	519	41	0.67	0.2	2.0	518	34	17	-	-	-
22	peak	+	-	grt19	ph9	+	-	-	gln1	-	chl8	-	-	gr	0.85	0.35	518	19	-0.78	1.1	1.7	547	29	21	588	10	12
	post-p	+	-	grt1	ph1	+	bi1	-	brs5	-	chl2	-	fsp, parq, cel, feel, ts, clin, phl, ann, fact	gr	0.55	0.09	540	13	0.46	0.8	1.6	506	15	29	-	-	
	pre-p	+	+	grt16	-	-	-	omp5	gln19	-	chl2	-	tlc, lws	rieb, fgl	2.75	0.02	481	16	0.23	0.3	1.6	-	-	-	-	-	
135	pre-p	+	+	grt22	-	-	-	omp2	gln8	-	-	-	tlc, lws	rieb, fgl	2.76	0.02	513	18	0.26	0.7	1.7	-	-	-	-	-	
	peak	+	+	grt27	ph2	-	-	omp4	gln1	-	-	-	tlc, lws	jd, fgl, pa	2.77	0.03	562	11	0.34	1.0	1.5	-	-	-	-	-	
	post-p	+	-	-	ph20	+	-	-	act4	-	chl1	-	fsp, lws	ames, an, fact, cel	1.03	0.12	462	20	0.76	0.8	1.7	-	-	-	-	-	
UH	pre-p	+	+	grt10	ph12	-	-	-	-	-	chl4	-	tlc, lws	clin, feel, daph	2.74	0.02	474	15	0.29	1.0	1.7	523	20	19	-	-	
26	peak	+	+	grt17	ph6	-	-	-	-	-	chl2	-	tlc, lws	ames, daph, clin	2.75	0.05	507	32	0.31	2.0	1.7	-	-	-	-	-	
	post-p	+	-	grt1	ph8	+	-	-	-	-	chl11	-	fsp, lws	gr, clin, an, daph	1.15	0.10	494	21	0.68	0.1	2.0	-	-	-	-	-	
117	pre-p	+	-	grt7	ph13	-	-	-	brs1	-	chl2	-	lws	clin, gr, ames, ts	1.87	0.07	473	9	0.40	0.9	1.6	497	19	26	-	-	
	peak	+	-	grt1	ph14	+	-	-	gln4	-	chl3	-	lws	clin, fgl	2.08	0.11	514	14	0.30	1.3	1.6	-	-	-	-	-	
EB	pre-p	+	-	grt21	-	-	-	-	brs5	-	chl3	-	lws	mnctd, gr, parq	1.81	0.11	499	14	-0.22	0.7	1.7	-	-	-	-	-	
32	peak	+	-	grt1	ph6	+	-	-	gln2	-	chl2	-	lws	cel, feel, spss, fgl	1.99	0.15	519	12	0.56	0.5	2.0	527	19	24	502	26	7
	post-p	+	-	-	ph11	+	bi2	-	act3	-	chl1	-	fsp, lws	parq, fact, cel, east, ames, feel	0.94	0.12	486	28	0.86	1.2	1.6	-	-	-	-	-	
157	pre-p	+	-	-	-	-	-	-	-	-	+	-	fsp	out of avPT ^d	-	-	-	-	-	-	-	501	35	25	-	-	-
MU	pre-p	+	-	grt8	-	-	-	-	act21	czo3	-	-	-	gl, py	0.95	0.18	464	28	0.54	0.76	1.73	-	-	-	-	-	
158	peak	+	-	grt18	ph6	+	-	omp2	gln7	-	chl2	-	tlc, lws	hed, rieb, py, feel, gr, andr	1.46	0.16	484	29	-0.11	0.51	1.96	-	-	-	-		
	post-peak	+	-	grt20	-	+	-	-	brs9	czo5	chl1	-	fsp	parq, an, py	0.93	0.06	556	13	0.49	0.76	1.54	-	-	-	-		
147	pre-peak	+	-	grt6	ph12	-	-	-	gln1	czo4	-	tlc, rt	-	-	0.82	0.29	364	52	0.80	1.06	1.73	528	33	19	585	21	11
	peak	+	-	grt27	-	pg1	bi1	-	gln5	-	chl1	-	fsp	ames, east, ann, rieb, daph, py	0.92	0.08	473	21	0.74	0.00	1.96	-	-	-	-		
GT	peak	+	-	grt6	ph1	-	-	-	-	-	chl8	-	fsp	feel	0.81	0.01	516	15	-0.28	0.23	1.96	522	27	22	-	-	
71	-	+	-	-	-	-	-	-	-	-	+	-	-	-	-	-	-	-	-	-	-	500	20	13	-	-	
146	-	+	-	-	-	-	-	-	-	-	+	-	tlc	-	-	-	-	-	-	-	-	535	15	17	-	-	
GS2	-	+	-	-	-	-	-	-	-	-	+	-	-	-	-	-	-	-	-	-	-	-	-	-	-	-	-

Table 17: ^aTHERMOCALC (version 3.3.3 [Holland and Powell, 1990, 1998]). The analyses quoted here can be found in Table 16. Mineral abbreviations are the same as for Table 16.

^bEnd-members present only in small amounts (inducing a large uncertainty in the results) that were removed in the calculations (cel, celadonite; fcel, Fe-celadonite; ann, annite; ames, amesite; fact, Fe-actinolite; parq, paragonite; ts, tschermakite; clin, clinoclhorite; phl, phlogopite; rieb, riebeckite; fgl, Fe-glaucophane; jd, jadeite; pa, paragonite; daph, daphnite; gr, grossular; spss, spessartite; an, anorthite; mnctd, Mn-chloritoid; east, eastonite; py, pyrope; hed, hedenbergite; andr, andradite).

^cFit corresponds to a threshold value: results of the calculations (column Fit) should be lower than this value to ensure reliability (see Holland and Powell [1998] for further details).

^dSamples with too simply mineral assemblage (e.g., qz + chl + ph) to give a potential avPT fit.

6.6.3. Thermobarometric results

P-T estimates were obtained with THERMOCALC for 13 samples (Figure 59a; see Table 17 for details on calculations and Table 16 for corresponding analyses), except for three GS facies samples whose mineral assemblage are too high-variant to ensure a satisfactory fit. Metavolcanoclastics from the UH sub-unit, with $\text{Grt}_{\text{core/mantle/rim}}\text{-Qz(Coe)-Lws(Pseudomorph)}\pm\text{Ph}\pm\text{Gln}\pm\text{Omp}\pm\text{Tlc}$ assemblages (*samples 135, 26*, Figure 56a, 65c) yield UHP peak burial P-T conditions around 480-560°C and 2.75 GPa (± 0.1) on average. The $\text{Grt}_{\text{mantle}}\text{-Qz-Brs-Lws(Pseudomorph)}\pm\text{Ph}\pm\text{Ctd}\pm\text{Chl}$ and $\text{Grt}_{\text{rim}}\text{-Qz-Gln-Lws(Pseudomorph)}\pm\text{Ph}\pm\text{Ctd}\pm\text{Chl}$ assemblages of samples *117* and *32* from the EC/BS EB unit (Figure 56b-c) record a prograde increase in pressure and temperature from 1.8 GPa (± 0.10), 490°C (± 15), to peak burial ~ 2.1 GPa (± 0.15), 505°C (± 15). The P-T history of the meta-mafic/-ultramafic unit (MU) is constrained by sample *158*, Figure 56e-g), which experienced a much lower pressure. Three stages are recognized, respectively constrained by $\text{Grt}_{\text{core}}\text{-Act-Ep}\pm\text{Qz}$, $\text{Grt}_{\text{rim}}\text{-Gln-Omp-Ph-Ep}\pm\text{Qz}\pm\text{Pg}$ and $\text{Grt}_{\text{out-rim}}\text{-Brs-Ep-Chl}\pm\text{Qz}\pm\text{Pg}\pm\text{Ab}$ assemblages, from prograde ~ 0.95 GPa (± 0.18) and 464°C (± 28) to peak burial ~ 1.46 GPa (± 0.16), 484°C (± 29) and post-peak ~ 0.93 GPa (± 0.06), 556°C (± 13). P-T estimates for samples located to the north and south of the AMC (GS1 and GS2 sub-units) and from the transitional GT sub-unit (samples *J2, 102, 22, 147, 148*, Figure 56h, 65a-b, g-i) reveal broadly comparable GS to lower-BS facies P-T histories, with peak burial around 0.7-1.0 GPa, 470-520°C and post-peak conditions of ~ 0.4 -0.6 GPa, 520-570°C for $\text{Chl-Qz-Ph-Ab}\pm\text{Grt}_{\text{relict}}\pm\text{Gln/Brs}\pm\text{Bi}\pm\text{Pg}$ assemblages. Similar GS to lower-BS facies conditions around 0.90-1.10 GPa, 460-

500°C were obtained for Chl-Qz-Ph-Ab±Grt_{out-rim}±Act±Lws±Bi±Pg assemblages formed as retrograde overprint on metavolcanoclastics from the UH (samples, 135, 26) and EB units (sample, 32).

RSCM temperature estimates for metavolcanoclastics from the UH unit range between $506 \pm 15^\circ\text{C}$ (n=29) and $523 \pm 20^\circ\text{C}$ (n=19) with an average value of $515 \pm 9^\circ\text{C}$. Similar temperatures are found for the EB unit, between $497 \pm 19^\circ\text{C}$ (n=26) and $527 \pm 19^\circ\text{C}$ (n=24) with an average value of $512 \pm 15^\circ\text{C}$. RSCM temperature for rocks from the GS1, GS2 and GT units clusters between $521 \pm 36^\circ\text{C}$ (n=15), $518 \pm 34^\circ\text{C}$ (n=17), $547 \pm 29^\circ\text{C}$ (n=21), $501 \pm 35^\circ\text{C}$ (n=25), $528 \pm 33^\circ\text{C}$ (n=19), $522 \pm 27^\circ\text{C}$ (n=22), $500 \pm 20^\circ\text{C}$ (n=13) and $535 \pm 15^\circ\text{C}$ (n=17) with an average value of $522 \pm 16^\circ\text{C}$. Those RSCM temperatures are somewhat lower/higher than T estimated with THERMOCALC for some individual samples, but the discrepancy remains within the bounds of the RSCM calibration ($\pm 50^\circ\text{C}$, Beyssac et al., 2002). Overall, good fits exist samples for which both the RSCM temperature and the peak P-T estimates are available (samples, 102, 22, 26, 117, 32, 148, Figure 59a). The RSCM temperature estimates in this study are also consistent with previous works which propose 500-600°C maximum peak temperature for the AMC (Bayet et al., 2018; Meyer et al., 2016).

Titanium-in-biotite thermometry on biotite-bearing samples J2, 22, 147 (GS1 and GT units) and 32 (EB unit) yields estimates between $588 \pm 19^\circ\text{C}$ (n=10), $588 \pm 10^\circ\text{C}$ (n=12), $502 \pm 26^\circ\text{C}$ (n=7) and $585 \pm 21^\circ\text{C}$ (n=11) with a slightly higher average value than THERMOCALC and RSCM estimates (i.e., $566 \pm 43^\circ\text{C}$; Figure 59a). This

estimate is nevertheless in agreement with the recent Zr-in-titanite temperature constraints at ~569-608°C for retrograde eclogite in the AMC (Zhang et al., 2018).

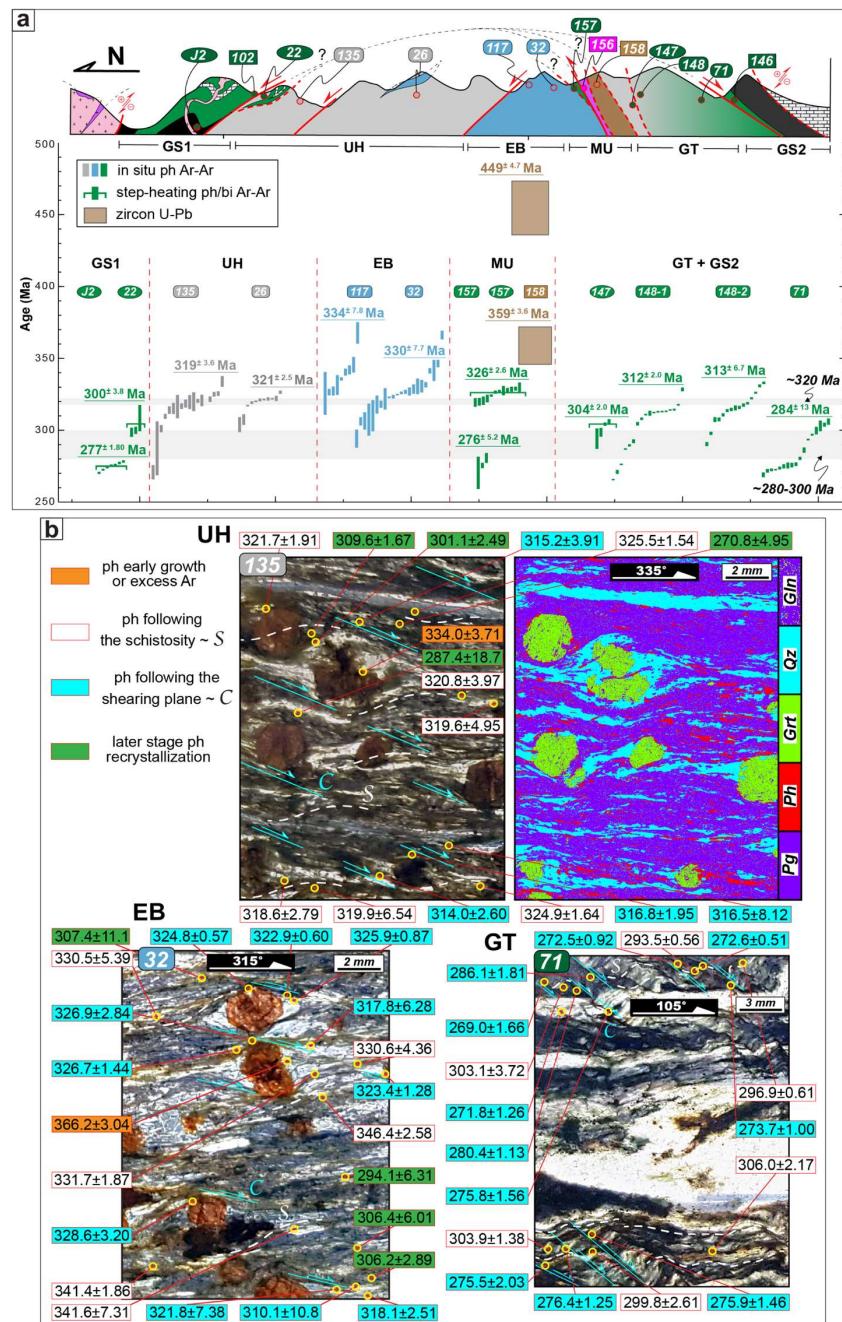


Figure 60: (a) Radiometric ages obtained for all samples, with respect to respective localities on Kebuerte section. Check Table 18, 20 and 21 for detailed isotopic results. (b) Examples of in situ ⁴⁰Ar-³⁹Ar laser probe ablation result. Overlays show surface areas from which argon was extracted during measurement, and numbers correspond to ages obtained. Phengite grains following the schistosity are marked as white overlays, while light blue overlays represent those encountered along late shear bands. The in situ Ar-Ar probing ages (e.g., used in Figure 59b, 60a, 61 and text) for constraining the deformation around peak metamorphism of each samples are calculated from the average of absolute ages obtained from phengite grains following the schistosity and shear bands. Orange overlays indicate phengite grains with ambiguous old age that probably results from excess Ar or imply early growth of phengite. Green overlays locate phengite grains with relative younger age which could indicate later stage recrystallization. Colored sketch, which exported from the combined microprobe mapping matrix data via Xmaptools (<https://www.xmaptools.com>, Lanari et al., 2014), clearly show the mineral assemblage with respect to deformation. Detail of the rest of in situ Ar-Ar probing results are illustrated in Figure 66 (Table 18).

6.6.4. Radiochronological results

Radiometric ages from in situ phengite ^{40}Ar - ^{39}Ar dating range between 269.0 and 366.2 Ma (Figure 60a, Table 18). Individual samples span the range 304-326 and 271-334 Ma for the UH unit, 326-368 and 294-366 Ma for the EB unit, 270-281, 266-333 and 269-306 Ma for regional GS facies units (i.e., GS1, GS2 and GT). Despite the age scatter, even within individual samples, none of them shows significant co-variations in $^{37}\text{Ar}/^{39}\text{Ar}$ and $^{38}\text{Ar}/^{39}\text{Ar}$ ratios, or in atmospheric contribution, that could account for age dispersion (Table 18).

The ages or age clusters amongst the various samples therefore either reflect 'real' tectonic episodes or the presence of excess argon, as documented in some HP settings (e.g., Arnaud et al., 1995; Ruffet et al., 1997; Gao & Klemd, 2003) but not systematically (e.g., Agard et al., 2002; Augier et al., 2005). In detail, most radiometric ages respect the chronological relationship inferred from mineral textures, i.e. phengite in shear bands cutting across the schistosity are effectively younger. This is the case for samples *135*, *32* and *71* (Figure 60b). Sample *135* shows that highly substituted phengite grains ($\text{Si}^{4+} \sim 3.50\text{-}3.60$) following the schistosity yield ages between 319 and 326 Ma, whereas younger ages on average ca. 314-317 Ma are obtained along shear bands with lower Si content phengite ($\text{Si}^{4+} \sim 3.40\text{-}3.50$). Younger ages $\sim 271\text{-}310$ Ma in small disoriented microdomains adjacent to the shear bands could relate to latest stage phengite recrystallization. One older age (~ 334 Ma) was obtained from an inclusion within garnet with very high Si content ($\text{Si}^{4+} \sim 3.64$): this could represent the real age of an early grown (UHP) phengite and/or some excess argon sequestered in garnet (as

is likely in sample 117; Fig. S4), or both. Similar age patterns with deformation-controlled phengite recrystallization can be observed for the rest of the metavolcanoclastics dated by in situ ^{40}Ar - ^{39}Ar (Figure 60b, 66), except sample 157 whose rare phengite grains along a weak schistosity yield ages ~270-281 Ma.

Weighted plateau ages of phengite in samples *J2*, *22*, *157* and *147*, from regional GS facies units (GS1, GS2 and GT, Figure 52a, d, 60a), are 276.6 ± 1.8 , 299.9 ± 3.8 , 326.1 ± 2.6 and 304.1 ± 2.0 Ma respectively (Figure 67, Table 20). Dated phengites are moderately substituted in all samples (Si^{4+} : 3.05-3.15 for *J2*, 3.25-3.35 for *22*, 3.10-3.30 for *157* and 3.30-3.40 for *147*, Figure 58c, Table 16), with stronger retrogressive effects for samples *22* and *147* (Figure 56h, 65g). The plateau age ~277 Ma of phengite in sample *J2*, which exhibits clear GS facies shear sense indicators (Figure 64d, 65a), may relate to dextral strike-slip shearing along the western part of SCTSZ (Figure 50c, 51a). The plateau age ~326 Ma of phengite in weakly schistosed sample *157* is significantly older than ages obtained by in situ measurements (~276 Ma, Figure 66), which is a bit puzzling but may reflect local recrystallization and/or fluid circulation (De Jong et al., 2001; Di Vincenzo et al., 2016).

Zircon grains of the metamafic sample *158* from the MU unit present core-rim texture in CL image (Figure 67) with apparent $^{206}\text{Pb}/^{238}\text{U}$ ages varying from 351 to 2075 Ma (Th/U ~0.09-0.99, Table 21). Dark/grey oscillatory zircon cores (Figure 67) were characterized by typically Ce positive and Pr & Eu negative anomalies, steep positive slope from LREEs to HREEs ($(\text{Lu}/\text{La})_{\text{N}}$ ~1984-248266), significant enrichment in HREEs ($(\text{Lu}/\text{Sm})_{\text{N}}$ ~50.9-147.4) and inclined HREEs pattern ($(\text{Lu}/\text{Tb})_{\text{N}}$

~9.2-14.4, Table 21) in chondrite-normalized REEs diagram, with Th/U ~0.52-0.99 and a weighted mean age (if exclude discordant, older inherited core) of 448.5 ± 4.7 Ma (MSWD=0.56, n=9). These observations support a magmatic origin (e.g., Corfu et al., 2003; Schaltegger & Davies, 2017). The bright zircon rims yield a weighted mean age of 359.2 ± 3.6 Ma (MSWD=1.14, n=8), with relatively gentle slope from LREEs to HREEs ((Lu/La)_N ~13.7-141.0) and obvious HREEs plateau ((Lu/Tb)_N ~1.3-2.2, Table 21) but no detectable Ce/Pr/Eu anomalies in chondrite-normalized REEs diagram. The REEs pattern of bright zircon rims and their smaller Th/U ~0.09-0.26 could suggest a metamorphic origin equilibrated with the growth of relatively L/MREEs-poor & HREEs-rich phase (e.g., garnet; see Rubatto, 2017; Tan et al., 2017).

Results of In Situ Phengite ⁴⁰ Ar- ³⁹ Ar Radiometric Data															
Run	⁴⁰ Ar/ ³⁹ Ar	± 1σ	⁴⁰ Ar/ ³⁹ Ar	± 1σ	⁴⁰ Ar/ ³⁹ Ar	± 1σ	% Atm	Age (Ma)	± 1σ						
	Ar		Ar		Ar		Ar		Ar		Ar				
	*1000		*1000		*1000		*1000		*1000		*1000				
UHP/HP complex (UH)															
135.1	42.05	0.38	0.12	0.01	22.95	0.20	1373.84	391.09	22.55	5.38	3.51	301.07	2.49		
135.2	45.19	0.29	0.04	0.00	21.89	0.14	672.37	291.21	0.00	0.00	1.10	321.67	1.91		
135.3	45.78	0.24	0.04	0.00	21.57	0.11	406.82	194.71	9.53	3.76	1.25	325.51	1.54		
135.4	45.05	0.61	0.10	0.01	21.51	0.28	898.34	573.32	0.00	0.00	3.09	307.76	3.97		
135.5	37.50	0.74	0.31	0.02	24.21	0.46	1367.28	850.98	48.03	12.22	9.26	270.78	4.95		
135.6	47.08	0.57	0.10	0.01	20.62	0.24	149.29	481.25	0.00	0.00	2.94	333.98	3.71		
135.7	44.87	0.74	0.26	0.01	20.55	0.33	2261.40	699.05	13.06	8.54	7.79	319.61	4.86		
135.8	45.70	0.25	0.02	0.00	21.73	0.12	0.00	0.00	0.00	0.00	0.70	324.98	1.64		
135.9	44.39	1.24	0.27	0.02	20.72	0.56	2079.51	1201.15	1.52	13.79	316.48	8.12			
135.1	44.72	0.43	0.04	0.01	22.12	0.21	0.00	0.00	0.00	0.00	1.12	318.57	2.79		
135.11	44.92	1.00	0.19	0.02	21.02	0.46	0.00	0.00	0.00	0.00	5.59	319.88	6.54		
135.12	44.44	0.30	0.16	0.00	21.46	0.14	1225.63	856.93	10.93	17.85	4.65	316.77	1.95		
135.13	44.99	0.20	0.03	0.00	22.02	0.10	264.24	436.48	2.89	11.22	0.85	320.09	1.30		
135.14	43.35	0.25	0.17	0.00	21.94	0.13	1189.83	591.43	13.84	16.39	4.92	309.65	1.67		
135.15	44.19	0.60	0.57	0.01	18.85	0.24	3239.75	1393.88	86.92	37.97	16.72	315.15	3.91		
135.16	39.98	2.82	1.21	0.04	16.07	1.10	8015.25	7348.50	9.81	183.45	35.74	287.39	18.71		
135.17	44.02	0.40	0.14	0.01	21.77	0.19	725.84	876.02	33.36	24.84	4.17	314.01	2.60		
														319.48*	3.67*
26.1	45.32	0.09	0.03	0.00	21.90	0.04	237.67	91.60	7.31	1.55	0.77	317.14	0.58		
26.2	45.78	0.09	0.05	0.00	21.55	0.04	226.38	84.83	3.63	1.05	1.35	320.09	0.59		
26.3	45.99	0.10	0.06	0.00	21.34	0.05	23.94	125.33	4.62	1.43	1.89	321.40	0.66		
26.4	46.07	0.10	0.17	0.00	20.64	0.04	805.67	104.57	2.00	1.29	4.92	321.92	0.62		
26.5	46.10	0.28	0.11	0.00	20.65	0.05	20.65	0.00	0.00	41.39	3.84	336	1.82		
26.6	46.78	0.18	0.06	0.00	21.00	0.08	0.00	0.00	0.00	18.62	1.81	177	326.49	1.13	
26.7	43.81	0.57	0.20	0.01	21.49	0.28	0.00	0.00	0.00	43.08	9.44	5.87	307.40	3.71	
26.8	46.04	0.18	0.07	0.00	21.30	0.08	0.00	0.00	29.34	2.62	1.97	321.76	1.15		
26.9	45.95	0.15	0.18	0.00	20.59	0.07	0.00	0.00	13.17	14.40	5.42	321.13	0.98		
26.1	45.65	0.14	0.04	0.00	21.67	0.07	184.58	183.79	10.13	1.93	98.07	319.26	0.69		
26.11	43.27	0.81	0.29	0.01	21.10	0.39	0.00	0.00	94.97	11.68	88.32	303.90	5.24		
														321.26*	2.53*
EC/SB facies blueschist horizon (EB)															
117.1	46.01	0.49	0.14	0.01	20.84	0.21	1044.18	273.29	12.51	5.70	4.12	327.29	3.16		
117.2	47.30	0.17	0.21	0.00	19.85	0.07	1794.54	108.76	14.71	2.40	6.14	335.68	1.11		
117.3	48.04	0.37	0.09	0.01	20.27	0.15	1203.95	207.31	24.74	5.33	2.62	340.47	2.39		
117.4	48.84	0.84	0.24	0.01	19.01	0.32	1747.16	792.39	40.42	15.19	7.16	345.80	5.42		
117.5	45.89	0.35	0.08	0.01	21.28	0.16	0.00	0.00	0.00	0.00	2.35	326.51	2.28		
117.6	46.66	1.05	0.12	0.02	20.65	0.45	1557.17	2508.17	0.00	0.00	3.69	331.59	6.84		
117.7	48.29	0.49	0.38	0.01	18.37	0.18	2007.54	1122.35	18.57	2.40	11.30	342.04	3.13		
117.8	52.29	1.18	0.19	0.02	18.07	0.39	2069.29	2639.76	5.03	4.63	5.54	367.69	7.48		
117.9	45.76	2.29	0.45	0.04	18.85	0.91	0.00	0.00	0.00	0.00	13.32	325.85	14.91		
														334.34*	7.75*
32.1	52.08	0.48	0.36	0.00	17.18	0.16	1704.37	391.84	0.00	0.00	10.54	366.23	3.04		
32.2	45.20	1.13	0.56	0.01	18.48	0.46	4271.03	834.69	0.00	0.00	16.51	321.84	7.38		
32.3	48.20	0.29	0.22	0.00	19.38	0.11	892.70	502.58	11.14	7.50	6.62	341.35	1.86		
32.4	42.84	0.91	0.43	0.01	20.41	0.42	3497.24	2368.28	0.00	0.00	12.59	306.44	6.01		
32.5	42.81	0.44	0.11	0.01	22.59	0.23	3428.86	990.54	0.00	0.00	3.30	306.21	2.89		
32.6	40.98	0.95	0.28	0.02	22.38	0.50	3810.01	2725.01	54.49	0.00	8.20	294.12	6.31		
32.7	44.62	0.38	0.11	0.01	21.71	0.18	1967.26	730.23	0.00	0.00	3.15	318.08	2.51		
32.8	43.40	1.65	0.32	0.04	20.84	0.74	2553.68	6010.35	0.00	0.00	9.56	310.09	10.84		
32.9	48.24	1.13	0.43	0.01	18.08	0.42	744.26	721.41	10.13	13.24	12.82	341.60	7.31		
32.1	45.83	0.13	0.29	0.00	19.86	0.06	0.00	0.00	7.49	1.31	8.56	325.97	0.87		
32.11	46.70	0.29	0.16	0.00	20.37	0.12	0.00	0.00	30.65	3.68	4.87	331.65	1.87		
32.12	48.98	0.40	0.19	0.01	19.26	0.15	0.00	0.00	63.84	16.79	5.71	346.36	2.58		
32.13	44.58	0.96	0.76	0.01	17.39	0.37	0.00	0.00	78.57	27.59	22.50	317.84	6.28		
32.14	45.64	0.09	0.12	0.00	21.16	0.04	0.00	0.00	5.68	2.31	3.45	324.75	0.57		
32.15	45.36	0.09	0.09	0.00	21.46	0.04	378.49	40.87	0.13	1.51	2.70	322.89	0.60		
32.16	45.55	0.07	0.06	0.00	20.98	0.09	0.00	0.00	9.48	12.18	0.46	330.64	4.36		
32.17	45.98	0.44	0.08	0.00	21.26	0.20	161.57	401.86	15.88	8.32	2.25	326.98	1.84		
32.18	45.84	0.22	0.04	0.00	21.53	0.10	0.00	0.00	0.10	3.49	1.09	326.70	2.44		
32.19	42.99	1.69	0.29	0.01	21.28	0.83	0.00	0.00	0.00	0.00	8.55	307.41	11.09		
32.2	45.43	0.20	0.05	0.00	21.67	0.09	0.00	0.00	3.18	2.76	1.59	323.35	1.28		
32.21	46.24	0.49	0.07	0.00	21.16	0.22	0.00	0.00	0.00	0.00	0.00	328.61	3.20		
32.22	46.53	0.83	1.17	0.01	14.05	0.24	0.00	0.00	47.61	18.68	34.66	330.51	5.39		
														330.23*	7.65*
Contact between EB and MU															
157.1	38.24	0.28	0.21	0.00	24.51	0.18	0.00	0.00	33.50	17.82	6.30	275.50	1.86		
157.2	39.02	0.52	0.33	0.01	23.11	0.30	0.00	0.00	60.05	32.38	9.86	280.74	3.44		
157.3	37.47	1.68	1.57	0.02	14.29	0.62	0.00	0.00	289.20	107.70	46.49	270.35	11.24		
														275.53*	5.20*
GS facies transitional zone (GT)															
148-1.1	43.76	0.09	0.06	0.00	22.47	0.04	2.32	1.14	0.00	0.00	1.67	312.88	0.56		
148-1.2	43.78	0.08	0.02	0.00	22.68	0.04	0.00	0.00	0.00	0.00	0.72	312.99	0.51		
148-1.3	43.46	0.08	0.03	0.00	22.78	0.04	0.00	0.00	2.19	0.95	1.04	310.85	0.52		
148-1.4	43.68	0.08	0.05	0.00	22.55	0.04	8.03	1.60	1.38	1.17	1.54	312.31	0.50		
148-1.5	43.81	0.08	0.02	0.00	22.68	0.04	2.87	0.97	1.60	1.05	0.67	313.20	0.50		
148-1.6	43.95	0.08	0.04	0.00	22.47	0.04	14.58	1.87	2.34	1.45	1.48	314.12	0.51		
148-1.7	40.65	0.20	0.11	0.00	23.81	0.12	5.67	5.29	6.54	2.32	3.23	292.35	1.33		
148-1.8	42.50	0.18	0.05	0.00	23.19	0.10	0.00	0.00	0.00	0.00	1.47	304.54	1.21		
148-1.9	37.46	0.20	0.07	0.00	26.12	0.14	23.42	5.81	0.00	0.00	2.20	270.99	1.35		
148-1.10	43.02	0.13	0.05	0.00	22.88	0.07	0.00	0.00	0.00	0.00	1.60	307.88	0.85		
148-1.11	43.61	0.13	0.03	0.00	22.02	0.13	9.19	6.30	1.50	1.50	1.15	311.85	1.74		
148-1.12	46.14	0.20	0.07	0.00	21.21	0.09	5.86	5.15	0.00	0.00	2.15	328.41	1.33		
148-1.13	39.84	0.08	0.06	0.00	24.64	0.05	3.78	2.18	6.11	1.56	1.86	286.93	0.51		
148-1.14	43.99	0.09	0.04	0.00	22.44	0.05	15.63	1.35	1.29	0.82	1.33	314.34	0.62		
148-1.15	44.51	0.08	0.05	0.00	22.16	0.04	6.17	1.18							

6.7. Discussions

6.7.1. Distinct metamorphic sub-units?

We identified major contacts across domains with slightly different lithologies and/or tectonic patterns (as illustrated on the cross-section of Figure 52d), that we regard as distinct km-scale tectonic sub-units. Overall, asymmetric shearing is more pronounced in UH, while upright symmetrical folding is typical of EB. Mafic boudins are also more numerous in UH. The lateral extension of these sub-units is shown in Figure 54a, but was limited by the presence of glaciers to the east. For example, the more mafic EB unit likely corresponds to the pillow unit described by Bayet et al. (2018). As discussed below, the metamorphic evolution and ages tend to support the view that there are indeed distinct sub-units.

Our observations (Figure 52-54) highlight the following deformation patterns:

- BS facies asymmetric shear senses with a northward component prevail for all lithologies and sub-units (except in the MU unit, where kinematic indicators are rare and not statistically significant). This points to the importance of simple shear under retrograde conditions, hence during exhumation (also see Bayet et al., 2018). No indication of dominant syn-eclogite pure shear deformation was found at the outcrop scale, and is possibly only preserved in boudins (e.g., LPO measurements of Soldner et al., 2017).
- top to NEE and a few top to N/S GS facies shear senses are restricted to the GS1, GS2, GT units and the north margin of the MU.

We propose that the top to NNW shear senses (mostly BS facies, and more rarely transitional EC/BS or BS/GS) correspond to exhumation dynamics following northward subduction (Scheltens et al., 2015), while regional dextral strike-slip deformation is marked by the dominance of top to NEE GS facies shear sense.

P-T estimates inferred from average P-T calculations suggest contrasting peak burial for the sub-units. Care in selecting potentially co-stable minerals/analyses and statistical fits obtained make these estimates relatively robust. In the UHP/HP complex (UH, Figure 59a), maximum burial P-T estimates cluster around 480-560°C, 2.75GPa (± 0.1), similar to most recent estimates (Bayet et al., 2018; Lü & Bucher, 2018), and consistent with the range of 480-580°C, 2.2-3.0GPa obtained by earlier studies (e.g., Du et al., 2014; Lü & Zhang, 2016; Tan et al., 2017; Yang et al., 2013; Zhang et al., 2018) and the widespread occurrence of coesite (Figure 50c, 51a, d; Bayet et al., 2018; Lü et al., 2009; Lü & Zhang, 2012; Tan et al., 2017; Yang et al., 2013). In contrast, somewhat lower peak pressure of ~ 2.1 GPa (± 0.15), 505°C (± 15) were obtained for the EB unit, with moderately to highly substituted phengite and in general lesser amounts of omphacite than in UH (Figure 59a), in agreement with the preliminary P-T estimates for blueschists close to the EB unit (Beinlich et al., 2010). We regard the possibility of having 'missed' UHP samples and/or that retrogression was so pervasive that all hints of UHP metamorphism was removed as fairly unlikely but still possible. This unit resembles the pillow-basalt bearing unit (Figure 51d, 52e) of Bayet et al. (2018), for which P-T conditions were unfortunately not determined. Different conditions were also obtained for the MU ultramafic/mafic unit equilibrated at ~ 1.46 GPa (± 0.16),

484°C (± 29). Rocks from the northern- and southernmost units (GS1, GS2 and GT, Figure 59a) yield GS to lower-BS facies P-T conditions around 0.4-1.0GPa, 470-570°C. The GT unit shows evidence for an earlier, higher pressure blueschist facies episode whose P-T conditions could not be determined. Similar GS to lower-BS facies conditions around 0.90-1.10GPa, 460-500°C (using moderately substituted phengite) were determined for the retrograde overprint of the UH and EB samples (135, 26, 32).

Different age clusters (discussed further below) also emerge for peak burial of the sub-units from the data obtained in this study: schematically ~ 320 Ma for UH, ~ 330 Ma for EB, ~ 360 Ma for MU (from metamorphic zircon overgrowth). A similar age of 360 Ma was in fact obtained by Ar-Ar dating on the MU unit (Figure 61c, Table 22). Similar ages around 300-310 Ma are found, in contrast, for early exhumation of these units and for GS facies metamorphism (Figure 59b, 61b-e).

These observations and field mapping (e.g., cross-section of Figure 52d) therefore suggest that the Akeyasi metamorphic complex, at least in the surroundings of the Kebuerte valley, is a metamorphic dome made of a stack of individual sub-units or nappes. This rules out the view that the AMC might be a subduction *mélange* in the sense of Cloos & Shreve (1988a, 1988b) or Meyer et al. (2016). That the exposed core of the metamorphic dome (i.e., the EB unit) does not correspond to the most deeply buried slice requires thrusting at some point of the tectonic history. The contrasting ages for the different sub-units also indicate diachronous detachment from the subducting slab.

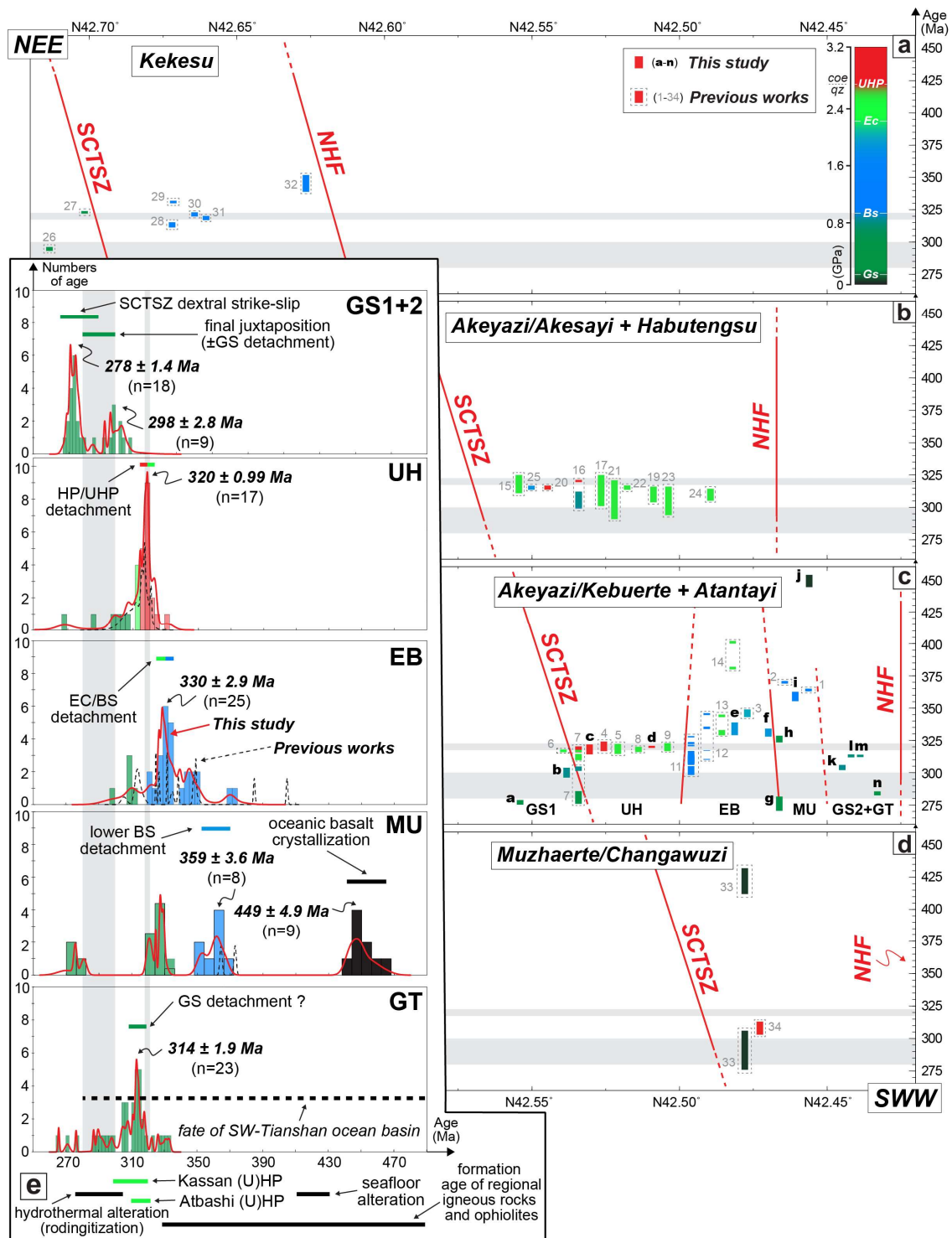


Figure 61: (a, b, c, d) The compilation of regional age reports with respect to sampling localities (ages versus latitude). Ages reported in key valleys (Kekesu, Akeyazi-Akesayi/-Habutengsu/-Kebuerte/-Atantayi, Muzhaerte-Changawuzi; Figure 50c, 69), are listed respectively from the top to bottom. Bars with bold letters marked results from this study, while those with grey numbers represent previous works. Dash-line rectangles mark previous works without precise P-T constraints (i.e., roughly tied to lithologies) or did not tie dated ages to metamorphism. The bar colors indicate the P-T estimates linked to ages (whatever roughly or precisely), and black bar marks ages with metasomatic or magmatic origins. Check Table 22 for the detail of exhaustive compilation of regional age reports and associated P-T estimates. (e) The age histogram of sub-units in the AMC from this study. Black dash-line spectrum represents age pattern of previous works from adjacent areas with respect to respective sub-units. Other major geological constraints are also recalled for comparison: i) discrete hydrothermal zircon ages obtained from regional rodingite (Li et al., 2010) probably witness the fate of SW-Tianshan ocean basin; ii) The range of formation age of regional igneous rocks and ophiolites are cited from Jiang et al. (2014) and Wang et al. (2018). iii) Metamorphic ages of (U)HP rocks from the Kyrgyz SW-Tianshan are cited from Loury et al. (2016), Loury et al. (2018) and Mühlberg et al. (2016).

6.7.2 P-T-t trajectories, exhumation rates and tectonic stacking

The successive detachment of sub-units (MU, EB then finally UH), if confirmed, reveals a change in metamorphic gradient with time, from an intermediate to cold subduction regime (i.e., from ~ 12 to $5-7^\circ\text{C}/\text{km}$; Figure 59b; also see Agard et al. (2018) and Angiboust et al. (2016)). The accuracy and significance of Ar-Ar ages (i.e., whether they are 'real' tectonic episodes or 'blended' ages with excess argon) is therefore critical and more thoroughly discussed here.

As outlined above (§ 6.4), a key observation is that most radiometric ages respect the chronological relationship inferred from mineral textures, i.e. phengite in shear bands cutting across the schistosity are effectively younger (e.g., as visible in samples *135* or *32*, Figure 60b, 66). Ages obtained from highly substituted phengite in the UH unit, at $\sim 320 \pm 1$ Ma, also match the results of previous geochronological studies (mostly focused on the UH unit in adjacent valleys), i.e. peak metamorphic conditions at 315 ± 5 Ma (Figure 61b-c, e, 69, Table 22; also see the compilation of Tan et al. (2017)). Another argument in favor of the absence of random excess argon is that the dispersion of in situ ages (Figure 60, 66) increases with a greater dispersion in mineral chemistry (Figure 58c; e.g., notably in samples *135*, *117*, *148-1*, *71*).

Our observations confirm that recrystallization enhanced by deformation and fluid circulation is commonly more effective than volume diffusion (Agard et al., 2002; Augier et al., 2005; Laurent et al., 2017), and that the 'closure temperature' for phengite is at least 550°C (as in Syros: Laurent et al., 2017), since all ages within a given sample should be the same otherwise. We therefore conclude that i) the radiometric ages

obtained here mainly result from phengite recrystallization in deformation sites and/or deformation-controlled reequilibrations, with only minor effects of excess argon (and/or contamination by minerals adjacent to phengite) and ii) that the sub-units UH and EB reached peak conditions diachronously at ~320 and ~330 Ma, respectively. The metamorphic zircon rim overgrowth constrains peak burial of the MU unit at ~360 Ma (whereas the magmatic core is ~450 Ma). This evolution reflects a change in metamorphic gradient and possibly of the subduction thermal regime with time (Figure 59b).

Peak burial for the EB unit at ~330 Ma is reminiscent of ages $\sim 328 \pm 26$ Ma obtained on 'blueschists' from the Atantayi/Akesayi valleys that closely paralleled to EB (Figure 61b-c, e, 69; Table 22) and the Kekesu valley (although located ~60km to the East; Figure 50c, 69), mostly with the Ar-Ar step-heating technique (Gao & Klemd, 2003; Gao et al., 2000, 2006; Klemd et al., 2005). Although this age dispersion was previously interpreted as reflecting some excess Ar (by us; e.g., Tan et al., 2017), or the prograde growth of an eclogite facies mineral assemblage (Klemd et al., 2011), these ages may be a further indication of the existence of a distinct metamorphic episode around 330 Ma in the AMC (Figure 61c, e).

For the MU unit, only two previous phengite/glaucophane Ar-Ar ages around ~364-370 Ma (Figure 61c, e; Table 22) were reported from samples immediately to the west of the MU unit (Gao et al., 2000). Some ultramafic lithologies were reported in the Changawuzi valley (~40 km to the west, Figure 50c, 69), with an age of 308 ± 5 Ma for blackwall formation (Shen et al., 2016), but no eclogite boudins or Ti-

chondrodite/clinochlore were found in the MU unit contrary to the Changawuzi samples.

Rocks from the GS facies sub-units (GS1, GS2 and GT, Figure 60a) yield ages around ~275-318 Ma matching i) retrogression ages (Figure 60, 66) found for the UH and EB sub-units, ii) the ~293-316 Ma phengite Ar-Ar plateau ages of regional GS facies rocks at the Kekesu valley (Wang et al., 2010; Xia et al., 2016), iii) the ca. 304 Ma titanite U-Pb age of retrograde eclogite (Zhang et al., 2018) along the western part of SCTSZ, and iv) the ~280-290 Ma mica Ar-Ar plateau ages of GS facies rocks related to dextral strike-slip shearing along the eastern part of SCTSZ (Laurent-Charvet et al., 2003).

The juxtaposition of the four sub-units preserving a HP-LT history (namely the UH, EB, MU and GT) and making the center of the AMC metamorphic dome could therefore take place around 280-300 Ma at ~20km (Figure 59-61), since ages from moderately substituted, recrystallized phengite were detected in all these samples (Figure 60b, 66). As for prograde paths, exhumation P-T paths is slightly different, with some moderate heating for the MU and GT units and an isothermal to cooling return path for the UH and EB units (Figure 59b, 62b-e).

Exhumation velocities could not be calculated for individual samples but a first-order constraint can be inferred: assuming that ages for samples 135 and 26 are representative of the average UHP to GS history (from ~320 to 280-300 Ma, Figure 59a, 60) the decrease from ~ 2.75GPa to ~0.65GPa in approximately 20-40 Ma yields ~1.8-3.5 mm/yr for the UH unit, consistent with our previous independent estimate for a coesite-

bearing oceanic eclogite in the same sub-unit (Tan et al., 2017). The same approach yields $\sim 0.8\text{-}1.3$ mm/yr for the EB unit, showing that both units have exhumation velocities comparable to most oceanic blueschists and eclogites (i.e., $\sim 1\text{-}5$ mm/yr; Agard et al., 2009).

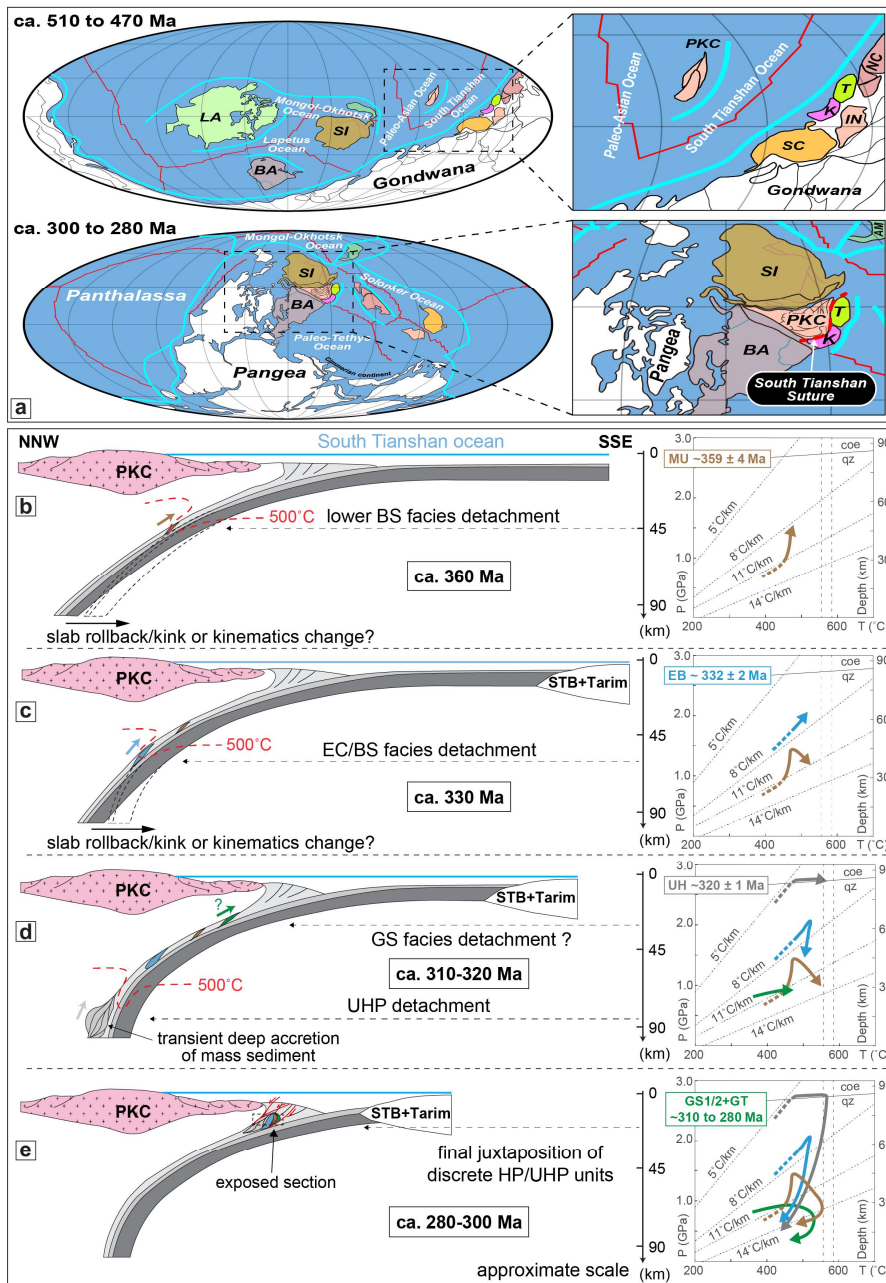


Figure 62: (a) Paleogeographic reconstruction during the Gondwana assembly at $\sim 510\text{-}470$ Ma and Pangea assembly at $\sim 300\text{-}280$ Ma (modified after Domeier & Torsvik (2014) and Wang et al. (2018)) with emphasizing the tectonic evolution of Paleo South Tianshan Ocean. LA = Laurentia, BA = Baltica, SI = Siberia, PKC = Paleo-Kazakhstan Continent, SC = South China Block, K = Karakum Craton, T = Tarim Craton, IN = Indochina, NC = North China Craton, AM = Amuria. (b) Interpretative sketches (inspired after Angiboust et al. (2016), Locatelli et al. (2018) and Plunder et al. (2015)) relating the formation and exhumation of the SW-Tianshan HP/UHP-LT accretionary complex during the period 360-280 Ma.

6.7.3 Implications for subduction dynamics and Late Carboniferous subduction history

Importantly, our P-T-time results suggest the diachronous recovery of different sub-units (Figure 59b), from ~45 km (MU; 360 Ma), ~65 km (EB; 330 Ma) and ~85 km depth (UH; 320 Ma). This rock record highlights discrete, transient episodes of detachment from the slab, in particular with respect to long-lived South Tianshan ocean subduction duration of ~120 Myr (Scheltens et al., 2015; Tan et al., 2017). This punctuated recovery likely results from changes in mechanical coupling (Agard et al., 2018), whose origin could be i) a change in slab geometry (e.g., slab rollback: Brun & Faccenna, 2008; slab kink: Klemd et al., 2011) (Figure 62b-c) and/or ii) a modification of the physical properties along the plate interface (i.e., mantle rheology, fluid regime, etc; Agard et al., 2018). Incidentally, whole-rock analyses (Figure 57) reveal that there was in first approximation no drastic change in volcanoclastic content throughout this subduction history.

Final tectonic stacking of the UH, EB, MU and GT units around 280-300 Ma at ~20km Ma also suggests, contrary to some interpretations (e.g., Gao et al., 2017; Wang et al., 2018; Zhang et al., 2018), that the peak burial of the UHP does not mark oceanic closure (and/or does not relate to continental collision). In particular, the ~300 Ma phengite ^{40}Ar - ^{39}Ar step-heating ages (Figure 60a, 67) from both the glaucophane-bearing GT and GS1 units suggest that subduction was still active around the Late Carboniferous (i.e., ~300 Ma). This inference is further supported by the following

regional magmatic indications (Figure 70): i) the histogram of the crystallization ages of regional igneous rocks from tectonic plates to the north (i.e., PKC: the Paleo Kazakhstan Continent) and south (i.e., STB + Tarim Craton) of the Paleo South Tianshan ocean show a broadly consistent peak around ~280-300 Ma; ii) Detrital zircon U-Pb ages of (meta-) sediments from both the north/south plates and the accretionary complex (including the AMC and Atbashi metamorphic complex at the western part of SCTSZ, and the Wuwamen complex at the eastern part of SCTSZ, Figure 50b) uniformly show either youngest detrital zircon ages of ~300 Ma or peaks around ~280-300 Ma; iii) ~285 Ma leucogranites cut across the STMB (Gao et al., 2011b). Overall, available magmatic and/or metamorphic constraints (e.g., this study) tend to show that the subduction of the Paleo South Tianshan ocean basin and relevant deposition were probably still active during the Late Carboniferous (Figure 62a). Final emplacement of the AMC complex could take place around early Permian-late carboniferous (i.e., ~280-300 Ma, Figure 62e), prior to the collision of the Paleo Kazakhstan Continent and the Tarim Craton (+STB, Figure 62a).

6.8. Conclusions

The main results of our study of the Akesayi metamorphic complex, in the Chinese Southwestern Tianshan metamorphic belt (i.e., a portion of the South Central Tianshan Suture Zone, which also comprises the Atbashi, Chatkal and Fan-Karategin (U)HP metamorphic complexes), can be summarized as follows:

- What was previously proposed as a HP/UHP “melange” should be subdivided into

several coherent, kilometre-scale, essentially metavolcanoclastic tectonic units bearing contrasting P-T-time-D histories (and to some extent lithologies).

- The present-day geometry of the AMC is that of a metamorphic dome preserving evidence for internal nappe stacking.
- Pervasive deformation following eclogite and/or blueschist-eclogite peak burial is marked by pervasive BS facies, exhumation-related shear senses with a top to the north component.
- At least four of the six sub-units identified here, namely the UH (480-560°C and 2.75 GPa), EB (~2.1 GPa and 505°C), MU (~1.45 GPa and 485°C) and GT units (>~0.7-1.0 GPa and 470-520°C) experienced subduction and were buried to depths of ~85, 65, 45 and 30km respectively.
- In situ laser probe ^{40}Ar - ^{39}Ar radiometric dating of phengite and zircon U-Pb dating yield peak burial ages of 320 ± 1 , 332 ± 2 , 359 ± 2 Ma and ~280-310 Ma, respectively, for the UH, EB, MU and regional GS facies units (GS1, GS2 and GT), with recrystallization enhanced by fluid circulation and deformation.
- At least four short-lived episodes of detachment (~5-10 Ma) occurred in the South Tianshan ocean subduction zone, beneath the Paleo Kazakhstan Continent, at ~320, ~330, ~360 and ~300-310 Ma, with respect to long-lived subduction processes (>120 Ma).
- The tectono-metamorphic evolution records a progressive change of metamorphic gradients from ~12°C/km to ~5-7 °C/km, which could reflect a cooling of the subduction system with time.

- Juxtaposition and exhumation of the UH, EB, MU and GT units to mid-crustal depth (~20 km) was accomplished around 290-300 Ma, at rates on the order of 1-3 mm/yr.
- The existence of ~300 Ma glaucophane-bearing BS/GS facies metavolcanoclastic units (i.e., the GT and part of GS1 units) suggests that the subduction of the Paleo South Tianshan ocean basin was probably still active during late Carboniferous.
- Final juxtaposition of the diverse sub-units making the metamorphic dome could have occurred at around ~280-290 Ma, and been broadly coeval with dextral strike-slip movements along the STCSZ.

Acknowledgements

This study was funded through projects of the National Natural Science Foundation of China to Prof. Gao Jun (No. 41390440, 41390445, 41025008) and by the International Training Network ZIP (Marie Curie Actions, Zooming In-between Plates, REA grant agreement No. 604713) to Prof. Philippe Agard. Additional supports were provided by programs of the Chinese Academy of Sciences of China (No. GJHZ1776, 2013047) to Prof. Wan Bo. We greatly benefitted from discussions with Labrousse L., Yang J-J., Chen Y., Li J-L., Locatelli M. and Bonnet G. We also thank Fialin M. and Rividi N. (CAMPARIS), Boudouma O. (ISTeP), Arnaud N. (Géosciences Montpellier) and Deldicque D. (ENS Paris, France) for analytical support, Delairis E. and Devaux D. (ISTeP) for the preparation of thin sections. We further thank the meticulous help of Prof. Klemd Reiner and Li J-L during field work.

Supplementary figures and tables

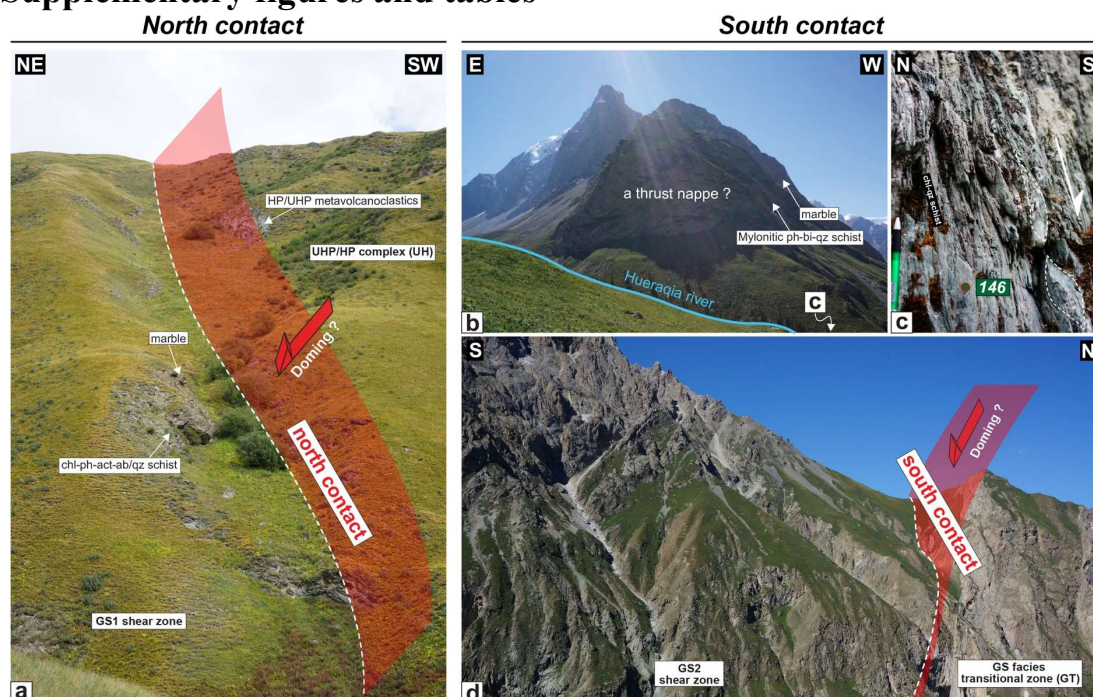


Figure 63: Panoramic views of the main north and south contacts in between the AMC and the SCTSZ mylonitized shear zone (GS1, GS2).

Results of bulk rock trace element compositions

Lithology	Metavolcanoclastics							Metavolcanics		Ultra-mafic rocks			
Sample	71	157	22	148	135	26	117	32	147	158	156-1	156-2	156-3
Trace elements (ug/g)													
Li	35.07	28.60	7.17	47.31	8.81	9.07	20.29	10.64	31.09	8.75	7.27	0.08	4.26
Be	-	-	0.74	-	-	0.56	-	0.77	0.89	1.10	0.02	0.01	0.11
Sc	21.18	33.92	11.78	39.74	15.85	12.50	9.54	27.33	23.02	33.29	32.79	10.89	33.85
V	134.13	128.64	80.92	221.77	93.90	72.64	59.88	181.13	184.09	258.78	203.32	51.75	188.14
Cr	97.37	154.58	53.77	462.86	55.08	44.72	26.19	27.70	161.95	69.95	353.02	2353.34	361.75
Co	20.80	24.88	8.98	32.81	6.27	10.09	7.39	17.11	30.63	37.05	49.41	86.47	34.48
Ni	54.45	26.83	32.80	101.92	33.28	12.14	24.36	9.88	58.85	51.46	246.02	1438.19	159.03
Cu	39.55	66.12	19.65	87.01	6.14	21.79	9.52	72.90	48.20	47.33	26.54	50.72	38.55
Zn	102.56	56.30	43.39	101.15	92.46	77.72	45.56	66.79	82.66	128.15	111.39	55.56	48.72
Ga	25.40	10.90	12.45	15.58	19.67	12.74	13.47	17.79	17.38	23.39	13.68	2.76	7.23
Rb	172.86	10.59	36.92	13.36	67.51	24.86	75.03	13.91	53.03	16.72	0.74	0.86	2.50
Sr	70.32	83.36	80.94	141.47	128.57	100.18	137.70	81.36	104.37	311.88	6.69	7.67	13.48
Y	16.25	5.85	16.46	17.94	6.12	12.59	17.10	16.06	20.76	33.27	41.35	1.01	17.47
Zr	4.22	4.33	166.00	4.86	4.44	94.43	4.60	64.65	140.90	200.22	51.90	0.65	34.88
Nb	9.82	0.27	5.53	0.41	4.55	2.61	6.99	2.58	11.66	16.30	20.19	0.16	1.52
Cs	8.27	0.89	1.67	1.26	2.12	1.23	3.69	0.51	2.29	0.57	0.04	0.11	0.02
Ba	1179.77	172.37	287.94	544.54	465.93	873.33	465.52	251.73	259.36	241.54	5.20	3.05	7.82
La	43.13	3.02	21.22	4.83	11.35	7.67	38.11	7.69	14.45	23.30	9.06	0.23	0.78
Ce	84.25	5.84	37.99	9.77	22.90	15.50	71.22	18.13	30.96	50.22	25.05	0.48	2.81
Pr	9.53	0.66	4.69	1.34	2.44	2.08	8.50	2.34	4.33	6.87	4.00	0.07	0.50
Nd	34.65	3.18	17.33	6.38	9.65	8.77	31.40	10.60	18.09	27.99	19.39	0.37	3.33
Sm	6.80	0.99	3.30	2.02	2.07	1.90	6.17	2.45	4.63	7.21	5.23	0.12	1.63
Eu	1.48	0.26	0.82	0.65	0.42	0.64	1.38	0.73	1.52	2.33	1.46	0.03	0.57
Gd	5.82	0.77	3.12	2.23	1.74	2.11	5.29	2.73	4.95	7.88	6.21	0.19	2.26
Tb	0.74	0.16	0.49	0.42	0.25	0.35	0.72	0.46	0.81	1.22	1.15	0.04	0.45
Dy	3.84	0.88	2.85	2.95	1.23	2.23	3.70	2.88	4.54	6.60	7.51	0.27	3.16
Ho	0.79	0.25	0.58	0.67	0.27	0.50	0.68	0.60	0.89	1.29	1.72	0.07	0.73
Er	1.49	0.49	1.71	1.92	0.50	1.41	1.55	1.68	2.21	3.33	4.72	0.20	2.10
Tm	0.19	0.08	0.27	0.31	0.08	0.21	0.20	0.26	0.31	0.47	0.68	0.03	0.32
Yb	0.96	0.50	1.73	2.05	0.39	1.42	1.13	1.66	1.88	2.81	4.25	0.24	2.08
Lu	0.12	0.09	0.28	0.30	0.14	0.22	0.16	0.27	0.27	0.41	0.59	0.04	0.32
Hf	0.17	0.17	4.78	0.21	0.22	2.70	0.19	1.96	3.66	5.21	1.40	0.03	1.17
Ta	0.66	0.05	0.43	0.04	0.26	0.13	0.50	0.13	0.80	1.09	1.15	0.01	0.07
Tl	-	-	0.17	-	-	0.12	-	0.08	0.22	0.09	0.03	0.00	0.03
Pb	12.74	4.34	4.07	4.32	3.13	5.64	10.40	1.08	2.35	3.45	1.37	1.94	3.16
Bi	-	-	0.12	-	-	0.03	-	0.16	0.02	0.02	0.00	0.01	0.00
Th	13.26	1.57	5.91	2.10	9.22	1.67	10.02	1.47	1.55	2.39	1.55	0.21	0.21
U	1.54	0.27	0.82	0.73	0.90	0.46	1.13	0.44	0.33	0.53	0.27	0.15	0.05
ΣREE	210.02	23.01	112.81	53.78	59.53	57.61	187.33	68.52	110.61	175.20	132.39	3.38	38.50
(La/Yb) _N	32.20	4.35	8.80	1.69	21.06	3.87	24.13	3.32	5.51	5.95	1.53	0.70	0.27
(La/Sm) _N	4.10	1.97	4.16	1.54	3.55	2.60	3.99	2.03	2.02	2.09	1.12	1.25	0.31
(Gd/Yb) _N	5.01	1.28	1.49	0.90	3.72	1.23	3.87	1.36	2.18	2.32	1.21	0.68	0.90
Nb/Ta	14.90	5.88	12.86	10.30	17.68	19.51	14.06	20.51	14.65	14.93	17.64	22.14	22.34
Zr/Hf	24.86	25.04	34.76	23.34	19.75	35.01	24.43	32.95	38.47	38.44	37.15	19.00	29.91
Th/Ta	20.12	34.76	13.73	53.22	35.80	12.54	20.14	11.65	1.95	2.19	1.35	29.57	3.07
Ta/Hf	3.88	0.26	0.09	0.19	1.15	0.05	2.64	0.06	0.22	0.21	0.82	0.21	0.06

Table 19: Results of bulk rock trace element compositions.

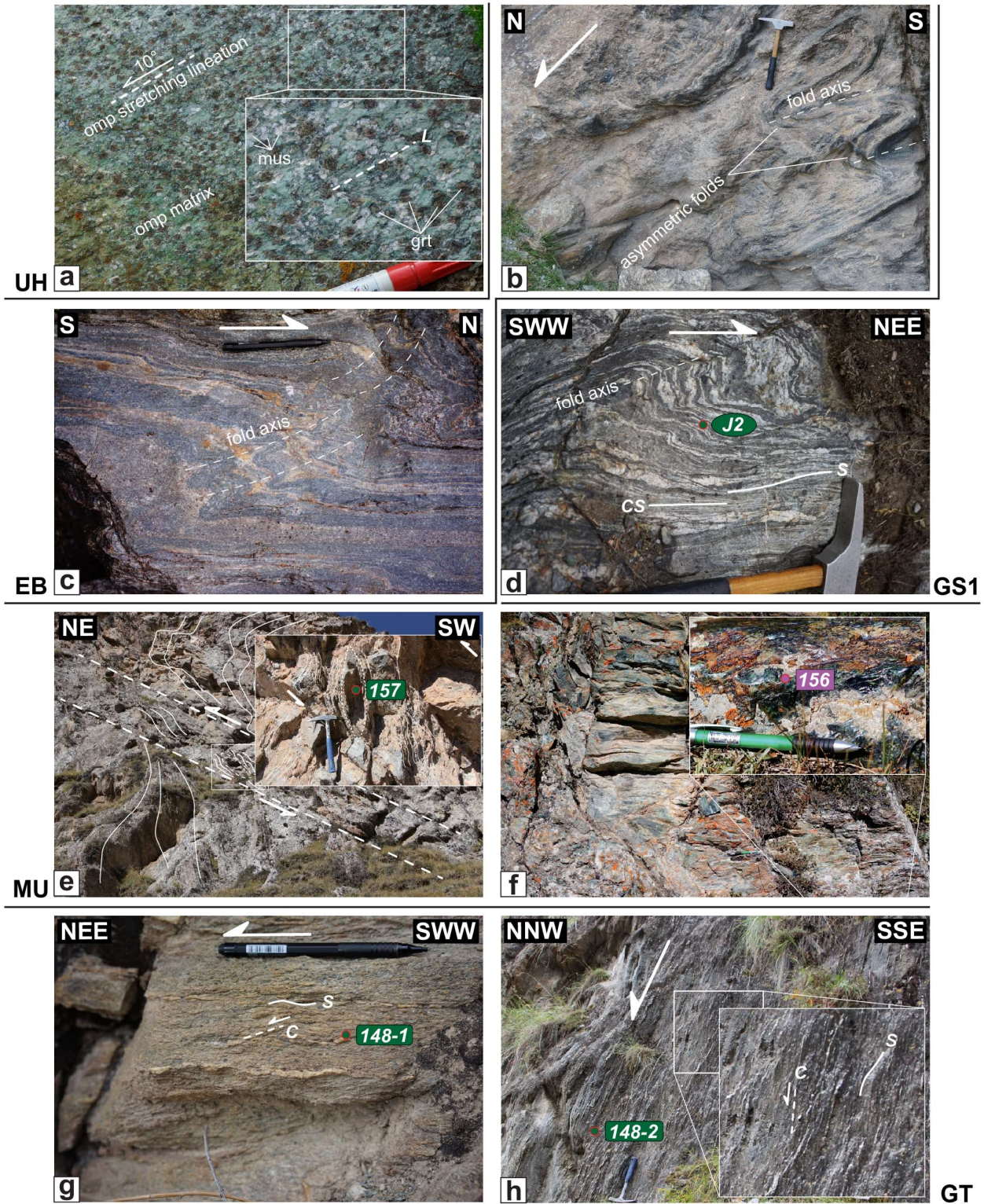


Figure 64: Outcrop observation of representative samples in this study. The letter of sub-figures corresponds to the localities marked in Figure 52c. (a) A fresh eclogite outcrop shows clear omphacite-stretching lineation. (b, c) Recumbent folds in the EC/BS facies blueschist horizon (EB unit). (d) Outcrop of sample J2 from the SCTSZ mylonitized shear zone, indicating asymmetrical folding over shear movement. (e) Relative ambiguous shear sense shown by complicated refolding and schistosity on the outcrop of sample 157. (f) Outcrop of the moderately schistosed serpentinitized ultra-mafic rock. (g) A top to NEE sense of shear found on the outcrop of sample 148-1 from the GT unit. (h) A top to NNW sense of shear found on the outcrop of sample 148-2 from the GT unit.

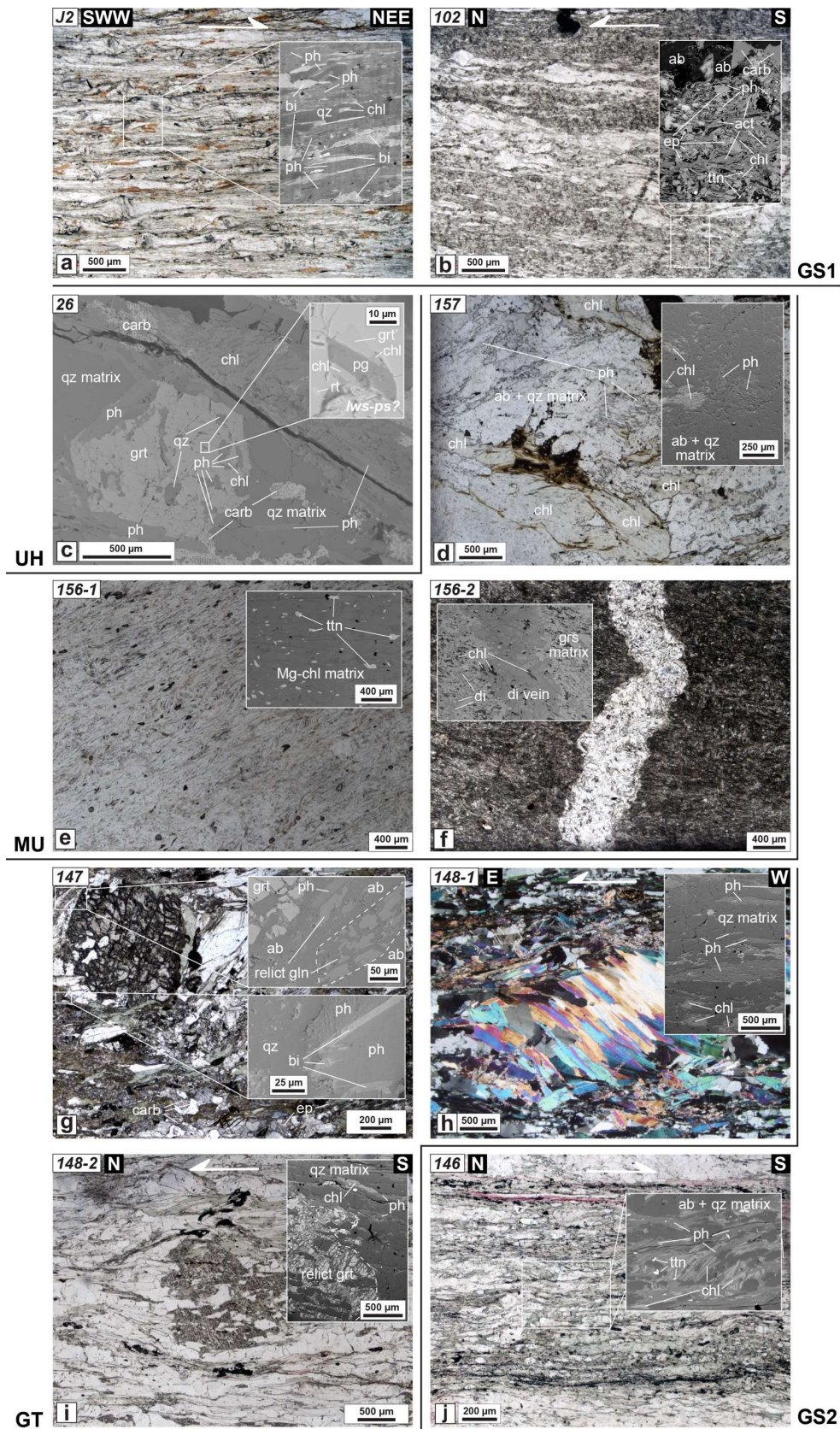


Figure 65: Microphotographs of some of the samples investigated in the present study. Mineral abbreviation follows the caption of Figure 56. (a) Ab-Chl-Ph-Bi-Qz assemblage in sample J2 from the GS1 unit. (b) Ab-Act-Ep-Chl±Carb±Ttn assemblage in sample 102 from the GS1 unit. (c) Grt-Ph-Qz-Chl-Rt±Pg±Ab±Ttn assemblage and relevant garnet inclusion pattern in sample 26 from the UH unit. (d) Chl-Ph-Qz-Ab assemblage in sample 157 from the MU unit. (e, f) Representative lithologies with MgChl-Ttn or Chl-Di-GrS assemblages in the MU unit. Ab-Gln-Chl-Ph-Grt-Qz±Ab±Carb assemblage in sample 147 from the GT unit. (h, i) Samples with Chl-Grt-Qz assemblage from the GT unit. (j) Chl-Ph-Ab-Qz±Ttn assemblage in sample 146 from the GS2 unit.

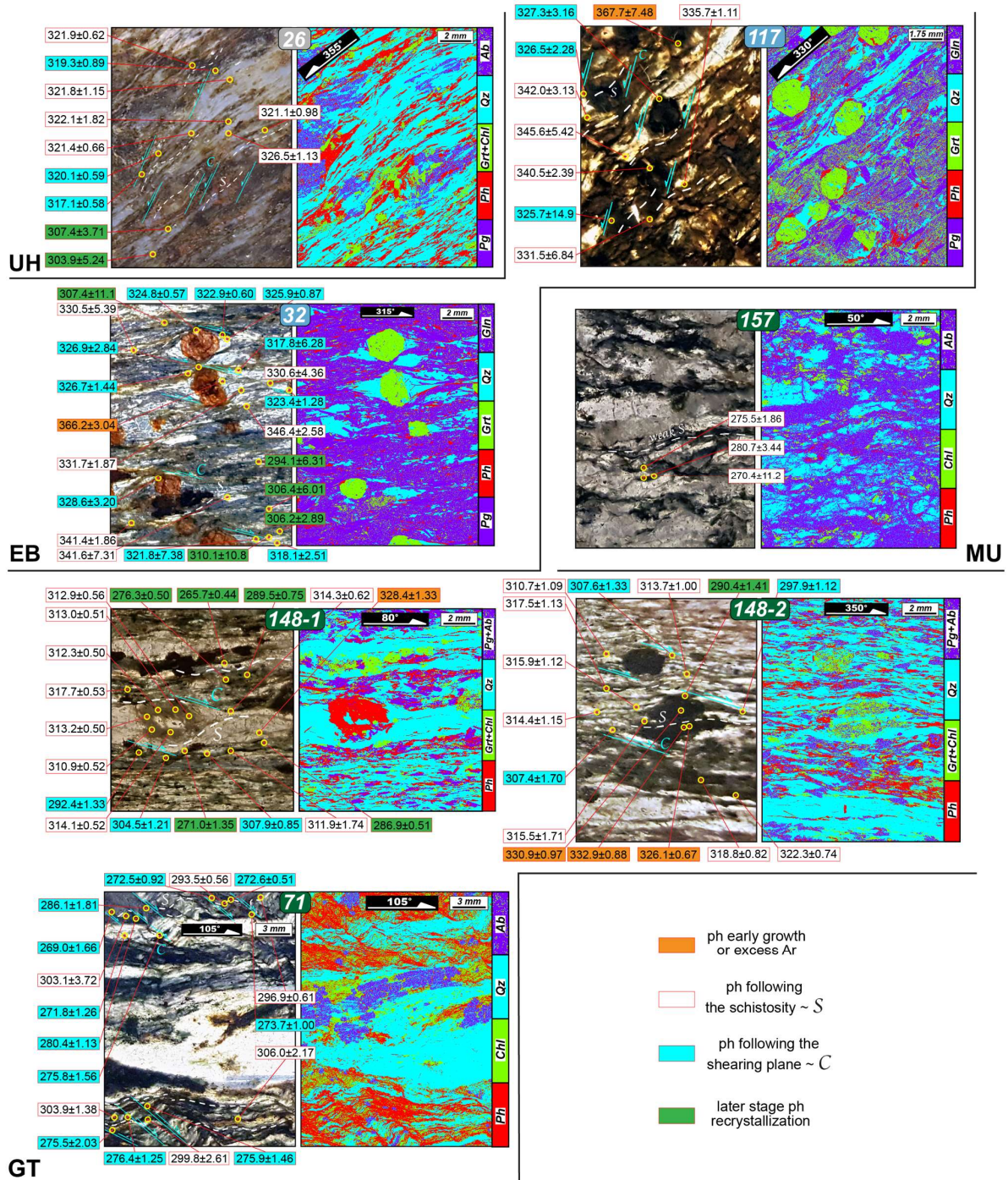


Figure 66: The rest of in situ ^{40}Ar - ^{39}Ar laser probe ablation results (Table 18).

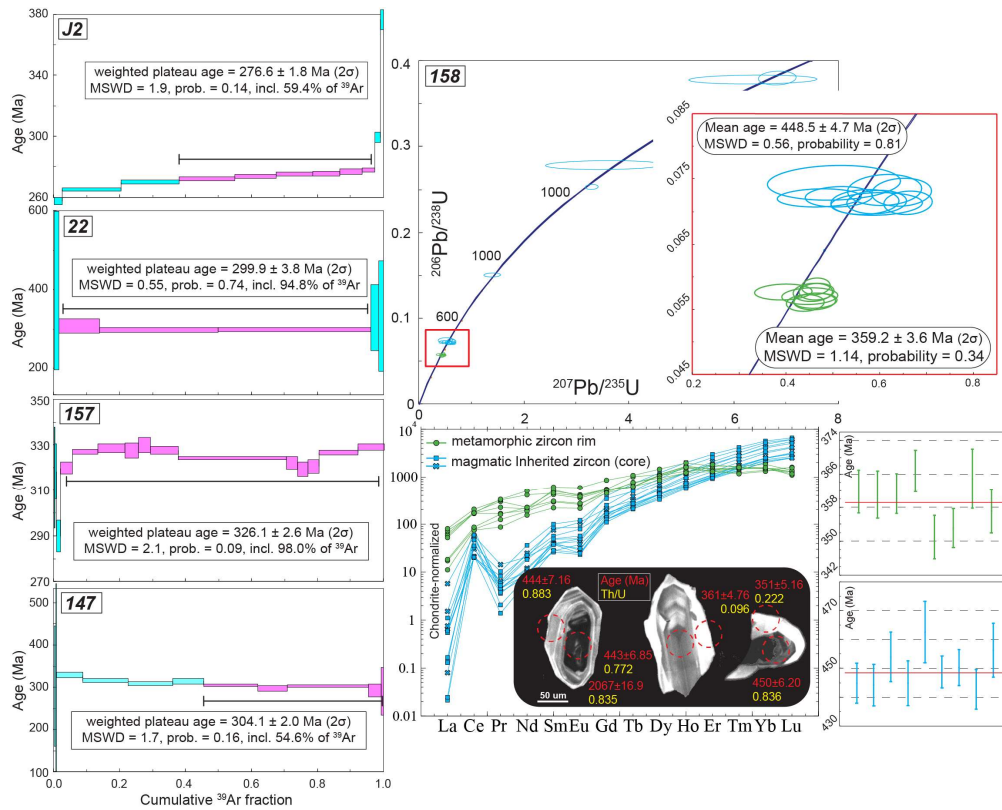


Figure 67: The phengite ^{40}Ar - ^{39}Ar step-heating results of regional GS to lower BS facies samples (J2, 22, 157 and 147), and the LA-ICP-MS zircon U-Pb radiometric results of meta-basite sample (158) (Table 20, 21).

Results of Phengite Step-Heating ^{40}Ar - ^{39}Ar Radiometric Data							
No.	$^{40}\text{Ar}/^{39}\text{Ar}$	$^{37}\text{Ar}/^{39}\text{Ar}$	$^{36}\text{Ar}/^{39}\text{Ar}$	$^{40}\text{Ar}^*/^{39}\text{Ar}$	$^{40}\text{Ar}^*$ (%)	$^{39}\text{Ar}_r$ (%)	Age (Ma) $\pm 2\sigma$
J2, Muscovite, $J = 0.0044200 \pm 0.0000111$							
1	35.88	0.03	0.00	34.68	96.65	2.47	257.89 2.38
2	36.03	0.01	0.00	35.79	99.32	17.74	265.56 1.16
3	36.64	0.01	0.00	36.48	99.56	17.64	270.34 1.42
4	36.93	0.01	0.00	36.80	99.65	16.92	272.54 1.27
5	37.17	0.01	0.00	37.04	99.63	12.43	274.16 1.25
6	37.44	0.02	0.00	37.25	99.49	11.31	275.59 1.23
7	37.58	0.04	0.00	37.30	99.25	8.01	275.95 1.39
8	37.90	0.04	0.00	37.48	98.89	6.77	277.20 1.61
9	38.32	0.05	0.00	37.63	98.21	3.98	278.24 1.56
10	42.70	0.18	0.01	40.76	95.45	1.76	299.55 3.53
11	55.43	0.44	0.01	52.43	94.55	0.97	376.90 6.46
22, Muscovite, $J = 0.00431376 \pm 0.00000863$							
1	63.98	0.00	0.02	57.10	89.26	1.31	398.20 201.82
2	45.59	0.21	0.01	43.12	94.57	12.53	308.47 18.22
3	43.77	0.46	0.01	41.62	95.06	35.89	298.60 6.31
4	43.67	0.41	0.01	41.82	95.75	46.38	299.93 4.93
5	46.44	0.00	0.00	46.44	99.98	2.43	330.16 84.01
6	46.96	0.00	0.00	46.95	99.98	1.47	333.48 140.46
147, Muscovite, $J = 0.00433328 \pm 0.00001300$							
1	48.25	0.00	0.02	42.34	87.76	0.38	304.61 142.74
2	45.33	0.00	0.00	45.32	99.98	0.23	324.24 221.17
3	46.73	0.00	0.00	46.32	99.12	8.13	330.77 7.07
4	45.06	0.02	0.00	44.36	98.45	13.76	317.96 4.14
5	44.28	0.20	0.00	43.22	97.59	13.33	310.42 4.20
6	44.65	0.02	0.00	44.03	98.60	9.55	315.75 5.86
7	44.20	0.34	0.01	42.55	96.25	16.38	306.00 3.41
8	43.65	0.55	0.01	41.43	94.88	8.84	298.60 6.12
9	43.37	0.32	0.00	42.29	97.47	24.73	304.25 2.33
10	43.60	0.47	0.01	40.76	93.46	3.75	294.15 14.23
11	44.23	0.00	0.01	40.40	91.34	0.93	291.70 56.31
157, Muscovite, $J = 0.00433328 \pm 0.00001300$							
1	45.05	0.00	0.00	44.04	97.74	0.25	315.81 22.11
2	45.40	0.00	0.00	44.45	97.91	0.43	318.55 12.12
3	43.45	0.00	0.01	40.16	92.43	1.29	290.15 6.95
4	46.60	0.00	0.01	44.70	95.92	3.54	320.16 2.67
5	46.21	0.00	0.00	45.80	99.11	7.71	327.40 1.10
6	46.08	0.00	0.00	46.04	99.90	8.21	326.93 1.80
7	46.04	0.00	0.00	45.89	99.87	4.01	327.98 3.30
8	46.27	0.00	0.00	46.26	99.98	3.80	330.29 3.32
9	46.22	0.00	0.00	45.92	99.34	8.31	328.14 1.71
10	45.73	0.00	0.00	45.36	99.18	32.87	324.51 0.82
11	45.32	0.00	0.00	45.05	99.40	3.45	322.44 2.70
12	44.77	0.00	0.00	44.63	99.69	3.14	319.69 3.01
13	44.95	0.00	0.00	44.81	99.68	3.19	320.88 2.93
14	45.89	0.00	0.00	45.73	99.65	11.82	326.94 1.08
15	46.28	0.00	0.00	46.11	99.63	7.99	329.38 1.35

√Data that constitutes the age plateau.

Table 20: Results of Phengite Step-Heating ^{40}Ar - ^{39}Ar Radiometric Data

Results of LA-ICP-MS Zircon U-Pb Radiometric Data of meta-basite sample

No.	Th	U	Th/U	²⁰⁷ Pb/ ²³⁸ Pb	1σ	²⁰⁷ Pb/ ²³⁵ U	1σ	²⁰⁶ Pb/ ²³⁸ U	1σ	t _{207/206}	1σ	t _{207/235}	1σ	t _{206/238}	1σ
1	187.81	189.88	0.989	0.060	0.004	0.594	0.042	0.071	0.001	616.69	159.24	473.41	27.04	444.86	6.94
2	79.16	89.65	0.883	0.068	0.004	0.661	0.034	0.071	0.001	872.22	120.37	515.10	20.57	444.18	7.16
3	21.12	191.84	0.110	0.059	0.003	0.466	0.025	0.058	0.001	553.74	116.65	388.63	17.04	361.84	5.15
4	41.02	78.63	0.522	0.066	0.005	0.647	0.042	0.073	0.001	794.45	178.70	506.37	25.79	454.03	8.55
5	79.62	98.27	0.810	0.059	0.005	0.569	0.048	0.071	0.001	553.74	180.53	457.43	30.89	444.85	7.72
6	19.27	201.56	0.096	0.050	0.005	0.395	0.040	0.058	0.001	194.53	211.08	338.32	29.35	361.37	4.76
7	314.85	377.23	0.835	0.123	0.015	6.368	0.809	0.378	0.004	1999.08	214.05	2027.82	111.50	2066.92	16.89
8	48.13	64.77	0.743	0.053	0.010	0.503	0.093	0.074	0.002	327.84	366.62	413.52	63.14	462.65	10.68
9	45.87	445.46	0.103	0.087	0.017	3.538	0.738	0.278	0.003	1372.23	378.24	1535.80	165.21	1583.69	15.86
10	173.39	205.40	0.844	0.048	0.006	0.471	0.059	0.072	0.001	116.76	255.52	392.09	40.83	448.75	5.51
11	408.37	970.34	0.421	0.067	0.005	1.397	0.108	0.151	0.001	850.00	150.00	887.73	45.74	904.69	8.40
12	43.26	457.63	0.095	0.057	0.002	0.464	0.020	0.059	0.001	505.60	94.43	387.18	14.03	366.69	4.94
13	57.72	260.35	0.222	0.057	0.004	0.442	0.027	0.056	0.001	498.19	138.87	371.40	18.81	350.99	5.16
14	31.92	114.92	0.278	0.057	0.004	0.463	0.031	0.056	0.001	498.82	158.27	385.88	21.69	353.09	4.63
15	40.32	401.44	0.100	0.061	0.008	3.289	0.082	0.253	0.002	635.20	271.27	1478.47	19.39	1455.34	10.25
16	36.42	396.74	0.092	0.056	0.005	0.452	0.039	0.057	0.001	494.63	188.27	376.92	27.31	357.13	5.16
17	43.22	353.14	0.122	0.058	0.006	0.462	0.029	0.056	0.001	503.08	135.55	371.62	14.70	364.86	7.10
18	69.93	83.62	0.836	0.062	0.005	0.513	0.047	0.072	0.001	793.98	153.25	400.16	28.67	450.27	6.20
19	32.61	324.17	0.101	0.128	0.004	6.837	0.236	0.380	0.005	2069.44	51.39	2090.53	30.67	2074.66	24.65
20	107.13	138.74	0.772	0.057	0.008	0.594	0.064	0.071	0.001	693.86	302.00	464.93	39.46	442.76	6.85
21	129.77	178.36	0.728	0.063	0.004	0.610	0.052	0.073	0.002	596.17	147.40	490.57	33.76	456.28	9.33
22	43.49	165.06	0.264	0.058	0.004	0.458	0.028	0.058	0.001	542.63	133.32	382.62	19.29	361.10	5.66

(continued) Corresponding Trace Elements Data of Analysed Zircon Grains

No.	La	Ce	Pr	Nd	Sm	Eu	Tb	Dy	Ho	Er	Tm	Yb	Lu	(Lu/La) _N	(Lu/Sm) _N	(Lu/Tb) _N	
1	0.04	21.65	0.98	16.87	15.32	6.98	70.22	18.24	197.25	70.14	313.26	71.08	690.99	129.34	30569.54	50.85	10.44
2	0.14	12.50	0.50	8.53	7.55	3.29	33.88	10.00	108.66	41.49	185.62	44.51	427.16	81.71	5401.15	65.16	12.03
3	4.35	52.83	15.27	104.11	46.34	15.77	92.03	23.47	216.19	69.55	301.52	40.51	267.72	29.69	63.61	3.86	1.86
4	0.13	12.84	0.43	4.21	5.75	1.43	22.54	7.81	83.47	31.79	160.28	35.82	346.15	63.37	4587.20	66.35	11.94
5	0.01	28.66	0.20	3.82	7.41	2.88	51.33	19.17	232.96	93.71	424.05	93.87	892.92	156.11	248266.33	126.98	11.99
6	2.65	45.85	8.26	71.81	33.59	18.22	94.72	28.88	240.87	68.82	216.37	39.51	253.98	39.87	140.53	7.15	2.03
7	0.03	36.35	0.36	3.86	5.77	1.80	25.60	8.27	95.57	35.48	164.22	38.50	391.27	69.03	21056.50	72.09	12.29
8	0.01	13.24	0.13	2.99	4.39	1.44	28.10	11.00	137.77	54.73	258.13	61.00	582.12	107.34	198266.66	147.42	14.36
9	0.15	12.14	0.78	10.55	8.64	4.58	35.46	9.66	105.44	37.01	167.18	41.08	419.28	78.56	5030.31	54.78	11.97
10	0.03	29.69	0.56	9.34	12.89	4.92	80.30	26.77	310.28	113.78	495.86	106.35	965.33	167.65	47935.45	78.35	9.22
11	0.26	19.82	0.34	4.67	3.99	1.35	25.58	7.76	89.60	33.19	152.71	34.85	345.91	64.20	2288.23	96.82	12.19
12	4.09	47.65	11.83	87.04	44.45	15.59	104.75	27.53	266.62	90.88	216.09	29.87	224.29	40.82	93.03	5.53	2.18
13	12.43	104.20	31.52	233.34	93.09	36.57	175.07	40.51	371.23	111.56	281.91	42.98	313.70	34.97	26.26	2.26	1.27
14	19.07	125.64	30.35	192.01	68.90	19.21	109.80	22.99	272.70	75.16	235.00	37.65	265.58	27.94	13.67	2.44	1.79
15	0.02	12.89	0.61	11.57	11.54	6.35	44.10	11.69	131.26	48.18	214.84	52.30	540.27	103.90	51085.86	54.24	13.09
16	17.27	101.69	15.91	90.53	63.66	18.62	105.39	23.47	271.31	86.65	222.32	31.55	237.96	33.05	17.86	3.13	2.07
17	13.79	103.72	21.37	97.12	80.25	20.09	112.96	37.45	289.24	95.23	247.35	39.91	258.59	33.36	22.57	2.50	1.31
18	0.18	18.56	0.60	4.56	4.22	2.19	25.84	8.64	105.66	36.81	173.89	39.42	369.50	64.30	3345.56	91.83	10.95
19	1.36	35.26	1.36	9.67	5.98	2.53	39.90	14.20	177.41	70.43	345.74	81.44	819.62	155.06	1062.40	156.30	16.07
20	0.15	33.26	0.43	5.31	5.97	2.87	32.11	11.48	146.87	58.69	294.97	70.78	729.07	140.58	8558.48	141.82	18.03
21	0.36	47.58	0.44	5.65	6.14	1.66	31.47	9.01	108.39	39.12	183.09	42.77	427.24	76.74	1984.03	75.25	12.55
22	15.06	108.99	28.28	104.90	74.85	19.93	111.25	23.31	282.77	93.60	240.76	39.68	264.19	32.63	20.22	2.63	2.06

Table 21: Results of LA-ICP-MS Zircon U-Pb Radiometric Data of meta-basite sample.

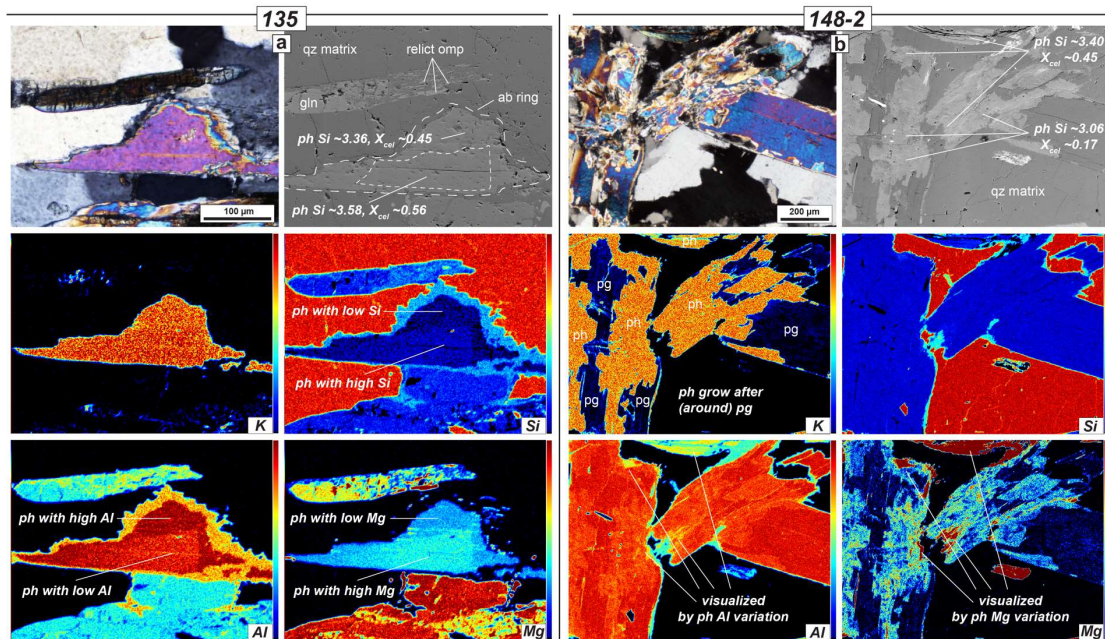


Figure 68: Examples of later stage phengite recrystallization in samples from distinct sub-units (UH versus GT units), which could account for the accordant appearance of relative younger in situ phengite Ar-Ar probed ages ~280-300 Ma in most of samples from all sub-units (Figure 60a).

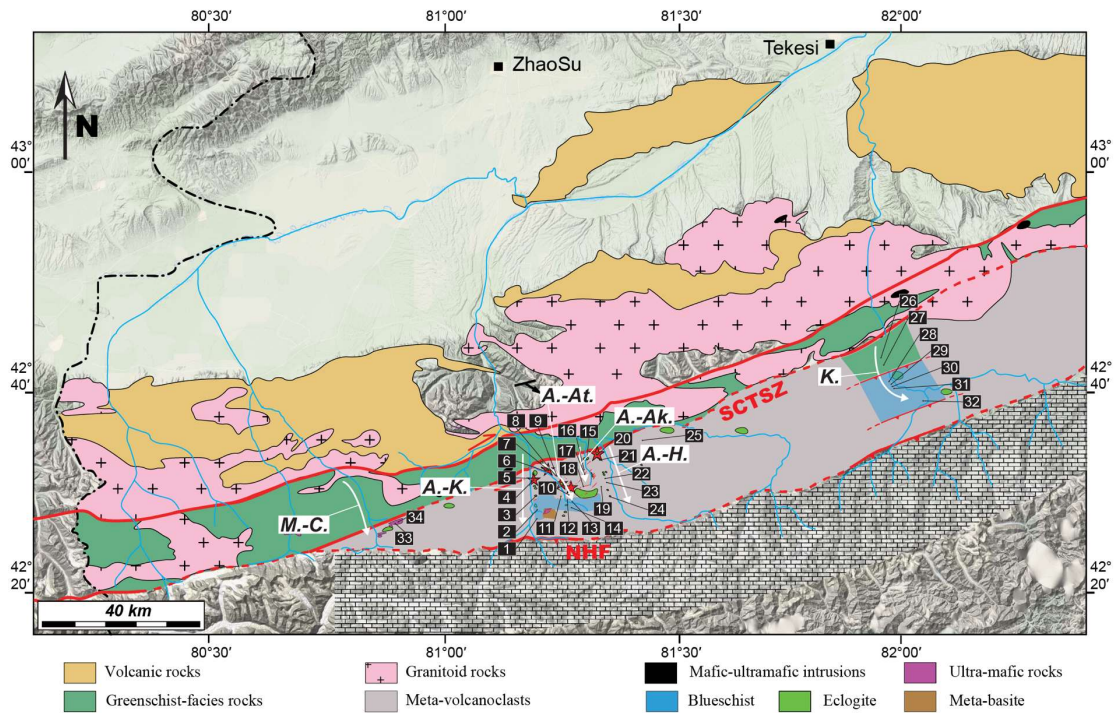


Figure 69: Geological map with the locality of previous age reports. Number corresponds to the detail of each previous works compiled in Table 22.

Exhaustive compilation of previous age reports and associated P-T estimates in Chinese SW-Tianshan HP/UHP-LT accretionary complex														
No.*	Lithology	Location	Coordinates ^b	Dating method	Age (Ma)	2σ-error	PT E. method ^c	Tie age to metamorphism ^d	P (GPa)	dP	T (°C)	dT	Interpretation of age ^e	Reference
This study														
a (J2)	chl-ph-bi-qz schist	Akeyazi-kebuerte	42.5531 81.1816	Phengite Ar-Ar step-heating	277	1.8	avPT	SRrPTh.	0.51	0.24	578	56	Dated the SCTSZ strike-slip deformation	-
b (22)	grt-bearing chl-ph-bi-qz schist	Akeyazi-kebuerte	42.5385 81.1969	Phengite Ar-Ar step-heating	300	3.8	avPT	SRrPTh.	0.85	0.35	518	19	Constrained the later stage GS-facies deformation during doming and/or final juxtaposition	-
c (135)	UHP meta-pelite	Akeyazi-kebuerte	42.5319 81.2035	Phengite in situ Ar-Ar	319	3.6	avPT	Directly in situ probing on kinematic structure	2.77	0.03	562	11	Dated the major shearing deformation around UHP peak metamorphism of UH unit	-
d (26)	UHP meta-graywack	Akeyazi-kebuerte	42.5132 81.2029	Phengite in situ Ar-Ar	321	2.5	avPT	Directly in situ probing on kinematic structure	2.75	0.05	507	32	Dated the major shearing deformation around UHP peak metamorphism of UH unit	-
e (117)	blueschist	Akeyazi-kebuerte	42.4839 81.2003	Phengite in situ Ar-Ar	334	7.8	avPT	Directly in situ probing on kinematic structure	2.08	0.11	514	14	Dated the major shearing deformation around HP BS/EC facies peak metamorphism of EB unit	-
f (32)	blueschist	Akeyazi-kebuerte	42.4739 81.1989	Phengite in situ Ar-Ar	330	7.7	avPT	Directly in situ probing on kinematic structure	1.99	0.15	519	12	Dated the major shearing deformation around UHP peak metamorphism of UH unit	-
g (157)	chl-ph-qz-ab schist	Akeyazi-kebuerte	42.4690 81.2076	Phengite in situ Ar-Ar	276	5.2	REaL.	Directly in situ probing on kinematic structure	0.50	0.40	400	100	Echoed the SCTSZ strike-slip deformation	-
h (157)	chl-ph-qz-ab schist	Akeyazi-kebuerte	42.4690 81.2076	Phengite Ar-Ar step-heating	326	2.6	REaL.	RTP.	0.50	0.40	400	100	Troubled by excess Ar or dated early stage ph growth	-
l (158)	grt-gln-ep meta-basite	Akeyazi-kebuerte	42.4589 81.2246	Zircon U-Pb	359	3.6	avPT	Tie zircon to garnet growth via REEs pattern	1.46	0.16	484	29	Constrained the major garnet growth event around lower BS facies peak metamorphism of MU unit	-
j (158)	grt-gln-ep meta-basite	Akeyazi-kebuerte	42.4589 81.2246	Zircon U-Pb	449	4.7	avPT	SRrPTh.	0.50	0.40	400	100	Protolith age	-
k (147)	retrograde blueschist	Akeyazi-kebuerte	42.4477 81.1899	Phengite Ar-Ar step-heating	304	2	avPT	SRrPTh.	0.92	0.08	473	21	Constrained the later stage GS-facies deformation during doming and/or final juxtaposition	-
l (148-1)	meta-graywack	Akeyazi-kebuerte	42.4447 81.1908	Phengite in situ Ar-Ar	313	0.9	avPT	Directly in situ probing on kinematic structure	0.81	0.10	516	15	Dated the major shearing deformation around GS-facies peak metamorphism of GT unit	-
n (148-2)	meta-graywack	Akeyazi-kebuerte	42.4447 81.1908	Phengite in situ Ar-Ar	313	1.1	avPT	Directly in situ probing on kinematic structure	0.81	0.10	516	15	Dated the major shearing deformation around GS-facies peak metamorphism of GT unit	-
n (71)	meta-graywack	Akeyazi-kebuerte	42.4358 81.1878	Phengite in situ Ar-Ar	284	1.5	REaL.	Directly in situ probing on kinematic structure	0.50	0.40	400	100	Echoed the SCTSZ strike-slip deformation	-
Previous works														
1	blueschist	Akeyazi-kebuerte	42.4515 81.1983	White-mica Ar-Ar	364	1	REaL.	RTL.	1.40	0.60	325	175	GS facies overprint	Gao et al., Chinese Science Bulletin (in CN), 2000
2	blueschist	Akeyazi-kebuerte	42.4654 81.1981	Gln Ar-Ar	370	1	REaL.	RTL.	1.40	0.60	325	175	BS facies overprint	Gao et al., Chinese Science Bulletin (in CN), 2000
3	eclogite	Akeyazi-kebuerte	42.4808 81.2003	Grt-gln Sm-Nd	346	3	CTB.	SRrPTh.	1.90	0.10	525	25	(HP/UHP?) EC facies metamorphism	Gao et al., Lithos, 2003
4	UHP mica schist	Akeyazi-kebuerte	42.5200 81.1916	Zircon U-Pb	320.4	3.7	Ps grt isopleth	SRrPTh.	2.70	0.20	560	15	UHP EC facies metamorphism	Yang et al., JAES, 2013
5	blueschist (used to be EC)	Akeyazi-kebuerte	42.5181 81.1950	Grt-gln-WR Sm-Nd	318.4	3.9	Ps grt isopleth	SRrPTh.	2.55	0.05	463	38	HP EC facies metamorphism	Soldner et al., GR, 2016
6	eclogite	Akeyazi-kebuerte	42.5367 81.2092	White-mica Ar-Ar	316.9	1	Ps grt isopleth	Tie phengite to garnet growth via thermodynamic modelling	2.20	0.20	505	25	HP EC facies prograde metamorphism	Tan et al., IGR, 2018
7	eclogite	Akeyazi-atalantay	42.5325 81.2103	Zircon U-Pb	318	2.3	Ps grt isopleth + CTB.	Tie zircon to garnet growth via REEs pattern	2.95	0.20	510	15	UHP EC facies metamorphism	Tan et al., Lithos, 2017
7	eclogite	Akeyazi-atalantay	42.5325 81.2103	Zircon U-Pb	316.8	0.83	Ps grt isopleth + CTB.	Tie zircon to garnet growth via REEs pattern	2.40	0.30	550	30	HP EC facies metamorphism	Tan et al., Lithos, 2017
7	eclogite	Akeyazi-atalantay	42.5325 81.2103	Zircon U-Pb	303.1	1.7	Ps grt isopleth + CTB.	SRrPTh.	0.90	0.30	400	110	GS/BS facies overprinting & deformation	Tan et al., Lithos, 2017
7	eclogite	Akeyazi-atalantay	42.5325 81.2103	Zircon U-Pb	280.8	4.9	Ps grt isopleth + CTB.	SRrPTh.	0.50	0.40	400	100	Near surface	Tan et al., Lithos, 2017
7	eclogite	Akeyazi-atalantay	42.5325 81.2103	Grt-gln-WR Sm-Nd	312.1	2.4	Ps grt isopleth + CTB.	Tie to deformation via observation	1.90	0.13	530	25	EC facies deformation	Tan et al., Lithos, 2017
8	eclogite	Akeyazi-atalantay	42.5139 81.2475	Zircon U-Pb	318	2	REaL.	RTL.	2.20	1.00	600	200	(HP/UHP?) EC facies metamorphism	Liu et al., Lithos, 2014
9	eclogite	Akeyazi-atalantay	42.5125 81.2477	Zircon U-Pb	319.8	3.1	REaL.	RTL.	2.20	1.00	600	200	(HP/UHP?) EC facies metamorphism	Su et al., EJM, 2010
10	blueschist	Akeyazi-atalantay	42.4955 81.2765	Zircon U-Pb	234	6	REaL.	RTL.	2.20	1.00	600	200	(HP/UHP?) EC facies metamorphism	Zhang et al., Lithos, 2007
11	blueschist	Akeyazi-atalantay	42.4949 81.2608	White-mica Ar-Ar	311.6	0.5	REaL.	RTL.	1.40	0.60	325	175	cooling or recrystallization	Klemd et al., AMG, 2005
11	blueschist	Akeyazi-atalantay	42.4949 81.2608	White-mica Ar-Ar	311.6	0.5	REaL.	RTL.	1.40	0.60	325	175	cooling or recrystallization	Klemd et al., AMG, 2005
11	blueschist	Akeyazi-atalantay	42.4949 81.2608	White-mica Ar-Ar	311.6	0.5	REaL.	RTL.	1.40	0.60	325	175	cooling or recrystallization	Klemd et al., AMG, 2005
11	blueschist	Akeyazi-atalantay	42.4949 81.2608	White-mica Ar-Ar	311.6	0.5	REaL.	RTL.	1.40	0.60	325	175	cooling or recrystallization	Klemd et al., AMG, 2005
11	blueschist	Akeyazi-atalantay	42.4949 81.2608	White-mica Ar-Ar	311.6	0.5	REaL.	RTL.	1.40	0.60	325	175	cooling or recrystallization	Klemd et al., AMG, 2005
11	blueschist	Akeyazi-atalantay	42.4949 81.2608	White-mica Ar-Ar	311.6	0.5	REaL.	RTL.	1.40	0.60	325	175	cooling or recrystallization	Klemd et al., AMG, 2005
11	blueschist	Akeyazi-atalantay	42.4949 81.2608	White-mica Ar-Ar	311.6	0.5	REaL.	RTL.	1.40	0.60	325	175	cooling or recrystallization	Klemd et al., AMG, 2005
11	blueschist	Akeyazi-atalantay	42.4949 81.2608	White-mica Ar-Ar	311.6	0.5	REaL.	RTL.	1.40	0.60	325	175	cooling or recrystallization	Klemd et al., AMG, 2005
11	blueschist	Akeyazi-atalantay	42.4949 81.2608	White-mica Ar-Ar	311.6	0.5	REaL.	RTL.	1.40	0.60	325	175	cooling or recrystallization	Klemd et al., AMG, 2005
11	blueschist	Akeyazi-atalantay	42.4949 81.2608	White-mica Ar-Ar	311.6	0.5	REaL.	RTL.	1.40	0.60	325	175	cooling or recrystallization	Klemd et al., AMG, 2005
11	blueschist	Akeyazi-atalantay	42.4949 81.2608	White-mica Ar-Ar	311.6	0.5	REaL.	RTL.	1.40	0.60	325	175	cooling or recrystallization	Klemd et al., AMG, 2005
11	blueschist	Akeyazi-atalantay	42.4949 81.2608	White-mica Ar-Ar	311.6	0.5	REaL.	RTL.	1.40	0.60	325	175	cooling or recrystallization	Klemd et al., AMG, 2005
11	blueschist	Akeyazi-atalantay	42.4949 81.2608	White-mica Ar-Ar	311.6	0.5	REaL.	RTL.	1.40	0.60	325	175	cooling or recrystallization	Klemd et al., AMG, 2005
11	blueschist	Akeyazi-atalantay	42.4949 81.2608	White-mica Ar-Ar	311.6	0.5	REaL.	RTL.	1.40	0.60	325	175	cooling or recrystallization	Klemd et al., AMG, 2005
11	blueschist	Akeyazi-atalantay	42.4949 81.2608	White-mica Ar-Ar	311.6	0.5	REaL.	RTL.	1.40	0.60	325	175	cooling or recrystallization	Klemd et al., AMG, 2005
11	blueschist	Akeyazi-atalantay	42.4949 81.2608	White-mica Ar-Ar	311.6	0.5	REaL.	RTL.	1.40	0.60	325	175	cooling or recrystallization	Klemd et al., AMG, 2005
11	blueschist	Akeyazi-atalantay	42.4949 81.2608	White-mica Ar-Ar	311.6	0.5	REaL.	RTL.	1.40	0.60	325	175	cooling or recrystallization	Klemd et al., AMG, 2005
11	blueschist	Akeyazi-atalantay	42.4949 81.2608	White-mica Ar-Ar	311.6	0.5	REaL.	RTL.	1.40	0.60	325	175	cooling or recrystallization	Klemd et al., AMG, 2005
11	blueschist	Akeyazi-atalantay	42.4949 81.2608	White-mica Ar-Ar	311.6	0.5	REaL.	RTL.	1.40	0.60	325	175	cooling or recrystallization	Klemd et al., AMG, 2005
11	blueschist	Akeyazi-atalantay	42.4949 81.2608	White-mica Ar-Ar	311.6	0.5	REaL.	RTL.	1.40	0.60	325	175	cooling or recrystallization	Klemd et al., AMG, 2005
11	blueschist	Akeyazi-atalantay	42.4949 81.2608	White-mica Ar-Ar	311.6	0.5	REaL.	RTL.	1.40	0.60	325	175	cooling or recrystallization	Klemd et al., AMG, 2005
11	blueschist	Akeyazi-atalantay	42.4949 81.2608	White-mica Ar-Ar	311.6	0.5	REaL.	RTL.	1.40	0.60	325	175	cooling or recrystallization	Klemd et al., AMG, 2005
11	blueschist	Akeyazi-atalantay	42.4949 81.2608	White-mica Ar-Ar	311.6	0.5	REaL.	RTL.	1.40	0.60	325	175	cooling or recrystallization	Klemd et al., AMG, 2005
11	blueschist	Akeyazi-atalantay	42.4949 81.2608	White-mica Ar-Ar	311.6	0.5	REaL.	RTL.	1.40	0.60	325	175	cooling or recrystallization	Klemd et al., AMG, 2005
11	blueschist	Akeyazi-atalantay	42.4949 81.2608	White-mica Ar-Ar	311.6	0.5	REaL.	RTL.	1.40	0.60	325	175	cooling or recrystallization	Klemd et al., AMG, 2005
11	blueschist	Akeyazi-atalantay	42.4949 81.2608	White-mica Ar-Ar	311.6	0.5	REaL.	RTL.	1.40	0.60	325	175	cooling or recrystallization	Klemd et al., AMG, 2005
11	blueschist	Akeyazi-atalantay	42.4949 81.2608	White-mica Ar-Ar	311.6	0.5	REaL.	RTL.	1.40	0.60	325	175	cooling or recrystallization	Klemd et al., AMG, 2005
11	blueschist	Akeyazi-atalantay	42.4949 81.2608	White-mica Ar-Ar	311.6	0.5	REaL.	RTL.	1.40	0.60	325	175	cooling or recrystallization	Klemd et al., AMG, 2005
11	blueschist	Akeyazi-atalantay	42.4949 81.2608	White-mica Ar-Ar	311.6	0.5	REaL.	RTL.	1.40	0.60	325	175	cooling or recrystallization	Klemd et al., AMG, 2005
11	blueschist	Akeyazi-atalantay	42.4949 81.2608	White-mica Ar-Ar	311.6	0.5	REaL.	RTL.	1.40	0.60	325	175	cooling or recrystallization	Klemd et al., AMG, 2005
11	blueschist	Akeyazi-atalantay	42.4949 81.2608	White-mica Ar-Ar	311.6	0.5	REaL.	RTL.	1.40	0.60	325	175	cooling or recrystallization	Klemd et al., AMG, 2005
11	blueschist	Akeyazi-atalantay	42.4949 81.2608	White-mica Ar-Ar	311.6	0.5	REaL.	RTL.	1.40	0.60	325	175	cooling or recrystallization	Klemd et al., AMG, 2005
11	blueschist	Akeyazi-atalantay	42.4949 81.2608	White-mica Ar-Ar	311.6	0.5	REaL.	RTL.	1.40	0.60	325	175	cooling or recrystallization	Klemd et al., AMG, 2005
11	blueschist	Akeyazi-atalantay	42.4949 81.2608	White-mica Ar-Ar	311.6	0.5	REaL.	RTL.	1.40	0.60	325	175	cooling or recrystallization	Klemd et al., AMG, 2005
11	blueschist	Akeyazi-atalantay	42.4949 81.2608	White-mica Ar-Ar	311.6	0.5	REaL.	RTL.	1.40	0.60	325	175	cooling or recrystallization	Klemd et al., AMG, 2005
11	blueschist	Akeyazi-atalantay	42.4949 81.2608	White-mica Ar-Ar	311.6	0.5	REaL.	RTL.	1.40	0.60	325	175	cooling or recrystallization	Klemd et al., AMG, 2005
11	blueschist	Akeyazi-atalantay	42.4949 81.2608	White-mica Ar-Ar	311.6	0.5	REaL.	RTL.	1.40	0.60	325	175	cooling or recrystallization	Klemd et al., AMG, 2005
11	blueschist	Akeyazi-atalantay	42.4949 81.2608	White-mica Ar-Ar	311.6	0.5	REaL.	RTL.	1.40	0.60	325	175	cooling or recrystallization	Klemd et al., AMG, 2005
11	blueschist	Akeyazi-atalantay	42.4949 81.2608	White-mica Ar-Ar	311.6	0.5	REaL.	RTL.	1.40	0.60	325	175	cooling or recrystallization	Klemd et al., AMG, 2005
11	blueschist	Akeyazi-atalantay	42.4949 81.2608	White-mica Ar-Ar	311.6	0.5	REaL.	RTL.	1.40	0.60	325	175	cooling or recrystallization	Klemd et al., AMG, 2005
11	blueschist	Akeyazi-atalantay	42.4949 81.2608	White-mica Ar-Ar	311.6	0.5	REaL.</							

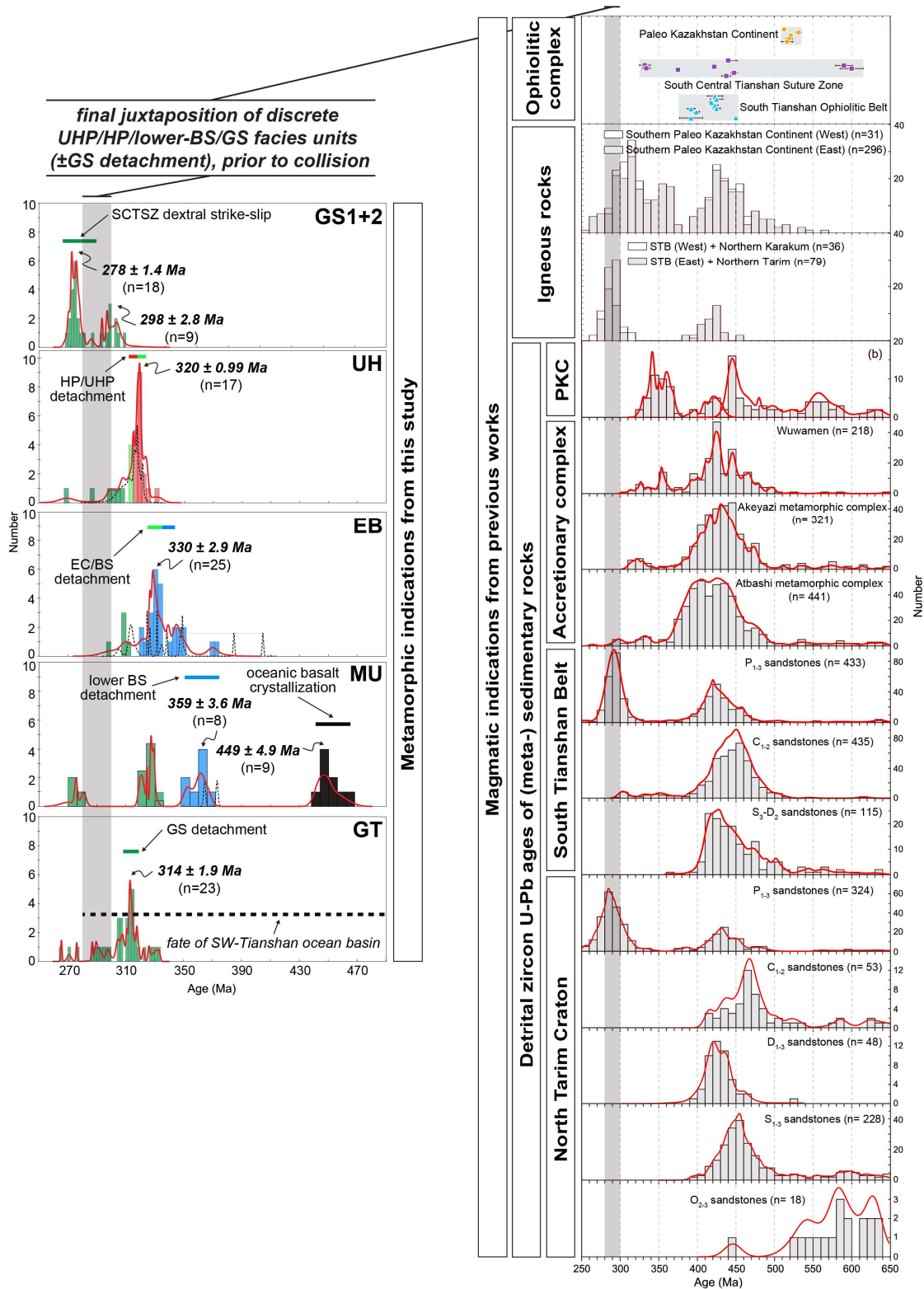


Figure 70: The comparison between ages from metamorphic indications (this study+ previous works) and those from magmatic indications (previous works) that related to the Paleo South Tianshan Ocean Basin subduction setting (i.e., upper plate: the Paleo Kazakhstan Continent at the North, and the STB+Tarim craton at the South; lower plate: the subducting ocean basin). Check compilation Tables in Wang et al. (2018) for the detail of regional magmatic ages.

7. Discussion and Perspective

7.1. Insight from regional P-T-time-lithologies review

Two decades have elapsed since eclogites were firstly reported from the STMB (Gao, 1997). Fruitful investigations on field occurrences, protoliths, petrological characteristics, peak metamorphic P-T conditions and ages, metamorphic fluids have been obtained (§2, also see Tan et al. (2017) for comprehensive review). The STMB has been interpreted as an accretionary *mélange* associated with the subduction of the South Tianshan Ocean (Gao et al., 1998; Gao and Klemd, 2000; Li et al., 2016a). In that sense it would represent the largest oceanic-type UHP belt in the world (Zhang et al., 2013; Zhang et al., 2007; Zhang et al., 2018), though not in the sense of an oceanic lithosphere: it is essentially made of metavolcanoclastics and lacks thick mafic and ultramafic horizons. An opposite interpretation considers the SMTB as the result of continental subduction (Loury et al., 2018).

Although the metamorphic evolution of eclogites and host micaschists has been studied in detail (§2), controversy on the exhumation mechanism of these rocks still exist: i) some early studies suggested that the exhumation of HP-UHP rocks underwent an early syn-subduction wedge extrusion stage and a later thrust stage (Gao et al., 1995; Gao and Klemd, 2003); ii) Lü et al. (2012) divided the metamorphic terrane into a northern “UHP unit” and a southern “HP unit” (separated by a somewhat cryptic contact) juxtaposed from different depths; iii) Li et al. (2016a, 2016b) tentatively proposed a subduction channel model, considering eclogites as discrete blocks within a buoyant micaschist matrix facilitating their exhumation; iv) a surprisingly long

exhumation period (>70 Myr) was tentatively proposed for the UHP terrane by Zhang et al. (2013).

Two questions are therefore of particular interest, prior to answering how the AMC can be recovered (i.e., Agard et al., 2018):

- 1) does the STMB behave like an oceanic-type fossil subduction remnant (e.g., with respect to W. Alpine and/or Franciscan remnants)?
- 2) Can we clarify exhumation mechanisms?

A tentative estimate of the abundance (vol%) of the different lithologies exposed in the STMB (Figure 52) can be made based on our field investigations (§2 and 6) and

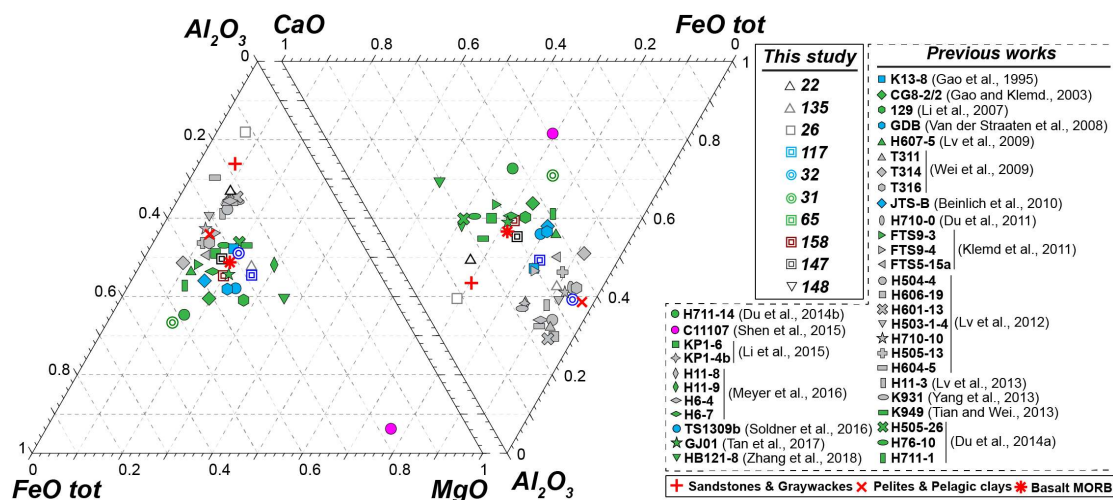


Figure 71: Major elements composition of selected samples in this PhD thesis and those from previous works.

literature data (e.g., Bayet et al., 2018; Gao et al., 1999, 1995; Z. Lü et al., 2012; Meyer et al., 2016; Soldner et al., 2017).

Exposures of meta-ultramafic rocks are limited (<5 vol%) in the STMB, with rare occurrences only reported at present in the adjacent Muzaerte-Changawuzi (Gao et al., 1999; Li et al., 2007) and Kebuerte-Akesayi valley (§6). Metavolcanic blocks or

boudins/lenses/slices of various scales are commonly found within the STMB (not only limited to the AMC) but amount to $\leq 10\text{-}15$ vol% (Figure 52).

Potential buoyancy contrasts for the various rock types are assessed below using P-T-density pseudosections. Previous P-T estimates are used (Figure 72) to identify whether the average exhumed eclogite, blueschist, and ultramafic rocks are buoyant or not (Figure 71). Eclogitic metavolcanics with pervasive dehydrated dense phases (e.g., omphacite, garnet) are essentially too dense ($\sim 3.28\text{-}3.46$ g/cm³; Figure 72a), whether at HP or UHP conditions, compared with mantle peridotite (> 3.3 g/cm³). Blueschists, in contrast, are less dense ($\sim 3.10\text{-}3.25$ g/cm³; Figure 72b), even when T_{peak} reach $\sim 600^\circ\text{C}$. Serpentinites (containing ~ 80 vol% antigorite at UHP peak in the area) are obviously lighter than the mantle, with estimated density ranging from 2.70 to 2.90 g/cm³, almost independent of pressure if $T < 500^\circ\text{C}$ (Figure 72c). In contrast, pseudosections performed for the average composition of regional metavolcanoclastics as well as for common felsic (sandstone & graywacke) and pelitic lithologies (Figure 73) shows that the metasedimentary matrix host rocks of the STMB are buoyant enough (i.e., < 3.3 g/cm³) even at UHP conditions.

Considering the compositional diversity of the entire STMB (e.g., assuming felsic:pelitic:mafic EC/BS:serpentinite $\sim 35:50:10:5$; according to our field investigations and those of Bayet et al. (2018); Figure 52), the bulk density will be ~ 3.02 g/cm³ at 2.75 GPa and 520°C . Computed densities are ~ 2.88 g/cm³ for a completely serpentinitized mantle and ~ 3.33 g/cm³ for a dry mantle (Angiboust and Agard, 2010). Even considering 30% of serpentinitization (i.e. density ~ 3.09 g/cm³), for

both the slab and upper plate mantle, the buoyancy contrast at peak conditions between the STMB slices and the surrounding mantle will be relatively small yet still positive ($\sim +0.05 \text{ g/cm}^3$). While changes in boundary conditions (e.g., transient mechanical coupling; Agard et al., 2009, 2018) are probably required at depth to detach the various sub-units (see §7.2), a continental buoy is thus not inherently needed to explain their preservation. Continental subduction (Loury et al., 2018) would be an additional help, but seems unlikely for now in the absence of key lithologies such as gneisses and/or felsic amphibolitic rocks (\pm garnet-bearing peridotites with mafic lenses as in Dora Maira, Dabie-Sulu or Kokchetav; Guillot et al. (2009)). Moreover, several internal contact and mass thick metasedimentary slices stacking had been proposed for the AMC, with pervasive coesite findings and EC/BS facies senses of shear (§2) observed in both metavolcanics and metavolcanoclastics (Figure 52; Bayet et al., 2018). This essentially rule out the possibility of ‘long exhumation period ($>70 \text{ Ma}$) of the UHP terrane in the AMC’ since the pervasive preservation of coesite and/or lawsonite (although less reported in the AMC, §2) imply the exhumation of the UHP terrane should be relatively fast enough before the ‘refrigerator’ condition could be broke by retrograde metamorphism and/or fluid-rock interaction during exhumation, while the so-called ‘long exhumation period ($>70 \text{ Ma}$)’ is too long compared with that of worldwide fossil oceanic subduction remnants ($\sim 15 \text{ Ma}$; Agard et al., 2018, 2009; Guillot et al., 2009). Hence, the recovery puzzle of the STMB is then located on how can rocks/slices detached from down-going slab through space and time, and how fast it should be for preserving some key mineralogical ‘information’.

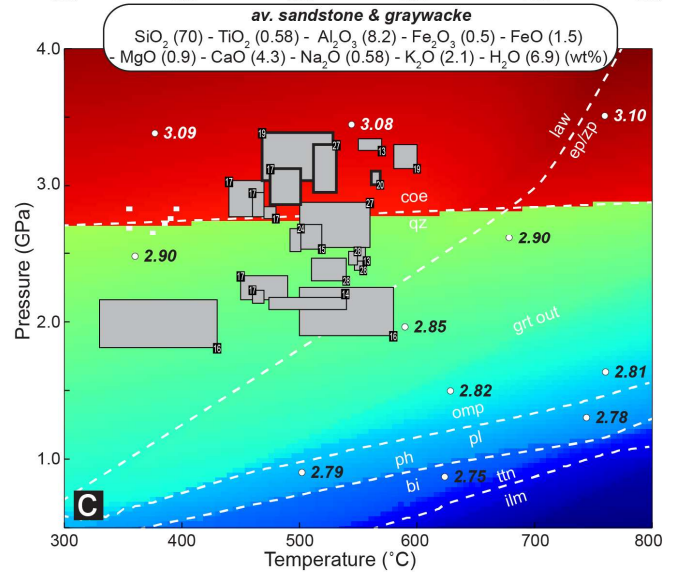
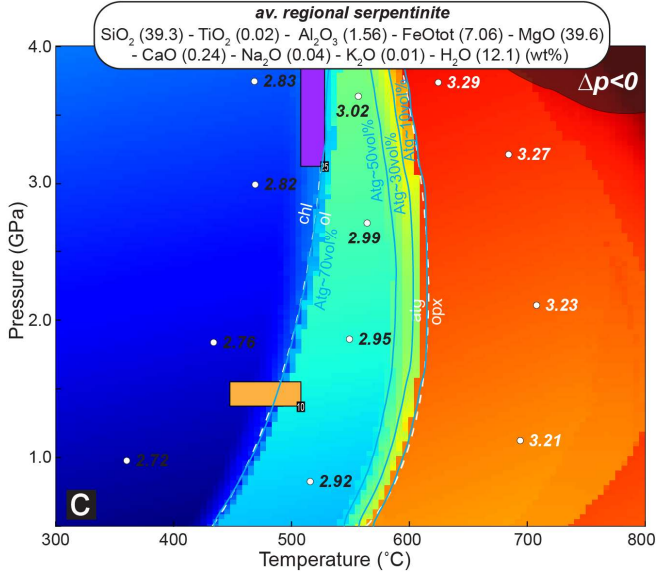
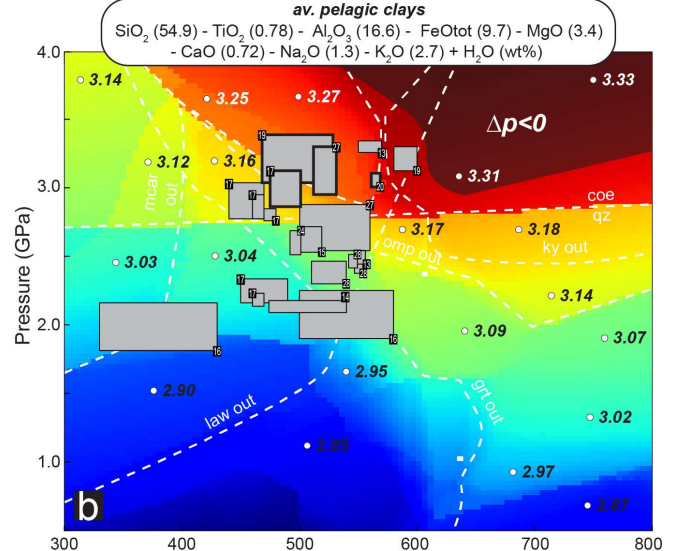
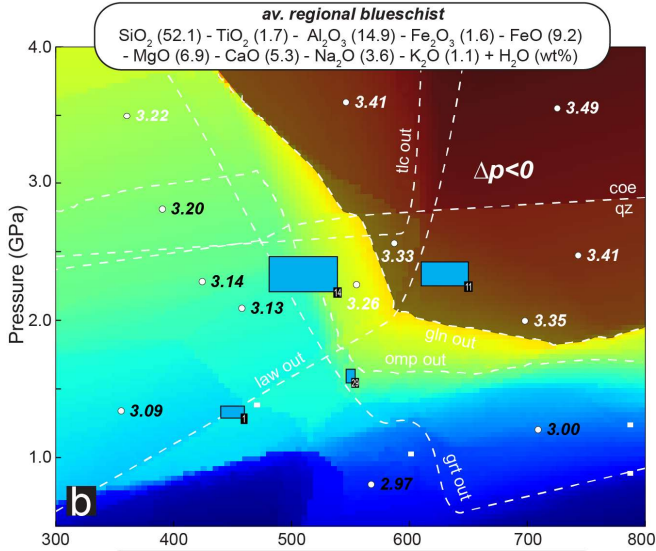
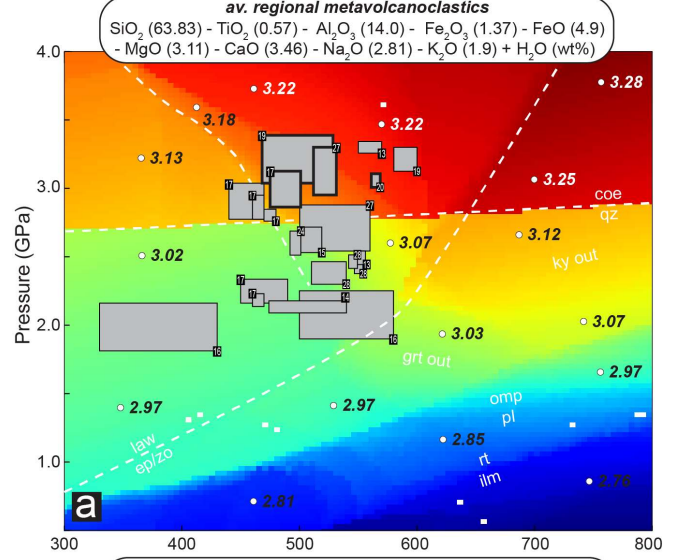
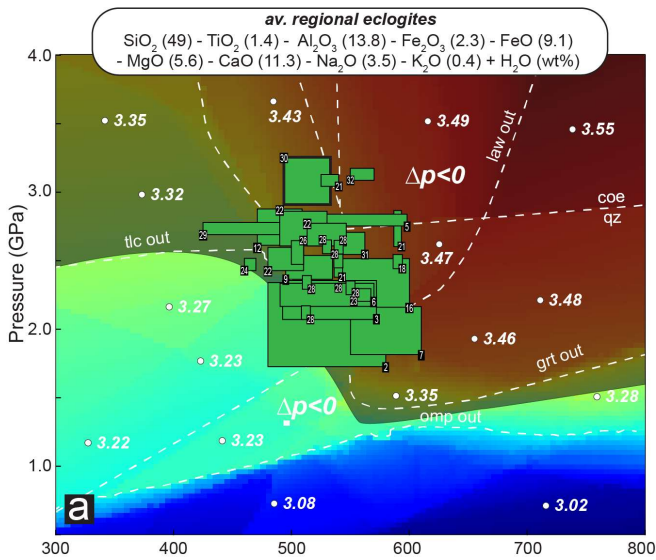


Figure 73: P-T-density pseudosections conducted for representative compositions of regional eclogite, blueschist and serpentinite.

Figure 72: P-T-density pseudosections conducted for representative compositions of metavolcanoclastics (regional and global)

7.2. Structure and Deformation Pattern

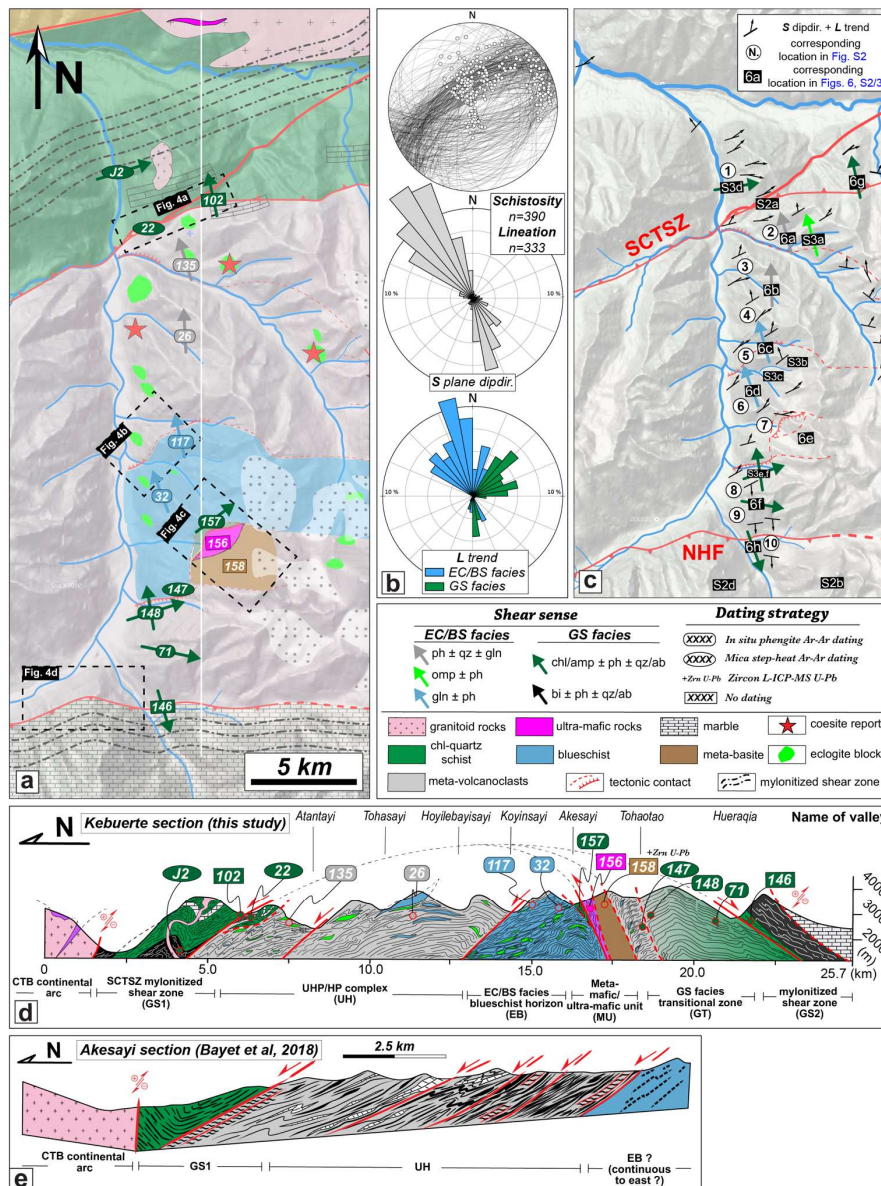


Figure 74: (a) Close-up view of the area along the Kebuerte valley showing sampling sites, measured shear senses and the location of field observations (Figure 53). (b) The summary of the pattern of regional schistosity and lineation. Detail data with respect to measurement location are presented in Figure 54. (c) Simple map with the plots of structural element showing the location of field observations corresponding to those in Figures 55, 64 and 65. (d) Approximately N-S ~30km-long section constructed, along the Kebuerte valley, across the previous so-called HP/UHP *mélange* (e.g., Klemd et al., 2011; Li et al., 2016) and further touch to the South margin of the STMB around the Northern Haerkeshan Fault (NHF), with detailed sample sites and analysis strategy. (e) The Akesayi section from recent work (Bayet et al., 2018) was also cited for comparison.

Structure and deformation pattern investigations have been performed both on moderately schistosed coesite-bearing oceanic eclogite slices (§4) and regional scale P-T-time-deformation mapping along the Kebuerte transect (§6), crossing through

different lithologies and sub-units. Preserved HP/UHP eclogitic facies deformation was occasionally identified by stretched omphacite in mafic boudins (Figure 21, §4) and inclusion trails in garnet (Figure 56c, §4) but could not be related to provide a large-scale picture of the prograde and/or near-peak deformation. Eclogite to blueschist facies lineations (Figure 55a-d, 60b, 64a-c, 66) cluster along a NNW-SSE strike at ~N160 (Figure 52a-c, 54). Most GS facies lineations have a more SW-NE trending orientation (Figure 55f-h, 56i, 60b, 64d-e, g-h, 65a-b, d, h-j, 66), except close to the north and south boundaries of the AMC where they are more N-S trending (Figure 52a-c, 54). Regional deformation is relatively non-coaxial, as exemplified by pervasive S-C structures (Figure 55, 56i, 60b, 64-66) and asymmetric folding. Shear senses associated with EC/BS and GS facies metamorphism, whether at outcrop scale or in thin-section, are very consistent throughout the area, and respectively top to NNW and top to NEE (Figure 52a-c), pointing to the importance of simple shear during exhumation (also see Bayet et al., 2018), following northward subduction (Scheltens et al., 2015). The dominance of top to NEE GS facies shear senses might relate, by contrast, to later regional dextral strike-slip deformation.

Contacts between domains with slightly different lithologies and/or tectonic patterns (e.g., asymmetric shearing and abundance of mafic boudins in UH, Figure 52d) are interpreted to mark distinct km-scale tectonic sub-units: from north to south the GS1, UH, EB, MU, GT, and GS2 units (e.g., Figure 74d). Our observations and field mapping (e.g., cross-section of Figure 52d) thus suggest that the Akeyasi metamorphic complex, at least in the surroundings of the Kebuerte valley, is a metamorphic dome

made of a stack of individual sub-units or nappes. This contradicts the view that the AMC might be a subduction mélange in the sense of Cloos & Shreve (1988a, 1988b) or Meyer et al. (2016). The lateral extension of the contacts can in places only be inferred, unfortunately, due the presence of glaciers (but the more mafic EB unit seems to correspond to the pillow unit described by Bayet et al. (2018)). This identification of distinct sub-units is nevertheless strengthened by our results on the patterns and timing of their metamorphic evolutions: the exposed core of the metamorphic dome (i.e., the EB unit) does not correspond to the most deeply buried slice (indicating thrusting at some point of the tectonic history) and contrasting ages were obtained for the different sub-units, suggesting diachronous detachment from the subducting slab.

7.3. P-T constraints

P-T conditions were estimated by thermodynamic modelling for the coesite-bearing oceanic eclogite (in the UH unit, §4). This yields UHP peak burial $\sim 2.95 \pm 0.2$ GPa, 510 ± 20 °C, with later reequilibration stages at $\sim 2.45 \pm 0.2$ GPa, 540 ± 20 °C and $\sim 2.0 \pm 0.15$ GPa, 525 ± 25 °C. These results are consistent with the P-T estimates of previous UHP reports (Lü et al., 2012; Wei et al., 2009; Yang et al., 2013). P-T estimates were also obtained using the THERMOCALC multi-equilibrium average PT approach for 13 samples along the Kebuerte transect. Metavolcanoclastics from the UH sub-unit (similar to the coesite-bearing oceanic eclogite sample), yield UHP peak burial P-T conditions around 480-560°C and 2.75GPa (± 0.1) on average. Samples from the EC/BS EB unit (Figure 56b-c) record a prograde increase in pressure and temperature

from 1.8 GPa (± 0.10), 490°C (± 15), to peak burial ~ 2.1 GPa (± 0.15), 505°C (± 15). The meta-mafic/-ultramafic unit experienced a much lower pressure from prograde ~ 0.95 GPa (± 0.18) and 464°C (± 28) to peak burial ~ 1.46 GPa (± 0.16), 484°C (± 29) and post-peak ~ 0.93 GPa (± 0.06), 556°C (± 13). P-T estimates for samples located to the north and south of the AMC (GS1 and GS2 sub-units) and from the transitional GT sub-unit reveal broadly comparable GS to lower-BS facies P-T histories, with peak burial around 0.7-1.0 GPa, 470-520°C and post-peak conditions of ~ 0.4 -0.6 GPa, 520-570°C.

Similar GS to lower-BS facies conditions around 0.90-1.10 GPa, 460-500°C were identified as retrograde overprint on metavolcanoclastics from the UH and EB units

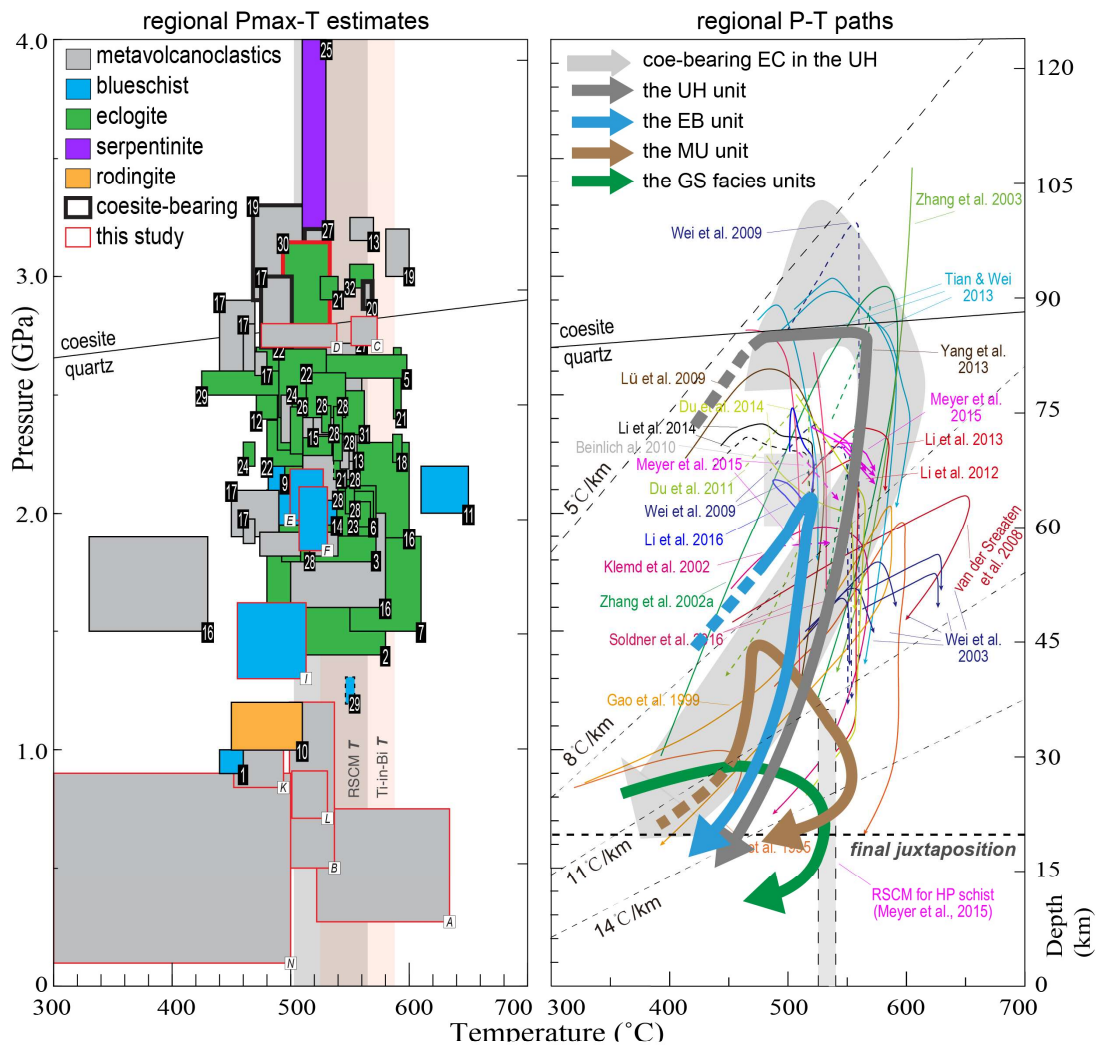


Figure 75 The compilation of regional Pmax-T estimates and P-T paths. Numbers in black box corresponds to the detail of previous works in Table 1. Letters in white box marks the P-T estimates from this PhD thesis (mainly §6), listed in Table 22.

(sample, 32). Ages (recalled below) support a change in metamorphic gradient with time, from an intermediate to cold subduction regime (i.e., from ~12 to 5-7°C/km; Figure 59b; also see Agard et al. (2018) and Angiboust et al. (2016)).

Previous P-T estimates (i.e., until this year, whether with conventional thermobarometry or pseudosection modeling; see §2 for the compilation) mainly focused on individual key samples in the UH unit with results clustering between HP and UHP conditions (i.e., 2.2 to 3.0 GPa, with ~70% located within the HP field, Figure 75). Homogeneous distribution of UHP conditions ≥ 2.5 GPa, however, has recently been argued based on Raman Quartz elastic barometry mapping results (Bayet et al., 2018). This conclusion is in fact supported by the recent study, by means of pseudosection modeling, of Lü and Bucher (2018). Altogether, claims of 'only' HP slices/blocks/boudins in the UH unit, as previously indicated (Du et al., 2014; Li et al., 2015; Meyer et al., 2016), are probably to be taken with caution.

7.4. Radiometric age constraints Implication for Late Carboniferous cold subduction dynamics

Our P-T-time study (e.g., Figure 76) was performed:

— for one representative coesite-bearing UHP eclogitic slice (§4) with informative zircon textures/inclusions, using U-Pb, Sm-Nd minerals-bulk rock radiometry.

— for samples from the different sub-units with reasonable texture control (§6), using in situ Ar-Ar probing on thin-sections (together with additional zircon U-Pb for the MU unit, and step-heating Ar-Ar radiometric dating for the GS facies units).

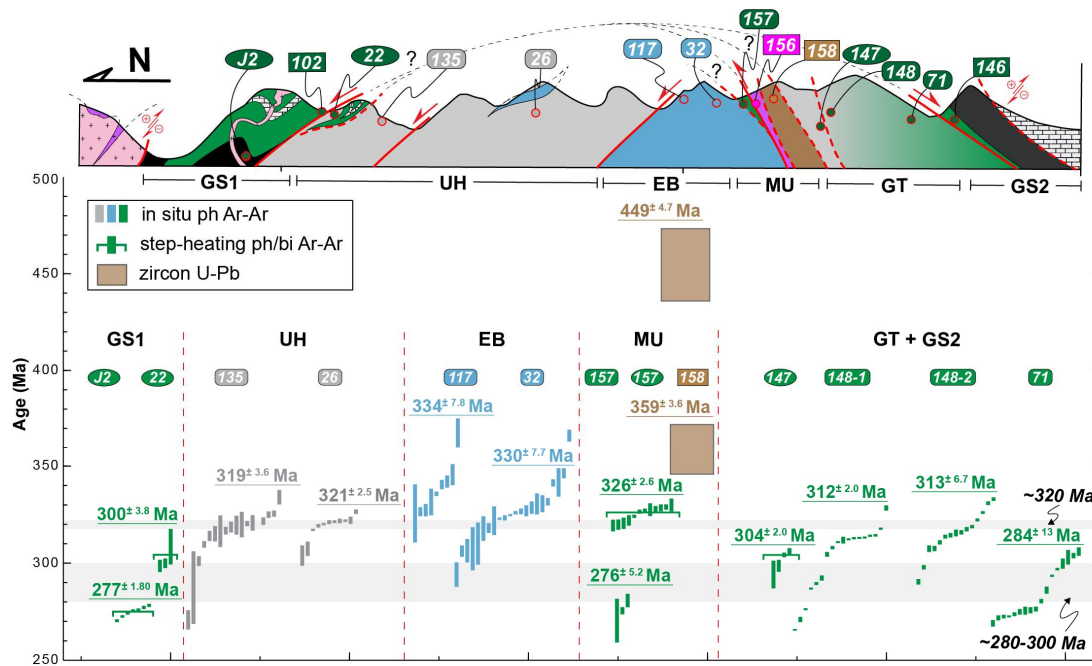


Figure 76: The summary of radiometric age constraints in this PhD thesis.

The coesite-bearing UHP sample yielded 318.0 ± 2.3 Ma for peak burial ($\sim 2.95 \pm 0.2$ GPa, 510 ± 20 °C), 316.8 ± 0.8 Ma and 312 ± 2.5 Ma for later reequilibration (from ~ 2.45 to 2 in the range 525 - 540 °C) and was exhumed to the near surface between ca. 303 and ca. 280 Ma. Ages obtained from highly substituted phengite in the UH unit yielded consistent results at $\sim 320 \pm 1$ Ma. These results match previous geochronological estimates (mostly focused on the UH unit in adjacent valleys), i.e. peak metamorphic conditions at 315 ± 5 Ma).

The other HP-LT sub-units reached peak conditions diachronously (EB: ~ 330 Ma; MU: ~ 360 Ma), reflecting a change in metamorphic gradient and possibly of the subduction thermal regime with time (Figure 59b). Overall, exhumation velocities estimate yields ~ 1.8 - 3.5 mm/yr for the UH unit, whether by U/Pb or Ar/Ar dating, and ~ 0.8 - 1.3 mm/yr for the EB unit, showing that both units have exhumation velocities comparable to most oceanic blueschists and eclogites (Agard et al., 2009). Rocks from the GS facies sub-units (GS1, GS2 and GT, Figure 60a) yield ages around ~ 275 - 318

Ma, so that the most likely timing for the juxtaposition of the four sub-units preserving a HP-LT history (namely the UH, EB, MU and partly GT), and making the center of the AMC metamorphic dome, could be around 280-300 Ma (Figure 59-61).

P-T-time results suggest the diachronous recovery of different sub-units (Figure 59b), from ~45 km (MU; 360 Ma), ~65 km (EB; 330 Ma) and ~85 km depth (UH; 320 Ma), highlighting discrete, transient episodes of detachment from the slab, in particular with respect to long-lived South Tianshan ocean subduction duration of ~120 Myr (Scheltens et al., 2015). This punctuated recovery likely results from changes in mechanical coupling (Agard et al., 2018), whose origin could be i) a change in slab geometry (e.g., slab rollback: Brun & Faccenna, 2008; slab kink: Klemm et al., 2011) (Figure 62b-c) and/or ii) a modification of the physical properties along the plate interface (i.e., mantle rheology, fluid regime, etc; Agard et al., 2018).

Final tectonic stacking of the UH, EB, MU and GT units around 280-300 Ma at ~20km Ma suggests, contrary to some interpretations (e.g., Gao et al., 2017; Wang et al., 2018; Zhang et al., 2018), that the peak burial of the UHP does not mark oceanic closure (and/or does not relate to continental collision). In particular, the ~300 Ma phengite ^{40}Ar - ^{39}Ar step-heating ages (Figure 60a, 67) from both the glaucophane-bearing GT and GS1 units suggest that subduction was still active around the Late Carboniferous (i.e., ~300 Ma). This inference is further supported by the regional magmatic indications (Figure 70). Overall, available magmatic and/or metamorphic constraints (e.g., this study) tend to show that the subduction of the Paleo South Tianshan ocean basin and relevant deposition were probably still active during the Late

Carboniferous (Figure 62a). Final emplacement of the AMC complex could take place around early Permian-late carboniferous (i.e., ~280-300 Ma, Figure 62e), prior to the collision of the Paleo Kazakhstan Continent and the Tarim Craton (+STB, Figure 62a).

7.5. A witness of transient rock dynamics

One striking feature of the STMB is the pervasive preservation of coesite both in the metavolcanics blocks and the metavolcanoclastics matrix host rocks (e.g, Figure 11) (and lawsonite, but only rarely reported as inclusions in robust phases). This further implies the existence of short-lived detachment of tectonic slices maintaining relatively refrigerating conditions. Luckily, detailed petrological investigations on major and trace elements geochemistry of garnet highlight an unusual garnet zoning with concordant, annular enrichment in Mn, HREEs and Y (Figure 38a-c), but not in other major (Fe, Ca, Mg) or key trace elements (L/MREEs, Ti, Sr, Zr, Sc, Rb and P; Figure 38). This is visible at the outcrop- and probably km-scale, in a nearby representative UHP oceanic eclogitic slice. This pattern coincides with a transient ~80 °C increase in temperature revealed by Zr-in-rutile thermometry. Mineral compositions together with thermodynamic modeling indicate that mineral breakdown cannot account alone for this unusual garnet zonation. Based on Zr-in-rutile thermometry and detailed petrology, geochemical diffusion and thermodynamic modeling (Figure 42), we show that this ~80°C short-lived thermal pulse (~300 kyrs assuming a 5 Myr overall garnet growth duration) is tentatively tied to the fast movement of detached UHP oceanic slices towards the hotter mantle wedge (Figure 44).

7.6. Perspective

Based on detailed geochemical, lithological, tectonic/structural, metamorphic and chronological investigations for samples along the Kebuerte valley of the Akeyazi metamorphic complex (AMC), this PhD thesis provides answers to some of the questions raised up the introduction (§1.4). We also propose a comprehensive geodynamic model for the tectonic-metamorphic evolution of the AMC-STMB through space and time.

Major controversies and/or questions are nevertheless still pending:

i) Is the N-S tectonic organization observed in the Kebuerte transect also visible laterally, along the SCTSZ? Only ambiguous answers exist for now, with the ultramafic unit reported in Muzhaerte-Changawuzi valley (~40km to the west of the AMC, which may have reached UHP conditions around ~310Ma).

ii) What is the duration of fluid-rock interactions and/or of the transient thermal excursion revealed by garnet zoning?

iii) Opposite subduction polarity of the Paleo South Tianshan ocean basin was proposed in the literature on the basis of structural and magmatic data.

8. Conclusions

This PhD thesis focuses on the structure and evolution of the Akeyazi metamorphic complex of the STMB, through a N-S ~30km-long transect along the Kebuerte valley. Contrasting P-T-time-deformation histories of key representative

samples from diverse sub-units have been found. What was previously proposed as a HP/UHP “mélange” should be subdivided into several coherent, kilometre-scale, metavolcanoclastic units bearing contrasting P-T-time-deformation histories. At least four of the six sub-units identified here, namely the UH (480-560°C and 2.75 GPa), EB (~2.1 GPa and 505°C), MU (~1.45 GPa and 485°C) and GT units (>~0.7-1.0 GPa and 470-520°C) experienced subduction and were buried to depths of ~85, 65, 45 and 30km respectively. The discovery of an unusual zonation in a UHP eclogitic garnet reveals the existence of a transient episode of heating at ~80km.

More precisely results indicate that:

i) The present-day geometry of the AMC is that of a metamorphic dome preserving evidence for internal nappe stacking.

ii) In situ laser probe ^{40}Ar - ^{39}Ar radiometric dating of phengite and zircon U-Pb dating yield peak burial ages of 320 ± 1 , 332 ± 2 , 359 ± 2 Ma and ~280-310 Ma, respectively, for the UH, EB, MU and regional GS facies units (GS1, GS2 and GT), with recrystallization enhanced by fluid circulation and deformation.

iii) Juxtaposition and exhumation of the UH, EB, MU and GT units to mid-crustal depth (~20 km) was accomplished around 290-300 Ma, at rates on the order of 1-3 mm/yr.

iv) The existence of ~300 Ma glaucophane-bearing BS/GS facies metavolcanoclastic units (i.e., the GT and part of GS1 units) suggests that the subduction of the Paleo South Tianshan ocean basin was probably still active during late Carboniferous.

v) Final juxtaposition of the diverse sub-units making the metamorphic dome could have occurred at around ~280-290 Ma, and been broadly coeval with dextral strike-slip movements along the STCSZ.

References

Abers, G.A., 2005. Seismic low-velocity layer at the top of subducting slabs: observations, predictions, and systematics. *Physics of the Earth and Planetary Interiors* 149, 7-29.

Agard, P., Jolivet, L., Goffe, B., 2001. Tectonometamorphic evolution of the Schistes Lustrés Complex; implications for the exhumation of HP and UHP rocks in the Western Alps. *Bull. la Société géologique Fr.* 172, 617–636.

Agard, P., Monié, P., Gerber, W., Omrani, J., Molinaro, M., Meyer, B., Labrousse, L., Vrielynck, B., Jolivet, L., Yamato, P., 2006. Transient, synobduction exhumation of Zagros blueschists inferred from P-T, deformation, time, and kinematic constraints: Implications for Neotethyan wedge dynamics. *J. Geophys. Res. Solid Earth* 111. <https://doi.org/10.1029/2005jb004103>

Agard, P., Monié, P., Jolivet, L., Goffé, B., 2002. Exhumation of the Schistes Lustrés complex: in situ laser probe $^{40}\text{Ar}/^{39}\text{Ar}$ constraints and implications for the Western Alps. *J. Metamorph. Geol.* 20, 599–618.

Agard, P., Plunder, A., Angiboust, S., Bonnet, G., Ruh, J., 2018. The subduction plate interface: Rock record and mechanical coupling (from long to short time scales). *Lithos* #pagerange#. <https://doi.org/10.1016/j.lithos.2018.09.029>

Agard, P., Yamato, P., Jolivet, L., and Burov, E., 2009, Exhumation of oceanic blueschists and eclogites in subduction zones: timing and mechanisms: *Earth-Science Reviews*, v. 92, no. 1, p. 53-79.

Ague, J.J., Baxter, E.F., 2007. Brief thermal pulses during mountain building recorded by Sr diffusion in apatite and multicomponent diffusion in garnet. *Earth and Planetary Science Letters* 261, 500-516.

Ague, J.J., Carlson, W.D., 2013. Metamorphism as garnet sees it: The kinetics of nucleation and growth, equilibration, and diffusional relaxation. *Elements* 9, 439-445.

Ague, J.J., Nicolescu, S., 2014. Carbon dioxide released from subduction zones by fluid-mediated reactions. *Nat. Geosci.* 7, 355–360. <https://doi.org/10.1038/ngeo2143>

Alexander, C.M.D., 2011. Modeling diffusive dissolution in silicate melts. *Geochimica et Cosmochimica Acta* 75, 588-607.

Allen, M., Windley, B., and Zhang, C., 1993, Palaeozoic collisional tectonics and magmatism of the Chinese Tien Shan, central Asia: *Tectonophysics*, v. 220, no. 1, p. 89-115.

Angiboust, S., Agard, P., 2010. Initial water budget: The key to detaching large volumes of eclogitized oceanic crust along the subduction channel? *Lithos* 120, 453–474. <https://doi.org/10.1016/j.lithos.2010.09.007>

Angiboust, S., Agard, P., De Hoog, J.C.M., Omrani, J., Plunder, A., 2013. Insights on deep, accretionary subduction processes from the Sistan ophiolitic “mélange” (Eastern Iran). *Lithos* 156–159, 139–158. <https://doi.org/10.1016/j.lithos.2012.11.007>

Angiboust, S., Agard, P., Glodny, J., Omrani, J., Oncken, O., 2016. Zagros blueschists: Episodic underplating and long-lived cooling of a subduction zone. *Earth Planet. Sci. Lett.* 443, 48–58. <https://doi.org/10.1016/j.epsl.2016.03.017>

Angiboust, S., Agard, P., Yamato, P., Raimbourg, H., 2012. Eclogite breccias in a subducted ophiolite: A record of intermediate-depth earthquakes? *Geology* 40, 707-710.

Augier, R., Agard, P., Monie, P., Jolivet, L., Robin, C., Booth-Rea, G., 2005. Exhumation, doming and slab retreat in the Betic Cordillera (SE Spain): in situ $^{40}\text{Ar}/^{39}\text{Ar}$ ages and P-T-d-t paths for the Nevado-Filabride complex. *J. Metamorph. Geol.* 23, 357–381. <https://doi.org/10.1111/j.1525-1314.2005.00581.x>

Austrheim, H., Putnis, C.V., Engvik, A.K., Putnis, A., 2008. Zircon coronas around Fe-Ti oxides: a physical reference frame for metamorphic and metasomatic reactions. *Contributions to Mineralogy and Petrology* 156, 517-527.

Bassett, D., Watts, A.B., 2015. Gravity anomalies, crustal structure, and seismicity at subduction zones: 2. Interrelationships between fore-arc structure and seismogenic behavior. *Geochemistry, Geophys. Geosystems* 16, 1541–1576. <https://doi.org/10.1002/2014GC005685>

Baumgartner, L.P., Skora, S., Nancy, J., Johnson, C., 2005. Modeling diffusion limited uptake of trace elements by eclogite garnets, 2005 Salt Lake City Annual Meeting.

Baxter, E., Caddick, M., Dragovic, B., 2017. Garnet: A rock-forming mineral petrochronometer. *Reviews in Mineralogy and Geochemistry* 83, 469-533.

Baxter, E.F., Ague, J.J., Depaolo, D.J., 2002. Prograde temperature–time evolution in the Barrovian type–locality constrained by Sm/Nd garnet ages from Glen Clova, Scotland. *Journal of the Geological Society* 159, 71-82.

- Bayet, L., John, T., Agard, P., Gao, J., Li, J.L., 2018. Massive sediment accretion at ~80 km depth along the subduction interface: Evidence from the southern Chinese Tianshan. *Geology* 46, 495–498. <https://doi.org/10.1130/G40201.1>
- Bebout, G.E., 2007. Metamorphic chemical geodynamics of subduction zones. *Earth Planet. Sci. Lett.* 260, 373–393. <https://doi.org/10.1016/j.epsl.2007.05.050>
- Bebout, G.E., 2013. Metasomatism in Subduction Zones of Subducted Oceanic Slabs, Mantle Wedges, and the Slab-Mantle Interface 289–349. https://doi.org/10.1007/978-3-642-28394-9_9
- Beinlich, A., Klemd, R., John, T., Gao, J., 2010. Trace-element mobilization during Ca-metasomatism along a major fluid conduit: Eclogitization of blueschist as a consequence of fluid-rock interaction. *Geochim. Cosmochim. Acta* 74, 1892–1922. <https://doi.org/10.1016/j.gca.2009.12.011>
- Berg, C.A., Carlson, W.D., Connelly, J.N., 2013. Strain rates at high temporal resolution from curved inclusion trails in garnet, Passo del Sole, Central Swiss Alps. *Journal of Metamorphic Geology* 31, 243–262.
- Beysac, O., Bollinger, L., Avouac, J.P., Goffé, B., 2004. Thermal metamorphism in the lesser Himalaya of Nepal determined from Raman spectroscopy of carbonaceous material. *Earth Planet. Sci. Lett.* 225, 233–241. <https://doi.org/10.1016/j.epsl.2004.05.023>
- Beysac, O., Goffé, B., Chopin, C., Rouzaud, J.N., 2002. Raman spectra of carbonaceous material in metasediments: A new geothermometer. *J. Metamorph. Geol.* 20, 859–871. <https://doi.org/10.1046/j.1525-1314.2002.00408.x>
- Blake Jr, M.C., Moore, D.E., Jayko, A.S., 1995. The role of serpentinite melanges in the unroofing of UHPM rocks: An example from the Western Alps of Italy. *Ultrapress. Metamorph.* 182–205.
- Blanco-Quintero, I.F., García-Casco, A., Gerya, T. V., 2011. Tectonic blocks in serpentinite mélange (eastern Cuba) reveal large-scale convective flow of the subduction channel. *Geology* 39, 79–82. <https://doi.org/10.1130/g31494.1>
- Bonnet, G., Agard, P., Angiboust, S., Monié, P., Jentzer, M., Omrani, J., Whitechurch, H., Fournier, M., 2018. Tectonic slicing and mixing processes along the subduction interface: The Sistan example (Eastern Iran). *Lithos* 310–311, 269–287. <https://doi.org/10.1016/j.lithos.2018.04.016>

Brady, J.B., Cherniak, D.J., 2010. Diffusion in minerals: an overview of published experimental diffusion data. *Reviews in mineralogy and geochemistry* 72, 899-920.

Brun, J.P., Faccenna, C., 2008. Exhumation of high-pressure rocks driven by slab rollback. *Earth Planet. Sci. Lett.* 272, 1–7. <https://doi.org/10.1016/j.epsl.2008.02.038>

Bucher, K., and Grapes, R., 2011, *Petrogenesis of metamorphic rocks*, Springer Science & Business Media.

Burov, E., Francois, T., Yamato, P., Wolf, S., 2014. Mechanisms of continental subduction and exhumation of HP and UHP rocks. *Gondwana Res.* 25, 464–493. <https://doi.org/10.1016/j.gr.2012.09.010>

Caddick, M.J., Kohn, M.J., 2013. Garnet: Witness to the Evolution of Destructive Plate Boundaries. *Elements* 9, 427-432.

Caddick, M.J., Konopásek, J., Thompson, A.B., 2010. Preservation of Garnet Growth Zoning and the Duration of Prograde Metamorphism. *Journal of Petrology* 51, 2327-2347.

Carlson, W.D., 1989. The significance of intergranular diffusion to the mechanisms and kinetics of porphyroblast crystallization. *Contributions to Mineralogy and Petrology* 103, 1-24.

Carlson, W.D., 2006. Rates of Fe, Mg, Mn, and Ca diffusion in garnet. *American Mineralogist* 91, 1-11.

Carlson, W.D., 2011. Porphyroblast crystallization: linking processes, kinetics, and microstructures. *International Geology Review* 53, 406-445.

Carlson, W.D., 2012. Rates and mechanism of Y, REE, and Cr diffusion in garnet. *American Mineralogist* 97, 1598-1618.

Carroll, A., Graham, S., Hendrix, M., Ying, D., and Zhou, D., 1995, Late Paleozoic tectonic amalgamation of northwestern China: sedimentary record of the northern Tarim, northwestern Turpan, and southern Junggar basins: *Geological Society of America Bulletin*, v. 107, no. 5, p. 571-594.

Carroll, A.R., Graham, S.A., Hendrix, M.S., Ying, D., Zhou, D., 1995. Late Paleozoic tectonic amalgamation of northwestern China: sedimentary record of the northern Tarim, northwestern Turpan, and southern Junggar Basins. *Geol. Soc. Am. Bull.* 107, 571–594. [https://doi.org/10.1130/0016-7606\(1995\)107<0571:LPTAON>2.3.CO;2](https://doi.org/10.1130/0016-7606(1995)107<0571:LPTAON>2.3.CO;2)

Carson, C., Powell, R., and Clarke, G., 1999, Calculated mineral equilibria for eclogites in CaO–Na₂O–FeO–MgO–Al₂O₃–SiO₂–H₂O: application to the Pouébo Terrane,

Pam Peninsula, New Caledonia: *Journal of Metamorphic Geology*, v. 17, no. 1, p. 9-24.

Carson, C.J., Powell, R., Clarke, G.L., 1999. Calculated mineral equilibria for eclogites in CaO–Na₂O–FeO–MgO–Al₂O₃–SiO₂–H₂O: application to the Pouébo Terrane, Pam Peninsula, New Caledonia. *J. Metamorph. Geol.* 17, 9–24.

Carswell, D. A., 1990, *Eclogite facies rocks*, Springer.

Castro, J.M., Beck, P., Tuffen, H., Nichols, A.R., Dingwell, D.B., Martin, M.C., 2008. Timescales of spherulite crystallization in obsidian inferred from water concentration profiles. *American Mineralogist* 93, 1816-1822.

Chemenda, A.I., Mattauer, M., Malavieille, J., Bokun, A.N., 1995. A mechanism for syn-collisional rock exhumation and associated normal faulting: Results from physical modelling. *Earth Planet. Sci. Lett.* 132, 225–232.

Chen, Y., Ye, K., Wu, T.F., Guo, S., 2013. Exhumation of oceanic eclogites: thermodynamic constraints on pressure, temperature, bulk composition and density. *J. Metamorph. Geol.* n/a-n/a. <https://doi.org/10.1111/jmg.12033>

Chen, Z.-Y., Zhang, L.-F., Du, J.-X., Lü, Z., 2012. Zr-in-rutile thermometry in eclogite and vein from southwestern Tianshan, China. *Journal of Asian Earth Sciences*.

Cheng, H., King, R.L., Nakamura, E., Vervoort, J.D., Zhou, Z., 2008. Coupled Lu-Hf and Sm-Nd geochronology constrains garnet growth in ultra-high-pressure eclogites from the Dabie orogen. *Journal of Metamorphic Geology* 26, 741-758.

Cherniak, D.J., Manchester, J., Watson, E.B., 2007. Zr and Hf diffusion in rutile. *Earth and Planetary Science Letters* 261, 267-279.

Chopin, C., 1984. Coesite and pure pyrope in high-grade blueschists of the Western Alps: a first record and some consequences. *Contrib. to Mineral. Petrol.* 86, 107–118.

Chu, X., Ague, J.J., 2015. Analysis of experimental data on divalent cation diffusion kinetics in aluminosilicate garnets with application to timescales of peak Barrovian metamorphism, Scotland. *Contributions to Mineralogy and Petrology* 170.

Clift, P., Vannucchi, P., 2004. Controls on tectonic accretion versus erosion in subduction zones: Implications for the origin and recycling of the continental crust. *Rev. Geophys.* 42. <https://doi.org/10.1029/2003RG000127>

Cloos, M., Shreve, R.L., 1988. Subduction-channel model of prism accretion, melange formation, sediment subduction, and subduction erosion at convergent plate margins:

1. Background and description. *Pure Appl. Geophys.* PAGEOPH 128, 455–500. <https://doi.org/10.1007/BF00874548>

Cloos, M., Shreve, R.L., 1996. Shear-zone thickness and the seismicity of Chilean- and Marianas-type subduction zones. *Geology* 24, 107–110. [https://doi.org/10.1130/0091-7613\(1996\)024<0107:SZTATS>2.3.CO;2](https://doi.org/10.1130/0091-7613(1996)024<0107:SZTATS>2.3.CO;2)

Cocker, J., Griffin, B., and Muehlenbachs, K., 1982, Oxygen and carbon isotope evidence for seawater-hydrothermal alteration of the Macquarie Island ophiolite: *Earth and Planetary Science Letters*, v. 61, no. 1, p. 112-122.

Coggon, R., and Holland, T., 2002, Mixing properties of phengitic micas and revised garnet-phengite thermobarometers: *Journal of Metamorphic Geology*, v. 20, no. 7, p. 683-696.

Coggon, R., Holland, T.J.B., 2002. Mixing properties of phengitic micas and revised garnet-phengite thermobarometers. *J. Metamorph. Geol.* 20, 683–696.

Connolly, J.A.D., 1990. Multivariable phase diagrams; an algorithm based on generalized thermodynamics. *Am. J. Sci.* 290, 666–718.

Connolly, J.A.D., 2005. Computation of phase equilibria by linear programming: a tool for geodynamic modeling and its application to subduction zone decarbonation. *Earth Planet. Sci. Lett.* 236, 524–541. <https://doi.org/https://doi.org/10.1016/j.epsl.2005.04.033>

Connolly, J.A.D., Kerrick, D.M., 2002. Metamorphic controls on seismic velocity of subducted oceanic crust at 100–250 km depth. *Earth Planet. Sci. Lett.* 204, 61–74.

Connolly, J.A.D., Trommsdorff, V., 1991. Petrogenetic grids for metacarbonate rocks: pressure-temperature phase-diagram projection for mixed-volatile systems. *Contrib. to Mineral. Petrol.* 108, 93–105.

Corfu, F., Hanchar, J.M., Hoskin, P.W.O., Kinny, P., 2003. Atlas of zircon textures. *Rev. Mineral. Geochemistry* 53, 469–500.

Dachs, E., Geiger, C., and Benisek, A., The uncertainty of the standard entropy and its effect on petrological calculations, in *Proceedings EGU General Assembly Conference Abstracts2012*, Volume 14, p. 4439.

De Jong, K., Feraud, G., Ruffet, G., Amouric, M., Wijbrans, J., 2001. Excess argon incorporation in phengite of the Mulhacen Complex: submicroscopic illitization and fluid ingress during late Miocene extension in the Betic. *Chem. Geol.* 178, 159–195.

de Jong, K., Wang, B., Faure, M., Shu, L., Cluzel, D., Charvet, J., Ruffet, G., and Chen, Y., 2009, New $^{40}\text{Ar}/^{39}\text{Ar}$ age constraints on the Late Palaeozoic tectonic evolution of the western Tianshan (Xinjiang, northwestern China), with emphasis on Permian fluid ingress: *International Journal of Earth Sciences*, v. 98, no. 6, p. 1239-1258.

Degeling, H., Eggins, S., and Ellis, D., 2001, Zr budgets for metamorphic reactions, and the formation of zircon from garnet breakdown: *Mineralogical Magazine*, v. 65, no. 6, p. 749-758.

Dewey, J.F., Bird, J.M., 1970. Mountain belts and the new global tectonics. *J. Geophys. Res.* 75, 2625–2647.

Di Vincenzo, G., Grande, A., Prosser, G., Cavazza, W., DeCelles, P.G., 2016. ^{40}Ar – ^{39}Ar laser dating of ductile shear zones from central Corsica (France): Evidence of Alpine (middle to late Eocene) syn-burial shearing in Variscan granitoids. *Lithos* 262, 369–383. <https://doi.org/10.1016/j.lithos.2016.07.022>

Diener, J.F.A., Powell, R., White, R.W., Holland, T.J.B., 2007. A new thermodynamic model for clino- and orthoamphiboles in the system Na_2O - CaO - FeO - MgO - Al_2O_3 - SiO_2 - H_2O - O . *J. Metamorph. Geol.* 25, 631–656. <https://doi.org/10.1111/j.1525-1314.2007.00720.x>

Dimanov, A., Sautter, V., 2000. “Average” interdiffusion of (Fe,Mn)-Mg in natural diopside. *European Journal of Mineralogy* 12, 749-760.

Dimanov, A., Wiedenbeck, M., 2006. (Fe, Mn)-Mg interdiffusion in natural diopside: effect of $p\text{O}_2$. *European Journal of Mineralogy* 18, 705-718.

Dohmen, R., Chakraborty, S., 2003. Mechanism and kinetics of element and isotopic exchange mediated by a fluid phase. *American Mineralogist* 88, 1251-1270.

Du, J.-X., Zhang, L.-D., Lü, Z., Chu, X., 2011. Lawsonite-bearing chloritoid–glaucophane schist from SW Tianshan, China: Phase equilibria and P–T path. *Journal of Asian Earth Sciences* 42, 684-693.

Du, J.X., Zhang, L.F., Bader, T., Chen, Z.Y., Lü, Z., 2014. Metamorphic evolution of relict lawsonite-bearing eclogites from the (U) HP metamorphic belt in the Chinese southwestern Tianshan. *Journal of Metamorphic Geology* 32, 575-598.

Du, J.X., Zhang, L.F., Shen, X.J., Bader, T., 2014. A new P-T-t path of eclogites from Chinese southwestern Tianshan: Constraints from P-T pseudosections and Sm-Nd isochron dating. *Lithos* 200–201, 258–272. <https://doi.org/10.1016/j.lithos.2014.04.009>

Ernst, W., 2001. Subduction, ultrahigh-pressure metamorphism, and regurgitation of buoyant crustal slices—implications for arcs and continental growth. *Physics of the Earth and Planetary Interiors* 127, 253-275.

Ernst, W.G., 2006. Preservation/exhumation of ultrahigh-pressure subduction complexes. *Lithos* 92, 321–335. <https://doi.org/10.1016/j.lithos.2006.03.049>

Evans, T., 2004, A method for calculating effective bulk composition modification due to crystal fractionation in garnet-bearing schist: implications for isopleth thermobarometry: *Journal of Metamorphic Geology*, v. 22, no. 6, p. 547-557.

Federico, L., Capponi, G., Crispini, L., Scambelluri, M., and Villa, I., 2005, ³⁹Ar/⁴⁰Ar dating of high-pressure rocks from the Ligurian Alps: Evidence for a continuous subduction–exhumation cycle: *Earth and Planetary Science Letters*, v. 240, no. 3-4, p. 668-680.

Federico, L., Crispini, L., Scambelluri, M., Capponi, G., 2007. Ophiolite mélange zone records exhumation in a fossil subduction channel. *Geology* 35, 499–502. <https://doi.org/10.1130/G23190A.1>

Ferry, J.M., Watson, E.B., 2007. New thermodynamic models and revised calibrations for the Ti-in-zircon and Zr-in-rutile thermometers. *Contrib. to Mineral. Petrol.* 154, 429–437. <https://doi.org/10.1007/s00410-007-0201-0>

Frezzotti, M.L., Selverstone, J., Sharp, Z.D., Compagnoni, R., 2011. Carbonate dissolution during subduction revealed by diamond-bearing rocks from the Alps. *Nat. Geosci.* 4, 703.

Ganguly, J., 2010. Cation Diffusion Kinetics in Aluminosilicate Garnets and Geological Applications. *Reviews in Mineralogy and Geochemistry* 72, 559-601.

Gao, J., 1997. The discovery of eclogites and its tectonic implication, Southwest Tianshan. *Chinese Bull. Sci.* 42, 737–740.

Gao, J., and Klemd, R., 2000, Eclogite Occurrences in the Southern Tianshan High-Pressure Belt, Xinjiang, Western China: *Gondwana Research*, v. 3, no. 1, p. 33-38.

Gao, J., He, G., Li, M., Xiao, X., Tang, Y., Wang, J., Zhao, M., 1995. The mineralogy, petrology, metamorphic PTdt trajectory and exhumation mechanism of blueschists, south Tianshan, northwestern China. *Tectonophysics* 250, 151–168. [https://doi.org/10.1016/0040-1951\(95\)00026-6](https://doi.org/10.1016/0040-1951(95)00026-6)

Gao, J., John, T., Klemd, R., Xiong, X., 2007. Mobilization of Ti-Nb-Ta during subduction: Evidence from rutile-bearing dehydration segregations and veins hosted in

eclogite, Tianshan, NW China. *Geochim. Cosmochim. Acta* 71, 4974–4996. <https://doi.org/10.1016/j.gca.2007.07.027>

Gao, J., Klemd, R., 2003. Formation of HP-LT rocks and their tectonic implications in the western Tianshan Orogen, NW China: Geochemical and age constraints. *Lithos* 66, 1–22. [https://doi.org/10.1016/S0024-4937\(02\)00153-6](https://doi.org/10.1016/S0024-4937(02)00153-6)

Gao, J., Klemd, R., Qian, Q., Zhang, X., Li, J., Jiang, T., Yang, Y., 2011. The collision between the Yili and Tarim blocks of the Southwestern Altaids: Geochemical and age constraints of a leucogranite dike crosscutting the HP-LT metamorphic belt in the Chinese Tianshan Orogen. *Tectonophysics* 499, 118–131. <https://doi.org/10.1016/j.tecto.2011.01.001>

Gao, J., Klemd, R., Zhang, L., Wang, Z., and Xiao, X., 1999, PT path of high-pressure/low-temperature rocks and tectonic implications in the western Tianshan Mountains, NW China: *Journal of Metamorphic Geology*, v. 17, p. 621-636.

Gao, J., Klemd, R., Zhu, M., Wang, X., Li, J., Wan, B., Xiao, W., Zeng, Q., Shen, P., Sun, J., Qin, K., Campos, E., 2017. Large-scale porphyry-type mineralization in the Central Asian metallogenic domain: A review. *J. Asian Earth Sci.* <https://doi.org/10.1016/j.jseaes.2017.10.002>

Gao, J., Li, M.-S., Xiao, X.-C., Tang, Y.-Q., He, G.-Q., 1998. Paleozoic tectonic evolution of the Tianshan Orogen, northwestern China. *Tectonophysics* 287, 213-231.

Gao, J., Long, L., Klemd, R., Qian, Q., Liu, D., Xiong, X., Su, W., Liu, W., Wang, Y., Yang, F., 2009a. Tectonic evolution of the South Tianshan orogen and adjacent regions, NW China: Geochemical and age constraints of granitoid rocks. *Int. J. Earth Sci.* 98, 1221–1238. <https://doi.org/10.1007/s00531-008-0370-8>

Gao, J., Long, L.-L., Klemd, R., Qian, Q., Liu, D.-Y., Xiong, X.-M., Su, W., Liu, W., Wang, Y.-T., Yang, F.-Q., 2009. Tectonic evolution of the South Tianshan orogen and adjacent regions, NW China: geochemical and age constraints of granitoid rocks. *International Journal of Earth Sciences* 98, 1221-1238.

Gao, J., Long, L.-L., Qian, Q., Huang, D.-Z., Su, W., and KLEMD, R., 2006, South Tianshan: Late Paleozoic or Triassic collision orogenic belt?: *Acta Petrologica Sinica* (in Chinese), v. 22, no. 5, p. 1049-1061.

Gao, J., Maosong, L., Xuchang, X., Yaoqing, T., and Guoqi, H., 1998, Paleozoic tectonic evolution of the Tianshan Orogen, northwestern China: *Tectonophysics*, v. 287, no. 1, p. 213-231.

Gao, J., Maosong, L., Xuchang, X., Yaoqing, T., Guoqi, H., 1998. Paleozoic tectonic evolution of the Tianshan Orogen, northwestern China. *Tectonophysics* 287, 213–231. [https://doi.org/10.1016/S0040-1951\(98\)80070-X](https://doi.org/10.1016/S0040-1951(98)80070-X)

Gao, J., Qian, Q., Long, L.L., Zhang, X., Li, J.L., Su, W., 2009b. Accretionary orogenic process of Western Tianshan, China. *Geol. Bull. China* 28, 1804–1816. <https://doi.org/10.1126/science.1132916>

Gao, J., Zhang, L.-F., Liu, S.-W., 2000. The formation of blueschist and eclogite in West tianshan mountains, China and its uplift history insight from the Ar/Ar ages. *Chinese Sci. Bull.* 45, 89–94.

García-Casco, A., Torres-Roldán, R., Millán, G., Monié, P., Schneider, J., 2002. Oscillatory zoning in eclogitic garnet and amphibole, Northern Serpentinite Melange, Cuba: a record of tectonic instability during subduction? *Journal of Metamorphic Geology* 20, 581-598.

Gerya, T. V., Stöckhert, B., and Perchuk, A. L., 2002, Exhumation of high-pressure metamorphic rocks in a subduction channel: A numerical simulation: *Tectonics*, v. 21, no. 6, p. 6-1-6-19.

Glodny, J., Lohrmann, J., Echtler, H., Gräfe, K., Seifert, W., Collao, S., Figueroa, O., 2005. Internal dynamics of a paleoaccretionary wedge: Insights from combined isotope tectonochronology and sandbox modelling of the South-Central Chilean forearc. *Earth Planet. Sci. Lett.* 231, 23–39. <https://doi.org/10.1016/j.epsl.2004.12.014>

Green, E., Holland, T., and Powell, R., 2007, An order-disorder model for omphacitic pyroxenes in the system jadeite-diopsidehedenbergite-acmite, with applications to eclogitic rocks: *American Mineralogist*, v. 92, no. 7, p. 1181-1189.

Green, E., Holland, T., Powell, R., 2007. An order-disorder model for omphacitic pyroxenes in the system jadeite-diopsidehedenbergite-acmite, with applications to eclogitic rocks. *Am. Mineral.* 92, 1181–1189. <https://doi.org/10.2138/am.2007.2401>

Green, H.W., 2005. Psychology of a changing paradigm: 40+ years of high-pressure metamorphism. *International Geology Review* 47, 439-456.

Groppo, C., Beltrando, M., Compagnoni, R., Sciences, P., 2009. The P – T path of the ultra-high pressure Lago Di Cignana and adjoining high-pressure meta-ophiolitic units : insights into the evolution of the subducting Tethyan slab 207–231. <https://doi.org/10.1111/j.1525-1314.2009.00814.x>

Groppo, C., Castelli, D., 2010. Prograde P–T evolution of a lawsonite eclogite from the Monviso meta-ophiolite (Western Alps): dehydration and redox reactions during subduction of oceanic FeTi-oxide gabbro. *Journal of Petrology* 51, 2489-2514.

Guillot, S., Hattori, K., Agard, P., Schwartz, S., and Vidal, O., 2009, Exhumation processes in oceanic and continental subduction contexts: a review, *Subduction zone geodynamics*, Springer, p. 175-205.

Guillot, S., Hattori, K., Agard, P., Schwartz, S., Vidal, O., 2009. Exhumation processes in oceanic and continental subduction contexts: a review, in: *Subduction Zone Geodynamics*. Springer, pp. 175–205.

Guillot, S., Schwartz, S., Reynard, B., Agard, P., and Prigent, C., 2015, Tectonic significance of serpentinites: *Tectonophysics*, v. 646, p. 1-19.

Guillot, S., Schwartz, S., Reynard, B., Agard, P., Prigent, C., 2015. Tectonic significance of serpentinites. *Tectonophysics* 646, 1–19. <https://doi.org/10.1016/j.tecto.2015.01.020>

Hawthorne, F. C., and Oberti, R., 2006, On the classification of amphiboles: *The Canadian Mineralogist*, v. 44, no. 1, p. 1-21.

Hegner, E., Klemd, R., Kröner, A., Corsini, M., Alexeiev, D. V., Iaccheri, L.M., Zack, T., Dulski, P., Xia, X., Windley, B.F., 2010. Mineral ages and PT conditions of Late Paleozoic high-pressure eclogite and provenance of mélange sediments from Atbashi in the south Tianshan orogen of Kyrgyzstan. *Am. J. Sci.* 310, 916–950.

Hegner, E., Klemd, R., Kröner, A., Corsini, M., Alexeiev, D., Iaccheri, L., Zack, T., Dulski, P., Xia, X., and Windley, B., 2010, Mineral ages and PT conditions of Late Paleozoic high-pressure eclogite and provenance of mélange sediments from Atbashi in the south Tianshan orogen of Kyrgyzstan: *American Journal of Science*, v. 310, no. 9, p. 916-950.

Hegner, E., Klemd, R., Kröner, A., Corsini, M., Alexeiev, D., Iaccheri, L., Zack, T., Dulski, P., Xia, X., Windley, B., 2010. Mineral ages and PT conditions of Late Paleozoic high-pressure eclogite and provenance of mélange sediments from Atbashi in the south Tianshan orogen of Kyrgyzstan. *American Journal of Science* 310, 916-950.

Henry, D.J., Guidotti, C. V., Thomson, J.A., 2005. The Ti-saturation surface for low-to-medium pressure metapelitic biotites: Implications for geothermometry and Ti-substitution mechanisms. *Am. Mineral.* 90, 316–328. <https://doi.org/10.2138/am.2005.1498>

Hesse, M.A., 2012. A finite volume method for trace element diffusion and partitioning during crystal growth. *Computers & Geosciences* 46, 96-106.

Hiraga, T., Anderson, I.M., Kohlstedt, D.L., 2004. Grain boundaries as reservoirs of incompatible elements in the Earth's mantle. *Nature* 427, 699-703.

Holland, T. J. B., and Powell, R., 2011, An improved and extended internally consistent thermodynamic dataset for phases of petrological interest, involving a new equation of state for solids: *Journal of Metamorphic Geology*, v. 29, no. 3, p. 333–383.

Holland, T., and Powell, R., 1998, An internally consistent thermodynamic data set for phases of petrological interest: *Journal of metamorphic Geology*, v. 16, no. 3, p. 309-343.

Holland, T., and Powell, R., 2003, Activity–composition relations for phases in petrological calculations: an asymmetric multicomponent formulation: *Contributions to Mineralogy and Petrology*, v. 145, no. 4, p. 492-501.

Holland, T., Powell, R., 2003. Activity–composition relations for phases in petrological calculations: an asymmetric multicomponent formulation. *Contrib. to Mineral. Petrol.* 145, 492–501.

Holland, T.J.B., Powell, R., 1990. An enlarged and updated internally consistent thermodynamic dataset with uncertainties and correlations: the system K₂O–Na₂O–CaO–MgO–MnO–FeO–Fe₂O₃–Al₂O₃–TiO₂–SiO₂–C–H₂–O₂. *J. Metamorph. Geol.* 8, 89–124.

Hollister, L.S., 1966. Garnet zoning: an interpretation based on the Rayleigh fractionation model. *Science* 154, 1647-1651.

Hu, Z., Zhang, W., Liu, Y., Gao, S., Li, M., Zong, K., Chen, H., Hu, S., 2015. “Wave” signal-smoothing and mercury-removing device for laser ablation quadrupole and multiple collector ICPMS analysis: Application to lead isotope analysis. *Anal. Chem.* 87, 1152–1157. <https://doi.org/10.1021/ac503749k>

Hyndman, R.D., 1995. The Lithoprobe corridor across the Vancouver Island continental margin: the structural and tectonic consequences of subduction. *Can. J. Earth Sci.* 32, 1777–1802. <https://doi.org/10.1139/e95-138>

John, T., Gussone, N., Podladchikov, Y.Y., Bebout, G.E., Dohmen, R., Halama, R., Klemd, R., Magna, T., Seitz, H.M., 2012. Volcanic arcs fed by rapid pulsed fluid flow through subducting slabs. *Nat. Geosci.* 5, 489–492. <https://doi.org/10.1038/ngeo1482>

John, T., Klemd, R., Gao, J., Garbe-Schönberg, C.-D., 2008. Trace-element mobilization in slabs due to non steady-state fluid–rock interaction: constraints from an eclogite-facies transport vein in blueschist (Tianshan, China). *Lithos* 103, 1-24. <https://doi.org/10.1016/j.lithos.2007.09.005>

John, T., Medvedev, S., Rüpke, L.H., Andersen, T.B., Podladchikov, Y.Y., Austrheim, H., 2009. Generation of intermediate-depth earthquakes by self-localizing thermal runaway. *Nat. Geosci.* 2, 137–140. <https://doi.org/10.1038/ngeo419>

John, T., Scherer, E. E., Haase, K., and Schenk, V., 2004, Trace element fractionation during fluid-induced eclogitization in a subducting slab: trace element and Lu–Hf–Sm–Nd isotope systematics: *Earth and Planetary Science Letters*, v. 227, no. 3-4, p. 441-456.

John, T., Scherer, E.E., Schenk, V., Herms, P., Halama, R., Garbe-Schönberg, D., 2010. Subducted seamounts in an eclogite-facies ophiolite sequence: The Andean Raspas Complex, SW Ecuador. *Contrib. to Mineral. Petrol.* 159, 265–284. <https://doi.org/10.1007/s00410-009-0427-0>

Jolivet, L., Raimbourg, H., Labrousse, L., Avigad, D., Leroy, Y., Austrheim, H., Andersen, T.B., 2005. Softening triggered by eclogitization, the first step toward exhumation during continental subduction. *Earth Planet. Sci. Lett.* 237, 532–547. <https://doi.org/10.1016/j.epsl.2005.06.047>

Jourdan, F., Renne, P.R., 2007. Age calibration of the Fish Canyon sanidine $^{40}\text{Ar}/^{39}\text{Ar}$ dating standard using primary K–Ar standards. *Geochim. Cosmochim. Acta* 71, 387–402.

Jun, G., Klemd, R., 2000. Eclogite Occurrences in the Southern Tianshan High-Pressure Belt, Xinjiang, Western China. *Gondwana Res.* 3, 33–38. [https://doi.org/10.1016/S1342-937X\(05\)70055-1](https://doi.org/10.1016/S1342-937X(05)70055-1)

Kelley, K. A., Plank, T., Ludden, J., and Staudigel, H., 2003, Composition of altered oceanic crust at ODP Sites 801 and 1149: *Geochemistry, Geophysics, Geosystems*, v. 4, no. 6, p. 8910.

Ketcham, R.A., Carlson, W.D., 2012. Numerical simulation of diffusion-controlled nucleation and growth of porphyroblasts. *Journal of Metamorphic Geology* 30, 489-512.

King, R.L., Bebout, G.E., Kobayashi, K., Nakamura, E., van der Klauw, S.N.G.C., 2004. Ultrahigh-pressure metabasaltic garnets as probes into deep subduction zone chemical cycling. *Geochemistry, Geophysics, Geosystems* 5, n/a-n/a.

Klemd, R., Bröcker, M., Hacker, B.R., Gao, J., Gans, P., Wemmer, K., 2005. New Age Constraints on the Metamorphic Evolution of the High-Pressure/Low-Temperature Belt in the Western Tianshan Mountains, NW China. *J. Geol.* 113, 157–168. <https://doi.org/10.1086/427666>

Klemd, R., Gao, J., Li, J.-L., and Meyer, M., 2014, Metamorphic evolution of (ultra)-high-pressure subduction-related transient crust in the South Tianshan Orogen (Central Asian Orogenic Belt): Geodynamic implications: *Gondwana Research*, v. 28, no. 1, p. 1-25.

Klemd, R., Gao, J., Li, J.L., Meyer, M., 2015. Metamorphic evolution of (ultra)-high-pressure subduction-related transient crust in the South Tianshan Orogen (Central Asian Orogenic Belt): Geodynamic implications. *Gondwana Res.* 28, 1–25. <https://doi.org/10.1016/j.gr.2014.11.008>

Klemd, R., John, T., Scherer, E.E., Rondenay, S., Gao, J., 2011. Changes in dip of subducted slabs at depth: Petrological and geochronological evidence from HP-UHP rocks (Tianshan, NW-China). *Earth Planet. Sci. Lett.* 310, 9–20. <https://doi.org/10.1016/j.epsl.2011.07.022>

Klemd, R., Schroter, F., Will, T., and Gao, J., 2002, P–T evolution of glaucophane–omphacite bearing HP–LT rocks in the western Tianshan Orogen, NW China: new evidence for ‘Alpine-type’ tectonics: *Journal of Metamorphic Geology*, v. 20, no. 2, p. 239-254.

Kohn, M. J., Corrie, S. L., and Markley, C., 2015, The fall and rise of metamorphic zircon: *American Mineralogist*, v. 100, no. 4, p. 897-908.

Kohn, M.J., Penniston-Dorland, S.C., Ferreira, J.C.S., 2016. Implications of near-rim compositional zoning in rutile for geothermometry, geospeedometry, and trace element equilibration. *Contributions to Mineralogy and Petrology* 171.

Konrad-Schmolke, M., Zack, T., O'Brien, P. J., and Jacob, D. E., 2008, Combined thermodynamic and rare earth element modelling of garnet growth during subduction: Examples from ultrahigh-pressure eclogite of the Western Gneiss Region, Norway: *Earth and Planetary Science Letters*, v. 272, no. 1-2, p. 488-498.

Konrad-Schmolke, M., Zack, T., O'Brien, P.J., Jacob, D.E., 2008. Combined thermodynamic and rare earth element modelling of garnet growth during subduction: Examples from ultrahigh-pressure eclogite of the Western Gneiss Region, Norway. *Earth and Planetary Science Letters* 272, 488-498.

Kuge, K., Kase, Y., Urata, Y., Campos, J., Perez, A., 2010. Rupture characteristics of the 2005 Tarapaca, northern Chile, intermediate-depth earthquake: Evidence for heterogeneous fluid distribution across the subducting oceanic plate? *J. Geophys. Res.* 115. <https://doi.org/10.1029/2009jb007106>

Kutterolf, S., Freundt, A., Schacht, U., Bürk, D., Harders, R., Mörz, T., Pérez, W., 2008. Pacific offshore record of plinian arc volcanism in Central America: 3. Application to

forearc geology. *Geochemistry, Geophys. Geosystems* 9.
<https://doi.org/10.1029/2007GC001826>

Lanari, P., Vidal, O., De Andrade, V., Dubacq, B., Lewin, E., Grosch, E.G., Schwartz, S., 2014. XMapTools: A MATLAB©-based program for electron microprobe X-ray image processing and geothermobarometry. *Computers & Geosciences* 62, 227-240.

Laurent, V., Huet, B., Labrousse, L., Jolivet, L., Monié, P., Augier, R., 2017. Extraneous argon in high-pressure metamorphic rocks: Distribution, origin and transport in the Cycladic Blueschist Unit (Greece). *Lithos* 272–273, 315–335.
<https://doi.org/10.1016/j.lithos.2016.12.013>

Laurent-Charvet, S., Charvet, J., Monié, P., Shu, L., 2003. Late Paleozoic strike-slip shear zones in eastern central Asia (NW China): New structural and geochronological data. *Tectonics* 22. <https://doi.org/10.1029/2001TC901047>

Leake, B. E., 1978, *Nomenclature of amphiboles: The Canadian Mineralogist*, v. 16, no. 4, p. 501-520.

Li, J.L., Gao, J., John, T., Klemd, R., Su, W., 2013. Fluid-mediated metal transport in subduction zones and its link to arc-related giant ore deposits: Constraints from a sulfide-bearing HP vein in lawsonite eclogite (Tianshan, China). *Geochim. Cosmochim. Acta* 120, 326–362. <https://doi.org/10.1016/j.gca.2013.06.023>

Li, J.L., Gao, J., Wang, X.S., 2016a. A subduction channel model for exhumation of oceanic-type high-pressure to ultrahigh-pressure eclogite-facies metamorphic rocks in SW Tianshan, China. *Sci. China Earth Sci.* 59, 2339–2354.
<https://doi.org/10.1007/s11430-016-5103-7>

Li, J.-L., Klemd, R., Gao, J., and John, T., 2016, Poly-cyclic Metamorphic Evolution of Eclogite: Evidence for Multistage Burial–Exhumation Cycling in a Subduction Channel: *Journal of Petrology*, v. 57, no. 1, p. 119-146.

Li, J.-L., Klemd, R., Gao, J., and Meyer, M., 2012, Coexisting carbonate-bearing eclogite and blueschist in SW Tianshan, China: petrology and phase equilibria: *Journal of Asian Earth Sciences*, v. 60, p. 174-187.

Li, J.L., Klemd, R., Gao, J., Jiang, T., Song, Y.H., 2015. A common high-pressure metamorphic evolution of interlayered eclogites and metasediments from the “ultrahigh-pressure unit” of the Tianshan metamorphic belt in China. *Lithos* 226, 169–182. <https://doi.org/10.1016/j.lithos.2014.12.006>

- Li, J.L., Klemd, R., Gao, J., John, T., 2016b. Poly-cyclic metamorphic evolution of eclogite: Evidence for multistage burial-exhumation cycling in a subduction channel. *J. Petrol.* 57, 119–146. <https://doi.org/10.1093/petrology/egw002>
- Li, Q. li, Lin, W., Su, W., Li, X. hua, Shi, Y. hong, Liu, Y., Tang, G. qiang, 2011. SIMS U-Pb rutile age of low-temperature eclogites from southwestern Chinese Tianshan, NW China. *Lithos* 122, 76–86. <https://doi.org/10.1016/j.lithos.2010.11.007>
- Li, Q.-L., Li, X.-H., Liu, Y., Tang, G.-Q., Yang, J.-H., and Zhu, W.-G., 2010a, Precise U–Pb and Pb–Pb dating of Phanerozoic baddeleyite by SIMS with oxygen flooding technique: *Journal of Analytical Atomic Spectrometry*, v. 25, no. 7, p. 1107-1113.
- Li, S., Jagoutz, E., Chen, Y., and Li, Q., 2000, Sm–Nd and Rb–Sr isotopic chronology and cooling history of ultrahigh pressure metamorphic rocks and their country rocks at Shuanghe in the Dabie Mountains, Central China: *Geochimica et Cosmochimica Acta*, v. 64, no. 6, p. 1077-1093.
- Li, S., Wang, S., Chen, Y., Liu, D., Qiu, J., Zhou, H., and Zhang, Z., 1994, Excess argon in phengite from eclogite: Evidence from dating of eclogite minerals by Sm–Nd, Rb–Sr and ^{40}Ar – ^{39}Ar methods: *Chemical Geology*, v. 112, no. 3, p. 343-350.
- Li, S., Wang, S., Chen, Y., Liu, D., Qiu, J.I., Zhou, H., Zhang, Z., 1994. Excess argon in phengite from eclogite: Evidence from dating of eclogite minerals by Sm–Nd, Rb–Sr and ^{40}Ar – ^{39}Ar methods. *Chem. Geol.* 112, 343–350.
- Li, X. H., Liu, Y., Li, Q. L., Guo, C. H., and Chamberlain, K. R., 2009, Precise determination of Phanerozoic zircon Pb/Pb age by multicollector SIMS without external standardization: *Geochemistry, Geophysics, Geosystems*, v. 10, no. 4, p. 573-575.
- Li, X. H., Long, W. G., Li, Q. L., Liu, Y., Zheng, Y. F., Yang, Y. H., Chamberlain, K. R., Wan, D. F., Guo, C. H., and Wang, X. C., 2010d, Penglai zircon megacrysts: a potential new working reference material for microbeam determination of Hf–O isotopes and U–Pb age: *Geostandards and Geoanalytical Research*, v. 34, no. 2, p. 117-134.
- Li, X., Liu, Y., Li, Q., Guo, C., Chamberlain, K.R., 2009. Precise determination of Phanerozoic zircon Pb/Pb age by multicollector SIMS without external standardization. *Geochemistry, Geophys. Geosystems* 10, 573–575.
- Li, X., Zhang, L., Wei, C., Ai, Y., Chen, J., 2007. Petrology of rodingite derived from eclogite in western Tianshan, *J. Metamorph. Geol.* 25, 363–382. <https://doi.org/10.1111/j.1525-1314.2007.00700.x>

Li, X.-H., Li, W.-X., and Li, Q.-L., 2010b, Petrogenesis and tectonic significance of the ~ 850 Ma Gangbian alkaline complex in South China: evidence from in situ zircon U–Pb dating, Hf–O isotopes and whole-rock geochemistry: *Lithos*, v. 114, no. 1, p. 1–15.

Li, X.P., Zhang, L.F., Wilde, S.A., Song, B., Liu, X.M., 2010. Zircons from rodingite in the Western Tianshan serpentinite complex: Mineral chemistry and U-Pb ages define nature and timing of rodingitization. *Lithos* 118, 17–34. <https://doi.org/10.1016/j.lithos.2010.03.009>

Li, Y.H., Schoonmaker, J.E., 2003. Chemical composition and mineralogy of marine sediments. na.

Lifshin, E., Gauvin, R., 2001. Minimizing Errors in Electron Microprobe Analysis. *Microsc. Microanal.* 7, 168–177. <https://doi.org/10.1007/s100050010084>

Lin, W., and Enami, M., 2006, Prograde pressure-temperature path of jadeite-bearing eclogites and associated high-pressure/low-temperature rocks from western Tianshan, northwest China: *Island Arc*, v. 15, no. 4, p. 483–502.

Lin, W., Faure, M., Shi, Y., Wang, Q., Li, Z., 2008. Palaeozoic tectonics of the southwestern Chinese Tianshan: new insights from a structural study of the high-pressure/low-temperature metamorphic belt. *Int. J. Earth Sci.* 98, DOI 10.1007/s00531-008-0371-7.

Liu, X., Su, W., Gao, J., Li, J., Jiang, T., Zhang, X., Ge, X., 2014. Paleozoic subduction erosion involving accretionary wedge sediments in the South Tianshan Orogen: Evidence from geochronological and geochemical studies on eclogites and their host metasediments. *Lithos* 210, 89–110. <https://doi.org/10.1016/j.lithos.2014.09.017>

Liu, X.-C., Wu, Y.-B., Gao, S., Wang, H., Zheng, J.-P., Hu, Z.-C., Zhou, L., and Yang, S.-H., 2014b, Record of multiple stage channelized fluid and melt activities in deeply subducted slab from zircon U–Pb age and Hf–O isotope compositions: *Geochimica et Cosmochimica Acta*, v. 144, p. 1–24.

Liu, Y., Gao, S., Hu, Z., Gao, C., Zong, K., Wang, D., 2009. Continental and oceanic crust recycling-induced melt-peridotite interactions in the Trans-North China Orogen: U-Pb dating, Hf isotopes and trace elements in zircons from mantle xenoliths. *J. Petrol.* 51, 537–571. <https://doi.org/10.1093/petrology/egp082>

Locatelli, M., Verlaguet, A., Agard, P., Federico, L., Angiboust, S., 2018. Intermediate-depth brecciation along the subduction plate interface (Monviso eclogite, W. Alps). *Lithos* 320–321, 378–402. <https://doi.org/10.1016/j.lithos.2018.09.028>

Long, L., Gao, J., Klemd, R., Beier, C., Qian, Q., Zhang, X., Wang, J., Jiang, T., 2011. Geochemical and geochronological studies of granitoid rocks from the Western Tianshan Orogen: Implications for continental growth in the southwestern Central Asian Orogenic Belt. *Lithos* 126, 321-340.

Loury, C., Rolland, Y., Cenko-Tok, B., Lanari, P., Guillot, S., 2016. Late Paleozoic evolution of the South Tien Shan: Insights from P – T estimates and allanite geochronology on retrogressed eclogites (Chatkal range, Kyrgyzstan). *J. Geodyn.* 96, 62–80. <https://doi.org/10.1016/j.jog.2015.06.005>

Loury, C., Rolland, Y., Guillot, S., Lanari, P., Ganino, C., Mélis, R., Jourdon, A., Petit, C., Beyssac, O., Gallet, S., Monié, P., Melis, R., Jourdon, A., Petit, C., Beyssac, O., Gallet, S., Monié, P., 2018. Tectonometamorphic evolution of the Atbashi high-pressure units (Kyrgyz CAOB, Tien Shan): implications for the closure of the Turkestan Ocean and continental subduction-exhumation of the South Kazakh continental margin. *J. Metamorph. Geol.* 959–985. <https://doi.org/10.1111/jmg.12423>

Lü, Z., Bucher, K., 2018. The coherent ultrahigh-pressure terrane of the Tianshan meta-ophiolite belt, NW China. *Lithos* 314–315, 260–273. <https://doi.org/10.1016/j.lithos.2018.06.004>

Lü, Z., Bucher, K., Zhang, L., Du, J., 2012. The Habutengsu metapelites and metagreywackes in western Tianshan, China: Metamorphic evolution and tectonic implications. *J. Metamorph. Geol.* 30, 907–926. <https://doi.org/10.1111/j.1525-1314.2012.01002.x>

Lü, Z., Zhang, L., 2016. Differential Evolution of High-Pressure and Ultrahigh-Pressure Metapelites from Habutengsu, Chinese Western Tianshan: Phase Equilibria Modelling and $^{40}\text{Ar}/^{39}\text{Ar}$ Geochronology. *Acta Geol. Sin.* 90, 628–640. <https://doi.org/10.1111/1755-6724.12695>

Lü, Z., Zhang, L., Du, J., and Bucher, K., 2008, Coesite inclusions in garnet from eclogitic rocks in western Tianshan, northwest China: convincing proof of UHP metamorphism: *American Mineralogist*, v. 93, no. 11-12, p. 1845-1850.

Lü, Z., Zhang, L., Du, J., Bucher, K., 2009. Petrology of coesite-bearing eclogite from Habutengsu Valley, western Tianshan, NW China and its tectonometamorphic implication. *J. Metamorph. Geol.* 27, 773–787. <https://doi.org/10.1111/j.1525-1314.2009.00845.x>

Lü, Z., Zhang, L., Du, J., Yang, X., Tian, Z., Xia, B., 2012. Petrology of HP metamorphic veins in coesite-bearing eclogite from western Tianshan, China: Fluid processes and elemental mobility during exhumation in a cold subduction zone. *Lithos* 136–139, 168–186. <https://doi.org/10.1016/j.lithos.2011.10.011>

Lü, Z., Zhang, L.F., 2012. Coesite in the eclogite and schist of the Atantayi Valley, southwestern Tianshan, China. *Chinese Sci. Bull.* 57, 1467–1472. <https://doi.org/10.1007/s11434-012-4979-4>

Lucassen, F., Dulski, P., Abart, R., Franz, G., Rhede, D., and Romer, R. L., 2010, Redistribution of HFSE elements during rutile replacement by titanite: Contributions to Mineralogy and Petrology, v. 160, no. 2, p. 279-295.

Ludwig, K.R., 2003. A Geochronological Toolkit for Microsoft Excel. Berkeley Geochronol. Center, California, Berkeley 39 pp.

Lv, Z., and Zhang, L.-F., 2016, Differential Evolution of High-Pressure and Ultrahigh-Pressure Metapelites from Habutengsu, Chinese Western Tianshan: Phase Equilibria Modelling and $40\text{Ar}/39\text{Ar}$ Geochronology: *Acta Geologica Sinica - English Edition*, v. 90, no. 2, p. 628-640.

Lyubetskaya, T., Ague, J.J., 2009. Effect of metamorphic reactions on thermal evolution in collisional orogens. *Journal of Metamorphic Geology* 27, 579-600.

Mako, C., Caddick, M., 2017. Magnitudes of Shear Heating in Metamorphic Systems With Temperature Dependent Rheology, AGU Fall Meeting Abstracts.

Maluski, H., Monié, P., 1988. 40Ar - 39Ar laser probe multi-dating inside single biotites of a Variscan orthogneiss (Pinet, Massif Central, France). *Chem. Geol. Isot. Geosci. Sect.* 73, 245–263. [https://doi.org/http://dx.doi.org/10.1016/0168-9622\(88\)90005-X](https://doi.org/http://dx.doi.org/10.1016/0168-9622(88)90005-X)

Martin, L. A. J., Duchêne, S., Deloule, E., and Vanderhaeghe, O., 2008, Mobility of trace elements and oxygen in zircon during metamorphism: Consequences for geochemical tracing: *Earth and Planetary Science Letters*, v. 267, no. 1-2, p. 161-174.

Martin, L., Duchêne, S., Deloule, E., and Vanderhaeghe, O., 2006, The isotopic composition of zircon and garnet: A record of the metamorphic history of Naxos, Greece: *Lithos*, v. 87, no. 3-4, p. 174-192.

Martin, L., Hermann, J., Gauthiez-Putallaz, L., Whitney, D., Vitale Brovarone, A., Fornash, K., Evans, N.J., 2014. Lawsonite geochemistry and stability—implication for trace element and water cycles in subduction zones. *Journal of Metamorphic Geology* 32, 455-478.

McKenzie, D.P., Parker, R.L., 1967. The North Pacific: an example of tectonics on a sphere. *Nature* 216, 1276–1280. <https://doi.org/10.1038/2161276a0>

Meyer, M., Klemd, R., John, T., Gao, J., and Menneken, M., 2016, An (in-) coherent metamorphic evolution of high-pressure eclogites and their host rocks in the Chinese southwest Tianshan?: *Journal of Metamorphic Geology*, v. 34, no. 2, p. 121-146.

Meyer, M., Klemd, R., John, T., Gao, J., Menneken, M., 2016. An (in-) coherent metamorphic evolution of high-pressure eclogites and their host rocks in the Chinese southwest Tianshan? *J. Metamorph. Geol.* 34, 121–146.

Miller, J., and Cartwright, I., 2000, Distinguishing between seafloor alteration and fluid flow during subduction using stable isotope geochemistry: examples from Tethyan ophiolites in the Western Alps: *Journal of Metamorphic Geology*, v. 18, no. 5, p. 467-482.

Moore, S., Carlson, W., Hesse, M., 2013. Origins of yttrium and rare earth element distributions in metamorphic garnet. *Journal of Metamorphic Geology* 31, 663-689.

Moreno, M.S., Bolte, J., Klotz, J., Melnick, D., 2009. Impact of megathrust geometry on inversion of coseismic slip from geodetic data: Application to the 1960 Chile earthquake. *Geophys. Res. Lett.* 36, 1–5. <https://doi.org/10.1029/2009GL039276>

Morimoto, N., 1988, Nomenclature of pyroxenes: *Mineralogy and Petrology*, v. 39, no. 1, p. 55-76.

Mühlberg, M., Hegner, E., Klemd, R., Pfänder, J.A., Kaliwoda, M., Biske, Y.S., 2016. Late Carboniferous high-pressure metamorphism of the Kassan Metamorphic Complex (Kyrgyz Tianshan) and assembly of the SW Central Asian Orogenic Belt. *Lithos* 264, 41–55. <https://doi.org/10.1016/j.lithos.2016.08.008>

Okay, A.I., Xu, S., Sengor, A.M.C., 1989. Coesite from the Dabie Shan eclogites, central China. *Eur. J. Mineral.* 1, 595–598.

Otamendi, J.E., Jesús, D., Douce, A.E.P., Castro, A., 2002. Rayleigh fractionation of heavy rare earths and yttrium during metamorphic garnet growth. *Geology* 30, 159-162.

Pearce, J. A., 2008, Geochemical fingerprinting of oceanic basalts with applications to ophiolite classification and the search for Archean oceanic crust: *Lithos*, v. 100, no. 1-4, p. 14-48.

Penniston-Dorland, S.C., Kohn, M.J., Manning, C.E., 2015. The global range of subduction zone thermal structures from exhumed blueschists and eclogites: Rocks are hotter than models. *Earth and Planetary Science Letters* 428, 243-254.

Penniston-Dorland, S.C., Kohn, M.J., Piccoli, P.M., 2018. A mélange of subduction temperatures: Evidence from Zr-in-rutile thermometry for strengthening of the subduction interface. *Earth and Planetary Science Letters* 482, 525-535.

Philippot, P., van Roermund, H.L.M., 1992. Deformation processes in eclogitic rocks: evidence for the rheological delamination of the oceanic crust in deeper levels of subduction zones. *J. Struct. Geol.* 14, 1059–1077. [https://doi.org/10.1016/0191-8141\(92\)90036-V](https://doi.org/10.1016/0191-8141(92)90036-V)

Plafker, G., 1965. Tectonic Deformation Associated with the 1964 Alaska Earthquake. *Science* (80-.). 148, 1675–1687. <https://doi.org/10.2307/1716697>

Plank, T., Langmuir, C.H., 1998. The chemical composition of subducting sediment and its consequences for the crust and mantle, *Chemical Geology*. na. [https://doi.org/10.1016/S0009-2541\(97\)00150-2](https://doi.org/10.1016/S0009-2541(97)00150-2)

Platt, J.P., 1986. Dynamics of orogenic wedges and the uplift of high-pressure metamorphic rocks. *Geol. Soc. Am. Bull.* 97, 1037–1053. [https://doi.org/10.1130/0016-7606\(1986\)97<1037:DOOWAT>2.0.CO;2](https://doi.org/10.1130/0016-7606(1986)97<1037:DOOWAT>2.0.CO;2)

Platt, J.P., 1987. The uplift of high-pressure-low-temperature metamorphic rocks. *Philos. Trans. A* 321, 87–103.

Plunder, A., Agard, P., Chopin, C., Pourteau, A., Okay, A.I., 2015. Accretion, underplating and exhumation along a subduction interface: From subduction initiation to continental subduction (Tavşanlı zone, W. Turkey). *Lithos* 226, 233-254.

Pollington, A.D., Baxter, E.F., 2010. High resolution Sm–Nd garnet geochronology reveals the uneven pace of tectonometamorphic processes. *Earth and Planetary Science Letters* 293, 63-71.

Prior, D.J., Wheeler, J., Peruzzo, L., Spiess, R., Storey, C., 2002. Some garnet microstructures: an illustration of the potential of orientation maps and misorientation analysis in microstructural studies. *Journal of Structural Geology* 24, 999-1011.

Pu, X.-F., Song, S.-G., Zhang, L.-F., and Wei, C.-J., 2011, Silurian arc volcanic slices and their tectonic implications in the southwestern Tianshan UHPM belt, NW China: *Acta Petrologica Sinica*, v. 27, no. 6, p. 1675-1687.

Pyle, J.M., Spear, F.S., 1999. Yttrium zoning in garnet: coupling of major and accessory phases during metamorphic reactions. *Geological Materials Research* 1, 1-49.

Qian, Q., Gao, J., Xiong, X., Long, L., and Huang, D., 2006, Petrogenesis and tectonic settings of Carboniferous volcanic rocks from north Zhaosu, western Tianshan

Mountains: constraints from petrology and geochemistry: *Acta Petrol Sin.*, v. 22, no. 5, p. 1307-1323.

Royden, L.H., 1993. The steady state thermal structure of eroding orogenic belts and accretionary prisms. *Journal of Geophysical Research: Solid Earth* 98, 4487-4507.

Rubatto, D., 2002, Zircon trace element geochemistry: partitioning with garnet and the link between U–Pb ages and metamorphism: *Chemical Geology*, v. 184, no. 1, p. 123-138.

Rubatto, D., 2017. Zircon: The Metamorphic Mineral. *Rev. Mineral. Geochemistry* 83, 261–295. <https://doi.org/10.2138/rmg.2017.83.10>

Rubatto, D., and Angiboust, S., 2015, Oxygen isotope record of oceanic and high-pressure metasomatism: a P–T–time–fluid path for the Monviso eclogites (Italy): *Contributions to Mineralogy and Petrology*, v. 170, no. 5-6.

Rubatto, D., and Hermann, J., 2003, Zircon formation during fluid circulation in eclogites (Monviso, Western Alps): implications for Zr and Hf budget in subduction zones: *Geochimica et Cosmochimica Acta*, v. 67, no. 12, p. 2173-2187.

Rubatto, D., Hermann, J., 2001. Exhumation as fast as subduction? *Geology* 29, 3-6.

Rudnick, R., and Gao, S., 2003, Composition of the continental crust: *Treatise on geochemistry*, v. 3, p. 1-64.

Rudnick, R.L., Gao, S., 2003. Composition of the Continental Crust. *Treatise on Geochemistry* 1, 1–51. <https://doi.org/10.1016/b978-0-08-095975-7.00301-6>

Ruffet, G., Gruau, G., Ballèvre, M., Féraud, G., and Philippot, P., 1997, Rb-Sr and ⁴⁰Ar-³⁹Ar laser probe dating of high-pressure phengites from the Sesia zone (Western Alps): underscoring of excess argon and new age constraints on the high-pressure metamorphism: *Chemical Geology*, v. 141, no. 1, p. 1-18.

Ruffet, G., Gruau, G., Ballèvre, M., Féraud, G., Philippot, P., 1997. Rb-Sr and ⁴⁰Ar-³⁹Ar laser probe dating of high-pressure phengites from the Sesia zone (Western Alps): underscoring of excess argon and new age constraints on the high-pressure metamorphism. *Chem. Geol.* 141, 1–18.

Ruh, J., Le Pourhiet, L., Agard, P., Burov, E., Gerya, T., 2015. Tectonic slicing of subducting oceanic crust along plate interfaces: Numerical modeling. *Geochemistry, Geophysics, Geosystems* 16, 3505-3531.

Samson, S.D., Alexander Jr, E.C., 1987. Calibration of the interlaboratory ⁴⁰Ar-³⁹Ar dating standard, MMhb-1. *Chem. Geol. Isot. Geosci. Sect.* 66, 27–34.

Sasaki, J., Peterson, N.L., Hoshino, K., 1985. Tracer impurity diffusion in single-crystal rutile (TiO₂-x). *J. Phys. Chem. Solids* 46, 1267–1283. [https://doi.org/10.1016/0022-3697\(85\)90129-5](https://doi.org/10.1016/0022-3697(85)90129-5)

Schaeffer, O., ... H.M.-L. and P., 1977, U., 1977. Laser Ar-39-Ar-40 study of Apollo 17 basalts. *Lunar Planet. Sci. Conf. Proc.* 8, 1489–1499.

Schaltegger, U., Davies, J.H.F.L., 2017. Petrochronology of Zircon and Baddeleyite in Igneous Rocks: Reconstructing Magmatic Processes at High Temporal Resolution. *Rev. Mineral. Geochemistry* 83, 297–328. <https://doi.org/10.2138/rmg.2017.83.10>

Scheltens, M., Zhang, L., Xiao, W., Zhang, J., 2015. Northward subduction-related orogenesis of the southern Altaids: Constraints from structural and metamorphic analysis of the HP/UHP accretionary complex in Chinese southwestern Tianshan, NW China. *Geosci. Front.* 6, 191–209. <https://doi.org/10.1016/j.gsf.2014.08.002>

Schumacher, R., Rötzler, K., Maresch, W., 1999. Subtle oscillatory zoning in garnet from regional metamorphic phyllites and mica schists, western Erzgebirge, Germany. *The Canadian Mineralogist* 37, 381-403.

Shen, T. ting, Wu, F. yuan, Zhang, L. fei, Hermann, J., Li, X. ping, Du, J. xue, 2016. In-situ U-Pb dating and Nd isotopic analysis of perovskite from a rodingite blackwall associated with UHP serpentinite from southwestern Tianshan, China. *Chem. Geol.* 431, 67–82. <https://doi.org/10.1016/j.chemgeo.2016.03.029>

Shen, T., Hermann, J., Zhang, L., Lü, Z., Padrón-Navarta, J.A., Xia, B., Bader, T., 2014. UHP metamorphism documented in Ti-chondrodite- and Ti-clinohumite-bearing serpentinitized ultramafic rocks from Chinese southwestern Tianshan. *J. Petrol.* 56, 1425–1458. <https://doi.org/10.1093/petrology/egv042>

Shen, T.-T., Hermann, J., Zhang, L.-F., Lü, Z., Padrón-Navarta, J. A., Xia, B., and Bader, T., 2015, UHP Metamorphism Documented in Ti-chondrodite- and Ti-clinohumite-bearing Serpentinized Ultramafic Rocks from Chinese Southwestern Tianshan: *Journal of Petrology*, v. 56, no. 7, p. 1425-1458.

Shutong, X., Okay, A.I., Shouyuan, J., Sengör, A.M.C., Wen, S., Yican, L., Laili, J., 1992. Diamond from the Dabie Shan metamorphic rocks and its implication for tectonic setting. *Science* (80-.). 80–82.

Simonov, V.A., Sakiev, K.S., Volkova, N.I., Stupakov, S.I., Travin, A. V, 2008. Conditions of formation of the Atbashi Ridge eclogites (South Tien Shan). *Russ. Geol. Geophys.* 49, 803–815. <https://doi.org/https://doi.org/10.1016/j.rgg.2008.04.001>

Simons, M., Minson, S.E., Sladen, A., Ortega, F., Jiang, J., Owen, S.E., Meng, L., Ampuero, J.P., Wei, S., Chu, R., Helmberger, D. V., Kanamori, H., Hetland, E., Moore, A.W., Webb, F.H., 2011. The 2011 magnitude 9.0 Tohoku-Oki earthquake: Mosaicking the megathrust from seconds to centuries. *Science* (80-.). 332, 1421–1425. <https://doi.org/10.1126/science.1206731>

Singh, S.C., Hananto, N., Mukti, M., Robinson, D.P., Das, S., Chauhan, A., Carton, H., Gratacos, B., Midnet, S., Djajadihardja, Y., Harjono, H., 2011. Aseismic zone and earthquake segmentation associated with a deep subducted seamount in Sumatra. *Nat. Geosci.* 4, 308–311. <https://doi.org/10.1038/ngeo1119>

Skora, S., Baumgartner, L.P., Mahlen, N.J., Johnson, C.M., Pilet, S., Hellebrand, E., 2006. Diffusion-limited REE uptake by eclogite garnets and its consequences for Lu–Hf and Sm–Nd geochronology. *Contributions to Mineralogy and Petrology* 152, 703–720.

Skora, S., Baumgartner, L.P., Mahlen, N.J., Lapen, T.J., Johnson, C.M., Bussy, F., 2008. Estimation of a maximum Lu diffusion rate in a natural eclogite garnet. *Swiss Journal of Geosciences* 101, 637–650.

Skora, S., Lapen, T.J., Baumgartner, L.P., Johnson, C.M., Hellebrand, E., Mahlen, N.J., 2009. The duration of prograde garnet crystallization in the UHP eclogites at Lago di Cignana, Italy. *Earth and Planetary Science Letters* 287, 402–411.

Smith, D.C., 1984. Coesite in clinopyroxene in the Caledonides and its implications for geodynamics. *Nature* 310, 641–644.

Sneeringer, M., Hart, S. R., and Shimizu, N., 1984, Strontium and samarium diffusion in diopside: *Geochimica et Cosmochimica Acta*, v. 48, no. 8, p. 1589-1608.

Soldner, J., Oliot, E., Schulmann, K., Štípská, P., Kusbach, V., Anczkiewicz, R., 2017. Metamorphic P–T–t–d evolution of (U)HP metabasites from the South Tianshan accretionary complex (NW China) — Implications for rock deformation during exhumation in a subduction channel. *Gondwana Res.* 47, 161–187. <https://doi.org/10.1016/j.gr.2016.07.007>

Sorensen, S. S., Grossman, J. N., and Perfit, M. R., 1997, Phengite-hosted LILE enrichment in eclogite and related rocks: implications for fluid-mediated mass transfer in subduction zones and arc magma genesis: *Journal of Petrology*, v. 38, no. 1, p. 3–34.

Spandler, C., Hermann, J., Arculus, R., Mavrogenes, J., 2003. Redistribution of trace elements during prograde metamorphism from lawsonite blueschist to eclogite facies; implications for deep subduction-zone processes. *Contributions to Mineralogy and Petrology* 146, 205–222.

Spandler, C., Pirard, C., 2013. Element recycling from subducting slabs to arc crust: A review. *Lithos* 170-171, 208-223.

Stacey, J. t., and Kramers, J., 1975, Approximation of terrestrial lead isotope evolution by a two-stage model: *Earth and Planetary Science Letters*, v. 26, no. 2, p. 207-221.

Stöckhert, B., Renner, J., 1998. Rheology of crustal rocks at ultrahigh pressure, in: *When Continents Collide: Geodynamics and Geochemistry of Ultrahigh-Pressure Rocks*. Springer, pp. 57–95.

Su, W., Gao, J., Klemd, R., Li, J.-L., Zhang, X., Li, X.-H., Chen, N.-S., Zhang, L., 2010. U–Pb zircon geochronology of Tianshan eclogites in NW China: implication for the collision between the Yili and Tarim blocks of the southwestern Altaids. *Eur. J. Mineral.* 22, 473–478. <https://doi.org/10.1127/0935-1221/2010/0022-2040>

Sun, S. -s., McDonough, W.F., 1989. Chemical and isotopic systematics of oceanic basalts: implications for mantle composition and processes. *Geol. Soc. London, Spec. Publ.* 42, 313–345. <https://doi.org/10.1144/GSL.SP.1989.042.01.19>

Sverjensky, D.A., Stagno, V., Huang, F., 2014. Important role for organic carbon in subduction-zone fluids in the deep carbon cycle. *Nat. Geosci.* 7, 909–913. <https://doi.org/10.1038/ngeo2291>

Syracuse, E.M., van Keken, P.E., Abers, G.A., 2010. The global range of subduction zone thermal models. *Phys. Earth Planet. Inter.* 183, 73–90. <https://doi.org/10.1016/j.pepi.2010.02.004>

Tan, Z., Agard, P., Gao, J., John, T., Li, J.L., Jiang, T., Bayet, L., Wang, X.S., Zhang, X.X., 2017. P–T–time–isotopic evolution of coesite-bearing eclogites: Implications for exhumation processes in SW Tianshan. *Lithos* 278–281, 1–25. <https://doi.org/10.1016/j.lithos.2017.01.010>

Tang, G.-Q., Li, X.-H., Li, Q.-L., Liu, Y., Ling, X.-X., and Yin, Q.-Z., 2015, Deciphering the physical mechanism of the topography effect for oxygen isotope measurements using a Cameca IMS-1280 SIMS: *J. Anal. At. Spectrom.*, v. 30, no. 4, p. 950-956.

Tang, G.-Q., Li, X.-H., Li, Q.-L., Liu, Y., Ling, X.-X., Yin, Q.-Z., 2015. Deciphering the physical mechanism of the topography effect for oxygen isotope measurements using a Cameca IMS-1280 SIMS. *J. Anal. At. Spectrom.* 30, 950–956. <https://doi.org/10.1039/c4ja00458b>

Tian, Z., and Wei, C., 2013, Metamorphism of ultrahigh-pressure eclogites from the Kebuerte Valley, South Tianshan, NW China: phase equilibria and P–T path: *Journal of Metamorphic Geology*, v. 31, no. 3, p. 281-300.

Tian, Z., Xiao, W., Sun, J., Windley, B.F., Glen, R., Han, C., Zhang, Z., Zhang, J., Wan, B., Ao, S., Song, D., 2014. Triassic deformation of Permian Early Triassic arc-related sediments in the Beishan (NW China): Last pulse of the accretionary orogenesis in the southernmost Altai. *Tectonophysics* 662, 363–384. <https://doi.org/10.1016/j.tecto.2015.01.009>

Tomkins, H.S., Powell, R., Ellis, D.J., 2007. The pressure dependence of the zirconium-in-rutile thermometer. *J. Metamorph. Geol.* 25, 703–713. <https://doi.org/10.1111/j.1525-1314.2007.00724.x>

Tsujimori, T., Ernst, W.G., 2013. Lawsonite blueschists and lawsonite eclogites as proxies for paleo-subduction zone processes: A review. *J. Metamorph. Geol.* n/a-n/a. <https://doi.org/10.1111/jmg.12057>

Tsujimori, T., Sisson, V.B., Liou, J.G., Harlow, G.E., Sorensen, S.S., 2006. Very-low-temperature record of the subduction process: A review of worldwide lawsonite eclogites. *Lithos* 92, 609–624.

Van Achterbergh, E., Ryan, C.G., Griffin, W.L., 1999. GLITTER: On-line interactive data reduction for the laser ablation inductively coupled plasma mass spectrometry microprobe, in: Ninth Annual VM Goldschmidt Conference.

van der Straaten, F., Halama, R., John, T., Schenk, V., Hauff, F., Andersen, N., 2012. Tracing the effects of high-pressure metasomatic fluids and seawater alteration in blueschist-facies overprinted eclogites: Implications for subduction channel processes. *Chem. Geol.* 292–293, 69–87. <https://doi.org/10.1016/j.chemgeo.2011.11.008>

van der Straaten, F., Schenk, V., John, T., Gao, J., 2008. Blueschist-facies rehydration of eclogites (Tian Shan, NW-China): Implications for fluid-rock interaction in the subduction channel. *Chem. Geol.* 255, 195–219. <https://doi.org/10.1016/j.chemgeo.2008.06.037>

van Keken, P.E., Hacker, B.R., Syracuse, E.M., Abers, G.A., 2011. Subduction factory: 4. Depth-dependent flux of H₂O from subducting slabs worldwide. *J. Geophys. Res.* 116. <https://doi.org/10.1029/2010jb007922>

Van Orman, J.A., Grove, T.L., Shimizu, N., 2001. Rare earth element diffusion in diopside: influence of temperature, pressure, and ionic radius, and an elastic model for diffusion in silicates. *Contributions to Mineralogy and Petrology* 141, 687-703.

Van Orman, J.A., Grove, T.L., Shimizu, N., Layne, G.D., 2002. Rare earth element diffusion in a natural pyrope single crystal at 2.8 GPa. *Contributions to Mineralogy and Petrology* 142, 416-424.

Vannucchi, P., Remitti, F., Bettelli, G., 2008. Geological record of fluid flow and seismogenesis along an erosive subducting plate boundary. *Nature* 451, 699–703. <https://doi.org/10.1038/nature06486>

Vannucchi, P., Sage, F., Phipps Morgan, J., Remitti, F., Collot, J.Y., 2012. Toward a dynamic concept of the subduction channel at erosive convergent margins with implications for interplate material transfer. *Geochemistry, Geophys. Geosystems* 13, 1–24. <https://doi.org/10.1029/2011GC003846>

Villa, I. M., 1998, *Isotopic closure: Terra Nova-Oxford*, v. 10, no. 1, p. 42-47.

Villa, I. M., and Puxeddu, M., 1994, Geochronology of the Larderello geothermal field: new data and the “closure temperature” issue: *Contributions to Mineralogy and Petrology*, v. 115, no. 4, p. 415-426.

Vitale Brovarone, A., Alard, O., Beyssac, O., Martin, L., Picatto, M., 2014. Lawsonite metasomatism and trace element recycling in subduction zones. *Journal of Metamorphic Geology* 32, 489-514.

Volkova, N., and Budanov, V., 1999, Geochemical discrimination of metabasalt rocks of the Fan–Karategin transitional blueschist/greenschist belt, South Tianshan, Tajikistan: seamount volcanism and accretionary tectonics: *Lithos*, v. 47, no. 3, p. 201-216.

Wada, I., Wang, K., 2009. Common depth of slab-mantle decoupling: Reconciling diversity and uniformity of subduction zones. *Geochemistry, Geophys. Geosystems* 10. <https://doi.org/10.1029/2009GC002570>

Wakabayashi, J., 2011. Mélanges of the Franciscan Complex, California: Diverse structural settings, evidence for sedimentary mixing, and their connection to subduction processes. *Geol. Soc. Am. Spec. Pap.* 480, 117–141.

Wakabayashi, J., 2015. Anatomy of a subduction complex: Architecture of the Franciscan Complex, California, at multiple length and time scales. *Int. Geol. Rev.* 57, 669–746. <https://doi.org/10.1080/00206814.2014.998728>

Waldhauser, F., Schaff, D.P., 2008. Large-scale relocation of two decades of Northern California seismicity using cross-correlation and double-difference methods. *J. Geophys. Res.* 113. <https://doi.org/10.1029/2007jb005479>

Wang, B., Faure, M., Shu, L., de Jong, K., Charvet, J., Cluzel, D., Jahn, B. m., Chen, Y., and Ruffet, G., 2010, Structural and geochronological study of high-pressure metamorphic rocks in the Kekesu section (northwestern China): Implications for the late Paleozoic tectonics of the Southern Tianshan: *The Journal of Geology*, v. 118, no. 1, p. 59-77.

Wang, B., Faure, M., Shu, L., de Jong, K., Charvet, J., Cluzel, D., Jahn, B., Chen, Y., Ruffet, G., 2010. Structural and Geochronological Study of High-Pressure Metamorphic Rocks in the Kekesu Section (Northwestern China): Implications for the Late Paleozoic Tectonics of the Southern Tianshan. *J. Geol.* 118, 59–77. <https://doi.org/10.1086/648531>

Wang, X.-S., Klemd, R., Gao, J., Jiang, T., Li, J.-L., Xue, S.-C., 2018. Final Assembly of the Southwestern Central Asian Orogenic Belt as Constrained by the Evolution of the South Tianshan Orogen: Links with Gondwana and Pangea. *J. Geophys. Res. Solid Earth* 0. <https://doi.org/doi:10.1029/2018JB015689>

Warren, C. J., 2013, Exhumation of (ultra-)high-pressure terranes: concepts and mechanisms: *Solid Earth*, v. 4, no. 1, p. 75-92.

Warren, C. J., Beaumont, C., and Jamieson, R. A., 2008, Modelling tectonic styles and ultra-high pressure (UHP) rock exhumation during the transition from oceanic subduction to continental collision: *Earth and Planetary Science Letters*, v. 267, no. 1-2, p. 129-145.

Warren, C., and Waters, D., 2006, Oxidized eclogites and garnet-blueschists from Oman: P–T path modelling in the NCFMASHO system: *Journal of Metamorphic Geology*, v. 24, no. 9, p. 783-802.

Warren, C.J., 2013. Exhumation of (ultra-)high-pressure terranes: concepts and mechanisms. *Solid Earth* 4, 75–92. <https://doi.org/10.5194/se-4-75-2013>

Warren, C.J., Beaumont, C., Jamieson, R.A., 2008. Formation and exhumation of ultra-high-pressure rocks during continental collision: Role of detachment in the subduction channel. *Geochemistry, Geophys. Geosystems* 9, n/a-n/a. <https://doi.org/10.1029/2007gc001839>

Watkins, J., Manga, M., Huber, C., Martin, M., 2008. Diffusion-controlled spherulite growth in obsidian inferred from H₂O concentration profiles. *Contributions to Mineralogy and Petrology* 157, 163-172.

Watson, E.B., Müller, T., 2009. Non-equilibrium isotopic and elemental fractionation during diffusion-controlled crystal growth under static and dynamic conditions. *Chemical Geology* 267, 111-124.

Watson, E.B., Wark, D.A., Thomas, J.B., 2006. Crystallization thermometers for zircon and rutile. *Contrib. to Mineral. Petrol.* 151, 413–433. <https://doi.org/10.1007/s00410-006-0068-5>

Weare, J.H., Stephens, J.R., Eugster, H.P., 1976. Diffusion metasomatism and mineral reaction zones; general principles and application to feldspar alteration. *American Journal of Science* 276, 767-816.

Wegener, A., 1912. Die Entstehung der Kontinente. *Geol. Rundschau* 3, 276–292. <https://doi.org/10.1007/bf02202896>

Wei, C. J., and Clarke, G. L., 2011, Calculated phase equilibria for MORB compositions: a reappraisal of the metamorphic evolution of lawsonite eclogite: *Journal of Metamorphic Geology*, v. 29, no. 9, p. 939-952.

Wei, C., Wang, W.E.I., Clarke, G.L., Zhang, L., Song, S., 2009. Metamorphism of High / ultrahigh-pressure Pelitic ^ Felsic Schist in the SouthTianshan Orogen , NW China : Phase Equilibria and P ^ T Path. *Petrology* 50, 1973–1991. <https://doi.org/10.1093/petrology/egp064>

Wei, C.-J., Powell, R., and Zhang, L.-F., 2003, Eclogites from the south Tianshan, NW China: petrological characteristic and calculated mineral equilibria in the Na₂O–CaO–FeO–MgO–Al₂O₃–SiO₂–H₂O system: *Journal of Metamorphic Geology*, v. 21, no. 2, p. 163-179.

Wei, C.-J., Wang, W., Clarke, G. L., Zhang, L.-F., and Song, S.-G., 2009, Metamorphism of high/ultrahigh-pressure pelitic–felsic schist in the South Tianshan Orogen, NW China: phase equilibria and P–T path: *Journal of Petrology*, v. 50, no. 10, p. 1973-1991.

Whitney, D. L., and Evans, B. W., 2010, Abbreviations for names of rock-forming minerals: *American Mineralogist*, v. 95, no. 1, p. 185-187.

Wiedenbeck, M., Alle, P., Corfu, F., Griffin, W.L., Meier, M., Oberli, F., Quadt, A. von, Roddick, J.C., Spiegel, W., 1995. Three natural zircon standards for U-Th-Pb, Lu-Hf, trace element and REE analyses. *Geostand. Newsl.* 19, 1–23.

Williams, I. S., 1998, U–Th–Pb geochronology by ion microprobe: *Reviews in Economic Geology*, v. 7, no. 1, p. 1-35.

Williams, M., and Jercinovic, M., The Assessment of Error in Electron Microprobe Trace Element Analysis, in *Proceedings AGU Spring Meeting Abstracts 2006*, Volume 1, p. 08.

Williams, M.L., Jercinovic, M.J., 2006. The Assessment of Error in Electron Microprobe Trace Element Analysis, in: AGU Spring Meeting Abstracts.

Wilson, J.T., 1973. Mantle plumes and plate motions. *Tectonophysics* 19, 149–164.
Worley, B., and Powell, R., 2000, High-precision relative thermobarometry: theory and a worked example: *Journal of Metamorphic Geology*, v. 18, no. 1, p. 91-102.

Xia, B., Zhang, L., Bader, T., Shen, T., Chen, N., 2016. Late Palaeozoic $^{40}\text{Ar}/^{39}\text{Ar}$ ages of the HP-LT metamorphic rocks from the Kekesu Valley, Chinese southwestern Tianshan: New constraints on exhumation tectonics. *Int. Geol. Rev.* 58, 389–404. <https://doi.org/10.1080/00206814.2015.1084487>

Xia, B., Zhang, L., Xia, Y., Bader, T., 2014. The tectonic evolution of the Tianshan Orogenic Belt: Evidence from U-Pb dating of detrital zircons from the Chinese southwestern Tianshan accretionary mélange. *Gondwana Res.* 25, 1627–1643. <https://doi.org/10.1016/j.gr.2013.06.015>

Xia, B., Zhang, L.-F., and Bader, T., 2014, Zircon U–Pb ages and Hf isotopic analyses of migmatite from the ‘paired metamorphic belt’ in Chinese SW Tianshan: Constraints on partial melting associated with orogeny: *Lithos*, v. 192-195, p. 158-179.

Xiao, W.-J., Zhang, L.-C., Qin, K.-Z., Sun, S., Li, J.-L., 2004. Paleozoic accretionary and collisional tectonics of the eastern Tianshan (China): Implications for the continental growth of central Asia. *Am. J. Sci.* 304, 370–395. <https://doi.org/10.2475/ajs.304.4.370>

Yamato, P., Agard, P., Burov, E., Le Pourhiet, L., Jolivet, L., Tiberi, C., 2007. Burial and exhumation in a subduction wedge: Mutual constraints from thermomechanical modeling and natural P-T-t data (Schistes Lustrés, western Alps). *J. Geophys. Res. Solid Earth* 112.

Yang, P., Rivers, T., 2003. The origin of Mn and Y annuli in garnet and the thermal dependence of P in garnet and Y in apatite in calc-pelite and pelite, Gagnon terrane, western Labrador. *American Mineralogist* 88, 1398-1398.

Yang, X., Zhang, L., Tian, Z., Bader, T., 2013. Petrology and U-Pb zircon dating of coesite-bearing metapelite from the Kebuerte Valley, Western Tianshan, China. *J. Asian Earth Sci.* 70–71, 295–307. <https://doi.org/10.1016/j.jseaes.2013.03.020>

Ye, K., Cong, B., Ye, D., 2000. The possible subduction of continental material to depths greater than 200 km. *Nature* 407, 734–736. <https://doi.org/10.1038/35037566>

Zack, T., Kronz, A., Foley, S.F., Rivers, T., 2002. Trace element abundances in rutiles from eclogites and associated garnet mica schists. *Chem. Geol.* 184, 97–122.

Zack, T., Moraes, R., Kronz, A., 2004. Temperature dependence of Zr in rutile: empirical calibration of a rutile thermometer. *Contrib. to Mineral. Petrol.* 148, 471–488.

Zhang LF, Lü, Z., Li XP, Bucher, K., 2007. A Comparative Study on the UHP Metamorphic Ophiolitic Rocks in Zermaat-Saas Zone, Western Alps and Western Tianshan, China. *Geol. J. China Univ.* 13, 498–506.

Zhang, L., Ai, Y., Li, X., Rubatto, D., Song, B., Williams, S., Song, S., Ellis, D., Liou, J.G., 2007. Triassic collision of western Tianshan orogenic belt, China: Evidence from SHRIMP U-Pb dating of zircon from HP/UHP eclogitic rocks. *Lithos* 96, 266–280. <https://doi.org/10.1016/j.lithos.2006.09.012>

Zhang, L., Chu, X., Zhang, L., Fu, B., Bader, T., Du, J., Li, X., 2018. The early exhumation history of the Western Tianshan UHP metamorphic belt, China: New constraints from titanite U–Pb geochronology and thermobarometry. *J. Metamorph. Geol.* 36, 631–651. <https://doi.org/10.1111/jmg.12422>

Zhang, L., Ellis, D.J., Arculus, R.J., Jiang, W., Wei, C., 2003. “Forbidden zone” subduction of sediments to 150 km depth - The reaction of dolomite to magnesite + aragonite in the UHPM metapelites from western Tianshan, China. *J. Metamorph. Geol.* 21, 523–529. <https://doi.org/10.1046/j.1525-1314.2003.00460.x>

Zhang, L., Wang, Y., Zhang, L., Lü, Z., 2018. Ultrahigh pressure metamorphism and tectonic evolution of southwestern Tianshan orogenic belt , China : a comprehensive review. *Geol. Soc. London, Spec. Publ.* 474.

Zhang, L.F., Du, J.X., Lü, Z., Yang, X., Gou, L.L., Xia, B., Chen, Z.Y., Wei, C.J., Song, S.G., 2013. A huge oceanic-type UHP metamorphic belt in southwestern Tianshan, China: Peak metamorphic age and P-T path. *Chinese Sci. Bull.* 58, 4378–4383. <https://doi.org/10.1007/s11434-013-6074-x>

Zhang, L.-J., Zhang, L.-F., Lü, Z., Bader, T., Chen, Z.-Y., 2016. Nb–Ta mobility and fractionation during exhumation of UHP eclogite from southwestern Tianshan, China. *Journal of Asian Earth Sciences* 122, 136-157.

Zheng, Y. F., Gao, T. S., Wu, Y. B., Gong, B., and Liu, X. M., 2007, Fluid flow during exhumation of deeply subducted continental crust: zircon U-Pb age and O-isotope studies of a quartz vein within ultrahigh-pressure eclogite: *Journal of Metamorphic Geology*, v. 25, no. 2, p. 267-283.

Zheng, Y.-f., 1991, Calculation of oxygen isotope fractionation in metal oxides: *Geochimica et Cosmochimica Acta*, v. 55, no. 8, p. 2299-2307.

Zong, K., Klemd, R., Yuan, Y., He, Z., Guo, J., Shi, X., Liu, Y., Hu, Z., Zhang, Z., 2017. The assembly of Rodinia: The correlation of early Neoproterozoic (ca. 900 Ma) high-grade metamorphism and continental arc formation in the southern Beishan Orogen, southern Central Asian Orogenic Belt (CAOB). *Precambrian Res.* 290, 32–48. <https://doi.org/10.1016/j.precamres.2016.12.010>

Appendix

Table S1: Sample list and analyses strategy

